

Functional Devices for Clean Energy and Advanced Sensor Applications

Guest Editors: Ruomeng Yu, Caofeng Pan, Owen J. Guy, Lin Dong,
and Matteo Tonzzer





Functional Devices for Clean Energy and Advanced Sensor Applications

Journal of Nanomaterials

Functional Devices for Clean Energy and Advanced Sensor Applications

Guest Editors: Ruomeng Yu, Caofeng Pan, Owen J. Guy,
Lin Dong, and Matteo Tonzzer



Copyright © 2016 Hindawi Publishing Corporation. All rights reserved.

This is a special issue published in "Journal of Nanomaterials." All articles are open access articles distributed under the Creative Commons Attribution License, which permits unrestricted use, distribution, and reproduction in any medium, provided the original work is properly cited.

Editorial Board

- Domenico Acierno, Italy
Katerina Aifantis, USA
Nageh K. Allam, USA
Margarida Amaral, Portugal
Martin Andersson, Sweden
Raul Arenal, Spain
Ilaria Armentano, Italy
Vincenzo Baglio, Italy
Lavinia Balan, France
Thierry Baron, France
Andrew R. Barron, USA
Reza Bayati, USA
Hongbin Bei, USA
Daniel Bellet, France
Stefano Bellucci, Italy
Enrico Bergamaschi, Italy
Samuel Bernard, France
D. Bhattacharyya, New Zealand
Sergio Bietti, Italy
Giovanni Bongiovanni, Italy
Theodorian Borca-Tasciuc, USA
Mohamed Bououdina, Bahrain
Torsten Brezesinski, Germany
C. Jeffrey Brinker, USA
Christian Brosseau, France
Philippe Caroff, Australia
Victor M. Castaño, Mexico
Albano Cavaleiro, Portugal
Bhanu P. S. Chauhan, USA
Shafiu Chowdhury, USA
Jin-Ho Choy, Republic of Korea
Kwang-Leong Choy, UK
Yu-Lun Chueh, Taiwan
Elisabetta Comini, Italy
Giuseppe Compagnini, Italy
David Cornu, France
Miguel A. Correa-Duarte, Spain
P. Davide Cozzoli, Italy
Shadi A. Dayeh, USA
Luca Deseri, USA
Yong Ding, USA
Philippe Dubois, Belgium
Zehra Durmus, Turkey
Joydeep Dutta, Oman
Ali Eftekhari, USA
- Jeffrey Elam, USA
Samy El-Shall, USA
Ovidiu Ersen, France
Claude Estournès, France
Andrea Falqui, KSA
Matteo Ferroni, Italy
Elena J. Foster, USA
Ilaria Fratoddi, Italy
Alan Fuchs, USA
Miguel A. Garcia, Spain
Siddhartha Ghosh, Singapore
P. K. Giri, India
Russell E. Gorga, USA
Jihua Gou, USA
Jean M. Greneche, France
Smrati Gupta, Germany
Kimberly Hamad-Schifferli, USA
Simo-Pekka Hannula, Finland
Michael Harris, USA
Yasuhiko Hayashi, Japan
F. Hernandez-Ramirez, Spain
Michael Z. Hu, USA
Nay Ming Huang, Malaysia
Shaoming Huang, China
David Hui, USA
Zafar Iqbal, USA
Balachandran Jeyadevan, Japan
Xin Jiang, Germany
Rakesh Joshi, Australia
J.-won Kang, Republic of Korea
Hassan Karimi-Maleh, Iran
Antonios Kelarakis, UK
Alireza Khataee, Iran
Ali Khorsand Zak, Iran
Philippe Knauth, France
Ralph Krupke, Germany
Christian Kübel, Germany
Prashant Kumar, UK
Michele Laus, Italy
Eric Le Bourhis, France
Jun Li, Singapore
Meiyong Liao, Japan
Shijun Liao, China
Silvia Licoccia, Italy
Wei Lin, USA
- Nathan C. Lindquist, USA
Zainovia Lockman, Malaysia
Nico Lovergine, Italy
Jim Low, Australia
Jue Lu, USA
Ed Ma, USA
Laura M. Maestro, Spain
Gaurav Mago, USA
Muhamamd A. Malik, UK
Devanesan Mangalaraj, India
Sanjay R. Mathur, Germany
Tony McNally, UK
Yogendra Mishra, Germany
Paulo Cesar Morais, Brazil
Paul Munroe, Australia
Jae-Min Myoung, Republic of Korea
Rajesh R. Naik, USA
Albert Nasibulin, Russia
Toshiaki Natsuki, Japan
Koichi Niihara, Japan
Natalia Noginova, USA
Sherine Obare, USA
Won-Chun Oh, Republic of Korea
Atsuto Okamoto, Japan
Abdelwahab Omri, Canada
Ungyu Paik, Republic of Korea
Piersandro Pallavicini, Italy
Edward A. Payzant, USA
Alessandro Pegoretti, Italy
Ton Peijs, UK
Oscar Perales-Pérez, Puerto Rico
Jorge Pérez-Juste, Spain
Alexey P. Popov, Finland
Philip D. Rack, USA
Peter Reiss, France
Orlando Rojas, USA
Marco Rossi, Italy
Ilker S. Bayer, Italy
Cengiz S. Ozkan, USA
Sudipta Seal, USA
Shu Seki, Japan
Vladimir Šepelák, Germany
Huaiyu Shao, Japan
Prashant Sharma, USA
Donglu Shi, USA



Bhanu P. Singh, India
Surinder Singh, USA
Vladimir Sivakov, Germany
Ashok Sood, USA
Adolfo Speghini, Italy
Marinella Striccoli, Italy
Xuping Sun, KSA
Ashok K. Sundramoorthy, USA
Angelo Taglietti, Italy
Bo Tan, Canada
Leander Tapfer, Italy
Valeri P. Tolstoy, Russia

Muhammet S. Toprak, Sweden
R. Torrecillas, Spain
Achim Trampert, Germany
Takuya Tsuzuki, Australia
Tamer Uyar, Turkey
Bala Vaidhyanathan, UK
Luca Valentini, Italy
Rajender S. Varma, USA
Ester Vazquez, Spain
Antonio Villaverde, Spain
Ajayan Vinu, Australia
Ruibing Wang, Macau

Shiren Wang, USA
Yong Wang, USA
Magnus Willander, Sweden
Ping Xiao, UK
Zhi Li Xiao, USA
Yangchuan Xing, USA
Doron Yadlovker, Israel
Yoke K. Yap, USA
Kui Yu, Canada
William Yu, USA
Michele Zappalorto, Italy
Renyun Zhang, Sweden

Contents

Functional Devices for Clean Energy and Advanced Sensor Applications

Ruomeng Yu, Caofeng Pan, Owen J. Guy, Lin Dong, and Matteo Tonezzer

Volume 2016, Article ID 9162634, 2 pages

A Self-Powered Triboelectric Nanosensor for PH Detection

Ying Wu, Yuanjie Su, Junjie Bai, Guang Zhu, Xiaoyun Zhang, Zhanolin Li, Yi Xiang, and Jingliang Shi

Volume 2016, Article ID 5121572, 6 pages

Cd²⁺ Exchange for Na⁺ and K⁺ in the Interlayer of Montmorillonite: Experiment and Molecular Simulation

Lefu Mei, Huashang Tao, Chao He, Xuebing Xin, Libing Liao, Limei Wu, and Guocheng Lv

Volume 2015, Article ID 925268, 9 pages

A General Synthesis Strategy for Hierarchical Porous Metal Oxide Hollow Spheres

Huadong Fu, Feng Ren, Weiming Su, Jinlin Yang, and Ruiping Liu

Volume 2015, Article ID 473853, 7 pages

Theoretical Studies of Electronic Structure and Photophysical Properties of a Series of Indoline Dyes with Triphenylamine Ligand

Xue-Feng Ren, Jun Zhang, and Guo-Jun Kang

Volume 2015, Article ID 605728, 9 pages

Power-Interrogated Refractive Index Sensor Using Long Period Grating in Photonic Crystal Fiber

X. L. Jiang, Z. T. Gu, and L. Zheng

Volume 2015, Article ID 126098, 4 pages

Recent Progress in Ohmic/Schottky-Contacted ZnO Nanowire Sensors

Xiaoli Zhao, Ranran Zhou, Qilin Hua, Lin Dong, Ruomeng Yu, and Caofeng Pan

Volume 2015, Article ID 854094, 20 pages

Hydrothermal Growth and Hydrogen Selective Sensing of Nickel Oxide Nanowires

Thi Thanh Le Dang, Matteo Tonezzer, and Van Hieu Nguyen

Volume 2015, Article ID 785856, 8 pages

Research on the Preparation and Mechanism of the Organic Montmorillonite and Its Application in Drilling Fluid

Xiaolong Wang, Baolin Liu, and Peizhi Yu

Volume 2015, Article ID 514604, 10 pages

In-Channel-Grown Polypyrrole Nanowire for the Detection of DNA Hybridization in an Electrochemical Microfluidic Biosensor

Thi Luyen Tran, Thi Xuan Chu, Phuc Quan Do, Duc Thanh Pham, Van Vu Quan Trieu, Dang Chinh Huynh, and Anh Tuan Mai

Volume 2015, Article ID 458629, 7 pages

Editorial

Functional Devices for Clean Energy and Advanced Sensor Applications

Ruomeng Yu,¹ Caofeng Pan,² Owen J. Guy,³ Lin Dong,⁴ and Matteo Tonezzer⁵

¹*School of Materials Science and Engineering, Georgia Institute of Technology, Atlanta, GA 30332-0245, USA*

²*Beijing Institute of Nanoenergy and Nanosystems, Chinese Academy of Sciences, Beijing 100083, China*

³*College of Engineering, Swansea University, Swansea SA2 8PP, UK*

⁴*School of Materials Science and Engineering, Zhengzhou University, Zhengzhou 450001, China*

⁵*IMEM-CNR, sede di Trento-FBK, Via alla Cascata 56/C, 38123 Povo, Italy*

Correspondence should be addressed to Ruomeng Yu; ruomengyu@gatech.edu

Received 29 February 2016; Accepted 1 March 2016

Copyright © 2016 Ruomeng Yu et al. This is an open access article distributed under the Creative Commons Attribution License, which permits unrestricted use, distribution, and reproduction in any medium, provided the original work is properly cited.

The recent global increase of awareness about the environment pollution and the limited resources which are being rapidly consumed needs solutions. Networks of sensors are needed to monitor in real-time the quality of water, air, and in general the health of the ambient we are living in. Methods to clean wastewater and requalify industrial waste are required in order to recover the scars from decades of consumerism. Novel ecofriendly technologies will allow increased production of green and sustainable energy and its safe storage and transportation.

Nanoscience and nanotechnology are powerful instruments helping to face these challenges. A good control on nanometric size of materials permits reaching a wide range of new physicochemical properties and addressing problems which could not otherwise be solved. This approach can be utilized in several ways in different contexts and applications, as can be seen in this special issue.

X. L. Jiang et al. studied theoretically a refractive index sensor based on a long period grating written in a specially designed photonic crystal fiber. They used hexagonal pattern with 5 rings of air holes around the central one. Using the finite element method and incorporating anisotropic perfectly matched layers as absorbing boundary conditions, they were able to evaluate the real and imaginary parts of the leaky mode. The shift of the resonant wavelength is sensitive only to the refractive index in the larger holes of the outer ring, which can be filled with a selected analyte.

H. Fu et al. developed a method to realize TiO₂ (or any other metal oxide) hollow spheres by using hydrothermally synthesized colloidal carbon spheres as template. By adjusting the growth temperature and duration, the diameter of the spheres could be changed from 350 to 600 nm, whilst their wall thickness and specific surface area can be regulated by adjusting the concentration of inorganic precursor. The monodispersed hollow spheres with hierarchically pore structure can be used as catalyst, battery, gas sensor, and functional material in several applications.

X. Wang et al. investigated, both theoretically and experimentally, a new type of environment-friendly montmorillonite, a clay mineral used to adjust rheology and fluid loss of drilling fluid. They chose a new kind of green and steady ionic liquid as the intercalated agent (1-hexadecyl-3-methylimidazolium chloride monohydrate or C₁₂mimCl) and varied its concentration from 10 to 5000 mg/L. Simulations and experimental data were compared and, changing the amount of intercalated C₁₂mimCl, functional parameters of the composite material such as viscosity and thixotropic loop area were improved for application as green clay composite for drilling fluid system.

X.-F. Ren et al. theoretically studied some novel environment-friendly dyes for dye-sensitized solar cells. The density functional theory was used to explore four dyes based on triphenylamine-containing indoline, changing some donor functional groups. The authors investigated the optimized

geometry of each dye, the electronic coupling interaction between the dyes and TiO_2 nanoparticles, and the HOMO and LUMO energy levels. They calculated the absorption spectra, the photoelectric conversion efficiency, and the light-harvesting efficiency of the four dyes, finding that one of them is expected to have an improved energy conversion efficiency compared to the commercial D149 dye.

T. L. Tran et al. developed an integrated three-electrode DNA sensor inside a microfluidic microchamber. Polypyrrole nanowires with diameters ranging from 80 to 110 nm were electrochemically synthesized *in situ* on a Pt working electrode inside the sealed microchamber. Then DNA probe sequences were immobilized on the PPy nanowires using the adsorption method, obtaining a specific DNA biosensor. The device can detect down to 20 pM of complementary DNA with a response time of few seconds at room temperature.

T. T. L. Dang et al. synthesized polycrystalline NiO nanowires via a two-step method consisting in a hydrothermal growth followed by a thermal annealing. Dropping the nanowires between two interdigitated electrodes, they fabricated sensitive and quick gas sensors with a good selectivity towards hydrogen.

The paper of X. Zhao et al. is an exhaustive review of the recent literature about ZnO nanowire based sensors. The manuscript examines experimental data and working mechanism of ohmic-contacted and Schottky-contacted ZnO nanostructures based sensors. Their findings demonstrate that Schottky barrier mechanism greatly improves (several orders of magnitude) the response of the sensors. Furthermore, the use of piezotronic effect to modulate the Schottky barrier height can lead to extremely high sensitivities.

L. Mei et al. investigated experimentally and through molecular simulation the cation exchange interactions in montmorillonite clays. They focused on montmorillonite with Na^+ and K^+ in the interlayer spaces, testing the absorption and substitution of these cations with Cd^{2+} . This phyllosilicate mineral can indeed be used for the removal and recovery of toxic cadmium from industrial wastewater. They found that Na^+ can be thoroughly exchanged by Cd^{2+} , whilst K^+ can only be partially replaced.

The manuscripts in the issue focus on diverse topics but have a transversal common point: nanoscience and nanomaterials at the service of real applications for a cleaner world. We think that these papers will give the readers useful information and good hints for a further development in the field.

Ruomeng Yu
Caofeng Pan
Owen J. Guy
Lin Dong
Matteo Tonzzer

Research Article

A Self-Powered Triboelectric Nanosensor for PH Detection

Ying Wu,¹ Yuanjie Su,² Junjie Bai,¹ Guang Zhu,³ Xiaoyun Zhang,¹
Zhanolin Li,¹ Yi Xiang,¹ and Jingliang Shi¹

¹Chongqing University of Science and Technology, Chongqing 401331, China

²State Key Laboratory of Electronic Thin Films and Integrated Devices, School of Optoelectronic Information, University of Electronic Science and Technology of China (UESTC), Chengdu 610054, China

³Beijing Institute of Nanoenergy and Nanosystems, Chinese Academy of Sciences, Beijing 100083, China

Correspondence should be addressed to Jingliang Shi; shijingliangcq@126.com

Received 21 August 2015; Accepted 19 January 2016

Academic Editor: Owen J. Guy

Copyright © 2016 Ying Wu et al. This is an open access article distributed under the Creative Commons Attribution License, which permits unrestricted use, distribution, and reproduction in any medium, provided the original work is properly cited.

A self-powered, sliding electrification based triboelectric sensor was developed for detecting PH value from a periodic contact/separation motion. This innovative, cost-effective, simply designed sensor is composed of a fluorinated ethylene propylene thin film and an array of electrodes underneath. The operation of the TENG (triboelectric nanogenerator) sensor relies on a repetitive emerging-submerging process with traveling solution waves, in which the coupling between triboelectrification and electrostatic induction gives rise to alternating flows of electrons between electrodes. On the basis of coupling effect between triboelectrification and electrostatic induction, the sensor generates electric output signals which are associated with PH value. Experimental results show that the output voltage of the TENG sensor increases with the increasing PH value, which indicate that the PH value of different solution can be real-time monitored. This work not only demonstrates a new principle in the field of PH value measurement but also greatly expands the applicability of triboelectric nanogenerator (TENG) as self-powered sensors.

1. Introduction

As one of the analytical devices, pH sensors play an important role in many fields such as environment monitors, biological analyses, blood monitors, and medical detection [1]. Over the past decade, major advances have occurred in PH measurement based on electrochemical effects, such as modification of nanostructured pH sensing electrodes [2] and doping of nanostructured single electrode of electrochemical sensors [3]. However, widespread usage of these techniques is likely to be shadowed by possible limitations, including structure complexity, requirement of sophisticated materials, and reliance on external power source. Recently, triboelectric nanogenerator [4–10], creative invention based on the coupling of the universally known contact electrification effect and electrostatic induction, has been extensively explored to establish cost-effective and robust self-powered sensing systems, including but not limited to vibration sensor [11], motion sensor [12], acoustic sensor [13], biosensor [14], displacement vector sensor [15], acceleration sensor [16], wind

vector sensor [17], tactile sensor [18], tracking sensor [19], and chemical sensor [20, 21]. Here, based on the previous research of harvesting water wave energy with TENG [22], we, for the first time, introduce a new principle in PH detection by fabricating a triboelectric sensor. The as-fabricated self-powered sensor is based on a periodic contact/separation between PH solution and a fluorinated ethylene propylene (FEP) film. The ions of the buffer solution with different PH value induced variation in surface potential are readily measured as a change in triboelectric voltage of the TENG sensor. Triggered by the output voltage signal, the PH value of the buffer solution can be real-time monitored. This work not only presents a new principle in the field of PH measurement but also greatly expands the applicability of TENGs as power self-powered sensors.

2. Results and Discussion

The presented self-powered PH sensor has a fork-finger structure, which is shown in Figure 1(a). On one side of

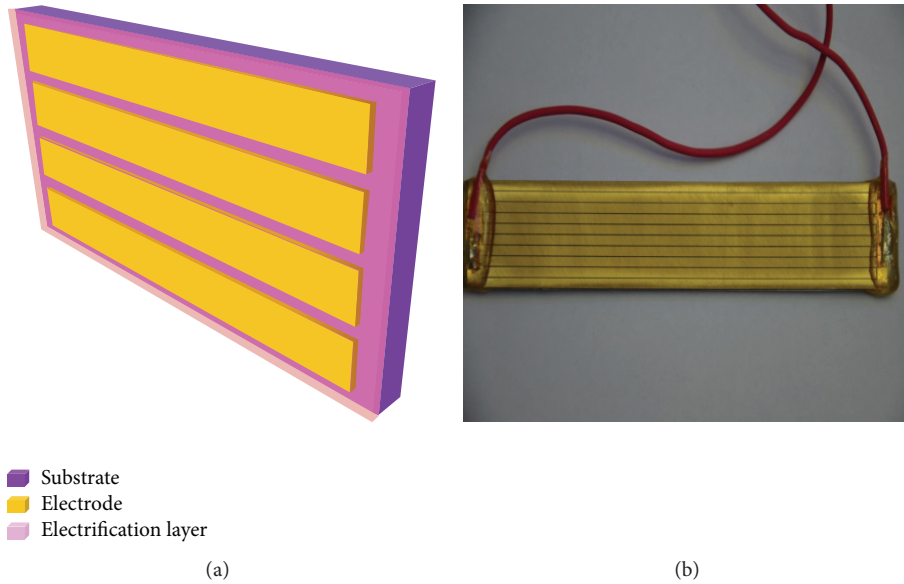


FIGURE 1: Structural design of the TENG sensor. (a) Schematic diagram of the fabricated sensor. (b) Photograph of the prepared TENG sensor.

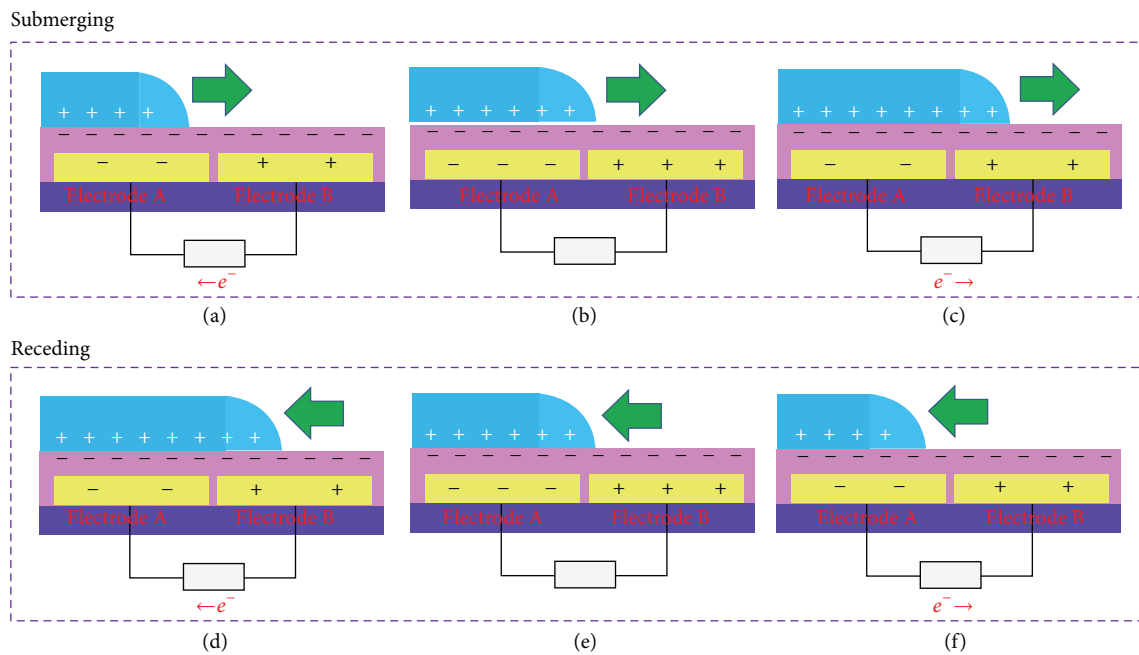


FIGURE 2: Working mechanism of the fabricated TENG sensor. (a) Electrode A is partially submerged. (b) The water surface levels with the middle point of the device. (c) Electrode B is being covered by water, (d) electrode B is partially exposed, (d) electrode B is completely exposed, and (f) electrode A is partially exposed.

a fluorinated ethylene propylene (FEP) thin film, four parallel strip-shaped electrodes are fabricated, which are discrete with a fine gap in between, as well as polyethylene terephthalate (PET) as the substrate. FEP is selected as the contact material for its hydrophobic property and high negativity in the triboelectric series [23]. As the area of the device submerged cyclically varies with the wave, free electrons are driven to flow alternately between electrodes, generating AC output electricity on the external load.

The operation of the TENG sensor involves a repetitive emerging-submerging process with traveling solution waves, which result in the coupling between triboelectrification and electrostatic induction between the TENG sensor and solution buffer and thus give rise to alternating flows of electrons. The electricity-generating process is described through a basic unit in Figure 2. We define the initial state (Figure 2(a)) and the final state (Figure 2(f)) as the states when the buffer solution is submerged with the bottom first-electrode area

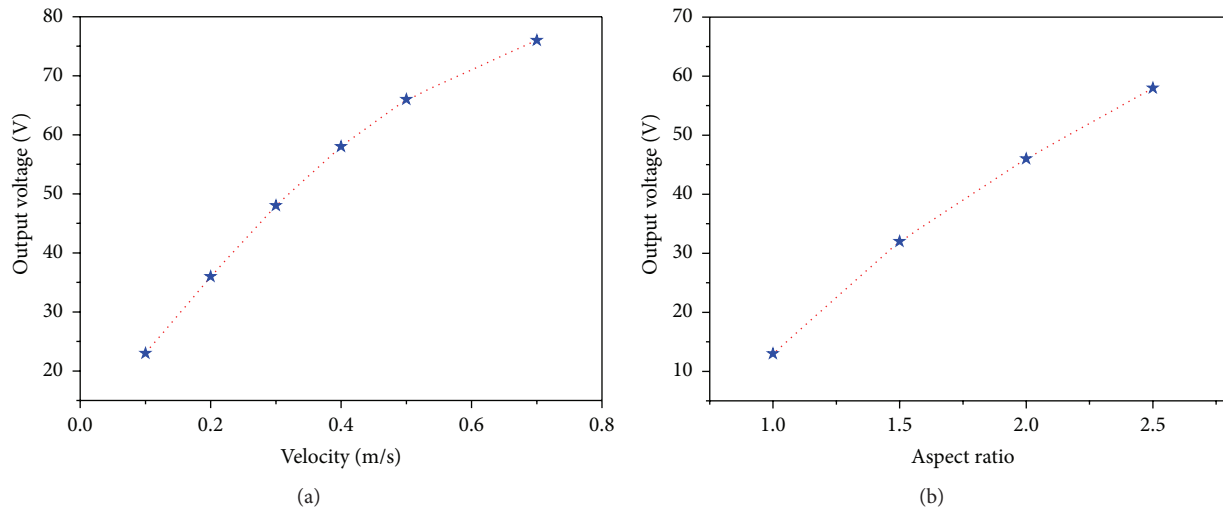


FIGURE 3: Electric measurement results of factors that influence the electric output. (a) Open-circuit voltage with increasing velocity. (b) Open-circuit voltage with increasing aspect ratio of the device.

and receded away from the bottom electrodes, respectively. The contact electrification between triboelectrically negative materials and solution renders the negative triboelectric charges on the surface of FEP thin film (Figure 2(a)). These surface charges can remain for a long period of time due to the insulating property of the polymer material [24]. When electrode A is increasingly submerged by the rising solution wave, positive ions in solution are attracted by the negative triboelectric charges on the FEP surface to form an interfacial electrical double layer (EDL). This asymmetric distribution of charges on FEP surface establishes the positive electric potential difference from electrode A to electrode B, driving electrons to flow from electrode B to electrode A (Figure 2(a)). Once the rising buffer solution reaches the gap between two electrodes, a maximum quantity of induced charges on the electrodes will be attained, leaving no electrons transferred (Figure 2(b)). As the rising water continues to submerge electrode B (Figure 2(c)), induced electrons flow back to electrode B since the electric potential difference between the two electrodes decreases until electrode B is fully submerged by buffer solution (Figure 2(c)). When the device is completely covered by buffer solution, a symmetric screening of triboelectric charges is achieved, and therefore the electric potential difference decreases to zero with no electrons transfer between electrodes. Then the wave begins to recede and expose electrode B and, thereby, the increasing electric potential difference drives electrons to flow from electrode B to electrode A (Figure 2(d)). Once the solution surface returns to the gap between two electrodes, a maximum quantity of induced charges on the electrodes will be obtained again without electron flowing (Figure 2(e)). Subsequently, the solution level falls down and exposes electrode A and the decreasing screening area results in electron flow from electrode A to electrode B (Figure 2(f)). Finally, the TENG sensor fully emerges from buffer solution and completes a whole cycle. The hydrophobic surface of FEP thin film repels solution immediately after emerging from

solution surface. Consequently, as the device submerges and emerges from the waving solution, two pairs of alternating electron flows are brought about between the two adjacent electrodes, leading to power generation and outputting the corresponding signal, which can indicate the PH value of buffer solution.

In the previous research, nanowire-based modification from polymer nanowires plays a key role in increasing the output power [22]. However, nanowire-based modification is not very good for the PH detection. Here, the electric output of the sensor was improved by investigating two factors, that is, velocity of the relative movement and aspect ratio of the device. For TENG, the velocity is an important factor. The bigger the velocity was, the more the kinetic energy was produced and thus more triboelectric charges were generated on the FEP surface. As shown in Figure 3(a), the output voltage V_{oc} has an approximately linear relationship with the velocity. The induced voltage increases as the velocity increases from 0.1 to 0.7 m/s, which was similar to the previous studies on electrification between a fluorinated polymer and water [23, 24]. At the same time, the aspect ratio of the device is another important parameter that has a decisive effect on the electric output of the TENG sensor. Previous studies reported that preexisting charges in the solution can influence subsequent charge transfer with a solid surface [25, 26]. In order to optimize the aspect ratio, the TENG sensor was driven by a linear motor in a fixed velocity. When the TENG sensors do the reciprocating motion in the solution, the charge resulting from triboelectrification will transfer between the surface part of the solution and the TENG surface. Once the TENG starts to dip into the buffer solution, the surface part of the solution is positively charged instantaneously. As the TENG continues to dip into the buffer solution, preexisting positive charges in the solution will be increased thus decreasing the electrification. The more the area of the TENG sensor that will be submerged into the solution, the weaker the electrification that will be produced.

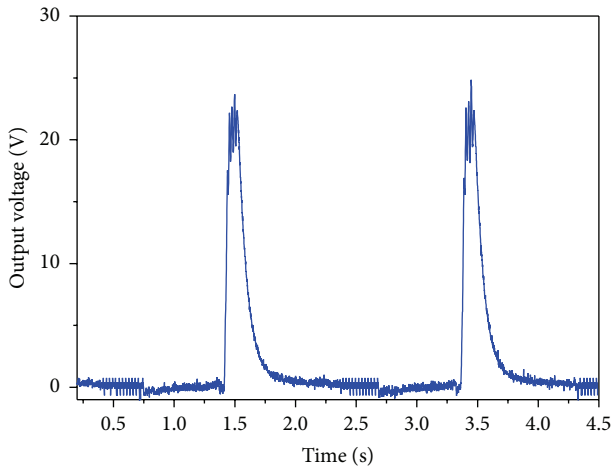


FIGURE 4: Open-circuit voltage results as the TENG is repetitively submerged into buffer solution.

Compared to the bottom part, the top part of the TENG may own a lower surface charging density.

For the fixed TENG surface area, more surface triboelectric charges and thus higher electric output will be produced accordingly for a narrower TENG with a higher aspect ratio has a shorter interaction distance with the solution, which was illustrated by the increasing V_{oc} in Figure 3(b). Therefore, according to the relationship between the electric output and the aspect ratio, the optimized size of the electrode and the TENG sensor with high performance will be achieved.

To demonstrate applications of the TENG for self-powered PH measurement, we mounted the sensor onto the linear motor to ensure reciprocating motion through the motor-controlling program for monitoring the PH value of the container in real-time.

Figure 4 shows the open-circuit output voltage of self-powered PH sensor. Here, the open-circuit voltage (V_{oc}) was defined as the electric potential difference between the two electrodes and the TENG sensors do the reciprocating motion in the buffer solution. In open-circuit condition, electrons cannot transfer between electrodes. When the TENG sensor submerged into the buffer solution, the open-circuit voltage is about 0 V. When the TENG sensor emerged from the buffer solution, the open-circuit voltage is also about 0 V. When the solution surface levels attain the middle point of the TENG sensor, the open-circuit voltage reaches the maximum.

The buffer solution was driven by linear motor mounted with the TENG sensor to form a repeated wave motion. According to the measurement results plotted in Figure 5, the output of TENG sensor is associated with the PH value. The output voltage increases with the increasing PH value. This result indicates that the output voltages of the TENG sensor are affected by the electrolytes in solution. This is due to the fact that FEP film cannot completely eliminate the adhesion of solution droplet after it emerges from solution. The residual electrolytical solution, including positive dissolved ions, remains on the surface and will partially screen the triboelectric charges on the FEP film, reducing

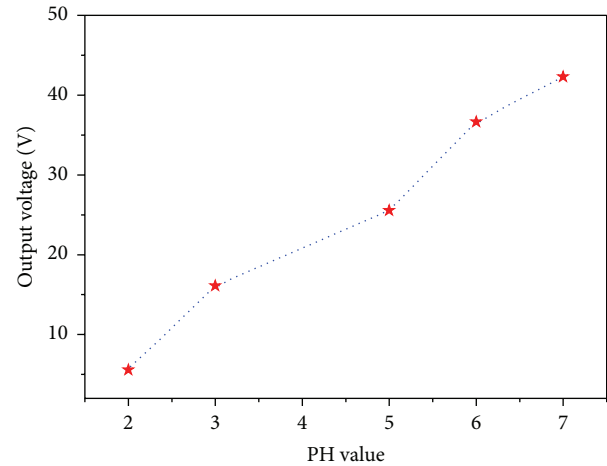


FIGURE 5: Relationship between output voltage and PH value.

the electrostatic induction and thus the electric output [26]. A low positive ion (H^+) concentration assists generation of the triboelectric charges, while a high concentration has the opposite effect [21]. The buffer solution with lower PH value indicates more H^+ concentration and renders more positive ions in electrolytical solution.

3. Conclusions

In summary, a self-powered sensor for PH measurement using triboelectrification was firstly demonstrated. The sensor has a fork-finger structure composed of FEP material and metal electrodes, as well as PET as the substrate. The reciprocating motion between TENG sensor and buffer solution leads to charge transfer between the adjacent Cu bottom electrodes, generating AC voltage in the external circuit. The output voltage of the TENG sensor varies with the buffer solution with different PH value due to the different ion concentration. And the PH value of buffer solution can be actively monitored in real-time by reading the output voltage. This work not only presents a new principle in the field of PH measurement but also greatly expands the applicability of TENGs as self-powered sensors. The electricity was generated through triboelectric effect at the solid-liquid interface upon directly interacting with ambient buffer solution, showing a practically feasible technology for water quality monitoring and environment protection.

4. Experimental Section

4.1. Fabrication of a TENG Sensor. A 1.5 mm thick acrylic sheet was cut into a hollow mask by precision laser cutting. The patterns in the mask were the same as electrodes. Then the mask was mounted onto the FEP film. The Cu layer was deposited onto the exposed PET surface by physical vapour deposition (PVD) to prepare the parallel electrode. Lead wires were connected to the electrodes as output terminals with one-to-one correspondence. Subsequently, a 75 mm thick FEP film was attached to the PET substrate.

4.2. *Experimental Setup for Electric Measurement.* TENG sensor was mounted vertically on the electrical linear motor. The sheet was immersed into the different PH buffer solution and perpendicular to the solution surface. The moving direction of the motor was perpendicular to the array of strip-shaped electrodes. A container filled with buffer solution was placed under the device with the water level adjacent to the device edge. The reciprocating motion of the TENG sensor was achieved through the motor-controlling program. The reciprocating motion of the linear motor forms waves of tap solution in the container. The output leads of TENG sensor were connected to Keithly 6514.

Conflict of Interests

The authors declare no competing financial interest.

Authors' Contribution

Ying Wu and Yuanjie Su contributed equally to this work.

Acknowledgments

This work was supported in part by the Research Foundation of Chongqing Municipal Education Committee (Grant no. KJ1401333) and Research Foundation of Chongqing University of Science & Technology (Grant no. CK2011Z08 and Grant no. CK2011Z09).

References

- [1] S. Zhuikov, "Solid-state sensors monitoring parameters of water quality for the next generation of wireless sensor networks," *Sensors and Actuators B: Chemical, Sensors and Actuators B*, vol. 161, no. 1, pp. 1–20, 2012.
- [2] B. Xu and W.-D. Zhang, "Modification of vertically aligned carbon nanotubes with RuO₂ for a solid-state pH sensor," *Electrochimica Acta*, vol. 55, no. 8, pp. 2859–2864, 2010.
- [3] R. Zhao, M. Xu, J. Wang, and G. Chen, "A pH sensor based on the TiO₂ nanotube array modified Ti electrode," *Electrochimica Acta*, vol. 55, no. 20, pp. 5647–5651, 2010.
- [4] Z. L. Wang, "Trielectronic nanogenerators as new energy technology for self-powered systems and as active mechanical and chemical sensors," *ACS Nano*, vol. 7, no. 11, pp. 9533–9557, 2013.
- [5] F.-R. Fan, Z.-Q. Tian, and Z. L. Wang, "Flexible triboelectric generator," *Nano Energy*, vol. 1, no. 2, pp. 328–334, 2012.
- [6] G. Zhu, C. Pan, W. Guo et al., "Trielectronic-generator-driven pulse electrodeposition for micropatterning," *Nano Letters*, vol. 12, no. 9, pp. 4960–4965, 2012.
- [7] G. Zhu, Z.-H. Lin, Q. Jing et al., "Toward large-scale energy harvesting by a nanoparticle-enhanced triboelectric nanogenerator," *Nano Letters*, vol. 13, no. 2, pp. 847–853, 2013.
- [8] S. Wang, Y. Xie, S. Niu, L. Lin, and Z. L. Wang, "Freestanding triboelectric-layer-based nanogenerators for harvesting energy from a moving object or human motion in contact and non-contact modes," *Advanced Materials*, vol. 26, no. 18, pp. 2818–2824, 2014.
- [9] L. Lin, Y. N. Xie, S. H. Wang et al., "Trielectronic active sensor array for self-powered static and dynamic pressure detection and tactile imaging," *ACS Nano*, vol. 7, no. 9, pp. 8266–8274, 2013.
- [10] Y. J. Su, Y. Yang, H. L. Zhang et al., "Enhanced photodegradation of methyl orange with TiO₂ nanoparticles using a triboelectric nanogenerator," *Nanotechnology*, vol. 24, Article ID 295401, 2013.
- [11] Q. J. Liang, Z. Zhang, X. Q. Yan et al., "Functional triboelectric generator as self-powered vibration sensor with contact mode and non-contact mode," *Nano Energy*, vol. 14, pp. 209–216, 2015.
- [12] X. N. Xia, G. L. Liu, H. Y. Guo, Q. Leng, C. G. Hu, and Y. Xi, "Honeycomb-like three electrodes based triboelectric generator for harvesting energy in full space and as a self-powered vibration alertor," *Nano Energy*, vol. 15, pp. 766–775, 2015.
- [13] J. Yang, J. Chen, Y. Liu, W. Yang, Y. Su, and Z. L. Wang, "Trielectronic-based organic film nanogenerator for acoustic energy harvesting and self-powered active acoustic sensing," *ACS Nano*, vol. 8, no. 3, pp. 2649–2657, 2014.
- [14] S. Wang, L. Lin, and Z. L. Wang, "Trielectronic nanogenerators as self-powered active sensors," *Nano Energy*, vol. 11, pp. 436–462, 2015.
- [15] C. Bao Han, C. Zhang, X. H. Li et al., "Self-powered velocity and trajectory tracking sensor array made of planar triboelectric nanogenerator pixels," *Nano Energy*, vol. 9, pp. 325–333, 2014.
- [16] Y. K. Pang, X. H. Li, M. X. Chen, C. B. Han, C. Zhang, and Z. L. Wang, "Trielectronic nanogenerators as a self-powered 3D acceleration sensor," *ACS Applied Materials & Interfaces*, vol. 7, no. 34, pp. 19076–19082, 2015.
- [17] Z.-H. Lin, G. Cheng, Y. Yang, Y. S. Zhou, S. Lee, and Z. L. Wang, "Trielectronic nanogenerator as an active UV photodetector," *Advanced Functional Materials*, vol. 24, no. 19, pp. 2810–2816, 2014.
- [18] Y. Yang, H. L. Zhang, X. D. Zhong et al., "Electret film-enhanced triboelectric nanogenerator matrix for self-powered instantaneous tactile imaging," *ACS Applied Materials and Interfaces*, vol. 6, no. 5, pp. 3680–3688, 2014.
- [19] Y. Su, G. Zhu, W. Yang et al., "Trielectronic sensor for self-powered tracking of object motion inside tubing," *ACS Nano*, vol. 8, no. 4, pp. 3843–3850, 2014.
- [20] C. Xu, C. Pan, Y. Liu, and Z. L. Wang, "Hybrid cells for simultaneously harvesting multi-type energies for self-powered micro/nanosystems," *Nano Energy*, vol. 1, no. 2, pp. 259–272, 2012.
- [21] Y. C. Wu, X. D. Zhong, X. Wang, Y. Yang, and Z. L. Wang, "Hybrid energy cell for simultaneously harvesting wind, solar, and chemical energies," *Nano Research*, vol. 7, no. 11, pp. 1631–1639, 2014.
- [22] G. Zhu, Y. Su, P. Bai et al., "Harvesting water wave energy by asymmetric screening of electrostatic charges on a nanostructured hydrophobic thin-film surface," *ACS Nano*, vol. 8, no. 6, pp. 6031–6037, 2014.
- [23] F. Saurenbach, D. Wollmann, B. D. Terris, and A. F. Diaz, "Force microscopy of ion-containing polymer surfaces: morphology and charge structure," *Langmuir*, vol. 8, no. 4, pp. 1199–1203, 1992.
- [24] K. Yatsuzuka, Y. Mizuno, and K. J. Asano, "Electrification phenomena of pure water droplets dripping and sliding on a polymer surface," *Journal of Electrostatics*, vol. 32, no. 2, pp. 157–171, 1994.
- [25] K. Yatsuzuka, Y. Mizuno, and K. Asano, "Electrification of polymer surface caused by sliding ultrapure water," *IEEE Transactions on Industry Applications*, vol. 32, no. 4, pp. 825–831, 1996.

- [26] Z. H. Lin, G. Cheng, L. Lin, S. Lee, and Z. L. Wang, "Water-solid surface contact electrification and its use for harvesting liquid-wave energy," *Angewandte Chemie International Edition*, vol. 52, no. 48, pp. 12545–12549, 2013.

Research Article

Cd^{2+} Exchange for Na^+ and K^+ in the Interlayer of Montmorillonite: Experiment and Molecular Simulation

Lefu Mei, Huashang Tao, Chao He, Xuebing Xin, Libing Liao, Limei Wu, and Guocheng Lv

Beijing Key Laboratory of Materials Utilization of Nonmetallic Minerals and Solid Wastes, National Laboratory of Mineral Materials, School of Materials Science and Technology, China University of Geosciences, Beijing 100083, China

Correspondence should be addressed to Lefu Mei; mlf@cugb.edu.cn and Libing Liao; clayl@cugb.edu.cn

Received 16 April 2015; Revised 11 June 2015; Accepted 14 June 2015

Academic Editor: Ruomeng Yu

Copyright © 2015 Lefu Mei et al. This is an open access article distributed under the Creative Commons Attribution License, which permits unrestricted use, distribution, and reproduction in any medium, provided the original work is properly cited.

Montmorillonite (Mt) has high cation exchange capacity and thus has been studied extensively for its cation exchange interactions with other cations. However, molecular simulations for the forces governing the cation exchange on Mt surfaces or in the interlayer spaces were limited. In this study, Mt with K^+ and Na^+ in the interlayer spaces was tested for its cation exchange with Cd^{2+} in solution and the forces driving the cation exchange reaction were simulated by molecular simulations. The experimental results showed that Na^+ in Na + Mt was completely exchanged by Cd^{2+} , while only 50% of K^+ in K + Mt was exchanged by Cd^{2+} . A larger d -value was noticed for Na + Mt in comparison to K + Mt, suggesting that the interlayer space is more hydrated with Na^+ as the interlayer space cation. Molecular dynamic simulations revealed a larger energy decrease when Cd^{2+} substitutes K^+ . However, the nice fit of the K^+ into the 12-coordinated interlayer space sites may restrict its hydration and thus reduce its interlayer space cation exchange capability by Cd^{2+} .

1. Introduction

Cadmium (Cd) has been extensively used in the fields of mining, electroplating, electrolyzing, painting, alloying, plastic generation, and textile processing [1–4]. As Cd is toxic even at very low concentrations, it is classified as a human carcinogen by the US National Toxicology Program. Significant amounts of Cd can be accumulated in food chain and eventually cause health problems in human beings, plants, and animals [1, 2, 5–7]. It is therefore important to develop methods to remove Cd from wastewater before it reaches the natural environments. Various methods developed for the removal and recovery of Cd from industrial wastewater include chemical precipitation, electrolysis, ion exchange, membrane process, and sorption [8–11].

Montmorillonite (Mt) is a 2:1 phyllosilicate mineral and has high cation exchange capacity (CEC) that can absorb and retain metal cations in its interlayer space to achieve electrical neutrality. Interlayer space hydrated cations are mainly stabilized by electrostatic interactions, and they could be exchanged by other cations in solution. The species of interlayer space hydrated cations would affect interlayer space,

surface area, adsorption, swelling, dispersion, and crystal stability of Mt [12]. The desorption of adsorbed water and interlayer space water in Mt is a one-step or two-step process according to the species of interlayer space cations. The conductivity of Mt is affected by the electrovalence of interlayer space cations much more than by the ionic radius.

Molecular modeling recently has been recognized as an efficient method for understanding the microstructure of interlayer spaces [13–18] in clay minerals. The advantages of molecular modeling include the following: (1) simultaneously present insight into the microstructure of the interlayer spaces at the atomic level and the thermodynamic information of the system [13–16]; (2) conveniently design different models for systematical investigation of the influence of various factors on the characteristics of clay minerals [14, 17, 18]. Numerous studies have employed molecular modeling for understanding the hydration characteristics of clay minerals [13–17]. Hydration energy of K^+ -, Na^+ -, or Li^+ -exchanged Mt was calculated by molecular dynamic (MD) simulations and the results provided thermodynamic explanations for the inhibition of Mt swelling by K^+ [14]. In addition, molecular modeling has also been used to study the adsorption

of contaminants at the interlayer spaces of Mt in several previous reports [19–25]. Moreover, MD simulations can directly predict the adsorption sites for organic contaminants within the interlayer space of organoclays, which include the siloxane surface and the spaces between organic cations [19].

In this study, we investigated cation exchange reaction of Cd^{2+} for K^+ or Na^+ in the interlayer space of Mt experimentally in conjunction with XRD analyses and MD simulation, in order to provide the driving force for interactions between the Mt layers and the interlayer space cation as affected by the cation radii and the degrees of hydration.

2. Materials and Methods

2.1. Materials. The montmorillonite used was SWy-2 obtained from the Clay Mineral Repositories in Purdue University (West Lafayette, IN) and was used without further purification. It has a chemical formula of $(\text{Ca}_{0.12} \text{Na}_{0.32} \text{K}_{0.05})[\text{Al}_{3.01} \text{Fe(III)}_{0.41} \text{Mg}_{0.54}][\text{Si}_{7.98} \text{Al}_{0.02}]\text{O}_{20}(\text{OH})_4$, a CEC of $85 \pm 3 \text{ mmol}_c/100 \text{ g}$ [26], a layer charge of 0.32 eq/mol per $(\text{Si}, \text{Al})_4\text{O}_{10}$ [27], an external specific surface area (SSA) of $23 \text{ m}^2/\text{g}$ [28], and a mean particle size of $3.2 \mu\text{m}$ with a d_{25} to d_{75} in the range of 3–10 μm .

2.2. Methods. The initial Cd^{2+} concentrations varied from 0.2 to 30 mmol/L for the adsorption isotherm study and were fixed at 2 mmol/L for the kinetic study and pH dependency study. The mass of SWy-2 used was 0.2 g while the volume of solution used was 10 mL for all studies except the kinetic study, in which 20 mL of solution was used. The solid and solution were combined in each 50 mL centrifuge tube and shaken for 2 h at 150 rpm and room temperature for all studies except the kinetic study, in which the shaking time was 1, 3, 5, 30, 60, 120, 600, and 1200 min. After the mixtures were centrifuged at 10000 rpm for 20 min, the supernatants were filtered through 0.22 μm syringe filters before being analyzed for equilibrium Cd^{2+} concentrations.

Free swelling was determined using 1 g of Mt and 100 mL of water in 100 mL graduated cylinder; the mixture was allowed to fully swell with periodic agitation and eventually to set out. The increase of volume after swelling was determined from the difference between the final swelling volume and the initial dry volume of the solid and expressed as mL/g.

Powder XRD analyses were performed on a Rigaku D/max-IIIa diffractometer (Tokyo, Japan) with a Ni-filtered $\text{CuK}\alpha$ radiation at 30 kV and 20 mA. Orientated samples were scanned from 4° to 10° at $2^\circ/\text{min}$ with a scanning step of 0.01° . Powder samples were packed in horizontally held trays. The changes in the XRD reflection positions reflect the hydrated size of the metal cations in the interlayer space of Mt.

X-ray fluorescence (XRF) measurements were carried out using a portable XRF spectrometer (Oxford Instruments) with a molybdenum anode, at 25 kV and 0.1 mA. A Si-PIN detector from AMPTEK was employed and characterized by an energy resolution of about 200 eV at 5.9 keV.

FTIR spectra of samples were collected on a Nicolet-560 spectrometer (Thermal Nicolet Co., USA) from 400 to 4000 cm^{-1} with a nominal resolution of 4 cm^{-1} . For each spectrum 16 runs were collected and averaged. The SWy-2

specimens were prepared by adding approximately 1% of the sample powder to dry KBr powder.

Thermogravimetric (TG) analyses were carried out on TGA Q-500 (TA Instruments, New Castle, USA) from room temperature to 800°C , at a heating rate of $10^\circ\text{C}/\text{min}$ under a nitrogen flow of 60 mL/min. TG curves were used to determine the percentage of mass loss. Differential scanning calorimetry (DSC) was performed using a differential scanning calorimeter (TA Instruments Q100) fitted with a cooling system using liquid nitrogen. It was calibrated with an indium standard. Samples of 6 mg of Mt were accurately weighed into aluminum pans, sealed, and then heated from 30 to 800°C at $10^\circ\text{C}/\text{min}$ under a nitrogen flow of 60 mL/min.

2.3. Computation Details. Molecular simulation was performed under the module “CASTEP” of Materials Studio 6.0 software to investigate the sorption sites of K^+ , Na^+ , and Cd^{2+} on SWy-2. The primitive unit cell of SWy-2 was optimized with the generalized gradient approximation (GGA) for the exchange-correlation potential (PW91) that is appropriate for the relatively weak interactions present in the models studied. The resulting primitive unit cell was characterized by the parameters $a = 15.540 \text{ \AA}$, $b = 17.940 \text{ \AA}$, $c = 12.56 \text{ \AA}$, and $\alpha = \gamma = 90^\circ$, $\beta = 99^\circ$. Based on the primitive unit cell, a series of $(3 \times 2 \times 1)$ supercells were built with the d -value of layers set to 10.55, 12.74, and 14.81 \AA for K + Mt, Na + Mt, and Cd + Mt, respectively.

3. Results and Discussion

3.1. Preparation of K + Mt. The cation exchangeability of Mt is affected by interaction force of interlayer space cation and Mt layer and force of binding water. To investigate the impact of species of interlayer space cation on cation exchangeability, the experiment was designed first to compare properties of K + Mt and Na + Mt, as Na^+ and K^+ belong to the same main group and have the same electrovalence, but different ionic radii. To keep all conditions the same, except the type of interlayer cations, the Na + Mt was first exchanged with K^+ to prepared K + Mt. After cation exchange by K^+ , the Na + Mt was completely converted to K + Mt (Table 1).

The thickness of dehydrated Mt is 9.8 \AA , and the interlayer space will be expanded when Na^+ and K^+ hydrated cations enter the interlayer space. As hydration ability of different cations varies, interlayer spaces of Mts with different cations in the interlayer space differ apparently. K^+ concentrations of varying multiples of CEC in solution will result in different amounts of K^+ uptake in Mt, which will result in a change in d_{001} spacing (Figure 1). The d_{001} of original Na + Mt was 12.74 \AA . As the amount of K^+ substitution increased, the interlayer space decreased. At an initial input of K^+ at 10 times the CEC of Mt, the d_{001} of Mt reduced to 10.55 \AA (Figure 1). However, this d -value is still greater than that of illite or mica, suggesting still presence of limited interlayer space water.

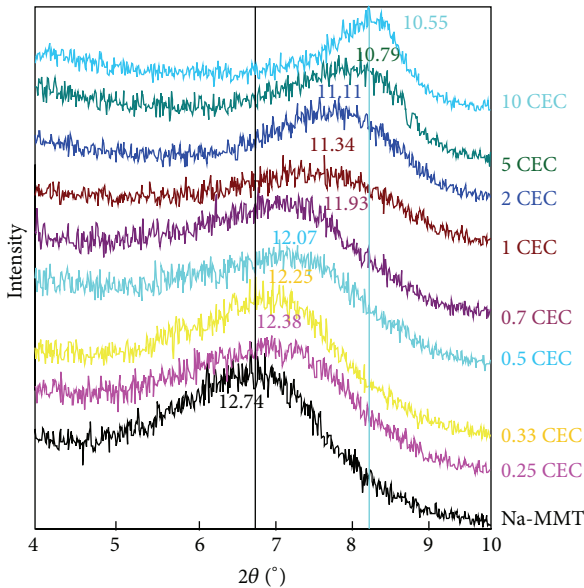
Hydration of cations on interlayer space and outer surface leads to volume expansion of Mt, called free swell. The free swelling of Mt decreased as the amount of K^+ uptake increased (Table 2). Pure Na + Mt had a free swelling of 41.5 mL/g. It decreased to 11.5 mL/g after Na^+ was fully

TABLE I: Chemical composition of Mts and their chemical formula.

Chemical composition (%)	Na + Mt	Na + Mt after Cd ²⁺ exchange	K + Mt	K + Mt after Cd ²⁺ exchange
SiO ₂	68.00	62.56	65.38	66.33
Al ₂ O ₃	15.43	14.60	15.16	15.23
Fe ₂ O ₃	5.64	6.75	6.62	6.55
MgO	3.35	2.86	3.51	2.87
CaO	2.36	2.95	3.35	2.12
Na ₂ O	1.70	0.00	0.24	0.00
K ₂ O	0.00	0.00	4.73	2.04
CdO	0.00	9.48	0.00	3.66
Chemical formula	(Na _{0.19} Ca _{0.15}) (Al _{1.08} Fe _{0.24} Mg _{0.29}) [Si ₄ O ₁₀](OH) ₄	(Cd _{0.29} Ca _{0.20}) (Al _{1.11} Fe _{0.33} Mg _{0.28}) [Si ₄ O ₁₀](OH) ₄	(K _{0.38} Ca _{0.22} Na _{0.03}) (Al _{1.11} Fe _{0.31} Mg _{0.33}) [Si ₄ O ₁₀](OH) ₄	(Cd _{0.10} K _{0.16} Ca _{0.14}) (Al _{1.12} Fe _{0.31} Mg _{0.26}) [Si ₄ O ₁₀](OH) ₄

TABLE 2: Free swelling (mL/g) of raw Na + Mt and Mt after being in contact with KCl of varying amounts for 120 min.

Na + Mt	0.25 CEC	0.33 CEC	0.5 CEC	0.7 CEC	1 CEC	2 CEC	5 CEC	10 CEC
41.5	36	30	27	21.5	18	14	12	11.5

FIGURE 1: X-ray diffraction patterns of K-MMT. The d -spacing is in Å.

replaced by K⁺. Generally, a higher free swelling means stronger hydration ability of cations in Mt interlayer space, and better expansion ability means better dispersion after adsorbing water [29]. Different cations have different radii and charges, therefore resulting in different interlayer space stabilities in Mt. As the hydration of Na⁺ is obviously stronger than that of K⁺, the interlayer space of Na + Mt is greater than that of K + Mt.

3.2. Cd²⁺ Uptake from K + Mt and Na + Mt. Interaction forces between Mt layer and interlayer space cation are

electrostatic attraction, intermolecular forces, van der Waals forces, and so forth. Owing to combination of these interactions, metal cations stay stable in the interlayer space place. The experiment used Cd²⁺ to exchange interlayer space cations of Na⁺ or K⁺ from Na + Mt or K + Mt. By discussing influence of time and concentration of Cd²⁺ on exchanging Na⁺ or K⁺ from Na + Mt or K + Mt, exchanging rate and volume of two cationic Mts can also be calculated. The difficulty of exchanging cation in Mt interlayer space is relevant with interaction force of interlayer cation and layer, which means stronger interaction force leading to more difficulty in exchange [30].

The cation exchange process of Cd²⁺ for Na⁺ or K⁺ in the interlayer space of Mt is relatively fast (Figure 2), which can reach 60% of total exchange capacity in 30 min and complete exchange in 2 h, especially for K + Mt, reaching the exchanging balance in 30 min. However, the amount of Cd²⁺ uptake on K⁺-Mt was lower than that on Na⁺-Mt. The maximal exchange capacity reached 0.43 mmol/g or 0.86 mmol/g. As the CEC of the original Mt was 0.85 mmol/g, it can be inferred that Na⁺ in Na + Mt was completely exchanged while K⁺ in K + Mt was only partially exchanged. The Cd²⁺ isotherm data agreed well with the chemical analysis data (Table 1 and Figure 2). This indicated that Mts with different interlayer cations lead to different exchange rate and capacity for Cd²⁺, which is directly related to the type of interlayer cation [31]. After linear fit of the experimental results, it was found that the exchange Cd²⁺ for Na⁺ or K⁺ followed the first-order kinetics. The rate constants for Ca²⁺ to exchange K⁺ or Na⁺ in K + Mt or Na + Mt were 9.8 g/mmol and 3.9 g/mmol, respectively.

The results of XRD analyses indicated the progressive completion of Cd²⁺ exchange for Na in Na + Mt and partial exchange of Cd²⁺ for K⁺ in K + Mt. This could be used to determine element composition and content of exchanged Na + Mt and K + Mt and then to calculate the amount of cations exchanged. XRF results showed that the content of Na⁺ for Na + Mt after being exchanged by Cd²⁺ is 0 (Table 1), which means interlayer cations are almost all comprised of Cd²⁺ and exchange rate is 100%. On the other hand, more than 40% of the original K⁺ was still remaining (Table 1)

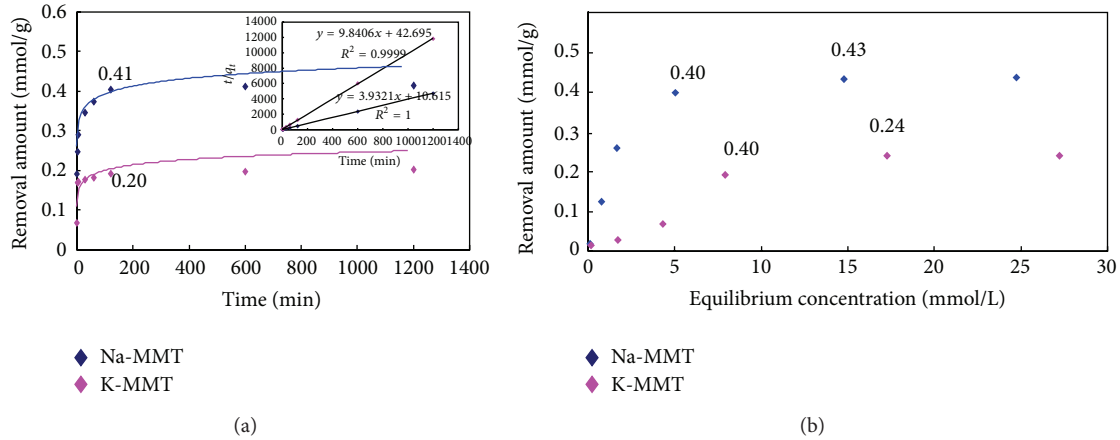


FIGURE 2: Effect of time/min (a) and Cd^{2+} equilibrium concentration/mmole/L (b) on Cd^{2+} exchanged quantities.

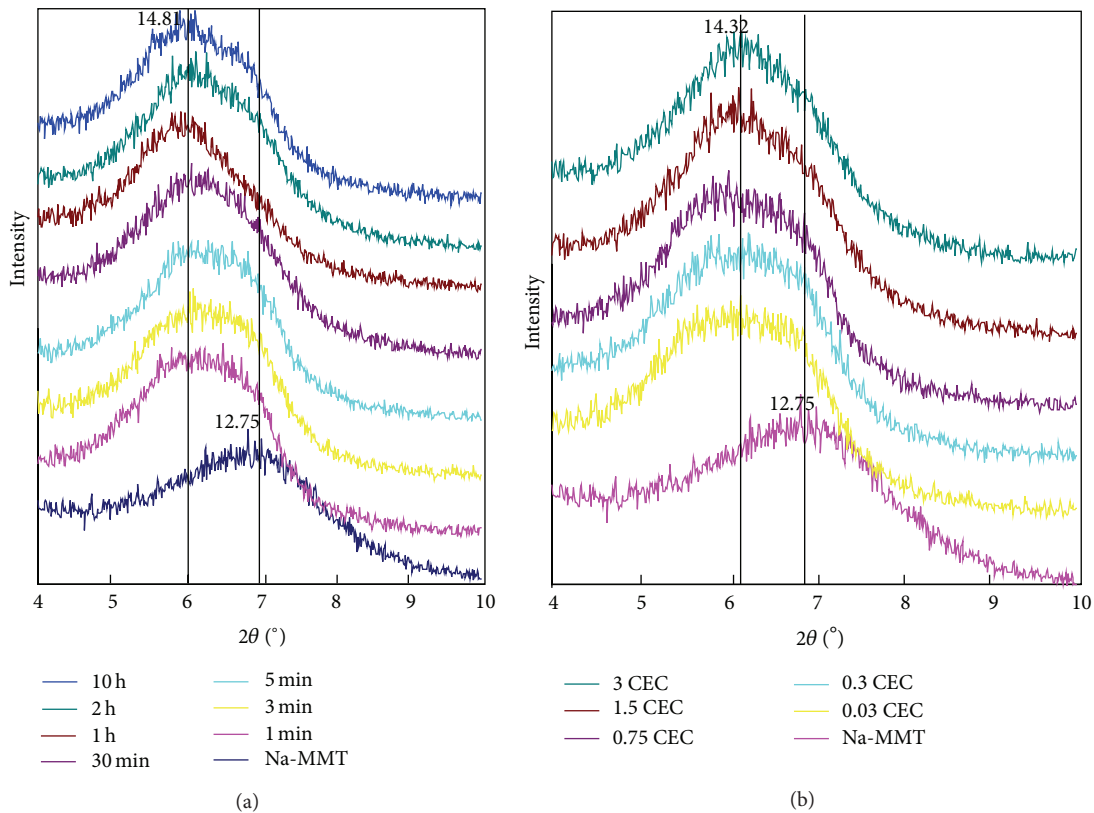


FIGURE 3: X-ray diffraction patterns of Na-MMT cations exchanged with Cd^{2+} (d in Å). Effect of time/min (a) and Cd^{2+} input in CEC (b).

indicating that K^+ cations were only partially exchanged, even though the input amount of Cd^{2+} was equivalent to 3 times the CEC of the Mt. These results showed that K^+ as the interlayer cation is more stable, as in the case of illite and mica.

The effect of initial solution concentration on exchange capacity had a similar result; that is, the interlayer cation Na^+ in Na + Mt can be completely exchanged by Cd^{2+} ions, the amount of exchange increases as Cd^{2+} concentration increased, and exchange balance was achieved when the input Cd^{2+} was 3 times the CEC. The discrepancy in exchange

amounts of Mts with different interlayer space cations is due to diverse interaction forces of layers and interlayer cations [32, 33]. The result of exchange amounts means interaction force between Mt layer and K^+ was greater than that between Mt layer and Na^+ . This larger interaction force may prevent complete Cd^{2+} exchange for K^+ in the interlayer space of Mt.

It can be indicated from interlayer space of Mt (Figure 3) that increasing concentration of solution prompts resulted in sharp and enhanced reflection of (001). The d_{001} value of Cd + Mt increased as the amount of Cd^{2+} adsorption increased and reflected at 14.8 Å. This value is larger than 13.15 Å for

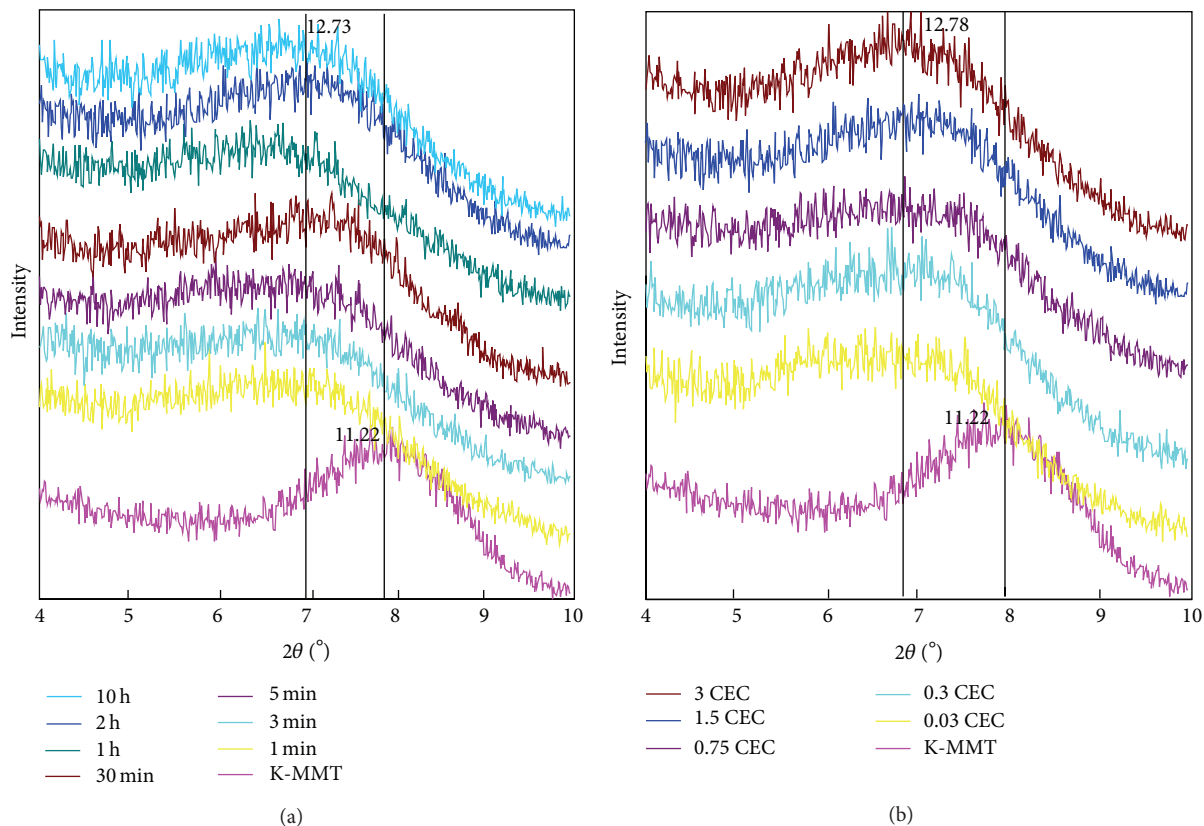


FIGURE 4: X-ray diffraction patterns of K-MMT cations exchanged with Cd^{2+} ($d/\text{\AA}$). Effect of time/min (a) and Cd^{2+} input in CEC (b).

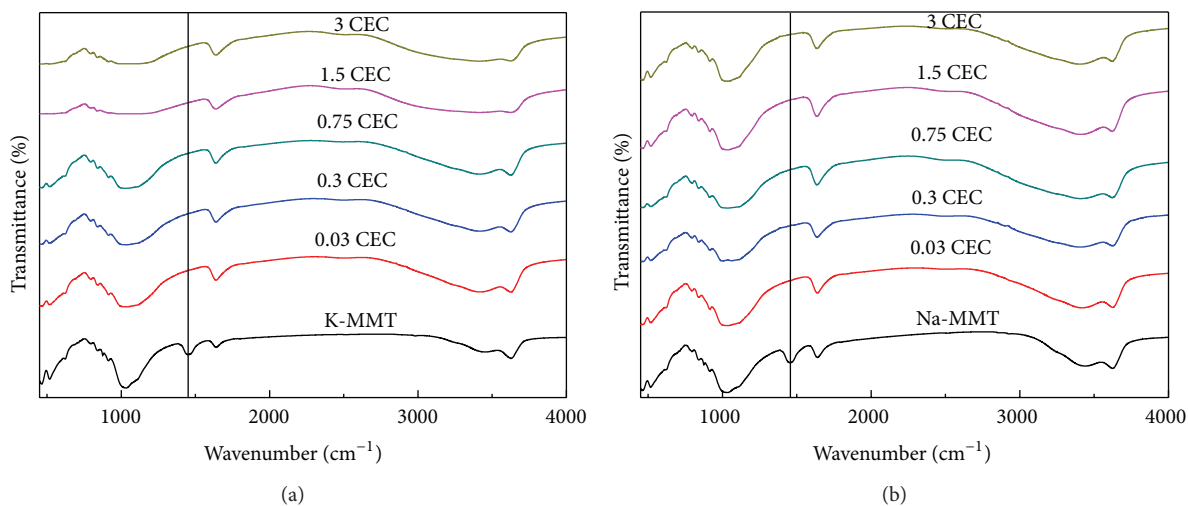


FIGURE 5: FTIR analyses of K-MMT, Na-MMT, and Cd-MMT.

Pb-exchanged Mt and smaller than 15.90\AA for Zn-exchanged Mt [34]. In contrast to Na + Mt, the (001) reflection of K + Mt after being exchanged with different amounts of Cd^{2+} was no longer present, suggesting delamination of Mt (Figure 4).

The FTIR spectra of Mt in contact with different amounts of Cd^{2+} were illustrated in Figure 5. The wide absorbing band

observed at 3625 cm^{-1} was assigned to Al-O-H stretching vibration of Mt structural water, and wide adsorbing band at 3436 cm^{-1} could be assigned to stretching of hydroxyl in adsorbed and interlayer space water [35]. The shoulder within $1630\text{--}1640\text{ cm}^{-1}$ was due to hydroxyl bending vibration of adsorbed water, while another shoulder observed at about

1035 cm^{-1} could be attributed to stretching of Si-O-Si in Mt lattice. The weak adsorb band observed at 914 cm^{-1} was owing to bending vibration of octahedral hydroxyl in Mt lattice, and the sharp band at 523 cm^{-1} is attributed to bending vibration of Si-O-Al [36].

For K + Mt, as the amount of Cd^{2+} uptake increased, the band within 1630~1640 cm^{-1} increased gradually, while band at 1447 cm^{-1} disappeared. Bands at these two positions are attributed to bending vibration of hydroxyl in adsorbed water, which means changes in interaction force between Mt layer and interlayer cation would lead to variation in position and intensity of these bands. However, the band at 1035 cm^{-1} representing bending vibration of Si-O-Si in Mt lattice and band at 3625 cm^{-1} representing bending of Al-O-H in Mt structural water both decrease as intercalation amount of Cd^{2+} increases, meaning interaction force of K^+ and Mt layer was stronger, leading to a minor change in Mt structure that affected force in layer. For Na + Mt, as Cd^{2+} exchange preceded, except for disappearance of absorption band at 1447 cm^{-1} and increase in transmittance at 1648 cm^{-1} , bands at other positions showed no apparent changes. It means that Na + Mt had a weaker interaction force between the Mt layer and interlayer cations in comparison to K + Mt. This would lead to an easy exchange of Cd^{2+} for Na^+ .

The mass change within 25~175°C was due to removal of adsorbed surface and interlayer space water of Mt [37]. For K + Mt, as Cd^{2+} uptake increased, mass loss within 25~175°C increased markedly, from initial 4.1% to 12.9% (Figure 6(a)). The result indicated less amount of interlayer space water in K + Mt in comparison to Cd + Mt, suggesting weaker interaction force between K^+ cation and water molecule than that between Cd^{2+} and water molecules; that is, K^+ was less hydrated than Cd^{2+} . The differential thermal analysis (DTA) curves showed a similar trend within 25~175°C (Figure 6(b)). The endothermic valley was due to removal of interlayer space and adsorbed water. As the amount of Cd^{2+} uptake increased, endothermic valley moves to a slightly higher temperature, indicating that interaction force between Cd^{2+} and water molecule was greater than that between K^+ and water. Mass loss of Na + Mt in 25~175°C was 10.8%, 6.7% more than that of K + Mt (Figure 6(c)), illustrating that Na^+ in Na + Mt was more hydrated than K^+ in K + Mt. As less interlayer space water resulted in smaller interlayer space, a stronger electrostatic attraction of interlayer cation and layers and difficult exchangeability would be anticipated. Therefore, amount of interlayer space water played an important role in easiness of cation exchange for Mt. The mass loss of Na + Mt in 25~175°C increased from initial 10.8% to 17% as the amount of Cd^{2+} uptake increased (Figure 6(c)), while the maximum mass loss after Cd^{2+} exchanging K^+ in K + Mt was only 12.9%. It indicated better cation exchangeability of Na + Mt than K + Mt by Cd^{2+} once again. And in DTA curve (Figure 6(d)), within 25~175°C, endothermic valley remained at the same position as the amount of Cd^{2+} uptake on Na + Mt increased, showing similar interaction force of Na^+ with Cd^{2+} to water molecule,

while the amount of combined water of Cd^{2+} was more than Na^+ .

3.3. Simulations. Based on the aforementioned experimental results, CASTEP module in Material Studio 6.0 was used to calculate energies of interactions between Mt layers and different cations in the interlayer space. The optimal configuration was speculated when stable cations coexist with Mt layer. The energy of interactions was -78425, -76537, and -75480 eV for Cd^+ , Na^+ , and K + Mt, respectively, which is positively related to the interlayer space of these three Mts and negatively related to the ionic radii of Cd^{2+} , Na^+ , and K^+ . Our results agree well with general observations that the smaller the cation, the more hydrated the cation. Apart from that, the interlayer space is also determined by hydration of cation; the more the water molecules surrounded a cation, the greater the interlayer space is [38]. The order of energies in three Mts demonstrates stability of interlayer cations and difficulty in exchange: the higher energy of interactions means better distribution in the interlayer space and more combining water, leading to weaker interaction force with layer, easily exchanged by other cations. Thus, the order of cation exchange preference followed $\text{Cd}^{2+} > \text{Na}^+ > \text{K}^+$.

The interlayer space of K + Mt, Na + Mt, and Cd + Mt was 10.55, 12.5, and 14.81 Å, respectively. MD simulation showed that minimum distances from K^+ , Na^+ , and Cd^{2+} to oxygen in Mt silicate-oxygen tetrahedron would be 2.303, 2.443, and 4.648 Å, respectively (Figure 7). From top view, it can be seen that K^+ , Na^+ , and Cd^{2+} are all located on oxygen hexagonal ring, which is above Mg substituting position of alumina in octahedron; maximum angles between the three ions to the nearest oxygen and diagonal oxygen were 102.58°, 103.36°, and 54.28°. From the relations of distance and angle of interlayer cation and oxygen in Mt, silica-oxygen tetrahedron, interaction force of K^+ and Mt layer is the strongest, the distance is less than 2.5 Å, and the angle is obtuse; thus it is possible to form chemical bonds. While interaction force of Na^+ and Mt layer is weaker than that of K^+ , so the exchange capacity of Na^+ is higher than that of K^+ . The interlayer cations are all hydrated, where minimal distance of K^+ , Na^+ , or Cd^{2+} to oxygen in water molecular was 2.965, 2.274, or 3.83 Å, respectively. Only Na^+ -O distance is less than 2.5 Å, suggesting forming a weak bond.

One Na^+ cation is surrounded by two water molecules, while distances from the central cation to the two water molecules were different. Distances from K^+ or Cd^{2+} to oxygen in water molecules were all longer than 2.5 Å, impossible to form a chemical bond. In addition, the position of Cd^{2+} to water differs from that of Na^+ and K^+ , as Na^+ and K^+ are surrounded by two water molecules, monolayer arranged, while Cd^{2+} is surrounded by four water molecules and bilayer arranged. This would lead to expansion of the interlayer space to 14.81 Å. The interaction force of K^+ and Mt layer is the strongest, and that of K^+ and

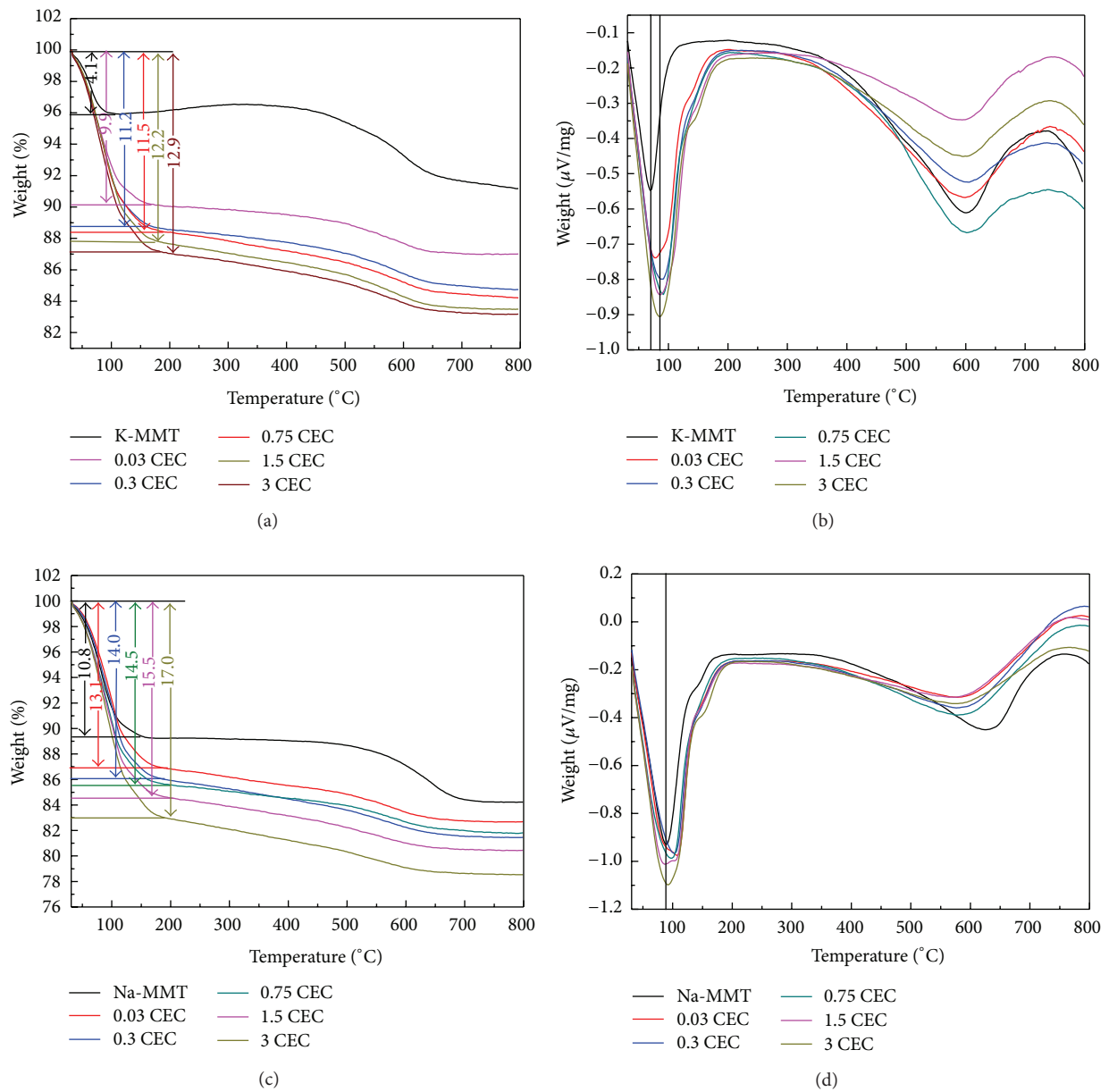


FIGURE 6: TG and DTA curves of K-MMT (a, b), Na-MMT (c, d), and Cd-MMT.

water molecular is the weakest; interaction force of Na^+ and water is the weakest, resulting in a higher free swelling of Na + Mt.

4. Conclusions

Cd^{2+} was tested to exchange with different interlayer cations in Mts. By comparing exchange capacity, interlayer space, and energy, we discovered great diversity in degrees of cation exchange of different Mts. Na + Mt can be thoroughly exchanged by Cd^{2+} . Conversely, only 60% of K in Mt can be exchanged by Cd^{2+} at an input amount equivalent to 3

times the CEC. The result of XRD indicated that exchange of Na^+ by Cd^{2+} in Mt was uniform and complete, and molecule dynamics simulation proved that electrostatic force of K^+ is larger than that of Na^+ , showing an easier cation exchange of Cd^{2+} for Na^+ . A better swelling was found for Na + Mt compared to K + Mt, suggesting a better hydration of Na^+ in the interlayer space of Mt. The result of molecule dynamic simulation showed energies of three Mts following Cd + Mt < Na + Mt < K + Mt. Interaction force with Mt layer followed $\text{K}^+ > \text{Na}^+ > \text{Cd}^{2+}$. Therefore, Mts with diverse interaction cations have different properties and should be used in different fields.

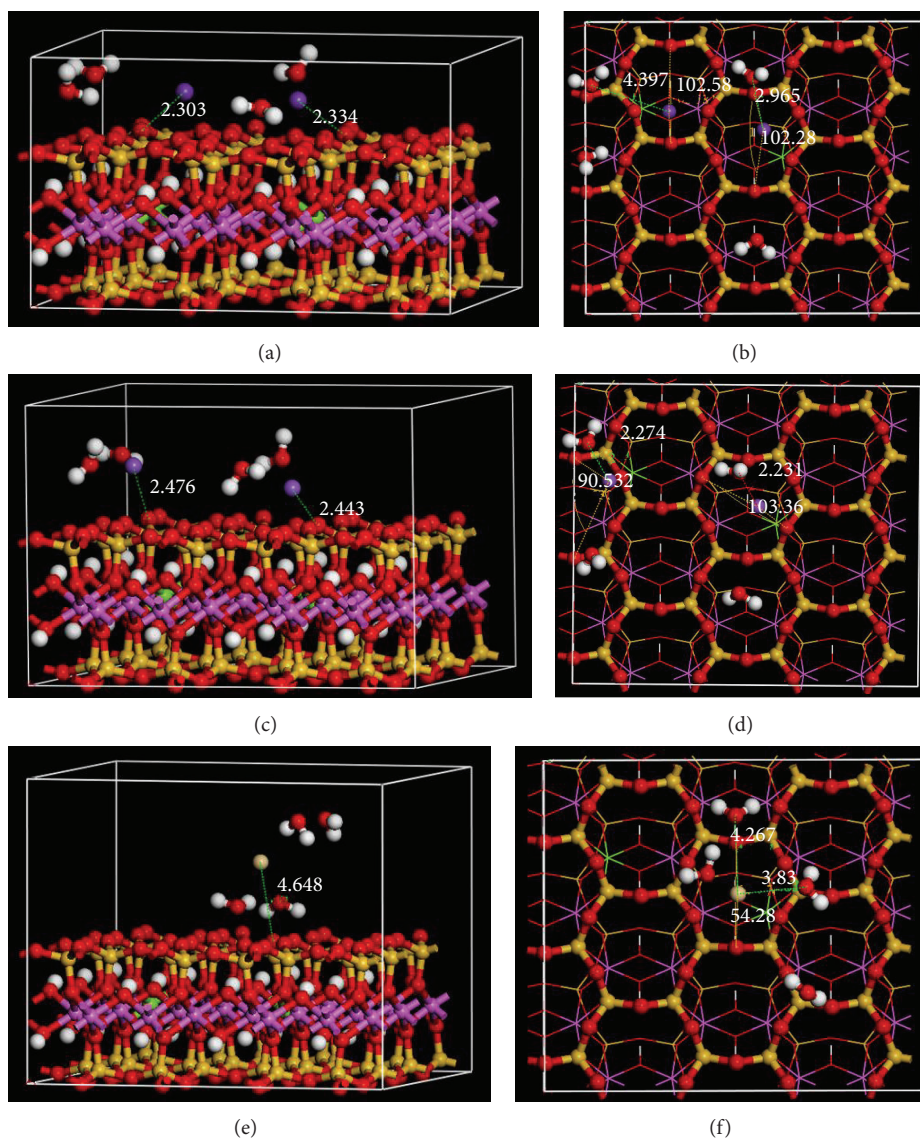


FIGURE 7: Molecular dynamic simulation of the distance and angle of K^+ (a, b), Na^+ (c, d), and Cd^{2+} (e, f) with $[SiO_4]$.

Conflict of Interests

The authors declare that there is no conflict of interests regarding the publication of this paper.

Acknowledgment

This present work was supported by the International S&T Cooperation (Grant no. 2014DFA91000).

References

- [1] W. Liu, P. J. Li, X. M. Qi et al., "DNA changes in barley (*Hordeum vulgare*) seedlings induced by cadmium pollution using RAPD analysis," *Chemosphere*, vol. 61, no. 2, pp. 158–167, 2005.
- [2] P. F. A. M. Römken, H. Y. Guo, C. L. Chu, T. S. Liu, C. F. Chiang, and G. F. Koopmans, "Prediction of cadmium uptake by brown rice and derivation of soil-plant transfer models to improve soil protection guidelines," *Environmental Pollution*, vol. 157, no. 8-9, pp. 2435–2444, 2009.
- [3] S. Satarug, J. R. Baker, S. Urbenjapol et al., "A global perspective on cadmium pollution and toxicity in non-occupationally exposed population," *Toxicology Letters*, vol. 137, no. 1-2, pp. 65–83, 2003.
- [4] E. Dopico, A. R. Linde, and E. Garcia-Vazquez, "Traditional and modern practices of soil fertilization: effects on cadmium pollution of river ecosystems in Spain," *Human Ecology*, vol. 37, no. 2, pp. 235–240, 2009.
- [5] Q. Cai, M.-L. Long, M. Zhu, Q.-Z. Zhou, L. Zhang, and J. Liu, "Food chain transfer of cadmium and lead to cattle in a lead-zinc smelter in Guizhou, China," *Environmental Pollution*, vol. 157, no. 11, pp. 3078–3082, 2009.
- [6] E. Krznaric, N. Verbruggen, J. H. L. Wevers, R. Carleer, J. Vangronsveld, and J. V. Colpaert, "Cd-tolerant *Suillus luteus*. A fungal insurance for pines exposed to Cd," *Environmental Pollution*, vol. 157, no. 5, pp. 1581–1588, 2009.
- [7] M. Vaculík, C. Konlechner, I. Langer et al., "Root anatomy and element distribution vary between two *Salix caprea* isolates with

- different Cd accumulation capacities," *Environmental Pollution*, vol. 163, pp. 117–126, 2012.
- [8] M. M. Matlock, B. S. Howerton, K. R. Henke, and D. A. Atwood, "A pyridine-thiol ligand with multiple bonding sites for heavy metal precipitation," *Journal of Hazardous Materials*, vol. 82, no. 1, pp. 55–63, 2001.
- [9] I. H. Lee, Y.-C. Kuan, and J.-M. Chern, "Factorial experimental design for recovering heavy metals from sludge with ion-exchange resin," *Journal of Hazardous Materials*, vol. 138, no. 3, pp. 549–559, 2006.
- [10] H.-J. Fan and P. R. Anderson, "Copper and cadmium removal by Mn oxide-coated granular activated carbon," *Separation and Purification Technology*, vol. 45, no. 1, pp. 61–67, 2005.
- [11] Z. Q. Xie, L. G. Sun, P. F. Zhang et al., "Preliminary geochemical evidence of groundwater contamination in coral islands of Xi-Sha, South China Sea," *Applied Geochemistry*, vol. 20, no. 10, pp. 1848–1856, 2005.
- [12] P. Yuan, F. Annabi-Bergaya, Q. Tao et al., "A combined study by XRD, FTIR, TG and HRTEM on the structure of delaminated Fe-intercalated/pillared clay," *Journal of Colloid and Interface Science*, vol. 324, no. 1-2, pp. 142–149, 2008.
- [13] V. Marry, B. Rotenberg, and P. Turq, "Structure and dynamics of water at a clay surface from molecular dynamics simulation," *Physical Chemistry Chemical Physics*, vol. 10, no. 32, pp. 4802–4813, 2008.
- [14] X.-D. Liu and X.-C. Lu, "A thermodynamic understanding of clay-swelling inhibition by potassium ions," *Angewandte Chemie International Edition*, vol. 45, no. 38, pp. 6300–6303, 2006.
- [15] J. Zhou, X. Lu, J. Zhu et al., "Interlayer structure and dynamics of HDTMA⁺-intercalated rectorite with and without water: a molecular dynamics study," *The Journal of Physical Chemistry C*, vol. 116, no. 24, pp. 13071–13078, 2012.
- [16] T. J. Tambach, P. G. Bolhuis, and B. Smit, "A molecular mechanism of hysteresis in clay swelling," *Angewandte Chemie*, vol. 43, no. 20, pp. 2650–2652, 2004.
- [17] H. He, J. Galy, and J. F. Gerard, "Molecular simulation of the interlayer structure and the mobility of alkyl chains in HDTMA⁺/montmorillonite hybrids," *The Journal of Physical Chemistry B*, vol. 109, no. 27, pp. 13301–13306, 2005.
- [18] Q. Zhao and S. E. Burns, "Microstructure of single chain quaternary ammonium cations intercalated into montmorillonite: a molecular dynamics study," *Langmuir*, vol. 28, no. 47, pp. 16393–16400, 2012.
- [19] R. Zhu, W. Chen, T. V. Shapley, M. Molinari, F. Ge, and S. C. Parker, "Sorption characteristics of organomontmorillonite toward organic compounds: a combined LFERs and molecular dynamics simulation study," *Environmental Science & Technology*, vol. 45, no. 15, pp. 6504–6510, 2011.
- [20] R. Zhu, W. Hu, Z. You, F. Ge, and K. Tian, "Molecular dynamics simulation of TCDD adsorption on organo-montmorillonite," *Journal of Colloid and Interface Science*, vol. 377, no. 1, pp. 328–333, 2012.
- [21] J. A. Greathouse and R. T. Cygan, "Water structure and aqueous uranyl(VI) adsorption equilibria onto external surfaces of beidellite, montmorillonite, and pyrophyllite: results from molecular simulations," *Environmental Science and Technology*, vol. 40, no. 12, pp. 3865–3871, 2006.
- [22] V. Aggarwal, Y.-Y. Chien, and B. J. Teppen, "Molecular simulations to estimate thermodynamics for adsorption of polar organic solutes to montmorillonite," *European Journal of Soil Science*, vol. 58, no. 4, pp. 945–957, 2007.
- [23] M. A. Chappell, D. A. Laird, M. L. Thompson et al., "Influence of smectite hydration and swelling on atrazine sorption behavior," *Environmental Science and Technology*, vol. 39, no. 9, pp. 3150–3156, 2005.
- [24] Q. Zhao and S. E. Burns, "Molecular dynamics simulation of secondary sorption behavior of montmorillonite modified by single chain quaternary ammonium cations," *Environmental Science and Technology*, vol. 46, no. 7, pp. 3999–4007, 2012.
- [25] P. A. Lock and N. T. Skipper, "Computer simulation of the structure and dynamics of phenol in sodium montmorillonite hydrates," *European Journal of Soil Science*, vol. 58, no. 4, pp. 958–966, 2007.
- [26] S. J. Chipera and D. L. Bish, "Baseline studies of the clay minerals society source clays: powder X-ray diffraction analyses," *Clays and Clay Minerals*, vol. 49, no. 5, pp. 398–409, 2001.
- [27] D. Borden and R. F. Giese, "Baseline studies of the clay minerals society source clays: cation exchange capacity measurements by the ammonia-electrode method," *Clays and Clay Minerals*, vol. 49, no. 5, pp. 444–445, 2001.
- [28] A. R. Mermut and G. Lagaly, "Baseline studies of the clay minerals society source clays: layer-charge determination and characteristics of those minerals containing 2:1 layers," *Clays and Clay Minerals*, vol. 49, no. 5, pp. 393–397, 2001.
- [29] N. Khaorapong and M. Ogawa, "Solid-state intercalation of 8-hydroxyquinoline into Li(I)-, Zn(II)- and Mn(II)-montmorillonites," *Applied Clay Science*, vol. 35, no. 1-2, pp. 31–38, 2007.
- [30] L. M. Wu, L. B. Liao, G. C. Lv, F. X. Qin, and Z. H. Li, "Microstructure and process of intercalation of imidazolium ionic liquids into montmorillonite," *Chemical Engineering Journal*, vol. 236, pp. 306–313, 2014.
- [31] N. Khaorapong, A. Ontam, and M. Ogawa, "Formation of ZnS and CdS in the interlayer spaces of montmorillonite," *Applied Clay Science*, vol. 50, no. 1, pp. 19–24, 2010.
- [32] A. Meleshyn, "Cetylpyridinium aggregates at the montmorillonite- and muscovite-water interfaces: a Monte Carlo study of surface charge effect," *Langmuir*, vol. 25, no. 11, pp. 6250–6259, 2009.
- [33] B. Schampera and S. Dultz, "Determination of diffusive transport in HDPy-montmorillonite by H₂O-D₂O exchange using in situ ATR-FTIR spectroscopy," *Clay Minerals*, vol. 44, no. 2, pp. 249–266, 2009.
- [34] W. Oueslati, M. Mefath, H. B. Rhaïem, and A. B. H. Amara, "Cation exchange selectivity versus concentration of competing heavy metal cations (Pb²⁺, Zn²⁺): case of Na-montmorillonite," *Physics Procedia*, vol. 2, pp. 1059–1063, 2009.
- [35] J. Madejová and P. Komadel, "Baseline studies of the clay minerals society source clays: infrared methods," *Clays and Clay Minerals*, vol. 49, no. 5, pp. 410–432, 2001.
- [36] G. C. Lv, L. Liu, Z. H. Li, L. B. Liao, and M. T. Liu, "Probing the interactions between chlorpheniramine and 2:1 phyllosilicates," *Journal of Colloid and Interface Science*, vol. 374, no. 1, pp. 218–225, 2012.
- [37] Z. H. Li and W.-T. Jiang, "A thermogravimetric investigation of alkylammonium intercalation into rectorite," *Thermochimica Acta*, vol. 483, no. 1-2, pp. 58–65, 2009.
- [38] X. Liu, X. C. Lu, R. C. Wang, H. Q. Zhou, and S. J. Xu, "Molecular dynamics insight into the cointercalation of hexadecyltrimethyl-ammonium and acetate ions into smectites," *The American Mineralogist*, vol. 94, no. 1, pp. 143–150, 2009.

Research Article

A General Synthesis Strategy for Hierarchical Porous Metal Oxide Hollow Spheres

Huadong Fu,¹ Feng Ren,² Weiming Su,² Jinlin Yang,² and Ruiping Liu²

¹*Institute for Advanced Materials and Technology, University of Science and Technology Beijing, Beijing 100083, China*

²*Department of Materials Science and Engineering, China University of Mining & Technology, Beijing 100083, China*

Correspondence should be addressed to Ruiping Liu; 201402@cumt.edu.cn

Received 28 July 2015; Accepted 6 September 2015

Academic Editor: Ruomeng Yu

Copyright © 2015 Huadong Fu et al. This is an open access article distributed under the Creative Commons Attribution License, which permits unrestricted use, distribution, and reproduction in any medium, provided the original work is properly cited.

The hierarchical porous TiO₂ hollow spheres were successfully prepared by using the hydrothermally synthesized colloidal carbon spheres as templates and tetrabutyl titanate as inorganic precursors. The diameter and wall thickness of hollow TiO₂ spheres were determined by the hard templates and concentration of tetrabutyl titanate. The particle size, dispersity, homogeneity, and surface state of the carbon spheres can be easily controlled by adjusting the hydrothermal conditions and adding certain amount of the surfactants. The prepared hollow spheres possessed the perfect spherical shape, monodispersity, and hierarchically pore structures, and the further experiment verified that the present approach can be used to prepare other metal oxide hollow spheres, which could be used as catalysis, fuel cells, lithium-air battery, gas sensor, and so on.

1. Introduction

Compared to the solid particles, hollow spheres have attracted much attention in recent years due to its outstanding properties, such as the controlled pore structure, low density, high specific surface area, high pore volume, and superior thermal and mechanical stability, in which widespread potential applications in catalysts, gas sensors, coatings, energy storage, conversion, and so forth can be found [1–4]. For example, the Co₃O₄ spheres with hollow structure could be used as an excellent catalyst for many key applications [5–9]; due to their large specific surface area and hierarchical pore structures, TiO₂ hollow spheres exhibit excellent photocatalytic performance [10–14], while SnO₂ hollow spheres could be used as an anode material for lithium ion batteries with high efficiency [15–18].

Recently, the design strategies and preparation methods of the hollow nano- or microspheres have been reported by many researchers, and the templates assisted synthesized method was commonly used as an effective approach to prepare hierarchical hollow spheres. The hard templates such as polymethyl methacrylate microspheres, polymer latex particles, polystyrene microspheres, and silica spheres and

soft templates such as emulsion droplets, twelve sodium dodecyl sulfate (SDS), micelles, and gas bubbles were usually used [19–22]. The synthesis and pore structure regulation of hollow spheres with size and shape controlled morphologies may obtain other excellent performances and broaden its applications. Among the above templates, the monodispersed carbonaceous microspheres synthesized by hydrothermally treating of aqueous solutions of glucose and sugar were thought to be an ideal hard template for preparation of the hollow spheres [23]. Due to the existence of the functional groups which were located at the surface of the colloidal carbon spheres, the templates were suited for the absorption of cationic metal ions and precipitation of metal precursors. Therefore, in the present work, we aimed to report a general synthesis approach applicable to prepare metal oxide hollow spheres with tunable structure by using the hydrothermally synthesized colloidal carbon spheres as the hard templates.

2. Experimental Procedure

2.1. Synthesis of Carbon Spheres. The colloidal carbon spheres used in the present study were prepared by hydrothermally treating of aqueous solutions of glucose. Typically, 9 grams of

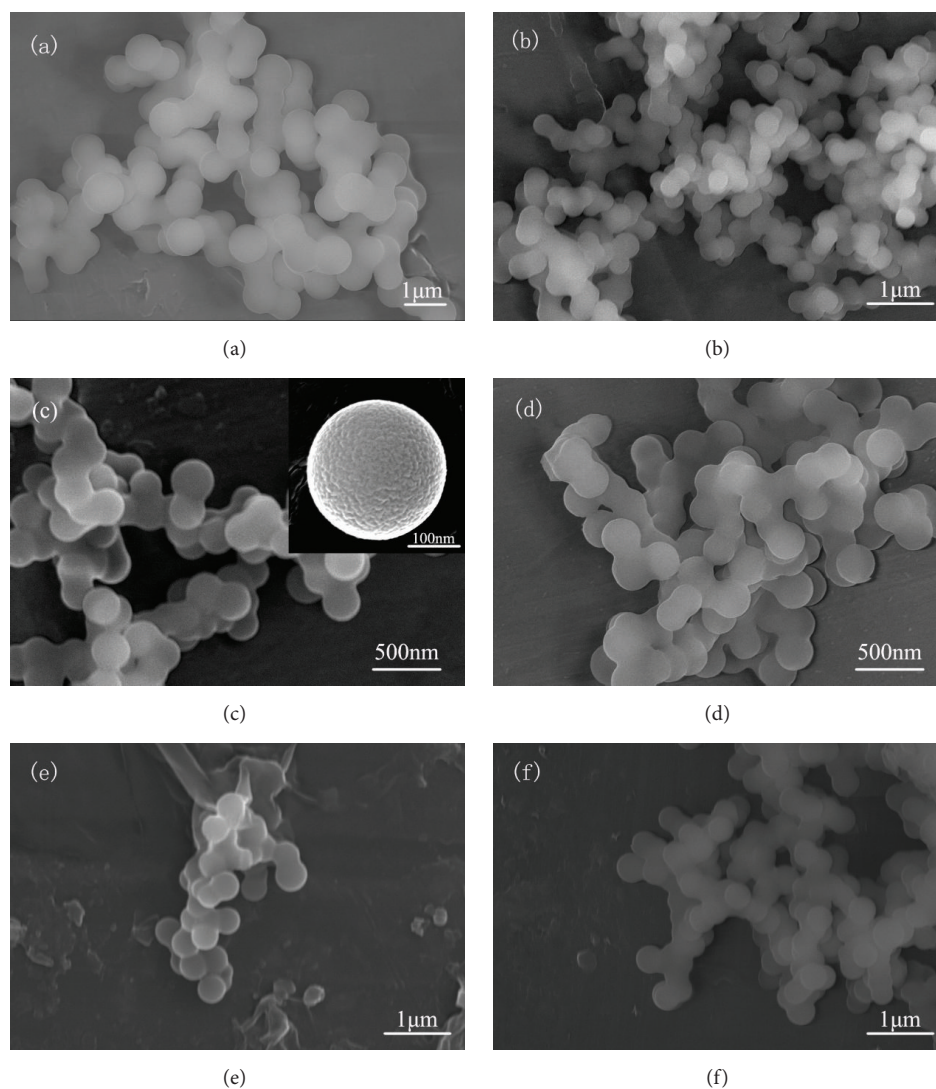


FIGURE 1: SEM photographs of carbon spheres prepared by different concentration of glucose, hydrothermal temperature, and time. (a) 0.5 mol/L, 220°C, 12 h; (b) 0.5 mol/L, 200°C, 12 h; (c) 0.5 mol/L, 180°C, 12 h; (d) 0.5 mol/L, 220°C, 10 h; (e) 0.5 mol/L, 220°C, 8 h; (f) 0.75 mol/L, 220°C, 12 h.

glucose (Beijing Chemical Reagent Factory, analytical purity) was dissolved in 90 mL deionized (DI) water to form a clear solution, which was then transferred to a 100 mL Teflon-sealed autoclave and maintained at certain temperature and time. The resultant black products were separated and purified by centrifugation and washed repeatedly in DI water and ethanol for three times, respectively, and finally dried in a vacuum oven at 80°C for 6 h. In order to regulate the dispersity and particle size of the as-obtained carbon spheres, the different hydrothermal treatment parameters and different kinds and amounts of the surfactants were used in the preparation of the carbon spheres.

2.2. Preparation of Metal Oxide Hollow Spheres. Take TiO_2 as an example, the details of a typical experiment for the synthesis of TiO_2 hollow spheres are described as follows. Firstly, 5 mL tetrabutyl titanate was dissolved in 50 mL

ethanol to form a clear solution, and then 0.1 grams of the newly synthesized carbon spheres was dispersed in the above suspension with the aid of ultrasonication. After stirred for 2 h, 20 mL of the mixed solutions of ethanol and DI water with the volume ratio of 5 : 1 was added dropwise to the suspension under vigorous stirring. The mixture was aged for 1 h and then subjected to centrifugation and washing to remove impurities and dried in a vacuum oven at 60°C for 5 h. Finally, the TiO_2 hollow spheres were obtained by strengthening the shell structure and removing the carbon spheres of the carbon-titania composites calcined in air at 450–850°C (heating rate of 2°C/min) for 4 h.

2.3. Characterization. The calcination procedure was determined by the thermogravimetric (TG) and differential scanning calorimetry (DSC) analysis. Nicolet Magna 750 was used to measure the FTIR spectra of carbon spheres, and the

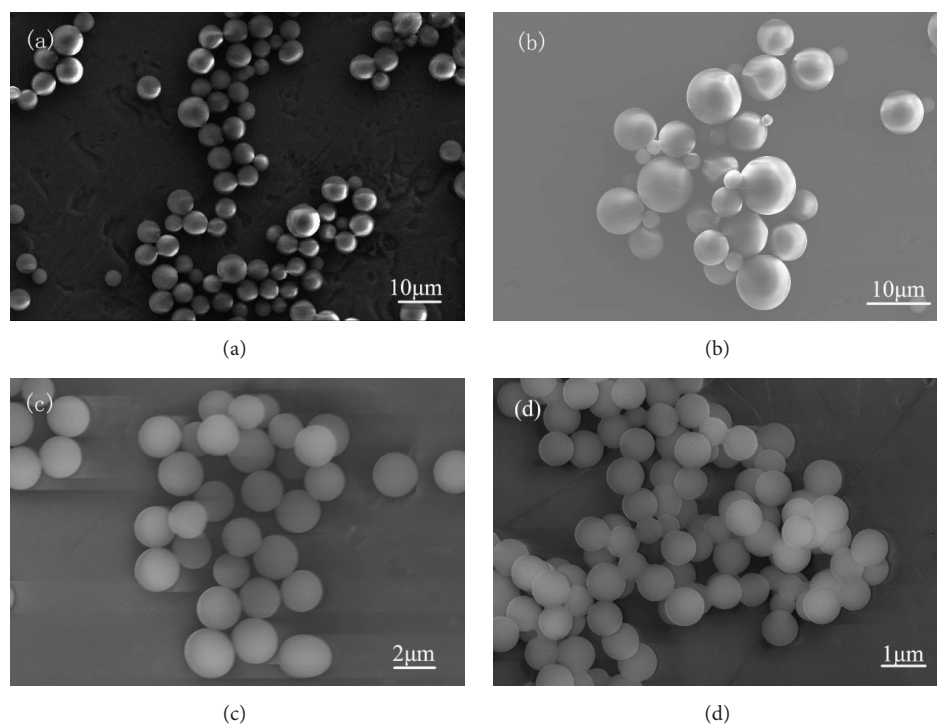


FIGURE 2: SEM photographs of carbon spheres prepared by adding different kinds and amounts of the surfactants. (a) 0.005 mol/L $\text{NH}_3 \cdot \text{H}_2\text{O}$; (b) 0.015 mol/L $\text{NH}_3 \cdot \text{H}_2\text{O}$; (c) 0.005 mol/L CTAB; (d) 0.015 mol/L CTAB.

wave number region ranged from 4000 to 500 cm^{-1} with 64 scans at 8 cm^{-1} resolution. X-ray diffraction (XRD) with the scanning speed of $4^\circ/\text{min}$ from 20 to 80° was carried out on a Bruker D8-Advance diffractometer using Ni filtered $\text{Cu K}\alpha$ radiation. The applied current and voltage were 40 mA and 40 kV , respectively. The microstructures of the carbon spheres and hollow TiO_2 spheres were observed by scanning electron microscopy (Carl Zeiss Jena scanning microscope, SEM) and transmission electron microscopy (JEOL JEM-2011, TEM). BET-surface area was measured by N_2 adsorption at liquid nitrogen temperature using a NOVA4000 automated gas sorption system.

3. Results and Discussion

3.1. Synthesis of Carbon Spheres. Figure 1 shows the SEM images of the as-prepared carbon spheres synthesized at different conditions. It can be seen that the dispersity and particle size of the as-synthesized carbon spheres were influenced by hydrothermal time, temperature, and concentration of glucose. With decreasing of the hydrothermal temperature, shortening of the hydrothermal time, and reducing of the concentration of the glucose, the particle size of the colloidal carbon spheres decreased, and, meanwhile, the dispersity of the carbon spheres was improved. For example, the particle size of the carbon spheres decreased from 500 nm to 350 nm when the hydrothermal temperature decreased from 220°C to 180°C (Table 1). On the other hand, with increasing of the hydrothermal temperature and hydrothermal time,

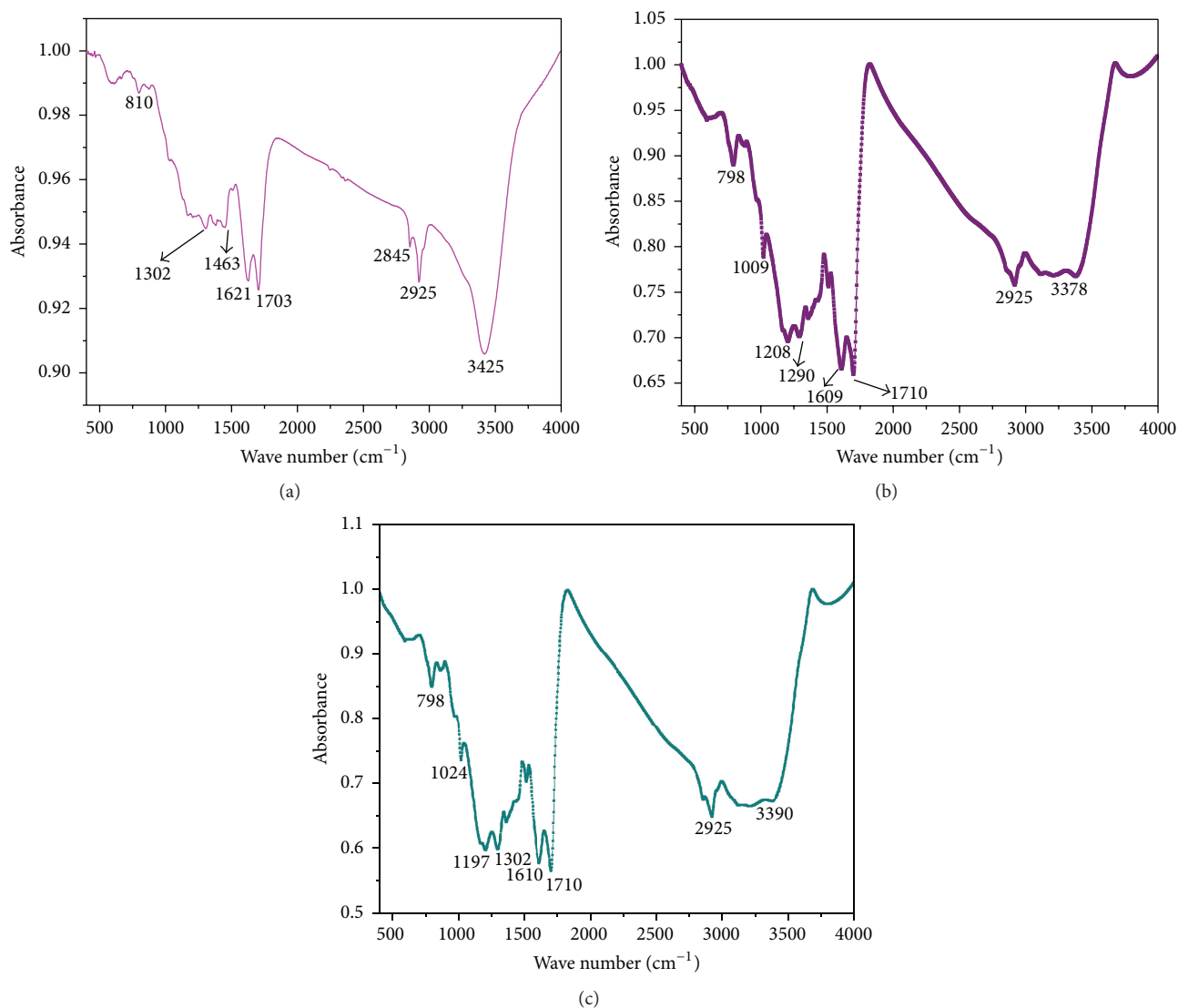
the particle size of carbon spheres tended to be monodispersed. It also can be found that the as-synthesized carbon spheres exhibit rough and porous surface, which will impart the carbon spheres with low density and large specific surface area.

The hydrothermal synthesis of carbon spheres can also be divided into two stages, including nucleation and growth. The increases of temperature in the early stage of synthesis process led to dehydration and condensation of the glucose molecules, and the polysaccharide molecular was formed. With extending the hydrothermal time, the polysaccharide was further polymerized to form a polymer chain, and the carbon spheres nuclei were formed by the cross linking of polymer chain. Then polymer polymerization occurred in the surface of nuclei, namely, the growth of the carbon spheres, and after further dehydration and carbonization the carbon spheres with certain size were obtained.

In order to further regulate the dispersity and particle size of the carbon spheres, the hydrothermal temperature and time were fixed to 200°C and 10 h , respectively, and the different kinds and amounts of the surfactant were added in the solution. The typical SEM images are shown in Figure 2. It can be seen clearly that the morphologies and particle size of carbon spheres can be changed obviously when the surfactants were added, and the dispersity of the carbon spheres was improved, accompanied by decreasing the homogeneity of the carbon spheres. With increasing of the ammonia concentration from 0.005 mol/L to 0.015 mol/L , the particle size of the carbon spheres increased from $2\text{--}4 \mu\text{m}$ to $6\text{--}9 \mu\text{m}$. The

TABLE 1: The diameter of the as-synthesized carbon spheres.

Concentration of the glucose (mol/L)	Hydrothermal temperature ($^{\circ}\text{C}$)	Hydrothermal time (h)	Additives	Diameter of the carbon spheres
0.5	220	12	—	500 nm
0.5	200	12	—	400 nm
0.5	180	12	—	350 nm
0.5	220	10	—	450 nm
0.5	220	8	—	430 nm
0.75	180	12	—	450 nm
0.75	220	12	—	520 nm
1 m	220	12	—	600 nm
0.5	200	10	Ammonia 0.005 mol/L	2–4 μm
0.5	200	10	Ammonia 0.015 mol/L	6–9 μm
0.5	200	10	CTAB 0.005 mol/L	1–2 μm
0.5	200	10	CTAB 0.015 mol/L	700 nm

FIGURE 3: Fourier transform infrared spectroscopy FTIR spectra of carbon spheres. (a) no surfactant; (b) 0.015 mol/L $\text{NH}_3\cdot\text{H}_2\text{O}$; (c) 0.015 mol/L CTAB.

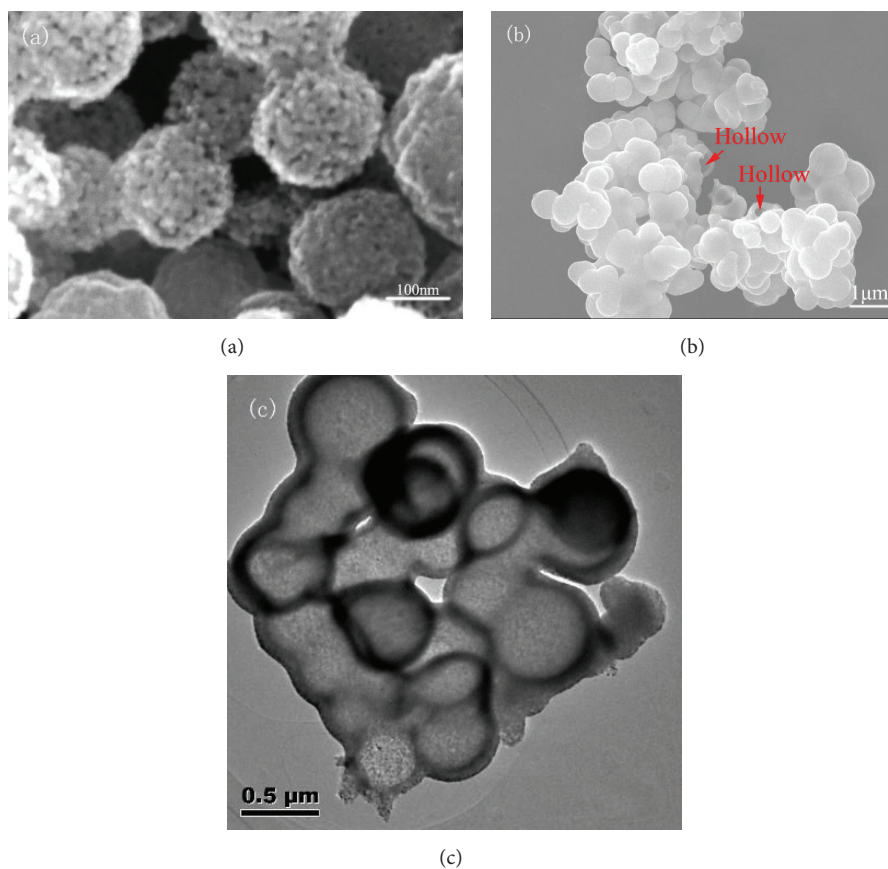


FIGURE 4: SEM images of (a) as-synthesized carbon-titania composite spheres; (b) titania hollow spheres; (c) TEM image of the titania hollow spheres.

monodispersed carbon spheres with the diameter of 700 nm can be obtained when adding the 0.015 mol/L cetyltrimethylammonium bromide (CTAB) under the hydrothermal conditions of 200°C and 10 h (Table 1).

Figure 3 presents the FTIR spectra of the as-synthesized carbon spheres under different conditions. It can be seen clearly that a large number of functional groups exist at the surface of the carbon spheres, including C-OH (1710 cm^{-1}), -OH ($3300\sim 3500\text{ cm}^{-1}$), C=C (1621 cm^{-1}), C=O (1302 cm^{-1}), and C-H (2925 cm^{-1}) groups, and, among them, the absorption of the metal ions formed by hydrolysis of inorganic precursors and synergistic reaction with the precursors will be promoted by the presence of the C-OH and -OH groups, while the other groups are harmful to the coating process. Regardless of $\text{NH}_3\cdot\text{H}_2\text{O}$ and CTAB, the -OH located at around $3300\sim 3500\text{ cm}^{-1}$ decreased when the surfactants were added in the solution, which will affect the subsequent deposition process of metal ions.

3.2. Synthesis of Metal Oxide Hollow Spheres. Figures 4(a) and 4(b) show the SEM images of the carbon-titania composite spheres before and after the thermal treatment at 450°C for 4 h, and it can be seen that the coated carbon/ TiO_2 composite spheres with monodispersed spherical shape were obtained,

indicating that the coating layer was uniform. There was a clear contrast between the edge and the center of the as-synthesized titania spheres which was observed in the TEM image (Figure 4(c)) indicating that they exhibited a hollow structure. The synthesis mechanism of the titania hollow spheres can be explained as follows. The replacement of the titanate groups and the -OH of the carbon spheres occurs when the carbon spheres are dispersed in the ethanol, and then the titanium atoms enter the hydrophilic surface of the carbon spheres through a -Ti-O- covalent bond. Once dropped in the mixed solution of water and ethanol, the hydrolysis and condensation reactions of titanate groups in the surface of the carbon spheres will occur, and with the increase of aging time the -Ti-O-Ti- groups are formed on the surface of carbon spheres, which will be transformed to titania shell after subsequent calcination at certain temperature.

In order to determine the crystal phase of the as-prepared hollow TiO_2 spheres, XRD measurements were carried out and the results are shown in Figure 5(a). It can be seen that after the calcination of carbon-titania composite spheres at 450°C the titania precursor was transformed into anatase TiO_2 . A distinct large hysteresis loop in the N_2 adsorption-desorption isotherms can be observed for all samples (Figure 5(b)), which is a typical IV isotherm with H1-shaped hysteresis loop, demonstrating the presence of

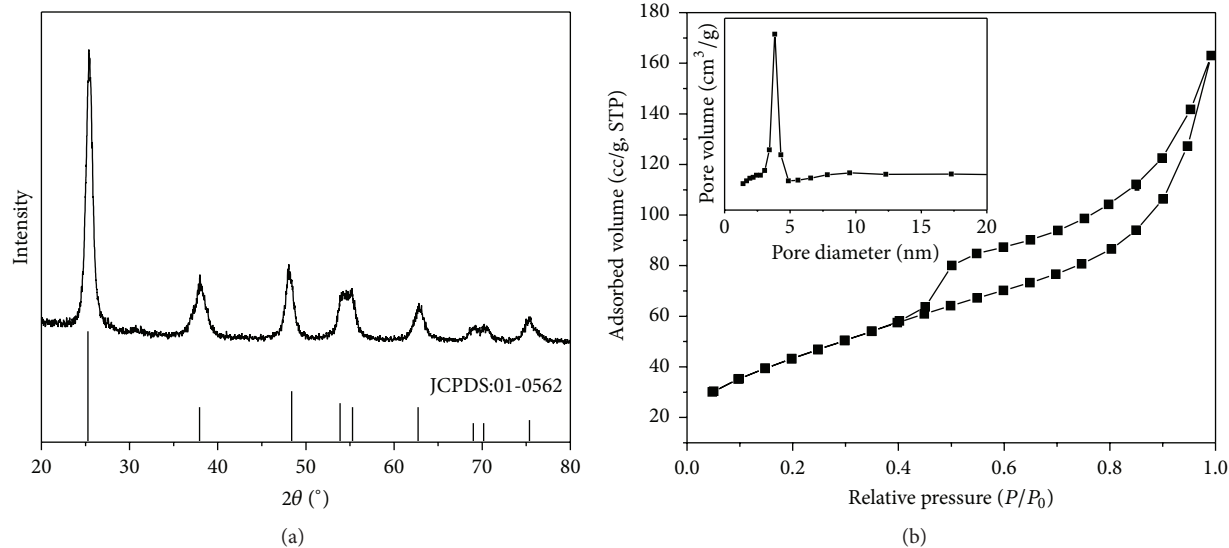


FIGURE 5: XRD pattern (a) and N_2 absorption-desorption isotherms of the titania hollow spheres, and the inset is the pore size distribution curve of the titania hollow spheres (b).

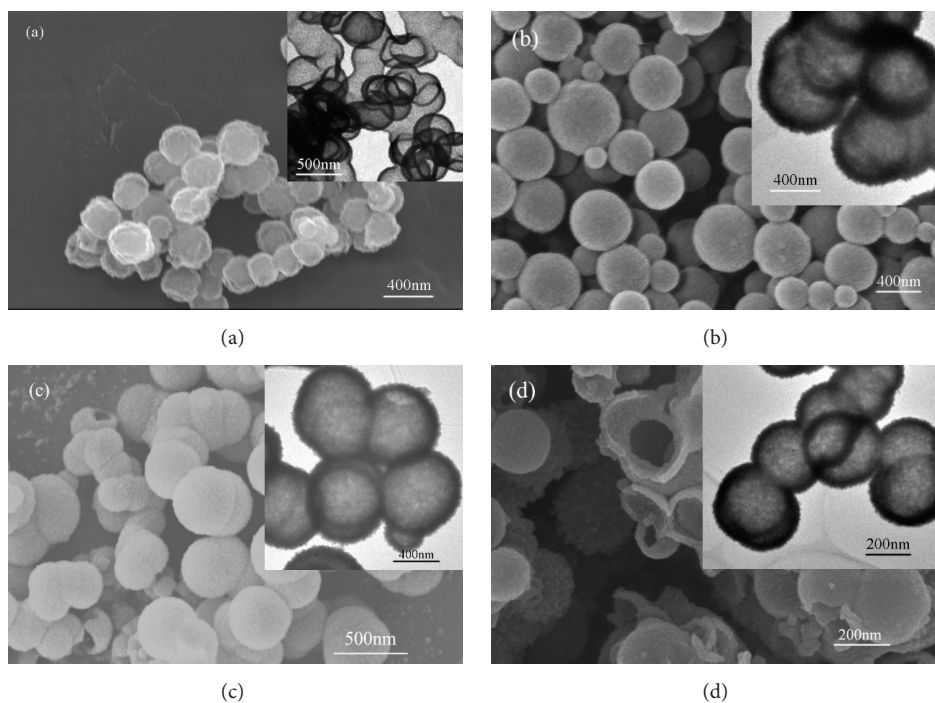


FIGURE 6: SEM images of SnO₂ (a), Co₃O₄ (b), YSZ (c), and CeO₂ (d) hollow spheres.

mesoporous structure. The titania hollow spheres with the maximum specific surface area of $100.179 \text{ m}^2/\text{g}$ and pore volume of 0.110 cc/g can be obtained when the mass ratio of carbon spheres and tetrabutyl titanate was 1:30. The inset in Figure 5(b) shows that the pore size distributions of the hollow spheres exhibits a sharp peak, and the average BJH mesopore size is 3.76 nm , indicating a uniform mesopore distributed in the shell of the titania hollow spheres.

The size and pore structure of the hollow TiO₂ spheres can be easily regulated by adjusting the synthesis parameters.

For example, the diameter of hollow TiO₂ spheres can be controlled by using the carbon spheres prepared under different conditions as hard templates, while the wall thickness and specific surface area of the titania hollow spheres can be regulated either by adjusting the concentration of tetrabutyl titanate or by controlling the number of the functional groups located on the surface of the carbon spheres prepared with the presence of surfactants of different types and amount.

The synthesis strategy presented above provides a simple and general approach for the synthesis of hierarchically

porous metal oxide hollow spheres, which can also be widely applied to other systems. As shown in Figure 6, when other inorganic precursors, such as SnCl_4 , $\text{Co}(\text{NO}_3)_2 \cdot 6\text{H}_2\text{O}$, $\text{Y}(\text{NO}_3)_3 \cdot 6\text{H}_2\text{O}$, $\text{ZrOCl}_2 \cdot 8\text{H}_2\text{O}$, and $\text{Ce}(\text{NO}_3)_3 \cdot 6\text{H}_2\text{O}$ were employed as templates, the as-prepared SnO_2 , Co_3O_4 , YSZ, and CeO_2 hollow spheres with different compositions were successfully prepared by adopting this synthesis strategy. All the prepared hollow spheres with different inorganic salts as precursors possess the well-developed spherical morphology.

4. Conclusions

In summary, we have developed a simple and general approach for preparing the metal oxide hollow spheres by using the hydrothermally synthesized colloidal carbon spheres as hard templates. The wall thickness and textural properties of the hollow spheres can be easily tailored by adjusting the concentration of inorganic precursor. The monodispersed hollow spheres with perfect spherical shape and hierarchically pore structures can be used as catalysis, lithium-air battery, fuel cells, gas sensor, and so on.

Conflict of Interests

The authors declare that there is no conflict of interests regarding the publication of the paper.

Acknowledgments

The authors would like to thank the financial support from the National Natural Science Foundation of China (NSFC, no. 51202117) and the Fundamental Research Funds for the Central Universities (no. 2014QJ02).

References

- [1] H. C. Zeng, "Synthetic architecture of interior space for inorganic nanostructures," *Journal of Materials Chemistry*, vol. 16, no. 7, pp. 649–662, 2006.
- [2] H. L. Xu and W. Z. Wang, "Template synthesis of multishelled Cu_2O hollow spheres with a single-crystalline shell wall," *Angewandte Chemie—International Edition*, vol. 46, no. 9, pp. 1489–1492, 2007.
- [3] H. L. Xu, W. Z. Wang, W. Zhu, L. Zhou, and M. L. Ruan, "Nanostructured single-crystalline twin disks of zinc oxide," *Crystal Growth & Design*, vol. 7, pp. 541–544, 2007.
- [4] D. Zhang, L. Qi, J. Ma, and H. Cheng, "Synthesis of submicrometer-sized hollow silver spheres in mixed polymer-surfactant solutions," *Advanced Materials*, vol. 14, no. 20, pp. 1499–1502, 2002.
- [5] Y. Zhao and L. Jiang, "Hollow micro/nanomaterials with multi-level interior structures," *Advanced Materials*, vol. 21, no. 36, pp. 3621–3638, 2009.
- [6] A. D. Dinsmore, M. F. Hsu, M. G. Nikolaidis, M. Marquez, A. R. Bausch, and D. A. Weitz, "Colloidosomes: selectively permeable capsules composed of colloidal particles," *Science*, vol. 298, no. 5595, pp. 1006–1009, 2002.
- [7] S. Park, J.-H. Lim, S.-W. Chung, and C. A. Mirkin, "Self-assembly of mesoscopic metal-polymer amphiphiles," *Science*, vol. 303, no. 5656, pp. 348–351, 2004.
- [8] J. V. Ryan, A. D. Berry, M. L. Anderson et al., "Electronic connection to the interior of a mesoporous insulator with nanowires of crystalline RuO_2 ," *Nature*, vol. 406, no. 6792, pp. 169–172, 2000.
- [9] T. K. Maji, R. Matsuda, and S. Kitagawa, "A flexible interpenetrating coordination framework with a bimodal porous functionality," *Nature Materials*, vol. 6, no. 2, pp. 142–148, 2007.
- [10] Y. H. Ao, J. J. Xu, D. G. Fu, and C. W. Yuan, "A simple method for the preparation of titania hollow sphere," *Catalysis Communications*, vol. 9, no. 15, pp. 2574–2577, 2008.
- [11] F. Caruso, "Hollow capsule processing through colloidal templating and self-assembly," *Chemistry*, vol. 6, no. 3, pp. 413–419, 2000.
- [12] J.-J. Zhu, S. Xu, H. Wang, J.-M. Zhu, and H.-Y. Chen, "Sonochemical synthesis of CdSe hollow spherical assemblies via an in-situ template route," *Advanced Materials*, vol. 15, no. 2, pp. 156–159, 2003.
- [13] C. Wang, K. Tang, Q. Yang, J. Hu, and Y. Qian, "Fabrication of BiTeI submicrometer hollow spheres," *Journal of Materials Chemistry*, vol. 12, no. 8, pp. 2426–2429, 2002.
- [14] J.-W. Shi, J.-W. Chen, H.-J. Cui et al., "One template approach to synthesize C-doped titania hollow spheres with high visible-light photocatalytic activity," *Chemical Engineering Journal*, vol. 195–196, pp. 226–232, 2012.
- [15] C. Wei, G. Zhang, Y. Bai et al., "Al-doped SnO_2 hollow sphere as a novel anode material for lithium ion battery," *Solid State Ionics*, vol. 272, pp. 133–137, 2015.
- [16] S. Ding, J. S. Chen, G. Qi et al., "Formation of SnO_2 hollow nanospheres inside mesoporous silica nanoreactors," *Journal of the American Chemical Society*, vol. 133, no. 1, pp. 21–23, 2011.
- [17] X. M. Yin, C. C. Li, M. Zhang et al., "One-step synthesis of hierarchical SnO_2 hollow nanostructures via self-assembly for high power lithium ion batteries," *The Journal of Physical Chemistry C*, vol. 114, no. 17, pp. 8084–8088, 2010.
- [18] X. Wang, Z. Li, Z. Zhang et al., "Mo-doped SnO_2 mesoporous hollow structured spheres as anode materials for high-performance lithium ion batteries," *Nanoscale*, vol. 7, no. 8, pp. 3604–3613, 2015.
- [19] J. G. Yu, W. Liu, and H. G. Yu, "A one-pot approach to hierarchically nanoporous titania hollow microspheres with high photocatalytic activity," *Crystal Growth and Design*, vol. 8, no. 3, pp. 930–934, 2008.
- [20] L. Shen, L. Yu, X.-Y. Yu, X. Zhang, and X. W. D. Lou, "Self-templated formation of uniform NiCo_2O_4 hollow spheres with complex interior structures for lithium-ion batteries and supercapacitors," *Angewandte Chemie—International Edition*, vol. 54, no. 6, pp. 1868–1872, 2015.
- [21] Z. Huang and F. Tang, "Preparation, structure, and magnetic properties of mesoporous magnetite hollow spheres," *Journal of Colloid & Interface Science*, vol. 281, no. 2, pp. 432–436, 2005.
- [22] X. M. Sun and Y. D. Li, "Colloidal carbon spheres and their core/shell structures with noble-metal nanoparticles," *Angewandte Chemie—International Edition*, vol. 43, no. 5, pp. 597–601, 2004.
- [23] M.-M. Titirici, M. Antonietti, and A. Thomas, "A generalized synthesis of metal oxide hollow spheres using a hydrothermal approach," *Chemistry of Materials*, vol. 18, no. 16, pp. 3808–3812, 2006.

Review Article

Theoretical Studies of Electronic Structure and Photophysical Properties of a Series of Indoline Dyes with Triphenylamine Ligand

Xue-Feng Ren,¹ Jun Zhang,¹ and Guo-Jun Kang^{1,2}

¹School of Chemical Engineering & Technology, China University of Mining and Technology, Xuzhou 221008, China

²Low Carbon Energy Institute, China University of Mining and Technology, Xuzhou 221008, China

Correspondence should be addressed to Guo-Jun Kang; gjkang@cumt.edu.cn

Received 9 March 2015; Accepted 15 April 2015

Academic Editor: Ruomeng Yu

Copyright © 2015 Xue-Feng Ren et al. This is an open access article distributed under the Creative Commons Attribution License, which permits unrestricted use, distribution, and reproduction in any medium, provided the original work is properly cited.

To design efficient organic sensitizer, a series of D- π -A indoline dyes with different donor parts have been investigated by density functional theory (DFT) and time-dependent DFT (TD-DFT) approach. The molecular geometries, frontier molecular orbitals, and absorption spectra of these dyes have been systematically investigated to provide comprehensive understanding of the structure-property relationships. Compared with D149, our designed dyes have proper HOMO and LUMO energy level, narrowed HOMO-LUMO energy gap, and broadened absorption band by introducing the N(CH₃)₂ and N(phenyl)₂ groups at the donor part. Furthermore, the dimeric dyes and dye-(TiO₂)₆ systems have been optimized by DFT method to simulate the intermolecular interactions, as well as interaction between the dyes dimmers and semiconductor interface, respectively. Through the analyses of absorption energies (E_{ads}), energy levels of the HOMO and LUMO, light harvesting efficiency (LHE), and the driving force of electrons injections (ΔG_{inject}), it is found that the designed dyes should have improved optical properties by importing the N(CH₃)₂ group. This work is hoped to provide a theoretical guiding role in design of new dyes for dye-sensitized solar cells.

1. Introduction

Due to increasing energy demands and concerning global warming, scientists have paid tremendous effort on developing cheap and easily accessible renewable energy sources. Dye-sensitized solar cells (DSSCs) have been regarded as one of the most promising next-generation photovoltaic cells due to their potentially low fabrication costs, easy production, and flexibility compared to traditional silicon-based solar cells [1]. A typical DSSC is constructed with the dye sensitizer, dye-absorbed nanocrystalline semiconductor oxide (such as TiO₂ or ZnO), electrolyte containing I⁻/I₃⁻ redox couples, and closed circuit. Obviously, the sensitizer plays a significant role for improving the efficiency of DSSCs. Therefore, considerable synthetic works have been carried out on Ru-based sensitizers [2–4] and metal-free organic dye sensitizers [5–10]. Among them, indoline dye sensitizers [11] have attracted much attention because of their high

molar extinction coefficient, relatively less expensive, and low pollution of environmental. Although the significant progress has been made in the organic dyes, the conversion efficiency of indoline type dyes is still lower than the Ru-based sensitizer [12]. Therefore, the investigation on the organic dye is very important for realizing large-scale commercial production.

Except the massive synthesized research, theoretical studies have been accepted as extremely powerful and comparably low-cost tools for revealing the effect of chemical modifications on the optical properties [13–18]. In spite of outstanding electronic and optical properties of triphenylamine derivatives in solar cell [19–22], to our knowledge, there is no detailed study on indoline-containing materials coupled with triphenylamine as donor part. Consequently, in order to reveal the role of triphenylamine on the photophysical properties and develop more efficient dyes, the donor part of D149 dye is replaced by triphenylamine unit. Then, triphenylamine-containing indoline dyes are designed by introducing

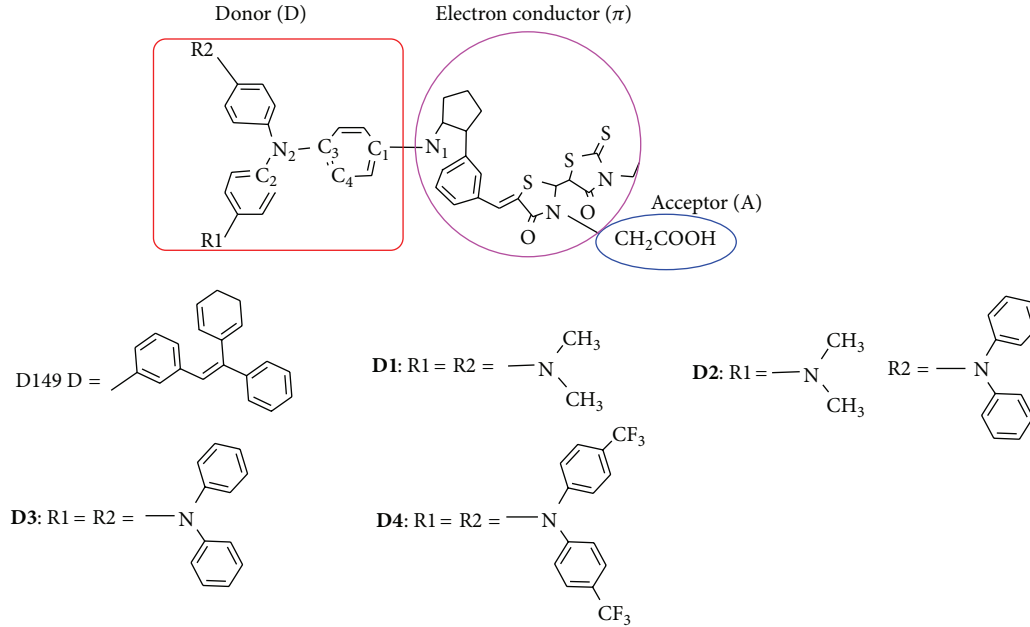


FIGURE 1: Sketch map of the studied dyes.

the $N(\text{CH}_3)_2$, $N(\text{phenyl})_2$, and CF_3 at the donor part of D149 in this work (see Figure 1). A systematic comparison and analysis of the geometries, frontier molecular orbitals, and absorption spectra of these dyes are carried out. Furthermore, the light harvesting efficiency (LHE) and the driving force of electrons injections (ΔG_{inject}) are calculated to estimate the short-circuit photocurrent density. In addition, the electron coupling of dimeric dyes and dye- $(\text{TiO}_2)_6$ systems is simulated by DFT method to testify the electron injection efficiency. This work is expected to reveal the effect of chemical modification on the DSSCs efficiency and provide valuable guidance for developing efficiency dyes.

2. Computational Details

All calculations were performed with the Gaussian 09 program package [23]. The density functional theory DFT (B3LYP) approach had been successfully used to calculate the ground geometries in indoline dye sensitizers [13–15, 24]. Therefore, in this work, the geometries structures of monomer and dimer dyes were fully optimized at the DFT level of B3LYP method [25, 26] using the 6-31G(d) basis set. Following the optimized geometry, the vibrational frequencies were calculated and the results confirmed that all the optimized monomer geometries were stable geometric structures. The absorption spectra of these dyes were investigated by TDDFT with the B3LYP approach associated with the polarized continuum model (PCM) [27, 28] in methanol media.

To investigate the electronic coupling interaction between these dyes and TiO_2 nanoparticles, the absorption geometries of dyes/ $(\text{TiO}_2)_6$ clusters were calculated by B3LYP method. The 6-31G(d) basis sets were used for C, H, O, N, S, and F atoms and LANL2DZ for Ti atom. Although $(\text{TiO}_2)_6$ cluster is a simplistic model, it was believed to qualitatively

reproduce the trend of the charge distribution [29]. The absorption energies (E_{ads}) of dyes/ $(\text{TiO}_2)_6$ were calculated by the following equation:

$$E_{\text{ads}} = E_{\text{dye}} + E_{(\text{TiO}_2)_6} - E_{[\text{dye}/(\text{TiO}_2)_6]}. \quad (1)$$

The E_{dye} , $E_{(\text{TiO}_2)_6}$, and $E_{[\text{dye}/(\text{TiO}_2)_6]}$ were the total energies of dyes, $(\text{TiO}_2)_6$ cluster, and dye/ $(\text{TiO}_2)_6$, respectively.

The short-circuit current density (J_{sc}) which is closely connected to the energy conversion efficiency (η) of the solar cell [30] can be determined by the following equation [31]:

$$J_{\text{sc}} = \int \text{LHE}(\lambda) \Phi_{\text{inject}} \eta_{\text{collect}} d\lambda, \quad (2)$$

where $\text{LHE}(\lambda)$ is the light-harvesting efficiency at a given wavelength [31], Φ_{inject} is the electron injection efficiency to the semiconductor substrate, and η_{collect} is the electron collection efficiency. η_{collect} can be assumed as a constant in the same DSSCs with sole different dyes [32]. As a result, the enhancement of J_{sc} should focus on improving the $\text{LHE}(\lambda)$ and Φ_{inject} . The Φ_{inject} is related to the driving force ΔG_{inject} for the electron injection. According to Preat's method [33], the ΔG_{inject} of electron injections from the excited states of dyes to semiconductor surface are calculated.

The light-harvesting efficiency $\text{LHE}(\lambda)$ can be calculated with

$$\text{LHE}(\lambda) = 1 - 10^{-f}, \quad (3)$$

where f is the oscillator strength of the maximum absorption spectra of dyes.

3. The Molecular Geometries of Dyes

The sketch map and the optimized geometries of D149 and D1–D4 are shown in Figures 1 and 2, respectively.

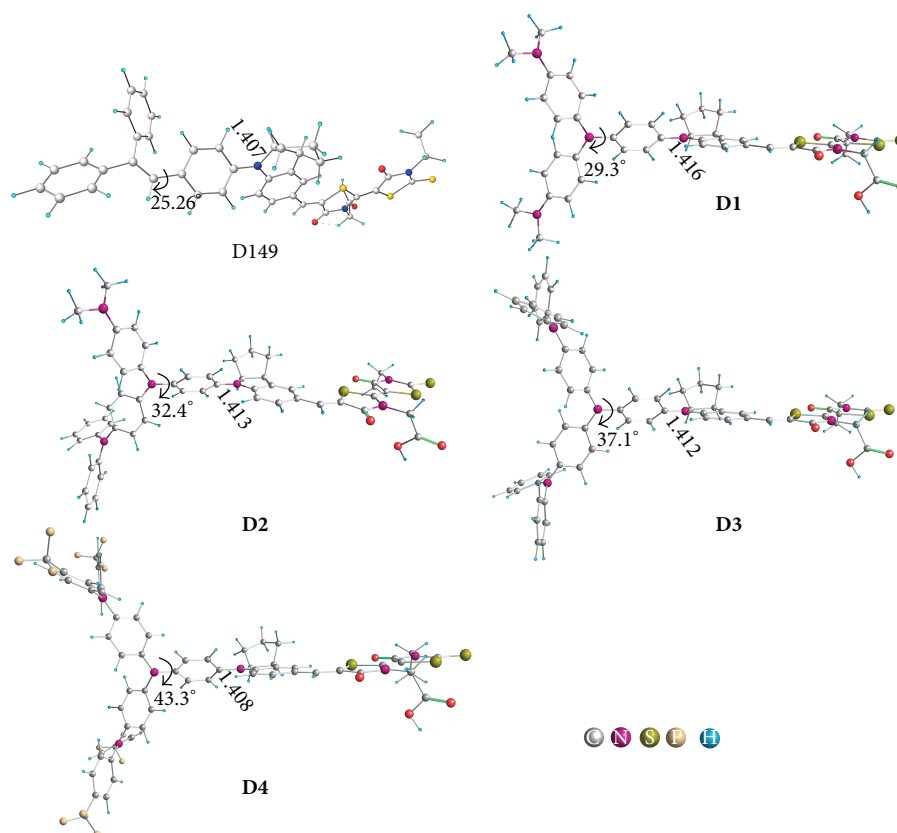


FIGURE 2: The optimized geometry of the studied dyes, together with the important bond length (Å) and dihedral angle (°).

The triphenylamine moiety, indoline and rhodanine group, and CH_2COOH act as an electron donor (D), electron conductor (π), and acceptor (A), respectively. As shown in Figure 2, the dihedral angle of $\text{C}_4\text{-C}_3\text{-N}_2\text{-C}_2$ for D149 is 25.26° . D2 and D3 have steric obstruction conformation by gradually adding the $\text{N}(\text{phenyl})_2$ groups in D1. For example, the dihedral angle of $\text{C}_4\text{-C}_3\text{-N}_2\text{-C}_2$ for D1–D3 is calculated to be 29.3° , 32.4° , and 37.1° , respectively. Note that the dihedral angle of $\text{C}_4\text{-C}_3\text{-N}_2\text{-C}_2$ increases from 37.1° (D3) to 43.3° (D4) by introducing the CF_3 group at the end of triphenylamine. Obviously, the steric obstruction can be justified by proper functional group and thus avoids the unfavorable dye aggregation on the TiO_2 surface. Besides the dihedral angle of $\text{C}_4\text{-C}_3\text{-N}_2\text{-C}_2$, the bond length $\text{C}_1\text{-N}_1$ between the D and π part increases in the following order: D4 (1.408 Å) < D3 (1.412 Å) < D2 (1.413 Å) < D1 (1.416 Å), indicating the bond conjugation ability decreases in the same order. This can be explained by the NBO charges on the C_1 and N_1 atoms. The NBO charges on N_1 atom of D2–D4 are similar with D1. But for C_1 atom, it decreases dramatically in the following order: D4 (0.148e) > D3 (0.133e) > D2 (0.127e) > D1 (0.117e), suggesting the bond conjugation ability has been enhanced by introducing $\text{N}(\text{phenyl})_2$ and CF_3 substitutions.

3.1. Frontier Molecular Orbital Analysis. The energy levels of the HOMO and LUMO, as well as the HOMO-LUMO gaps, are drawn in Figure 3, together with the energy levels of TiO_2 semiconductor conduction band (-4.00 eV) [34] and the redox potential of I^-/I_3^- (-4.80 eV) [35].

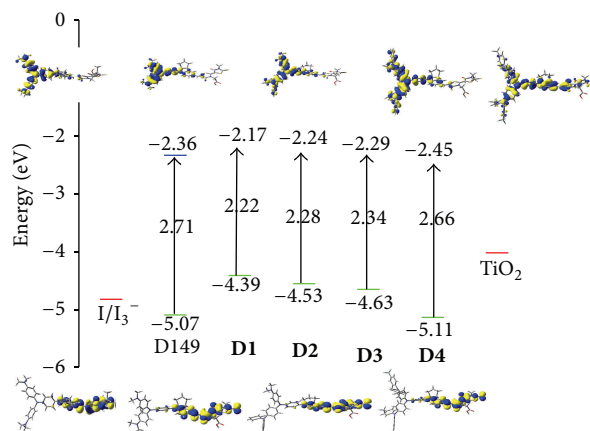


FIGURE 3: The energy levels and contour plot of HOMO and LUMO, as well as HOMO-LUMO energy gap (eV) of D149 and D1–D4. The redox potential of I^-/I_3^- (-4.80 eV) and energy level of conduction band (CB) of the TiO_2 surface (-4.00 eV) are drawn in red line.

As drawn in Figure 3, the HOMO and LUMO energy levels of D1–D3 increase remarkably (-4.39 eV and -2.17 eV for D1, -4.53 eV and -2.24 eV for D2, and -4.63 eV and -2.29 eV for D3) compared with D149 obtained by us (-5.07 eV and -2.36 eV) and previous work [24] (-5.009 eV and -2.408 eV), which means that the energy level of molecular orbital can be greatly changed by introduction of triphenylamine into

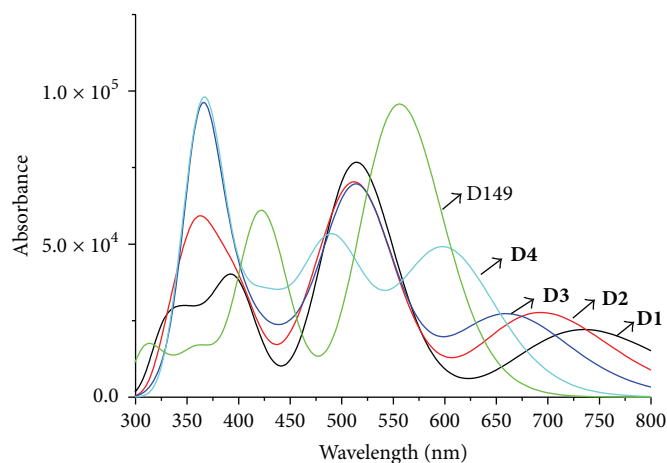


FIGURE 4: Simulated absorption spectra for D149 and D1–D4 obtained by B3LYP/6-31G* method in methanol media.

the donor part. Although the introduction of triphenylamine unit increases the HOMO values relative to D149, the HOMO level of D1–D3 still approaches the redox potential of Γ^-/I_3^- (−4.80 eV). The HOMO level of D4 (−5.11 eV) decreases dramatically by importing the CF_3 group at the end of the triphenylamine group, which is lower by 0.31 eV than Γ^-/I_3^- redox potential. This means that the studied dyes ensure efficient dye regeneration. In addition, the LUMO energy of D1–D4 is higher than the conduction band edge of TiO_2 , which would provide enough driving force for electron injection for ultrafast excited-state electron injection [36]. Thus, it is a good approach to enhance the ability of dye regeneration by introducing the $N(CH_3)_2$ and $N(phenyl)_2$ substitutions at the donor part, especially for CF_3 group. With the dramatically stabilized HOMO energy, the HOMO–LUMO energy gap of these dyes increases in the following order: D1 (2.22 eV) < D2 (2.28 eV) < D3 (2.34 eV) < D4 (2.66 eV). The energy gaps of our designed dyes D1–D3 are much smaller than the famous D149. As reported by previous work [37, 38], the sensitizers that have smaller energy gap values may show higher efficiency in the DSSCs. Thus, it can be inferred that our designed molecules may have improved light harvesting ability.

As drawn in Figure 3, the electron densities of the HOMO of D149 is mainly located on the donor part and indoline ring; the electron densities of its LUMO are mainly distributed around the π group. It suggests that the HOMO to LUMO transition is a good charge separated state. The electron distributions of the HOMOs and LUMOs for D1–D4 have the similar features. Both the HOMOs and LUMOs of D1–D4 possess π and π^* orbital delocalization. Therefore, it can be confirmed that the intramolecular charge transfer (ICT) may occur when electron excitation occurs from the HOMO to LUMO in these dyes.

3.2. The Absorption Spectra. On the basis of the optimized ground state geometries, the absorption spectra of dyes are calculated by TDDFT/B3LYP method with PCM in methanol media. The simulated electronic absorption spectra

are depicted in Figure 4, and the corresponding absorption data are collected in Table 1.

Figure 4 shows the absorption spectrum of D1–D3 displaying three major absorption bands in their UV/Vis spectra, the lowest energy absorption band (in the region of 600.0–800.0 nm), lower energy absorption band (in the region of 450.0 to 600.0 nm), and higher energy absorption band (in the region of 300.0 to 450.0 nm). Compared with D1–D3, the absorption spectra of D4 are different in the band locations and intensity, due to importing the electron-withdrawing CF_3 groups. From Figure 4 and Table 1, the lowest lying distinguishable absorption speak (S_1) of these dyes exhibits dramatically blue shift tendency: D1 (735.1 nm) > D2 (693.5 nm) > D3 (661.5 nm) > D4 (600.2 nm) > D149 (556.1 nm), which is closely related to the increased HOMO–LUMO energy gaps of these compounds (see Figure 3). Based on the analysis of electron density of HOMO and LUMO (see Section 3.2), all of the absorption behaviors of the S_1 can be ascribed to the intramolecular charge transfer (ICT) character. The maximum absorption speak of D1 and D2 is located at 517.5 and 518.7 nm, respectively, which is contributed by HOMO-1 \rightarrow LUMO transition. The HOMO-1 of D1 and D2 is contributed by 23.1% (D) + 76.8% (π) and 53.4% (D) + 42.6% (π), respectively. Thus it is reasonable to assign the 517.5 and 518.7 nm for D1 and D2 to ICT character. For D3, the absorption speak with the largest oscillator strength is located at 515.7 nm, which is contributed by HOMO-2 \rightarrow LUMO transition. The HOMO-2 of D3 is focused on 99.9% (D); therefore, the 515.7 nm of D3 still displays ICT character. With respect to D4, the absorption at 491.5 (attributed by HOMO-1 \rightarrow LUMO) and 371.3 nm (attributed by HOMO \rightarrow LUMO+4) are assigned to ICT character. The high-energy absorption speak for D1–D4 is located at 398.5, 362.2, 365.6, and 346.6 nm, respectively, which is ascribed to 19.9% (D) + 79.4% (π) \rightarrow 98.2% (π), 85.1% (D) + 14.5% (π) \rightarrow 20.8% (D) + 57.9% (π) + 21.3% (A), 86.9% (D) + 13.1% (π) \rightarrow 77.1% (D) + 21.2% (π), and 58.7% (D) + 41.1% (π) \rightarrow 83.2% (D) + 16.4% (π) transitions with the ICT character.

From the above calculations, it can be seen that all the absorption speaks of D1–D4 are covering the entire visible

TABLE 1: The calculated absorption wavelength λ (nm), excitation energy (eV), oscillator strength ($f > 0.2$), major configuration, and transition nature for D149 and **D1–D4** (H, L, D, π , and A denote the HOMO, LUMO, triphenylamine moiety, indoline and rhodanine group, and CH_2COOH , resp.).

		λ (nm)	E (eV)	f	Major configuration	Character
D149	S1	556.1	2.23	1.3220	99% H \rightarrow L	30.12% (D) + 69.8% (π) \rightarrow 95.5% (π)
	S2	425.8	2.91	0.6637	70% H-1 \rightarrow L	40.1% (D) + 59.4% (π) \rightarrow 95.5% (π)
	S3	410.5	3.02	0.2097	67% H \rightarrow L + 1	30.1% (D) + 69.8% (π) \rightarrow 51.8% (D) + 47.7% (π)
D1	S1	735.1	1.69	0.3047	100% H \rightarrow L	87.2% (D) \rightarrow 98.2% (π)
	S2	517.5	2.40	0.9613	99% H-1 \rightarrow L	23.1% (D) + 76.8% (π) \rightarrow 98.2% (π)
	S5	398.5	3.11	0.4368	69% H-3 \rightarrow L	19.9% (D) + 79.4% (π) \rightarrow 98.2% (π)
	S13	327.7	3.78	0.2404	78% H \rightarrow L + 6	87.2% (D) \rightarrow 57.8% (π) + 39.1% (A)
D2	S1	693.5	1.79	0.3812	99% H \rightarrow L	85.1% (D) + 14.5% (π) \rightarrow 90.9% (π)
	S2	518.7	2.39	0.8282	91% H-1 \rightarrow L	53.4% (D) + 42.6% (π) \rightarrow 90.9% (π)
	S4	469.6	2.64	0.2039	97% H \rightarrow L + 1	85.1% (D) + 14.5% (π) \rightarrow 92.8% (π)
	S5	402.7	3.08	0.3328	85% H-3 \rightarrow L	24.9% (D) + 65.6% (π) \rightarrow 90.9% (π)
	S10	362.4	3.42	0.3017	61% H \rightarrow L + 4	85.1% (D) + 14.5% (π) \rightarrow 20.8% (D) 57.9% (π) + 21.3% (A)
D3	S1	661.5	1.87	0.3729	99% H \rightarrow L	86.9% (D) + 13.1% (π) \rightarrow 97.2% (π)
	S2	515.7	2.40	0.9305	98% H-2 \rightarrow L	99.9% (D) \rightarrow 97.2% (π)
	S10	365.6	3.39	0.5877	92% H \rightarrow L + 4	86.9% (D) + 13.1% (π) \rightarrow 77.1% (D) + 21.2% (π)
	S11	363.8	3.41	0.2335	57% H-4 \rightarrow L	44.0% (D) + 55.3% \rightarrow 97.2% (π)
	S12	353.9	3.50	0.2481	47% H \rightarrow L + 2	86.9% (D) + 13.1% (π) \rightarrow 96.2% (D)
D4	S1	600.2	2.07	0.6676	99% H \rightarrow L	58.7% (D) + 41.1% (π) \rightarrow 96.4% (π)
	S2	491.5	2.52	0.7025	98% H-1 \rightarrow L	46.0% (D) + 53.6% (π) \rightarrow 96.4% (π)
	S4	427.9	2.90	0.3875	91% H \rightarrow L + 1	58.7% (D) + 41.1% (π) \rightarrow 89.2% (π)
	S7	371.3	3.34	0.7061	90% H \rightarrow L + 4	58.7% (D) + 41.1% (π) \rightarrow 99.6% (D)
	S12	357.1	3.47	0.2167	53% H-4 \rightarrow L	99.9% (π) \rightarrow 96.4% (π)
	S13	346.6	3.58	0.2581	64% H \rightarrow L + 6	58.7% (D) + 41.1% (π) \rightarrow 83.2% (D) + 16.4% (π)

region, which makes these dyes suitable for the application of DSSCs. The location and intensity of the absorption band of these dyes are greatly affected by introducing the $\text{N}(\text{CH}_3)_2$, $\text{N}(\text{phenyl})_2$, and CF_3 groups, which means the photophysical properties can be well tuned by proper substitutions. All the intense absorption bands of **D1–D4** correspond to the ICT transition, which will play an important role in conversion efficiencies.

3.3. Photoelectric Conversion Efficiency of Dyes. Rapid electron injection from the photoinduced excited states of dyes to the TiO_2 is desired for high performance of DSSCs. According to Preat's method [33], the driving force ΔG_{inject} of electrons injections from the excited states of dyes to semiconductor surface is calculated and the results are drawn in Figure 5.

Figure 5 shows that all the ΔG_{inject} values are very negative (in the region of -1.55 – -1.86 eV), which suggests that the dye excited state lies above the TiO_2 conduction band edge. Therefore, it is favorable for electron injection from the excited state dye to the TiO_2 conduction band edge. Compared with D149 (-1.08 eV), **D1–D4** have much more negative ΔG_{inject} values. As expected, the electron injection ability has been improved by replacing the donor part of D149 by triphenylamine. Furthermore, the ΔG_{inject} values of **D2** and **D3** are -1.74 eV and 1.66 eV, respectively, which are much more positive than **D1** (-1.86 eV), indicating that the introduction

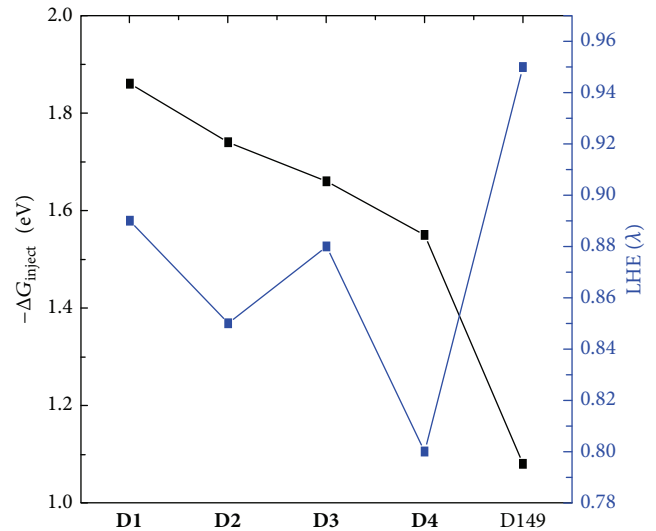


FIGURE 5: The calculated $-\Delta G_{\text{inject}}$ (in eV) and $\text{LHE}(\lambda)$ of studied complexes.

of diphenylamine at the end of triphenylamine unit results in destabilization of the oxidized dye and therefore reduces the electron injection. In addition, ΔG_{inject} value of **D4** (-1.55 eV) is positive than that of **D3**, indicating it would not

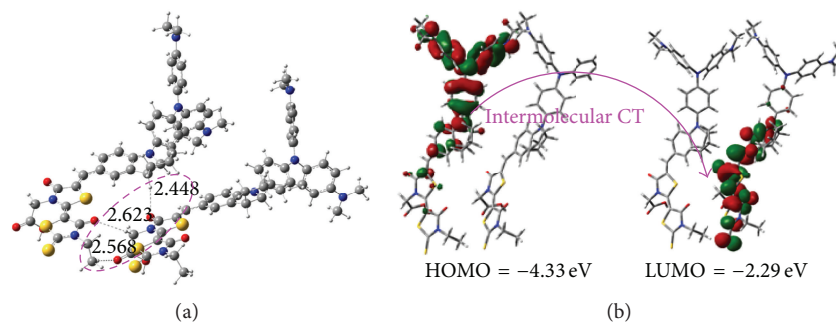


FIGURE 6: (a) The optimized ground geometry of D1 dimer and (b) its HOMO and LUMO orbital. The $\text{H}\cdots\text{O}$ bond length (\AA) is labeled in the optimized geometry.

be favorable to enhance the electron injection by importing the CF_3 group at the end of phenylamine. According to (3) in Section 2, the $\text{LHE}(\lambda)$ of studied complexes are calculated and the results are also drawn in Figure 5. As depicted in Figure 5, the **D1** has larger $\text{LHE}(\lambda)$ than **D2–D4**, which means that **D1** has more efficient light harvesting capability than others. As discussed in Section 2, the large values of ΔG_{inject} and $\text{LHE}(\lambda)$ are possible approaches to maximize the short-circuit (J_{sc}). Consequently, it is a promising approach to enhance the efficiency by introducing the $\text{N}(\text{CH}_3)_2$ group at the donor part.

3.4. Structures and Properties of Dye Dimers. The intermolecular interactions of these dyes dimer are investigated by B3LYP method to predict the stabilization upon dye aggregation. Figure 6 illustrates the optimized geometries of **D1 dimer**. Further survey of the HOMO and LUMO orbitals of **D1 dimer** is also collected in Figure 6. The properties of **D2–D3** dimers are given in Figure S1 in the supporting information (see Supplementary Material available online at <http://dx.doi.org/10.1155/2015/605728>).

As shown in Figure 6 and Figure S1, all these stable molecules have formed intermolecular $\text{H}\cdots\text{O}$ hydrogen bonds. Take **D1 dimer** as an example, the carboxyl and terminal carbonyl group of thiazolidine form three $\text{H}\cdots\text{O}$ hydrogen bonds. One $\text{H}\cdots\text{O}$ hydrogen bond is 2.568 \AA , which is formed by the carboxyl and one terminal H atoms in the ethyl. Another two $\text{H}\cdots\text{O}$ hydrogen bonds are 2.623 and 2.448 \AA , which are formed by the two O atoms in the carbonyl group of thiazolidines interact with the two H atoms. In addition, the HOMOs of dimers are mainly located on one monomer, while their LUMO are contributed by another monomeric unit. Clearly, the intermolecular charge transfer process between the dyes dimers may occur for all the dyes. Compared with the isolated dye monomer (see Figure 3), the HOMO energy of **D1 dimer** slightly increases by 0.06 eV, while the LUMO energy decreases by 0.12 eV, respectively. Because of the dramatically decreased LUMO energy, the HOMO-LUMO energy gap of **D1 dimer** becomes narrowed 0.18 eV compared with monomer. Similarly, the HOMO-LUMO energy gap of **D2 dimer** and **D3 dimer** decreases by 0.14 eV and 0.18 eV, respectively, compared with corresponding monomer. Normally, the narrowed HOMO-LUMO energy gap favors red shifted of absorption spectra.

As reported by Pastore and De Angelis [13], the red-shift of absorption spectra for indoline dye are due to the dye aggregation. Therefore dye aggregation is expected to be associated with the HOMO-LUMO energy gap of dye dimer. Since there are small differences of HOMO-LUMO energy gap of these dimers compared with corresponding monomer, introducing the $\text{N}(\text{phenyl})_2$ substitutions at the donor may play a slight effect on avoiding unfavorable dye aggregation.

3.5. Dye-(TiO_2)₆ Complexes. For a better understanding of the effect of the triphenylamine-based donor on the electron coupling, these dyes bound to (TiO_2)₆ cluster are optimized by B3LYP method. As well accepted, there are two common absorption models for dyes absorbed on the surface [39, 40]. One is a single Ti-O monodentate binding mode; another is a bidentate chelating structure mode. In this work, we take **D4** as an example to testify which mode is stable absorption configuration. The optimized geometries of **D4-(TiO₂)₆** in different models are drawn in Figure S2. It can be seen that the total energy of bidentate-chelating configuration is lower 3.75 kcal/mol than single monodentate mode. This agrees with the previous work; that is, the bidentate chelating structure mode is usually predicted to be stable [13, 41–43]. Therefore, the **D149** and **D1–D3** absorbed on the surface are optimized under the bidentate chelating structure mode. The optimized geometry, absorption energies (E_{ads}), and the contour plot of the HOMO and LUMO of dye-(TiO_2)₆ complexes are depicted in Figure 7. The energy level of frontier molecule orbital (eV) of the dye-(TiO_2)₆ and the energies differences between the dye and dye-(TiO_2)₆ are drawn in Figure 8.

As shown in Figure 7, the decreased order of E_{abs} for **D149** and **D1–D4** is **D149** (23.68 kcal/mol) > **D1** (20.81 kcal/mol) > **D2** (15.66 kcal/mol) > **D3** (10.32 kcal/mol) > **D4** (2.85 kcal/mol), indicating the interactions between the dye and TiO_2 surface is decreasing in the same order. In particular, for **D4**, the E_{abs} is so small that **D4** is difficult to be chemisorbed on the cluster. After absorption to the (TiO_2)₆ cluster, the calculated distances of **D1** between the carboxylic oxygen atoms and the (TiO_2)₆ cluster (Ti–O bond lengths) are about 2.032 \AA and 2.115 \AA . By introducing the $\text{N}(\text{phenyl})_2$ and CF_3 groups, the two Ti–O bond lengths increase to 2.032 \AA and 2.116 \AA for **D2**, 2.032 \AA and 2.117 \AA for **D3**, and 2.032 \AA and 2.119 \AA for **D4**. It suggests that the $\text{N}(\text{phenyl})_2$ and CF_3 groups

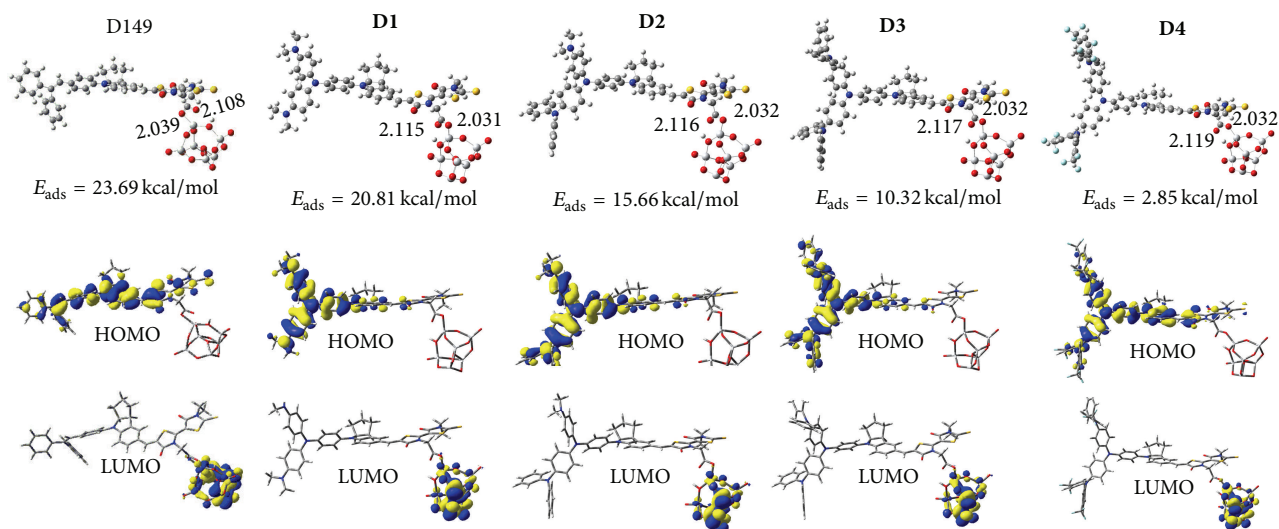


FIGURE 7: Optimized geometries, absorption energies (kcal/mol), and contour plot of HOMO and LUMO of studied molecule adsorbed on the $(\text{TiO}_2)_6$ cluster.

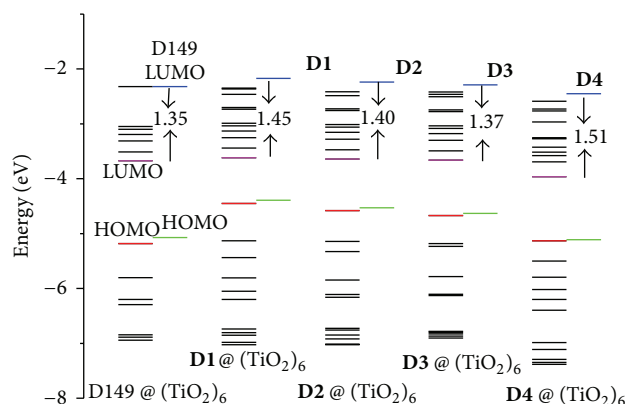


FIGURE 8: The energy diagram of frontier molecule orbital (eV) of the dye- $(\text{TiO}_2)_6$, as well as the HOMO and LUMO energy of dyes.

have decreased the electron coupling between the dyes and surface, which is consistent with the analyses of E_{ads} .

Molecular orbital spatial distribution shows that the HOMO of dye- $(\text{TiO}_2)_6$ is mainly localized over the donor part of dyes, while the LUMO is focused on the $(\text{TiO}_2)_6$ part. As expected, the interfacial electron injection from the dye to the TiO_2 surface may successively transfer when the dyes bind on the TiO_2 film. Furthermore, compared with the isolated sensitizer, the HOMOs have subtle changes (about 0.1 eV) when the D149 and D1–D4 absorb to $(\text{TiO}_2)_6$ cluster. The most noticeable difference between the isolated dyes and dye- $(\text{TiO}_2)_6$ is focused on the LUMO energy. The LUMO energy of (D1–D4)- $(\text{TiO}_2)_6$ dramatically decreases compared with D149- $(\text{TiO}_2)_6$, suggesting that the LUMOs of all designed dyes create relative strong electronic coupling with TiO_2 film and, as a result, further boost the electron injection. In addition, the LUMO of D1- $(\text{TiO}_2)_6$ is lower 1.45 eV than that of D1. While the lower-lying energy LUMO

of D149- $(\text{TiO}_2)_6$ (1.35 eV), D2- $(\text{TiO}_2)_6$ (1.40 eV), and D3- $(\text{TiO}_2)_6$ (1.37 eV) becomes smaller than that of D1, indicating that the electronic coupling to the TiO_2 surface decreases by importing the N(phenyl)₂.

4. Conclusions

The electronic structures, absorption spectra, and photo-physical properties of triphenylamine-based indoline dyes as photosensitizers for application in DSSCs were investigated by density functional theory (DFT) and time-dependent DFT (TD-DFT). The calculated results demonstrated that the donor parts had great effect on the structure and optical properties. Compared with D149, D1–D3 had proper HOMO and LUMO energy level as well as narrow HOMO-LUMO energy gap by introducing the N(CH₃)₂ and N(phenyl)₂ groups at the donor part; therefore D1–D3 may be good DSSC sensitizers. The absorption speaks of D1–D4 covered the entire visible region and the intense absorption bands of them all corresponded to the intramolecular charge transfer transition, which may play an important role in conversion efficiencies. The stable molecule of D1–D3 dimmers were formed by intermolecular H···O hydrogen bonds. The data of E_{abs} and the LUMO energy level of dye- $(\text{TiO}_2)_6$ suggested that D1 had the strongest interactions between the dye and TiO_2 surface of these dyes. Furthermore, D1 had larger ΔG_{inject} and LHE(λ) values than D2–D4, indicating that D1 may have improved energy conversion efficiency by introducing the N(CH₃)₂ group at the donor part of triphenylamine. We hope that this work will be helpful for designing the organic dyes with high efficiency.

Conflict of Interests

The authors declare that there is no conflict of interests regarding the publication of this paper.

Acknowledgments

Financial supports were received from NSFC (no. 21243006 and 51304193), the Basic Research Program of Jiangsu Province (no. BK20130172), and the Fundamental Research Funds for the Central Universities (nos. 2013QNA14 and 2010QNA10). A Project funded by the Priority Academic Program Development of Jiangsu Higher Education Institutions is acknowledged. The authors are grateful to the High Performance Computing Center of China University of Mining and Technology for the award of CPU hours to accomplish this work.

References

- [1] B. O'Reagen and M. Grätzel, "A low-cost, high-efficiency solar cell based on dye-sensitized colloidal TiO₂ films," *Nature*, vol. 353, pp. 737–740, 1991.
- [2] M. Grätzel, "Solar energy conversion by dye-sensitized photo-voltaic cells," *Inorganic Chemistry*, vol. 44, no. 20, pp. 6841–6851, 2005.
- [3] M. K. Nazeeruddin, A. Kay, I. Rodicio et al., "Conversion of light to electricity by cis-X2bis(2,2'-bipyridyl-4,4'-dicarboxylate)ruthenium(II) charge-transfer sensitizers (X = Cl-, Br-, I-, CN-, and SCN-) on nanocrystalline titanium dioxide electrodes," *Journal of the American Chemical Society*, vol. 115, no. 14, pp. 6382–6390, 1993.
- [4] M. K. Nazeeruddin, P. Péchy, T. Renouard et al., "Engineering of efficient panchromatic sensitizers for nanocrystalline TiO₂-based solar cells," *Journal of the American Chemical Society*, vol. 123, no. 8, pp. 1613–1624, 2001.
- [5] S. Chang, H. Wang, L. T. Lin Lee et al., "Panchromatic light harvesting by N719 with a porphyrin molecule for high-performance dye-sensitized solar cells," *Journal of Materials Chemistry C*, vol. 2, no. 18, pp. 3521–3526, 2014.
- [6] R. K. Kanaparthi, J. Kandhadi, and L. Giribabu, "Metal-free organic dyes for dye-sensitized solar cells: Recent advances," *Tetrahedron*, vol. 68, no. 40, pp. 8383–8393, 2012.
- [7] Y. Wu and W. Zhu, "Organic sensitizers from D- π -A to D-A- π -A: effect of the internal electron-withdrawing units on molecular absorption, energy levels and photovoltaic performances," *Chemical Society Reviews*, vol. 42, pp. 2039–2058, 2013.
- [8] B.-G. Kim, K. Chung, and J. Kim, "Molecular design principle of all-organic dyes for dye-sensitized solar cells," *Chemistry: A European Journal*, vol. 19, no. 17, pp. 5220–5230, 2013.
- [9] G. B. Consiglio, F. Pedna, C. Fornaciari et al., "Assessment of new gem-silane-diols as suitable sensitizers for dye-sensitized solar cells," *Journal of Organometallic Chemistry*, vol. 723, pp. 198–206, 2013.
- [10] W. H. Howie, F. Claeysens, H. Miura, and L. M. Peter, "Characterization of solid-state dye-sensitized solar cells utilizing high absorption coefficient metal-free organic dyes," *Journal of the American Chemical Society*, vol. 130, no. 4, pp. 1367–1375, 2008.
- [11] S. Ito, H. Miura, S. Uchida et al., "High-conversion-efficiency organic dye-sensitized solar cells with a novel indoline dye," *Chemical Communications*, no. 41, pp. 5194–5196, 2008.
- [12] M. K. Nazeeruddin, F. De Angelis, S. Fantacci et al., "Combined experimental and DFT-TDDFT computational study of photoelectrochemical cell ruthenium sensitizers," *Journal of the American Chemical Society*, vol. 127, no. 48, pp. 16835–16847, 2005.
- [13] M. Pastore and F. De Angelis, "Aggregation of organic dyes on TiO₂ in dye-sensitized solar cells models: an Ab initio investigation," *ACS Nano*, vol. 4, no. 1, pp. 556–562, 2010.
- [14] H. Fukunishi, S. Nakamura, and S. Fujieda, "Influence of conformation on the absorption spectra of flexible organic dyes used in dye-sensitized solar cells," *Computational and Theoretical Chemistry*, vol. 1014, pp. 29–36, 2013.
- [15] Q. Q. Li, L. L. Lu, C. Zhong et al., "New indole-based metal-free organic dyes for dye-sensitized solar cells," *The Journal of Physical Chemistry B*, vol. 113, no. 44, pp. 14588–14595, 2009.
- [16] P. Liu, J.-J. Fu, M.-S. Guo, X. Zuo, and Y. Liao, "Effect of the chemical modifications of thiophene-based N3 dyes on the performance of dye-sensitized solar cells: a density functional theory study," *Computational and Theoretical Chemistry*, vol. 1015, pp. 8–14, 2013.
- [17] S. Meng, E. Kaxiras, M. K. Nazeeruddin, and M. Grätzel, "Design of dye acceptors for photovoltaics from first-principles calculations," *Journal of Physical Chemistry C*, vol. 115, no. 18, pp. 9276–9282, 2011.
- [18] W.-L. Ding, D.-M. Wang, Z.-Y. Geng, X.-L. Zhao, and Y.-F. Yan, "Molecular engineering of indoline-based D-A- π -A organic sensitizers toward high efficiency performance from first-principles calculations," *Journal of Physical Chemistry C*, vol. 117, no. 34, pp. 17382–17398, 2013.
- [19] M. Liang and J. Chen, "Arylamine organic dyes for dye-sensitized solar cells," *Chemical Society Reviews*, vol. 42, no. 8, p. 3453, 2013.
- [20] W. Xu, B. Peng, J. Chen, M. Liang, and F. Cai, "New triphenylamine-based dyes for dye-sensitized solar cells," *Journal of Physical Chemistry C*, vol. 112, no. 3, pp. 874–880, 2008.
- [21] M. Liang, W. Xu, F. Cai et al., "New triphenylamine-based organic dyes for efficient dye-sensitized solar cells," *Journal of Physical Chemistry C*, vol. 111, no. 11, pp. 4465–4472, 2007.
- [22] H.-Q. Xia, J. Wang, F.-Q. Bai, and H.-X. Zhang, "Theoretical studies of electronic and optical properties of the triphenylamine-based organic dyes with diketopyrrolopyrrole chromophore," *Dyes and Pigments*, vol. 113, pp. 87–95, 2015.
- [23] M. J. Frisch, G. W. Trucks, H. B. Schlegel et al., *Gaussian 09, Revision B.04*, Gaussian, Wallingford, Conn, USA, 2009.
- [24] H. W. Ham and Y. S. Kim, "Theoretical study of indoline dyes for dye-sensitized solar cells," *Thin Solid Films*, vol. 518, no. 22, pp. 6558–6563, 2010.
- [25] C. Lee, W. Yang, and R. G. Parr, "Development of the Colle-Salvetti correlation-energy formula into a functional of the electron density," *Physical Review B*, vol. 37, no. 2, pp. 785–789, 1988.
- [26] A. D. Becke, "Density-functional thermochemistry. III. The role of exact exchange," *The Journal of Chemical Physics*, vol. 98, no. 7, p. 5648, 1993.
- [27] M. Cossi, G. Scalmani, N. Rega, and V. Barone, "New developments in the polarizable continuum model for quantum mechanical and classical calculations on molecules in solution," *Journal of Chemical Physics*, vol. 117, no. 1, pp. 43–54, 2002.
- [28] V. Barone, M. Cossi, and J. Tomasi, "A new definition of cavities for the computation of solvation free energies by the polarizable continuum model," *Journal of Chemical Physics*, vol. 107, no. 8, pp. 3210–3221, 1997.
- [29] R. Sánchez-De-Armas, J. Oviedo López, M. A. San-Miguel, J. F. Sanz, P. Ordejón, and M. Pruneda, "Real-time TD-DFT simulations in dye sensitized solar cells: the electronic absorption spectrum of alizarin supported on TiO₂ nanoclusters," *Journal*

- of Chemical Theory and Computation*, vol. 6, no. 9, pp. 2856–2865, 2010.
- [30] M. R. Narayan, “Review: dye sensitized solar cells based on natural photosensitizers,” *Renewable and Sustainable Energy Reviews*, vol. 16, no. 1, pp. 208–215, 2012.
- [31] J.-Z. Zhang, H.-B. Li, Y. Wu et al., “Modulation on charge recombination and light harvesting toward high-performance benzothiadiazole-based sensitizers in dye-sensitized solar cells: a theoretical investigation,” *Journal of Power Sources*, vol. 267, pp. 300–308, 2014.
- [32] J. Zhang, H.-B. Li, S.-L. Sun, Y. Geng, Y. Wu, and Z.-M. Su, “Density functional theory characterization and design of high-performance diarylamine-fluorene dyes with different π spacers for dye-sensitized solar cells,” *Journal of Materials Chemistry*, vol. 22, no. 2, pp. 568–576, 2012.
- [33] J. Preat, C. Michaux, D. Jacquemin, and E. A. Perpète, “Enhanced efficiency of organic dye-sensitized solar cells: triphenylamine derivatives,” *Journal of Physical Chemistry C*, vol. 113, no. 38, pp. 16821–16833, 2009.
- [34] M. Grätzel, “Photoelectrochemical cells,” *Nature*, vol. 414, no. 6861, pp. 338–344, 2001.
- [35] D. Cahen, G. Hodes, M. Grätzel, J. F. Guillemoles, and I. Riess, “Nature of photovoltaic action in dye-sensitized solar cells,” *Journal of Physical Chemistry B*, vol. 104, no. 9, pp. 2053–2059, 2000.
- [36] S. Meng and E. Kaxiras, “Electron and hole dynamics in dye-sensitized solar cells: influencing factors and systematic trends,” *Nano Letters*, vol. 10, no. 4, pp. 1238–1247, 2010.
- [37] W. M. Campbell, K. W. Jolley, P. Wagner et al., “Highly efficient porphyrin sensitizers for dye-sensitized solar cells,” *Journal of Physical Chemistry C*, vol. 111, no. 32, pp. 11760–11762, 2007.
- [38] R. Ma, P. Guo, H. Cui, X. Zhang, M. K. Nazeeruddin, and M. Grätzel, “Substituent effect on the meso-substituted porphyrins: theoretical screening of sensitizer candidates for dye-sensitized solar cells,” *The Journal of Physical Chemistry A*, vol. 113, no. 37, pp. 10119–10124, 2009.
- [39] M. Nara, H. Torii, and M. Tasumi, “Correlation between the vibrational frequencies of the carboxylate group and the types of its coordination to a metal ion: an ab initio molecular orbital study,” *Journal of Physical Chemistry*, vol. 100, no. 51, pp. 19812–19817, 1996.
- [40] G. B. Deacon and R. J. Phillips, “Relationships between the carbon-oxygen stretching frequencies of carboxylate complexes and the type of carboxylate coordination,” *Coordination Chemistry Reviews*, vol. 33, no. 3, pp. 227–250, 1980.
- [41] P. Chen, J. H. Yum, F. de Angelis et al., “High open-circuit voltage solid-state dye-sensitized solar cells with organic dye,” *Nano Letters*, vol. 9, no. 6, pp. 2487–2492, 2009.
- [42] H. Tian, X. Yang, R. Chen, R. Zhang, A. Hagfeldt, and L. Sun, “Effect of different dye baths and dye-structures on the performance of dye-sensitized solar cells based on triphenylamine dyes,” *Journal of Physical Chemistry C*, vol. 112, no. 29, pp. 11023–11033, 2008.
- [43] M. Pastore and F. D. Angelis, “Computational modeling of stark effects in organic dye-sensitized TiO₂ heterointerfaces,” *The Journal of Physical Chemistry Letters*, vol. 2, no. 11, pp. 1261–1267, 2011.

Research Article

Power-Interrogated Refractive Index Sensor Using Long Period Grating in Photonic Crystal Fiber

X. L. Jiang,^{1,2} Z. T. Gu,¹ and L. Zheng²

¹College of Science, University of Shanghai for Science and Technology, Shanghai 200093, China

²Department of Math and Physics, Shanghai Institute of Electric Power, Shanghai 200090, China

Correspondence should be addressed to X. L. Jiang; jiangxiuli@shiep.edu.cn and Z. T. Gu; zhengtiangu@163.com

Received 2 February 2015; Accepted 11 March 2015

Academic Editor: Ruomeng Yu

Copyright © 2015 X. L. Jiang et al. This is an open access article distributed under the Creative Commons Attribution License, which permits unrestricted use, distribution, and reproduction in any medium, provided the original work is properly cited.

We reported a long period grating (LPG) written in specially designed photonic crystal fiber (PCF) for refractive index (RI) sensing by interrogating the transmitted light power. The outermost ring of clad holes of the PCF is enlarged where the analyte is filled. We showed that the leakage loss of the clad mode increases with the RI in the larger holes. By numerically analyzing the complex couple mode equations for the core mode and the first clad mode, we found the depth of attenuation band in the transmitted spectra and the total transmitted power is sensitive to the leakage loss of the clad mode or the RI in the larger holes. We also demonstrated that the transmitted power is sensitive to the RI even less than that of the silica, which just avoids the limitation that the transmitted light power of LPG in conventional fiber is only sensitive to the RI of the external media higher than that of fiber clad.

1. Introduction

The introduction of periodic structure in optical fiber has been used in many optical fields. Long period fiber grating (LPFG) can couple the core mode to the cladding modes which are sensitive to the refractive index (RI) of the surrounding medium. A number of studies on the RI sensitivity of LPFGs have been conducted [1–4]. A study on RI sensing using LPFGs by Patrick et al. has demonstrated that a change in RI lower than the index of fiber clad causes wavelength shift, while a change in RI higher than the index of the fiber clad causes changes in shape and magnitude of attenuation bands [5]. Many experiments demonstrated that a long period grating in a photonic crystal fiber (PCF-LPG) can be used for RI sensing, in which a much smaller sample volume is possible by using the holes in the cladding as microfluidic channels [6–8]. The previous RI sensors using PCF-LPGs monitored the changes in RI by the shift of the resonant wavelength of the PCF-LPGs. However, one intrinsic problem of such sensors is their cross sensitivity to other parameters especially to the temperature; another practical disadvantage is complex wavelength-dispersive demodulator which is necessary.

This letter reports an LPG written in specially designed photonic crystal fiber, and its magnitude of the attenuation bands varies with the RI even lower than the fiber clad and so does the total transmitted light power. With this sensing mechanism, only an optical power meter is required for signal interrogation. The transverse geometry of the PCF and the computation model are depicted in Figure 1. The cross section of the fiber includes the following parts: the Ge-doped core, the clad consisting of five rings of air holes, the fifth ring of enlarged holes through which the analyte is transmitted, and the outermost silica region truncated by the perfectly matched layer (PML) [9].

The clad modes of PCF are leaky as some light can leak out of the cladding with finite rings of inclusions through the channels between every two of the inclusions. The leakage can be easily manipulated by changing the air hole structure or the RI of the medium in the holes [10, 11]. Here we numerically demonstrate that the leakage loss of the clad mode increases with the RI of the medium in the larger holes, which leads to the reduction of the coupling strength between the core mode and the clad mode and the changes in the magnitude of the attenuation band. The analyte is filled in the holes of the outermost layer, leaving others unfilled. There are

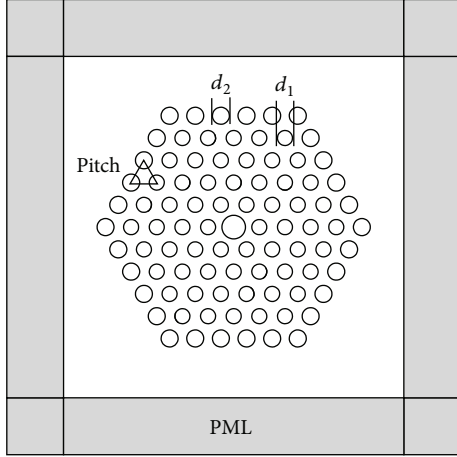


FIGURE 1: The transverse cross section of the PCF truncated by PML.

a number of techniques for achieving selective filling, including collapsing air holes and direct manual gluing [12].

2. Theory

The transmission characteristics of an LPG-PCF can be investigated by the complex coupled mode theory [13–15]. To illustrate the leakage loss of the m th clad mode in the PCF, an imaginary term should be introduced into the mode propagation constant $\beta_{cl,m} = \beta' + i\alpha$, so the complex couple mode equation for the core mode and the m th clad mode can be expressed as

$$\begin{aligned} \frac{dA_{co}}{dz} &= iKA_{cl,m} \exp(-\alpha z) \times \exp\left[-i\left(\beta_{co} - \beta' - \frac{2\pi}{\Lambda}\right)z\right], \\ \frac{dA_{cl,m}}{dz} &= iKA_{co} \exp(\alpha z) \times \exp\left[-i\left(\beta_{co} - \beta' - \frac{2\pi}{\Lambda}\right)z\right]. \end{aligned} \quad (1)$$

A_{co} and $A_{cl,m}$ are the amplitudes of the core mode and the m th clad mode, respectively. β_{co} is the propagation constant of the core mode, Λ is the grating period, K is the coupling coefficient which is proportional to the average refractive index modulation and overlap integral between the two coupled modes.

When the phase matching condition $\beta_{co} - \beta' - 2\pi/\Lambda = 0$ is satisfied, the couple mode equation can be rewritten as

$$\begin{aligned} \frac{dA_{co}}{dz} &= iKA_{cl,m} \exp(-\alpha z), \\ \frac{dA_{cl,m}}{dz} &= iKA_{co} \exp(\alpha z). \end{aligned} \quad (2)$$

Equation about A_{co} can be deduced from (2):

$$\frac{d^2 A_{co}}{dz^2} + \alpha \frac{dA_{co}}{dz} + K^2 A_{co} = 0. \quad (3)$$

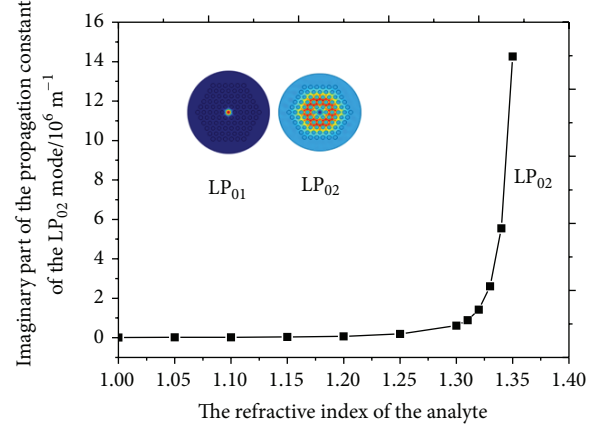


FIGURE 2: Effect of RI of the analyte on the imaginary part of propagation constant of the clad mode LP_{02} .

The amplitude of the core mode is just like a damped oscillator. The transmission at the resonant wavelength of the LPG with length of L can be got from (3):

$$\begin{aligned} I &= \frac{A_{co}^2(L)}{A_{co}^2(0)} = e^{-\alpha L} \cos^2\left(\sqrt{K^2 - \left(\frac{\alpha}{2}\right)^2} L - \varphi\right), \\ \varphi &= \tan^{-1}\left(\frac{\alpha/2}{\sqrt{K^2 - (\alpha/2)^2}}\right). \end{aligned} \quad (4)$$

3. Numerical Results

An efficient coupling between fundamental core modes LP_{01} and LP_{0m} group of clad modes that have similar electric field profiles and large overlap integrals will take place by periodic perturbation along the fiber. The mode properties of the core mode LP_{01} and the lowest-order clad mode LP_{02} and the coupling between the two modes have been theoretically investigated. The electric fields of the two modes are depicted in the inset of Figure 2. In the simulation, the refractive index of silica is obtained from Sellmeier formula, the refractive index of the Ge-doped core is 0.012 higher than that of the silica, and the diameter of the doped core is $4.14 \mu\text{m}$. The diameter of the inner four layers of air holes is $d_1 = 2.65 \mu\text{m}$, the diameter of the fifth layer holes is $d_2 = 3 \mu\text{m}$, and the hole pitch is $4.52 \mu\text{m}$.

The finite element method (FEM) incorporating anisotropic perfectly matched layers (PML) as absorbing boundary conditions allows us to evaluate the effective index of the leaky mode in PCFs including the real and imaginary part. The imaginary part of the propagation constant of the core mode equals zero due to the fact that the doped core has higher RI. The imaginary part of the propagation constant of clad mode LP_{02} versus the RI of the analyte in the larger holes is plotted and shown in Figure 2. With the outermost air holes enlarged, the imaginary part of the propagation constant of mode LP_{02} is negligible which is decreased by ~ 3 orders of magnitude compared to without enlarging the holes. The clad

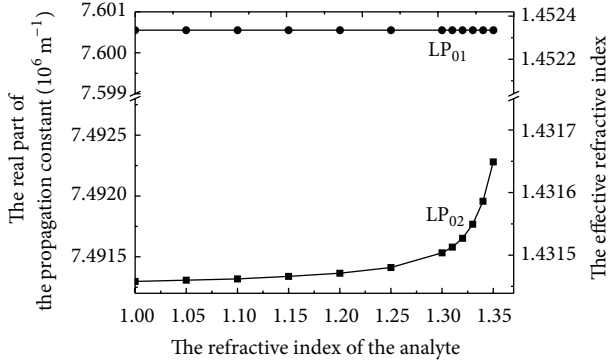


FIGURE 3: Effect of RI of the analyte on the real parts of propagation constant of the two modes: LP_{01} and LP_{02} .

mode is well confined by the enlarged air holes. As the RI of the analyte increases, the imaginary part (α) of the propagation constant of LP_{02} mode increases. The imaginary part of the propagation constant of LP_{02} increases drastically when the RI of the analyte exceeds 1.3 and increases to the same order of magnitude of K at the RI of 1.33. (The grating is designed to have the coupling coefficient K of $40/m^{-1}$ and coupling strength KL of $\pi/2$ for air in all the holes.) According to (3), the bigger the $\alpha/2$ is, the slower the A_{co} reaches zero. For certain grating length of L , obvious increase in the transmission at the resonant wavelength can be achieved due to the dramatic growth of the imaginary part of the clad mode when the RI of the analyte exceeds 1.3.

Figure 3 shows the effect of the refractive index of the analyte in the larger holes on the real parts of the two modes propagation constants. The wavelength is 1200 nm. It can be seen from Figure 3 that the core mode is not affected by the RI of the analyte, and the real part of the propagation constant of the LP_{02} mode increases as the RI of the analyte increases, which will cause the blue shift of the resonant wavelength.

The shift of the resonant wavelength caused by the changes of the RI in the larger holes has been calculated by the following steps. Firstly, the real parts of the effective refractive index of LP_{01} and LP_{02} at different wavelength for certain RI in the larger holes are calculated, and then a set of periodicities that meet the phase-matching condition $\lambda = (n_{LP_{01}} - n_{LP_{02}})\Lambda$ at given wavelengths are obtained. In Figure 4 we have plotted the calculated grating period versus the resonant wavelength for RI of 1, 1.33, and 1.34 in the larger holes. For the LPG with the period of $57.48 \mu\text{m}$, the resonant wavelength is 1200 nm, 1176 nm, and 1169 nm, respectively. The resonant wavelength shifts 7 nm from 1176 nm to 1169 nm when the RI in the larger holes changed from 1.33 to 1.34.

To study the response of the transmission spectra to the RI in the larger holes, we calculated the transmission spectra by integrating numerically the coupled-mode-equations (1) for the RI of 1, 1.33, and 1.34, respectively. The calculated spectra are plotted in Figure 5. The position of the resonant wavelength is consistent with the result of the previous method which manifests the resonant wavelength depending on the real part of the propagation constant of the two modes. The LPG is designed to completely couple the core mode to

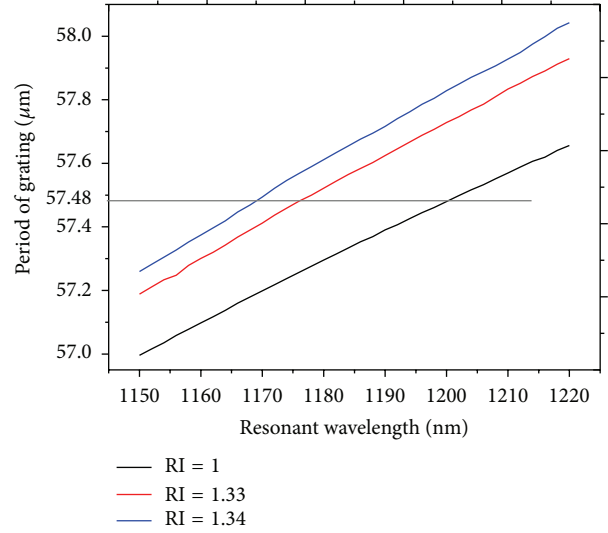


FIGURE 4: Relationship between grating periodicity and resonance wavelength.

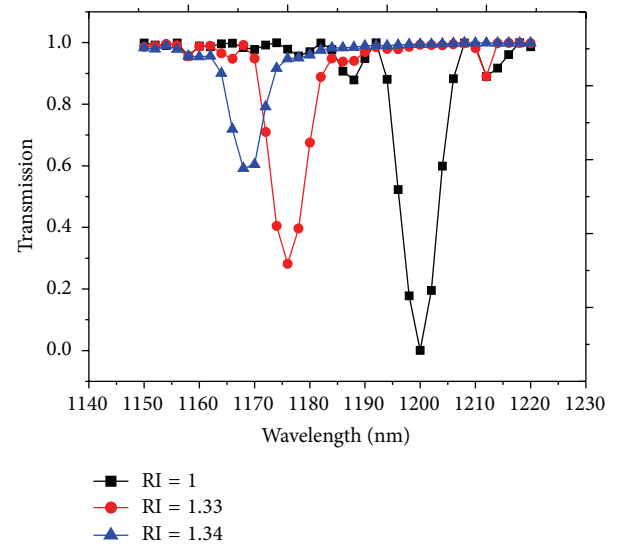


FIGURE 5: Transmission spectra for different RI in the enlarged holes.

the clad mode for the RI is 1 (air in the larger holes); hence the transmission at the resonant wavelength is equal to zero. When the RI in the larger holes increases from 1.33 to 1.34, the depth of the attenuation band decreases obviously; meanwhile the whole transmitted light power increases. Such variation is mainly caused by the increase in the imaginary part (α) of the propagation constant of LP_{02} .

Supposing a broadband LD light source with spectra range of 1160 nm–1184 nm and the spectral power of 0.1 mW/nm, the integrated transmitted power over the range of 1160 nm–1184 nm would be 1.83 mW and 2.06 mW for RI of 1.33 and 1.34, respectively, which indicates the possibility using LPG based on the proposed PCF as RI sensor by interrogating the transmitted light power. The less the attenuation band shifts, the narrower the incident spectral range can be chosen

and the greater the contrast the output light power has, that is, the more sensitive the sensor is. The shift of the resonant wavelength can be minimized by optimizing the air hole structure of the PCF.

4. Conclusion

In conclusion, we have demonstrated the feasibility of LPG-PCF RI sensor by interrogating the transmitted light power in this paper. The transmitted light power is sensitive to the RI less than that of the silica, which just avoided the limitation that the transmitted light of LPG in conventional fiber is only sensitive to the RI of the external media higher than that of fiber clad.

Conflict of Interests

The authors declare that there is no conflict of interests regarding the publication of this paper.

Acknowledgments

This work is jointly supported by National Science Foundation of China (Grant no. 60777035), National Science Foundation of China (Grant no. 11204172), Innovation Program of Shanghai Municipal Education (no. 13YZ104), Shanghai Leading Academic Discipline Project (no. S30502), and Innovation Project of Shanghai Municipal Education Committee (no. 11ZZ131).

References

- [1] Z. Gu, Y. Xu, and K. Gao, "Optical fiber long-period grating with solgel coating for gas sensor," *Optics Letters*, vol. 31, no. 16, pp. 2405–2407, 2006.
- [2] X. L. Jiang and Z. T. Gu, "Design of a gas sensor based on a sensitive film coated phase-shifted long-period fiber grating," *Journal of Optics*, vol. 12, no. 7, Article ID 075401, 2010.
- [3] S. W. James and R. P. Tatam, "Optical fibre long-period grating sensors: characteristics and application," *Measurement Science and Technology*, vol. 14, no. 5, pp. R49–R61, 2003.
- [4] L. Zheng, X. Chen, S. Tang, and R. Li, "Multiple quasi-phase-matching for enhanced generation of selected high harmonics in aperiodic modulated fibers," *Optics Express*, vol. 15, no. 26, pp. 17985–17990, 2007.
- [5] H. J. Patrick, A. D. Kersey, and F. Bucholtz, "Analysis of the response of long period fiber gratings to external index of refraction," *Journal of Lightwave Technology*, vol. 16, no. 9, pp. 1606–1612, 1998.
- [6] L. Rindorf, J. B. Jensen, M. Dufva, P. E. Høiby, L. H. Pedersen, and O. Bang, "Photonic crystal fiber long-period gratings for biochemical sensing," *Optics Express*, vol. 14, no. 18, pp. 8224–8231, 2006.
- [7] Z. He, Y. Zhu, and H. Du, "Long-period gratings inscribed in air- and water-filled photonic crystal fiber for refractometric sensing of aqueous solution," *Applied Physics Letters*, vol. 92, no. 4, Article ID 044105, 2008.
- [8] L. Rindorf and O. Bang, "Highly sensitive refractometer with a photonic-crystal-fiber long-period grating," *Optics Letters*, vol. 33, no. 6, pp. 563–565, 2008.
- [9] C.-H. Lai and H.-C. Chang, "Effect of perfectly matched layer reflection coefficient on modal analysis of leaky waveguide modes," *Optics Express*, vol. 19, no. 2, pp. 562–569, 2011.
- [10] T. P. White, R. C. McPhedran, C. M. De Sterke, L. C. Botten, and M. J. Steel, "Confinement losses in microstructured optical fibers," *Optics Letters*, vol. 26, no. 21, pp. 1660–1662, 2001.
- [11] Z. H. He, Y. A. Zhu, J. Kaňka, and H. Du, "Core-cladding mode coupling and recoupling in photonic crystal fiber for enhanced overlap of evanescent field using long-period gratings," *Optics Express*, vol. 18, no. 2, pp. 507–512, 2010.
- [12] B. T. Kuhlmeiy, B. J. Eggleton, and D. K. C. Wu, "Fluid-filled solid-core photonic bandgap fibers," *Journal of Lightwave Technology*, vol. 27, no. 11, pp. 1617–1630, 2009.
- [13] D. B. Stegall and T. Erdogan, "Leaky cladding mode propagation in long-period fiber grating devices," *IEEE Photonics Technology Letters*, vol. 11, no. 3, pp. 343–345, 1999.
- [14] X. Daxhelet and M. Kulishov, "Theory and practice of long-period gratings: when a loss becomes a gain," *Optics Letters*, vol. 28, no. 9, pp. 686–688, 2003.
- [15] X. L. Jiang and Z. T. Gu, "Impact of thin film extinction coefficient on coated long-period fiber grating transmission spectrum," *Acta Optica Sinica*, vol. 30, no. 8, pp. 2189–2195, 2010.

Review Article

Recent Progress in Ohmic/Schottky-Contacted ZnO Nanowire Sensors

Xiaoli Zhao,¹ Ranran Zhou,¹ Qilin Hua,¹ Lin Dong,² Ruomeng Yu,³ and Caofeng Pan¹

¹Beijing Institute of Nanoenergy and Nanosystems, Chinese Academy of Sciences, Beijing 100083, China

²School of Materials Science and Engineering, Zhengzhou University, Zhengzhou 450001, China

³School of Materials Science and Engineering, Georgia Institute of Technology, Atlanta, GA 30332-0245, USA

Correspondence should be addressed to Lin Dong; ldong@zzu.edu.cn, Ruomeng Yu; ruomengyu@gatech.edu, and Caofeng Pan; cpan@binn.cas.cn

Received 31 March 2015; Accepted 16 June 2015

Academic Editor: Meiyong Liao

Copyright © 2015 Xiaoli Zhao et al. This is an open access article distributed under the Creative Commons Attribution License, which permits unrestricted use, distribution, and reproduction in any medium, provided the original work is properly cited.

We review the recent progress of zinc oxide (ZnO) nanowire sensors with ohmic-contacted and Schottky-contacted configurations and the enhancement of the performances of Schottky-contacted ZnO NW sensors (SCZNSs) by the piezotronic effect. Comparing with the traditional ohmic-contacted ZnO NW sensors (OCZNSs), the SCZNSs have higher sensitivities and faster responses controlled by the barrier height at the metal-semiconductor (M-S) interface. The piezotronic effect was applied to tune the Schottky barrier height (SBH) with the strain-induced piezoelectric polarization charges at the interface of the M-S contact. The piezotronic effect can thus improve the detection limitation, sensitivity, and response time of the SCZNSs in different applications, such as UV detection, gas and bio/chemical sensing. These piezotronic-enhanced SCZNSs may find potential applications in human-machine interfacing and flexible electronics skin technologies.

1. Introduction

One-dimensional semiconductor nanomaterials have been studied extensively and regarded as one of the most promising candidates for realizing ultrasensitive sensors because of their large surface-to-volume ratios, polarized crystal orientation, short distances for minority carriers to travel, and high carrier mobility [1–3]. Zinc oxide (ZnO), a direct wide band gap semiconductor material with wurtzite structure, has been widely studied due to its extraordinary electrical, optical, and piezoelectric properties [4–6]. ZnO nanowire (NW) with desired morphology and aspect ratio can be easily obtained through various methods such as vapor-liquid-solid (VLS) or vapor-solid (VS) process, wet chemical growth, molecular beam epitaxy (MBE), and metal-organic chemical vapor deposition (MOCVD) and has attracted particular interest in UV detection, gas and bio/chemical sensing areas [7–10].

Most ZnO NW sensors are composed of a single ZnO NW with two ends fixed by the metal electrodes. The contacts between the metals and the ZnO NWs can be either ohmic

or Schottky. Generally, most NW sensors based on ohmic-contact are fabricated as field effect transistor (FET) structure, of which the current is controlled by modulating the “gate voltage” through the external adsorbed species. Although devices built with a NW of smaller diameter are expected to have improved detection limit and response time to the external stimuli because of its large surface-to-volume ratio, the fabrication process of devices with reduced dimension would be much more complicated and costly [11–16]. In order to further improve the sensitivity of the ohmic-contacted ZnO NW sensors (OCZNSs), some complicated methods have been applied, such as surface modification and post-anneal. Thus, the OCZNSs with smaller sized NW and higher specific surface make the device fabrication more complicated. In comparison, the performance of the Schottky-contacted ZnO NW sensors (SCZNSs) can be optimized by regulating the Schottky barrier height (SBH) at local metal-semiconductor (M-S) interface [17–19]. Therefore, higher sensitivity, faster response, and easier fabrication process can be achieved by SCZNS that consists of microwires with the diameter in the submicrometer range, and it

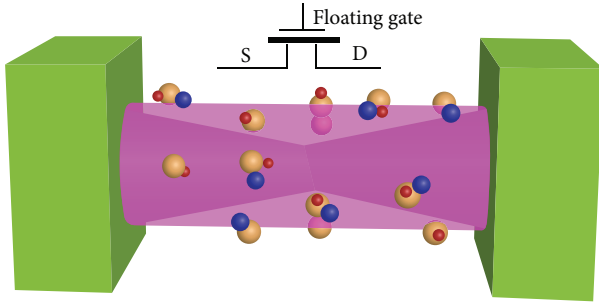


FIGURE 1: Schematic diagram of the working principle of a nanowire based nanosensor for a conventional FET configuration [3]. Copyright 2010, John Wiley and Sons.

aroused much interest in UV, gas and bio/chemical sensing system [20–24]. Wang’s group introduced the piezotronic effect [25–28] to modulate the charge carriers generation, transport, and recombination process by tuning the SBH at the local M-S interface with strain-induced piezoelectric polarization charges, hence improving the performance of the SCZNSs.

Herein, this paper reviews recent research progresses in the OCZNSs and SCZNSs for UV, gas and bio/chemical sensing. The working principle and performance optimizations of the OCZNSs and the SCZNSs are explored. A wide range of SCZNS with enhanced performance tuned by the piezotronic effect is included in this paper.

2. Ohmic-Contacted ZnO NW Sensors (OCZNSs)

2.1. Working Principle of the OCZNS. Ohmic contacts formed between the metal electrodes and semiconducting nanomaterials are in a dominant position during the early ages [29, 30]. The most typical structure of the OCZNS is FET, which utilizes a ZnO NW as the essential building block, with both ends bonded to a rigid substrate [31, 32]. The mechanism of FET is that the voltage applied across the gate and source terminals controls the flow of charge carriers from the source to drain by affecting the size and distribution of a “conductive channel” [33, 34].

The amount of target molecules adsorbed on the surface of the ZnO NW can be deduced by the change of the conductance, because the adsorbed molecules may modify the surface charges and states, change the local work function and band alignment, and alter the gate potential and the carrier mobility [35–37]. These changes are defined as a floating gate effect on the conducting channel of the FET [38], as shown in Figure 1. In order to maximize the gate effect, thin and usually short NWs are chosen to fabricate the device to obtain a higher sensitivity.

2.2. UV-OCZNSs. ZnO is a very good candidate for photonic devices in the UV range, with a direct band gap of 3.4 eV and a large exciton binding energy of 60 meV at room temperature. Soci et al. [39] demonstrated a kind of visible blind UV-OCZNS with high internal gain. Under the UV illumination

($\lambda = 390 \text{ nm}$, $P = 10 \mu\text{W}/\text{cm}^2$), a time-resolved measurement over a broad temporal domain in different ambient conditions is conducted to measure the photoconductivity of the ZnO NW. The current in the ZnO NW increases by several orders of magnitude, and the photoconductive gain can reach a high value of $G \sim 10^8$. The presence of oxygen-related hole-trap states at the NW surface, which hinders the charge carrier recombination, is regarded as the major reason for such an extremely high internal gain.

Kim and Chu [40] investigated the bias and gate voltage effects on the UV-OCZNS. The sensitivity can be increased by tuning the drain-source voltage (V_{ds}) and gate-source voltage (V_{gs}), as shown in Figure 2. When the bias voltage V_{ds} increases from 1 mV to 1 V, the on/off ratio under a hand-held UV lamp ($\lambda = 365 \text{ nm}$ and $P = 0.47 \text{ mW}/\text{cm}^2$) increases abruptly from ~ 70 to $\sim 3 \times 10^5$, and the photocurrent increases from $\sim 1 \text{ nA}$ to $\sim 1 \mu\text{A}$. So at the optimal gate voltage ($V_{gs} = -1 \text{ V}$) and bias voltage ($V_{ds} = 1 \text{ V}$), the on/off ratio reaches its maximum value of $\sim 10^6$.

2.3. Gas-OCZNSs. ZnO NW has also been regarded as a promising candidate for gas sensing owing to its high electron mobility and good thermal stability under various gas conditions. Besides, ZnO can be adopted in a broad range of gases, both the oxidizing gas (O_2 , NO) and the reducing gas (CO, H_2 , H_2S).

Fan et al. [32] fabricated the O_2 -OCZNS based on a single ZnO NW. The oxygen detection sensitivity can be modulated by the gate voltage. The ambient oxygen partial pressure has a considerable effect on the performance of the O_2 -OCZNS, due to the conductivity changes caused by surface band bending, which is induced by O_2 molecule absorption. The corresponding current decreases when the oxygen pressure increases. The relevant conductance ($\Delta G/G_0$) decreases as the NW radius increases (Figure 3); thus, a smaller diameter ZnO NW exhibits a higher sensitivity. The maximum sensitivity of 64% appears at -1.4 V , which is above the gate threshold voltage (-2.0 V) in 10 ppm O_2 .

The gas detection performance can be further enhanced by nanoparticles decoration. Joshi et al. [41] used Au decorated ZnO NWs to detect an invisible and odorless toxic gas, carbon monoxide (CO), at the room temperature. The Au nanoparticles are decorated on the ZnO NWs and act as a catalyst in chemical sensitization. A response time value of $\sim 5 \text{ s}$ is observed for 1000 ppm of CO in air. The improvement in gas sensing behavior is attributed to the transfer of electrons resulting from gas oxidation at the ZnO NWs surface.

2.4. Bio/Chemical-OCZNSs. ZnO NWs are widely adopted for bio/chemical sensors due to the advantages of ultralow detection limit, fast response, and impressive biocompatibility [42–45]. Liu et al. [46] synthesized a single ZnO NW-based biologically sensitive sensor for detection of different concentrations of uric acid solution. Before detecting, the surface of the ZnO NW is treated with the covalent modification method. The addition of uric acid with the concentrations from 1 pM to 0.5 mM resulted in the electrical conductance changes of up to 227 nS, and the response time turns out to be in the order of millisecond. The detection limit of the

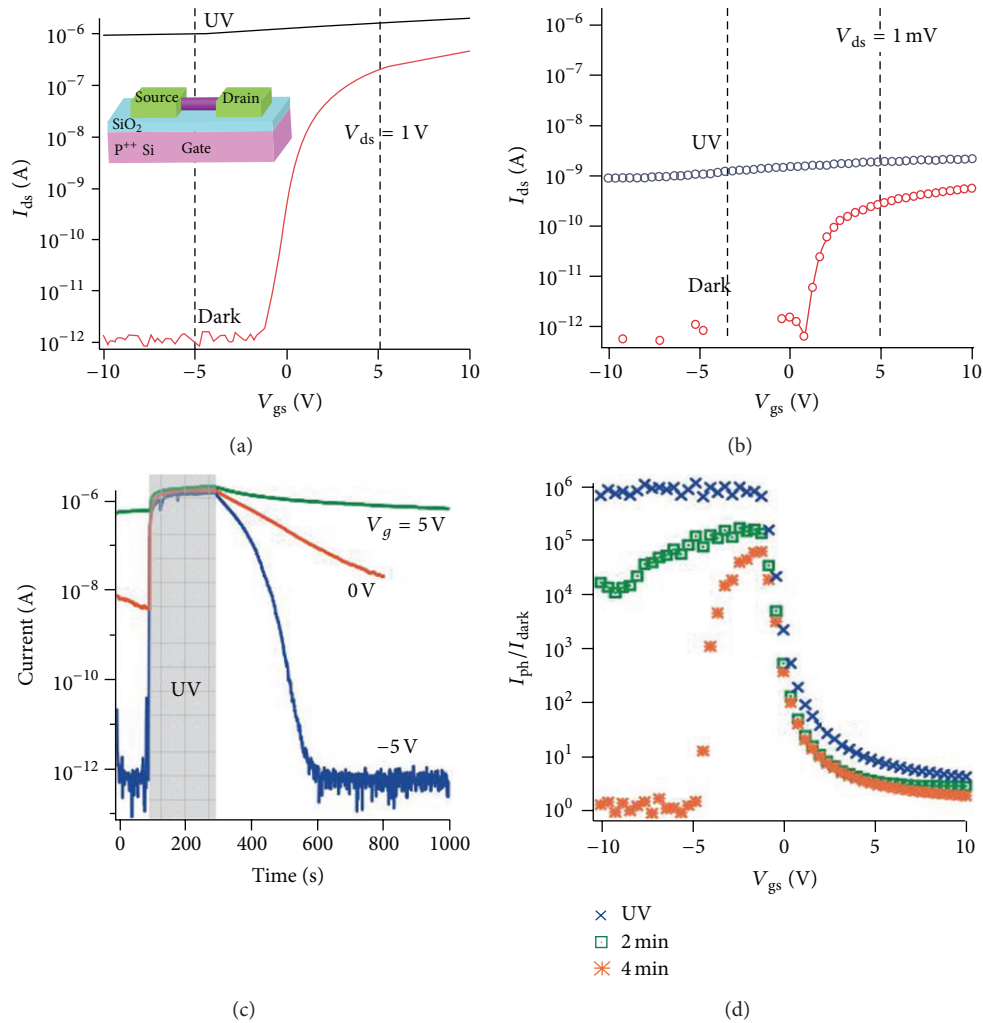


FIGURE 2: (a) Insert is a schematic of a ZnO NW FET. I_{ds} - V_{gs} characteristics under UV illumination and under darkness when $V_{ds} = 1$ V, and (b) when $V_{ds} = 1$ mV. (c) Drain-source current measured as a function of time (I_{ds} - t) while the light was on and off when $V_g = 5$ V, 0 V, and -5 V ($V_{ds} = 1$ V). (d) I_{ph}/I_{dark} as a function of gate voltage. Maximum I_{ph}/I_{dark} was obtained at $V_{gs} \sim -1$ V [40]. Copyright 2009, John Wiley and Sons.

ZnO NW biosensor can be as low as 1 pM with 14.7 nS of conductance increase.

Besides the detection of various biological molecules, the ZnO NW is also used as a pH sensor, ranging from 5 to 8.5 reported by Menzel et al. [47] after surface passivation of the ZnO NWs with a thin film of C₄F₈. The sensitivity of the pH-OCZNS obtained from the slope of the conductance reached -2.063 ± 0.14 (μ S/pH). The conductance of ZnO NW exhibits linear response over a wide pH range instantly, which mainly stems from the change of the surface charge during the protonation and deprotonation.

A control experiment is conducted by investigating ZnO nanotubes (NTs) and nanorods (NRs) based pH sensors, elaborated by Fulati et al. [48]. Both pH sensors show a linear response to the pH values (Figure 4). The developed ZnO NTs electrochemical potential pH sensors show faster response and higher sensitivity than the ZnO NRs pH sensors with the same dimensions, due to more subsurface O₂ vacancies and adsorption sites exist in the ZnO NTs.

In summary, OCZNSs with one-dimensional nanostructure have high surface-to-volume ratio, which is a key point to enhance the sensitivity and response time of the device [35, 36, 49–52]. In addition, various methods have been explored to improve the sensitivity of the OCZNSs, such as choosing proper bias and gate voltage [32, 40], surface modification [41, 46, 47], and increasing the O₂ vacancies and adsorption sites [48]. However, sophisticated decoration and fabrication process of the nanostructures may prohibit the widespread applications of the OCZNSs.

3. Schottky-Contacted ZnO NW Sensors (SCZNSs)

Many researchers investigate the Schottky-contacted structure for fabricating high performance ZnO NW sensors, because the SCZNSs have a higher sensitivity, a faster-response sensing behavior, and a lower-cost fabrication process [39, 53–56].

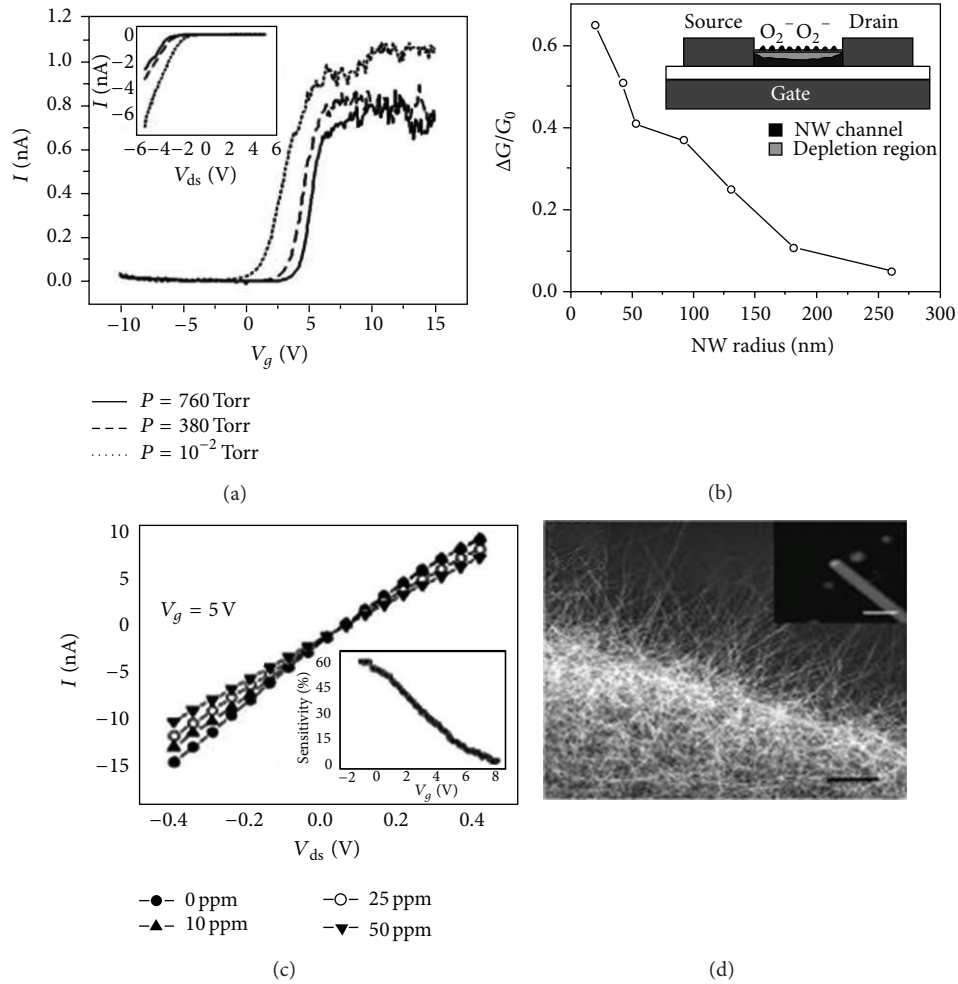


FIGURE 3: (a) Transconductance of a ZnO NW FET under different pressures at room temperature, and $V_{ds} = 200$ mV. Inset: I - V_{ds} curve of the NW under 760, 380, and 10^{-2} Torr. (b) Ratio of conductance change versus radius under a vacuum and atmosphere. Inset: a schematic of NW FET channel depletion (depicted by gray shading) caused by adsorption of oxygen molecules. (c) I - V_{ds} curves obtained in 0, 10, 25, and 50 ppm O_2 at $V_g = 5$ V. Conductance of ZnO NW decreases monotonically with increasing O_2 concentration. Inset: relationship between sensitivity and gate voltage. (d) FE-SEM image of as-grown ZnO NWs, scale bar is $20 \mu\text{m}$. Inset image shows a single ZnO NW terminated with a gold nanoparticle, and scale bar is 100 nm [32]. Copyright 2004, AIP Publishing LLC.

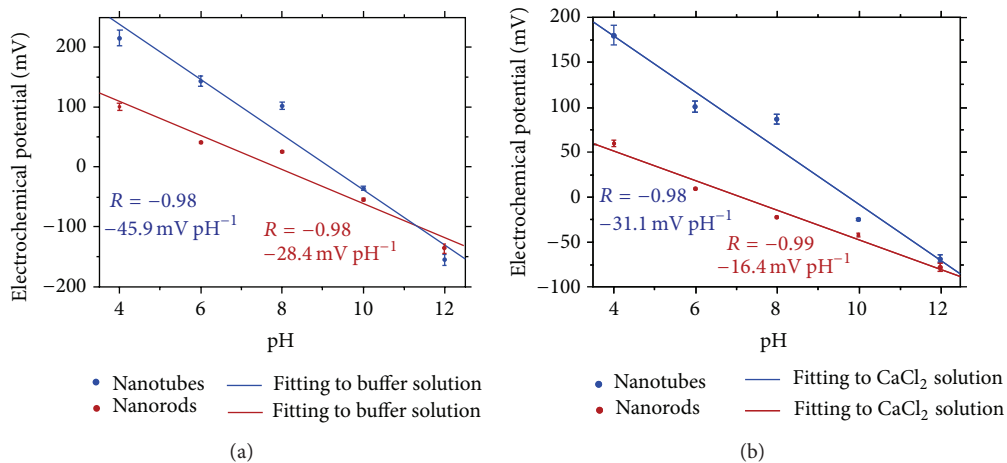


FIGURE 4: Experimental measurements of electrochemical potential versus pH comparison curves for ZnO nanorods and nanotubes immersed in (a) buffer and (b) CaCl_2 solutions [48]. Copyright 2009, Sensors.

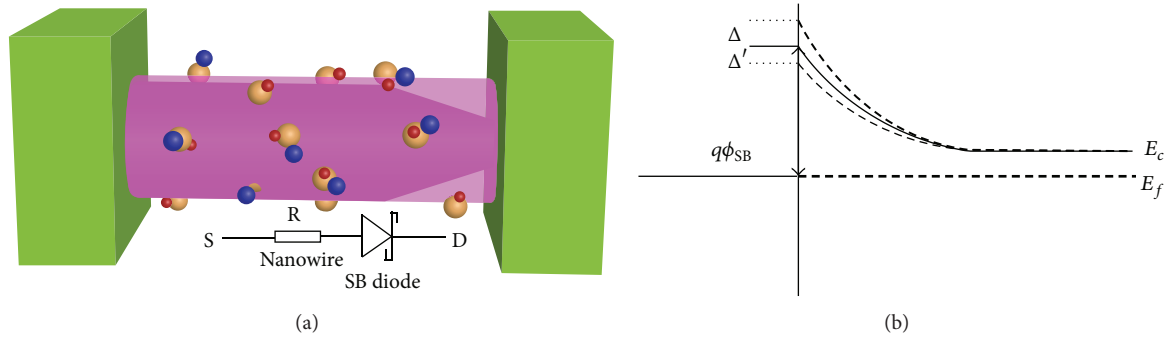


FIGURE 5: Schematic diagram of the working principle of a nanowire based nanosensor for (a) the Schottky-gated structure. (b) The energy-band diagram at the interface of the metal-ZnO contact, where a Schottky barrier is formed. The barrier height and width can be tuned in response to the change in the surrounding environment around the contact area [3]. Copyright 2010, John Wiley and Sons.

3.1. Working Principle of the SCZNSs. The typical SCZNSs contain Schottky barrier (SB) at least at one M-S interface, and the whole structure of the SCZNSs can be regarded as a NW with a SB diode in series (Figure 5). Therefore, the carrier transport through the whole device is dominated by the barrier height at local M-S interface [57], and the sensitivity is enhanced by changing the SBH at local M-S interface instead of the bulk conductance in the OCZNSs [58, 59].

The SBH at the local M-S interface plays a very important role in changing the carrier transport process. The original barrier height of local Schottky-contact is essential to the performance of the sensors, because an appropriate original barrier height of local Schottky-contact can promote the sensing performance. In order to further enhance the performance of the sensor, Wang presented the piezotronic effect [23, 60], which can change the original barrier height by inducing piezoelectric polarization charges at the local M-S interface. Therefore, the optimal performance of the Schottky-contacted sensor can be obtained.

3.2. Fundamentals of the Piezotronic Effect Enhanced the SCZNSs. Once the ZnO NW device is under strain, two typical effects may affect the carrier transport process. One is the piezoresistance effect, which is a common feature of any semiconductors, and this effect can change the band gap, charge carrier density, and possibly density of states in the conduction band of the semiconductor crystal under strain. The piezoresistance effect is a symmetric effect on the two end contacts and has no polarity, which will not affect the electrical performance of a sensor [61]. The other is the piezotronic effect [60, 62], a coupling effect between the semiconducting and piezoelectric properties of materials with non-Centrosymmetric structure, such as the wurtzite and zinc blende family. ZnO has a hexagonal structure with a large anisotropic property in *c*-axis direction (Figure 6). The Zn^{2+} cations and O^{2-} anions are tetrahedrally coordinated, and the centers of the positive ions and negative ions overlap with each other in the strain-free condition. If a stress is applied at an apex of the tetrahedron, a dipole moment is generated since the centers of the cations and anions separated. The cumulative effect of the dipole moments by all tetrahedron units in the crystal results in a macroscopic potential diversification along

the straining direction, that is, the piezoelectric potential (piezopotential).

For an n-type semiconductor and a metal contact, if the electron affinity of the semiconductor is lower than the work function of the metal, a SB is created at the interface. By applying a compressive or tensile strain from the external environment, a piezopotential distribution is induced in the semiconductor and piezoelectric polarization charges appear at the M-S interface in the semiconductor side, and they can affect the SBH at the M-S interface. Once a strain is created in the piezoelectric semiconductor, a negative piezopotential at the semiconductor side effectively increases the local SBH, while a positive piezopotential reduces the SBH [13, 30, 35, 43, 63–66]. As a result, for the Schottky-contacted sensors fabricated with the piezotronic semiconductor materials, external strains can be used as a “strain gate” to control the SBH and the electronic transport properties by inducing piezoelectric polarization charges at the local M-S interface. Thus, piezotronic effect can be used to optimize the performances of the SCZNSs.

3.3. UV-SCZNSs

3.3.1. UV-Sensors. Recently, based on the photoelectric property of individual ZnO NW, several important researches on the UV-SCZNSs have been published. Zhou et al. [59] grew the ZnO NWs by a VS process and transferred a single ZnO NW onto SiO_2/Si substrate, and Ti/Au and Pt electrodes were deposited at the end of the ZnO NW to obtain ohmic and Schottky-contact, respectively. They compared the response time of the UV-SCZNSs and the UV-OCZNSs. The ohmic structure and the characteristic of the OCZNSs are shown in Figure 7. Under the illumination of UV light ($\lambda = 365 \text{ nm}$, $P = 30 \mu\text{W}/\text{cm}^2$), the photocurrent is still unsaturated in the OCZNSs after about 260 s and the recovery time is over 2500 s, whereas for the SCZNSs the current changes from 0.04 to 60 nA within 0.6 s, and the reset time is 0.8 s. The Schottky junction could dramatically enhance the sensitivity and improve the response/recovery time. The local electric field at the SB area quickly separates the electrons and holes generated by photon excitation, which increase the carrier lifetime and free carrier density.

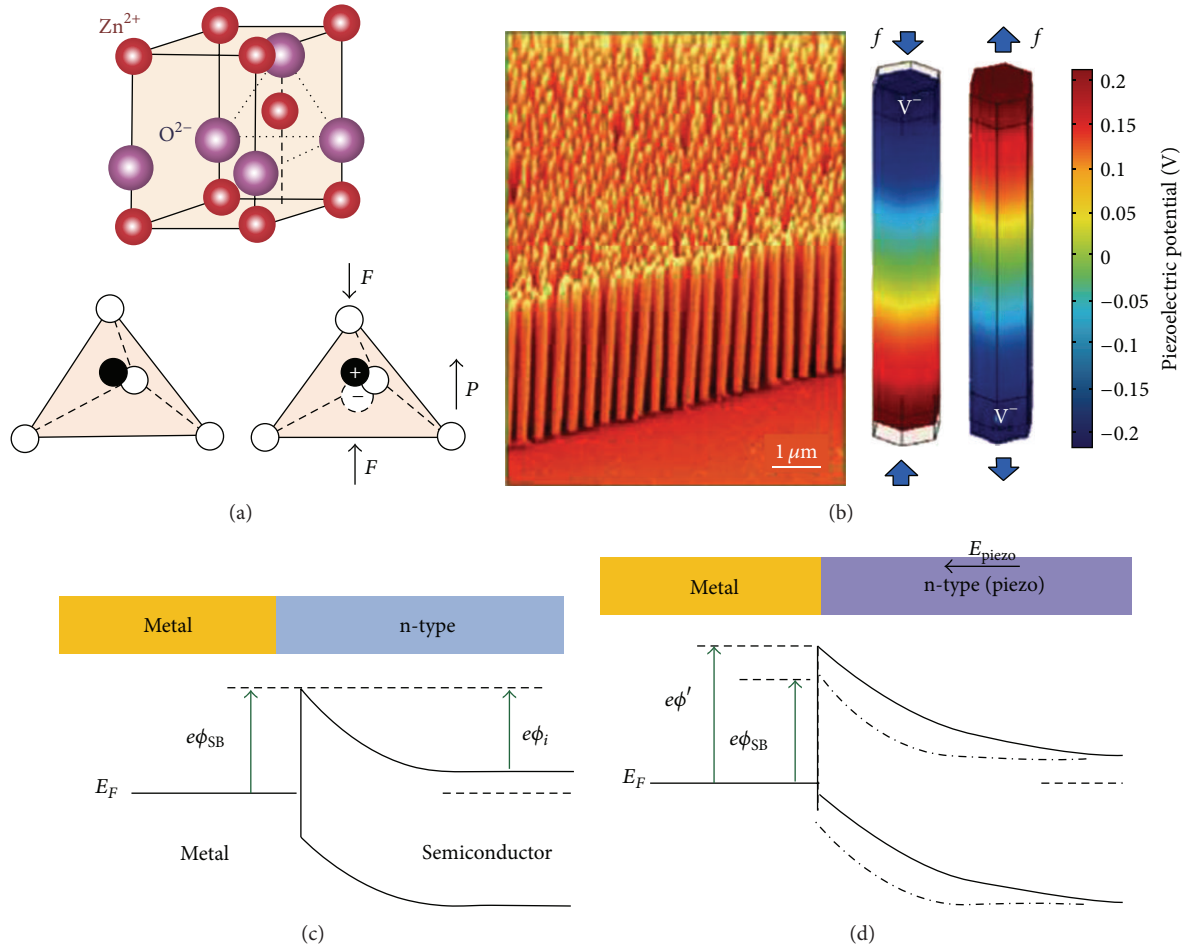


FIGURE 6: Piezopotential in wurtzite crystal. (a) Atomic model of the wurtzite structured ZnO. (b) Aligned ZnO nanowire arrays by solution based approach. Numerical calculated distribution of piezoelectric potential along a ZnO NW under axial strain. The growth direction of the NW is c -axis. The dimensions of the NW are $L = 600$ nm and $a = 25$ nm; the external force is $f_y = 80$ nN. (c) Band diagram of a Schottky-contacted M-S (n-type) interface. (d) Band diagram of the Schottky-contacted after applying a strain in the semiconductor. The piezopotential created in the semiconductor has a polarity with the end in contacting with the metal being low [62, 76]. Copyright 2012, John Wiley and Sons.

Besides, the UV illumination induces the removal of the absorbed O₂ at the SB and thus decreases the barrier height and width, which promotes the improvement of the sensitivity.

Cheng et al. [67] fabricated the UV sensor with a single ZnO NW; they demonstrated the high sensitivity and fast recovery speed of the SB as high performance UV-SCZNS. Under a UV light ($\lambda = 365$ nm, $P = 7.6$ mW/cm²), the sensitivity, photocurrent gain, and on/off ratio are $\sim 2.6 \times 10^3$ A/W, $\sim 8.5 \times 10^3$, and $\sim 4 \times 10^5$, respectively. The relevant time constant is as short as 46 ms, and the recovery time is 0.28 s when photocurrent decreases by 3 orders of magnitude. The fast recovery speed of UV-SCZNS is due to the following reason: the photocurrent of NW SB has more sensitive response to the amount of reabsorbed O₂⁻ and relaxed holes in SB interface, and the relaxation speed of holes in SB interface is faster than that on the NW surface.

3.3.2. Piezotronic Effect Enhanced UV-SCZNSs. Zhang et al. [68] fabricated a UV sensor based on the unique crystalline structure of the ZnO-CdS core-shell NW, and they studied the piezophototronic effect on the performance of the sensor under UV light illumination ($\lambda = 372$ nm and $P = 0.636$ μW/cm²). They find that the UV sensor had a compressive strain-dependent I - V characteristic (Figure 8). The absolute current of the sensor under a 2 V positive bias increases gradually from 12.9 to 144 nA, as the strain of 0% to -0.31% is applied. The sensitivity of the strained ZnO-CdS NW-based sensor is largely enhanced by more than 10 times compared to that of the unstrained NW. The reason is that both the SBHs at the source and drain contacts decrease with increased compressive strains.

Lu et al. [69] also studied the piezoelectric effect on the response of the ZnO/Au Schottky junction UV detector. The sensitivity increases 5 times when applying a 0.58% tensile strain (Figure 9) on the sensor. The enhancement is due to the

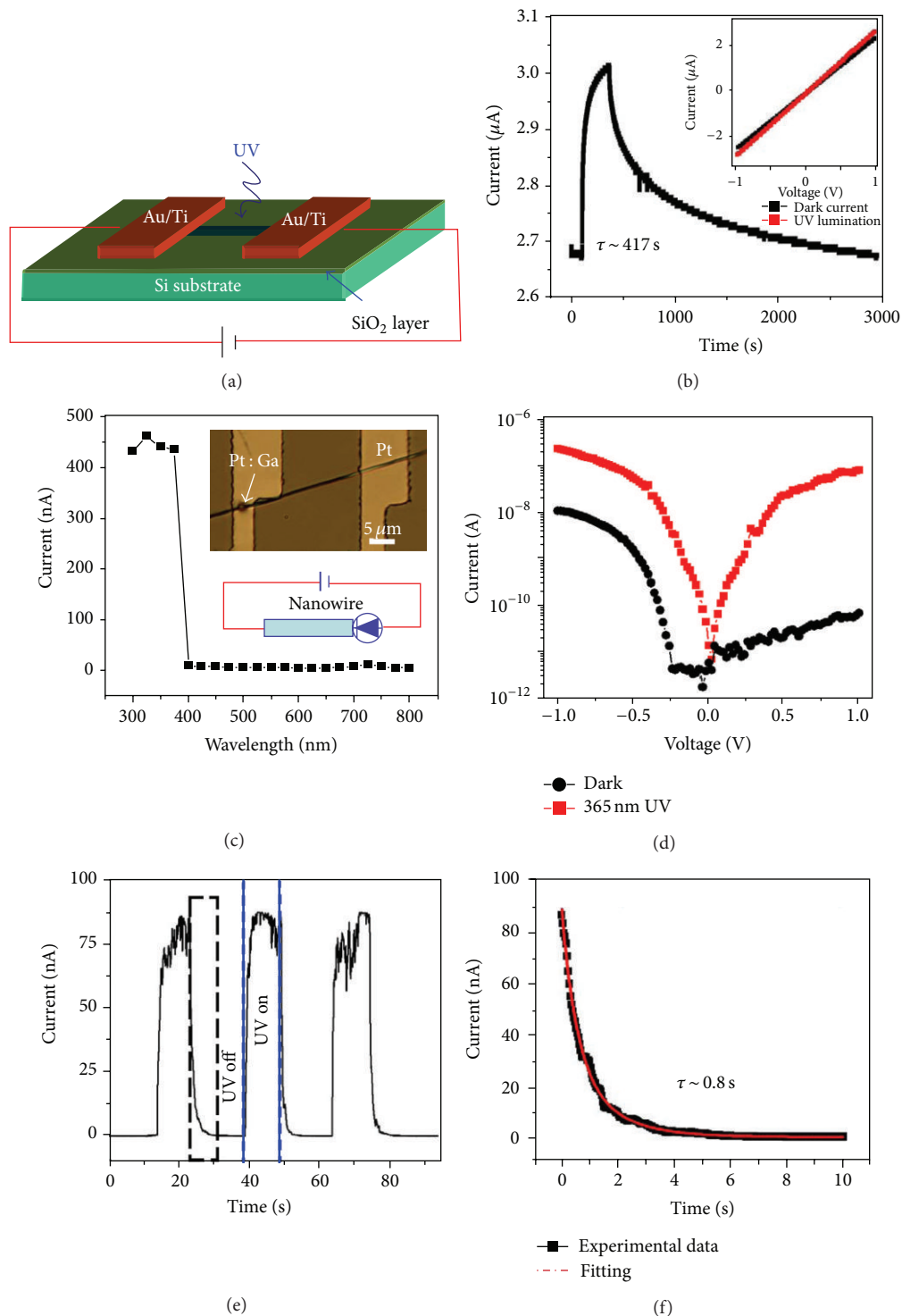


FIGURE 7: (a) Schematic of a ZnO NW UV sensor structure with ohmic-contacted. (b) Schematic of a ZnO NW UV sensor structure with ohmic-contact, when illuminated by $30 \mu\text{W}/\text{cm}^2$ UV source (365 nm). The inset shows the corresponding I - V characteristics in dark and under UV illumination. (c) Photon-response spectrum of the ZnO NW UV sensor as a function of wavelength of incident light. Upper inset is an optical image of Schottky-structured UV sensor. Lower inset shows the schematic structure of a sensor both in the dark (black cycle) and under 365 nm UV illumination (red rectangle). (d) I - V characteristics of the photocurrent growth and decay under periodic illumination of the 365 nm UV light on the device. The bias on the device is 1 V. (e) Time dependence of the photocurrent growth and decay under periodic illumination of the 365 nm UV light on the device. The bias on the device is 1 V. (f) Experimental curve (black) and fitted curve (red) of the photocurrent decay process [59]. Copyright 2009, AIP Publishing LLC.

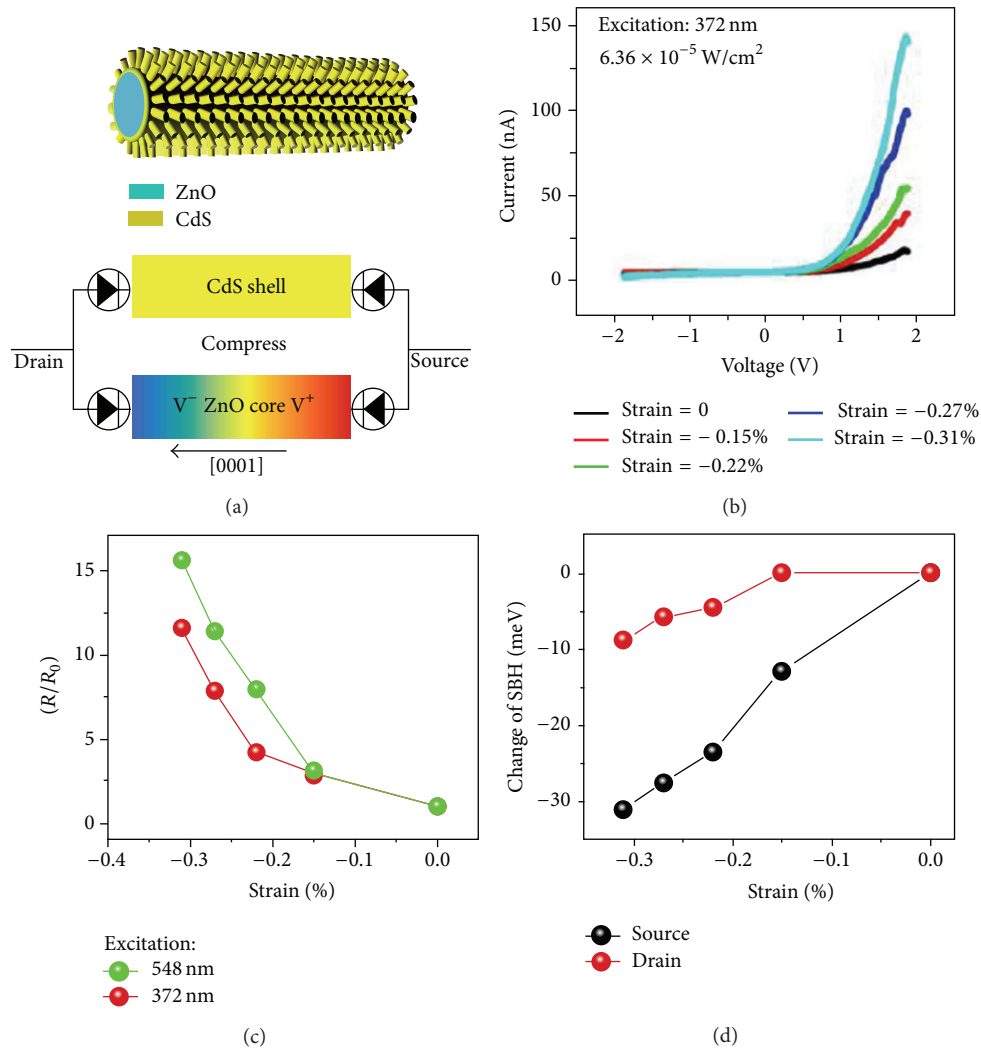


FIGURE 8: (a) Three-dimensional structure model of a ZnO-CdS core shell wire, showing the structure relationship between ZnO wire core and CdS nanowire array shell. (b) Typical IV characteristics of a single ZnO-CdS wire-based device under different compressive strains, excited by UV light centered at 372 nm. (c) The change of responsivity under compressive strains, excited by green light centered at 548 nm and UV light centered at 372 nm; R_0 is set as responsivity under zero strain. (d) The derived change in SBH as a function of compressive strains using the thermionic emission diffusion model. Black curve and red curve are the SBH change for source contact and drain contact at a source drain bias of $V = 2$ and -2 V, respectively [68]. Copyright 2012, American Chemical Society.

charges redistribution induced by piezoelectric polarization at the ZnO/Au interface.

3.4. Gas-SCZNSs

3.4.1. O₂-SCZNSs and CO-SCZNSs. Wang's group demonstrated that the sensitivity of the gas-SCZNSs is several orders higher than the gas-OCZNSs by utilizing the Schottky-contacted structure. Wei et al. [70] compared the performance of the OCZNSs and SCZNSs (Figures 10 and 11). They measure the device in N₂ and O₂ ambient at 275°C, and the linear I - V curve shows an excellent ohmic-contacted characteristic (Figure 10(a)). The devices possess a larger resistance in O₂ atmosphere since the chemisorbed O₂ species create a surface electron-depletion layer on the ZnO NW surface. The highest sensitivity of ohmic-contacted device is only 4.8%

with a response time of 500 s under 275°C, which indicates that compensating the surface defects can only slightly decrease the conductance. They measured the conductance performance of the SCZNSs at different temperature in N₂ atmosphere and in O₂ atmosphere, and the conductance for both forward and reverse bias modes was decreased because of the electron-depletion layer forming on the ZnO NW surface. Compared to the ohmic-contacted analogues, the Schottky-contacted device has higher sensitivities. Under the forward bias, the highest sensitivity of 257% is obtained at the response time of 500 s and temperature of 275°C, which is 54 times higher than 4.8% of the ohmic-contacted sensors under the same sensing conditions. While under the reverse bias, the highest sensitivity of 3235% is obtained for the Schottky-contacted device and the sensitivity was 27 times higher than that of the same device under forward

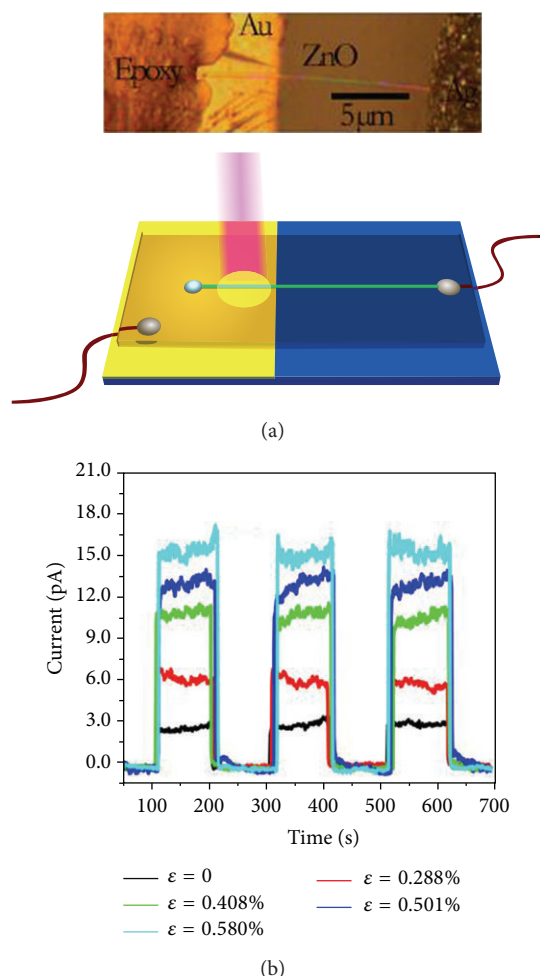


FIGURE 9: (a) Optical image (top) and schematic of the fabricated device (bottom). (b) Strain effect on the photo response characteristics [69]. Copyright 2014, American Chemical Society.

bias and 1085 times higher than that of the ohmic-contacted device.

CO sensing properties are also investigated, as shown in Figure 11. The blue region is O_2 conditioning and N_2 purge process, while the yellow region is the CO sensing for duration of 60 min. It shows that the sensitivity increases with the increase of CO concentration, consistent with the previous reports [71, 72]. The highest sensitivity of 32 000% for the CO-SCZNS under reverse bias mode is obtained in the 400 ppm CO concentration at $275^\circ C$, while the sensitivity of the ohmic-contacted device is only 3.8% at the same condition. Comparing with the ohmic-contacted device, the great success of the Schottky-contacted device relies on the modulation of the SBH through adsorption and removal of the negatively charged species.

3.4.2. Humidity-SCZNSs. Herrán et al. [73] presented a room temperature Ag/ZnO Schottky diode for relative humidity (RH) monitoring. The sensor can detect the RH based on the adsorption of the water molecules on the NR surface and the reduction of the majority of carriers in the conduction band

of the semiconductor. The sensitivity shows a logarithmic relation between 20% and 75% of RH and the response time is about 5 s; this is due to the physical behavior of the Schottky diode according to the M-S junction between the ZnO and the Ag.

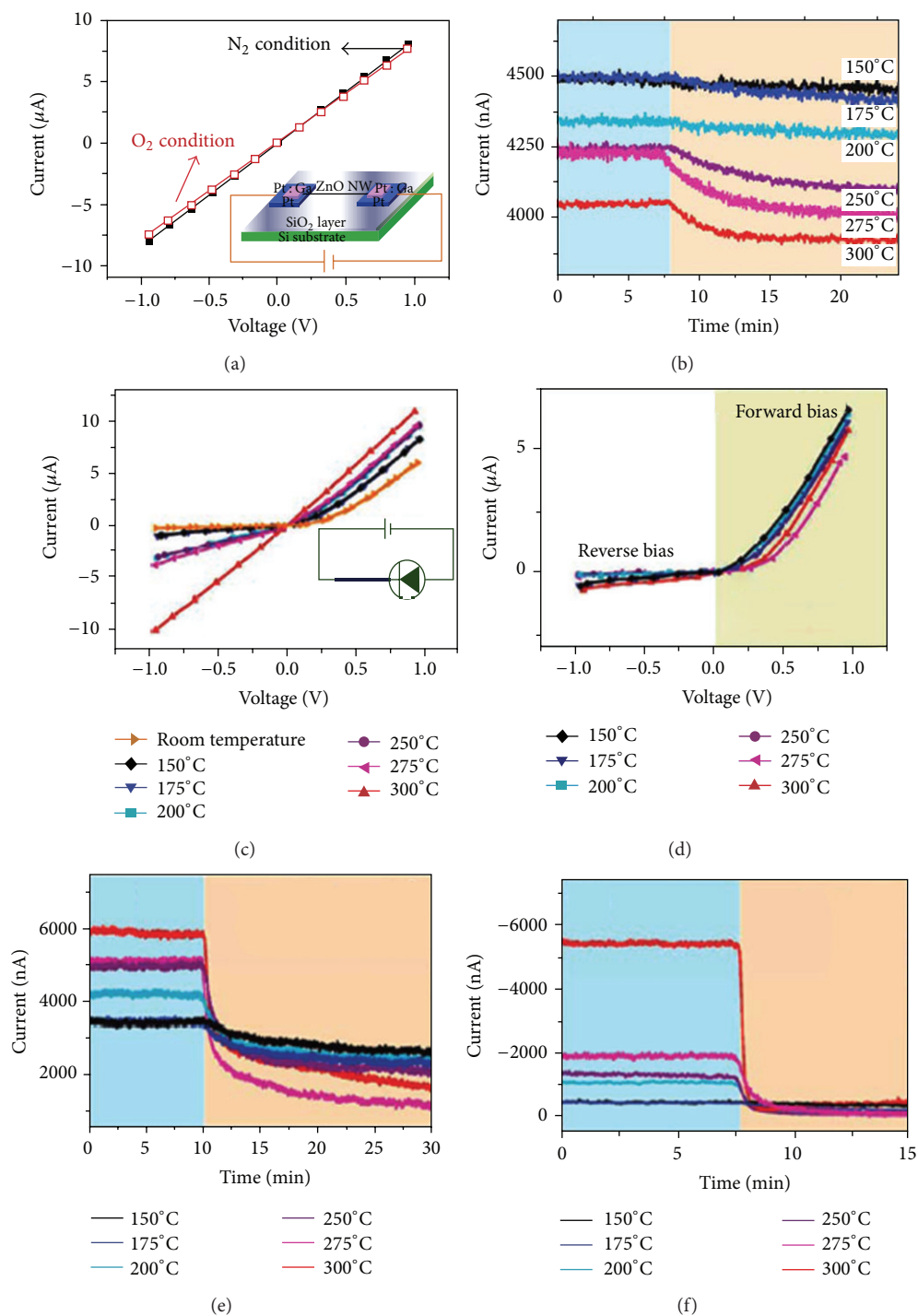
3.4.3. Piezotronic Effect Enhanced Gas-SCZNSs

(1) *Piezotronic Effect Enhanced O_2 -SCZNSs.* Niu et al. [74] studied the piezotronic effect on the O_2 -SCZNSs. The typical SEM image of the ZnO NWs, optical image, and a schematic of the measurement setup are shown in Figure 12. The electrical performance of the device is measured after a UV lamp ($\lambda = 254$ nm and $P = 23$ W) treatment. Under the 1 V bias, the current drops with the increase of either oxygen pressure or tensile strain, whereas under the bias of -1 V, the current slightly decreases with the tensile strain, while it greatly decreases with the increased O_2 pressure. In the 700 Torr O_2 pressures and applying 0 to 0.2% tensile strain, under the 1 V bias, the relative current enhances from -55.4% to -75.4% , while under the -1 V bias, the relative current increases from -87.3% to -93% , respectively. It is due to the adsorption of O_2 , an electron-depletion layer is formed on the ZnO NW surface and reduces the carrier density in the NW, and the O_2 adsorbed around the Schottky-contacted area increases the SBH, which reduces the overall current [75–77]. Besides, by applying a tensile strain, the already downward trend to O_2 can be further enhanced by piezotronic effect.

(2) *Piezotronic Effect Enhanced Humidity-SCZNSs.* Hu et al. [78] investigated the piezotronic effect on the performances of the humidity-SCZNSs. They fabricate the Schottky-contacted devices and detect the performance of the humidity sensor (Figure 13). The experiment is carried out at a fixed bias of 2.8 V under different humidity and strain conditions. By comparing the relative current response to different RH under each certain strain condition, it is concluded that the current increases with the increase of compressive strain and the decrease of RH. Furthermore, the slopes of curves become deeper with increasing the strain, which means that the relative sensitivity of humidity sensors is improved by the piezotronic effect. In the ZnO NW humidity sensor, a -0.22% compressive strain can optimize the performances by achieving the largest responsivity of 1,240%. These results demonstrate that the piezotronic effect can enhance the performance of humidity sensors at different RH and improve the sensing resolution by significantly enlarging the current differences between two RHs under certain strain condition.

3.5. Bio/Chemical-SCZNSs

3.5.1. Bio-SCZNSs. Yeh et al. [79] fabricated both the Schottky-contacted and ohmic-contacted ZnO NW devices. The conductance performance of the ohmic-contacted devices is shown in Figure 14. No obvious signal is observed when the concentration of the charged target molecules is lower than $800 \mu g/mL$, probably because the conductance of the ZnO NW is so high that the introduction of surface-absorbed molecules cannot change the conductance of the



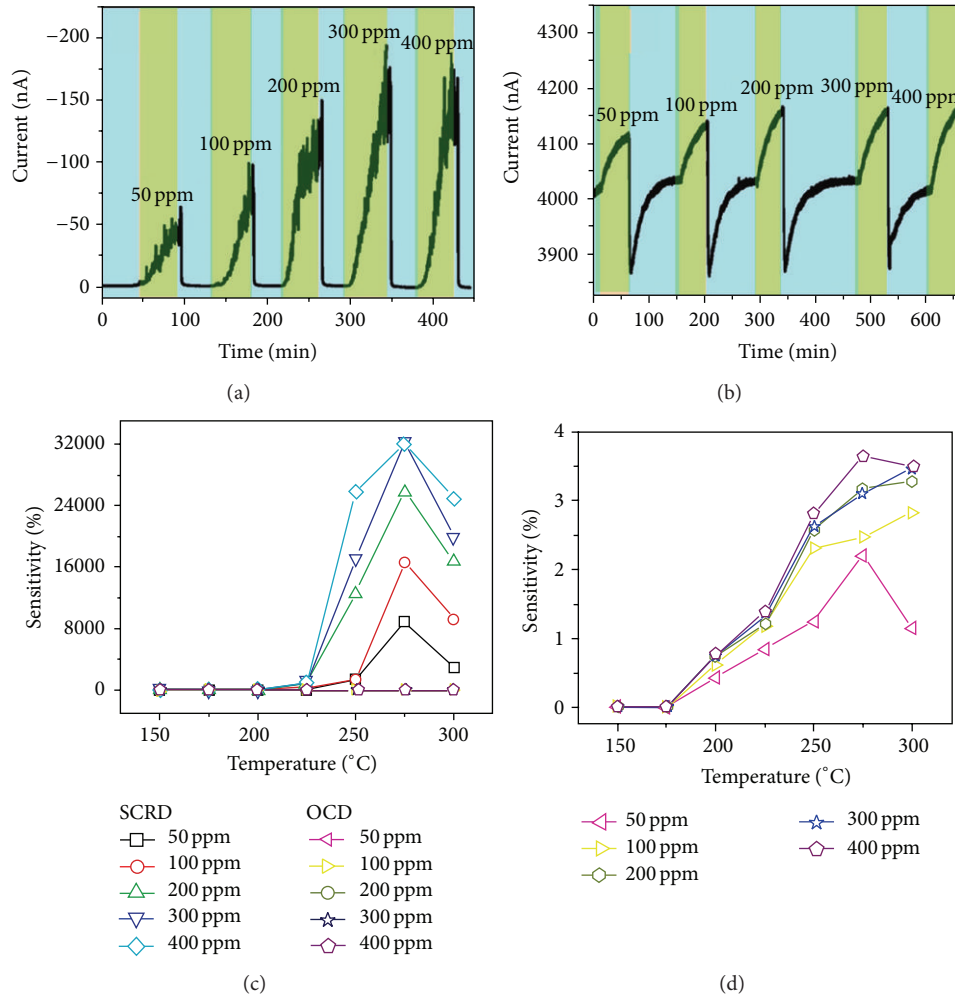


FIGURE 11: Response curves of the CO detection recorded at 275°C with the device exposed to increased concentration of CO: (a) for the Schottky-contacted device under reverse bias and (b) for the ohmic-contacted device. (c) Sensitivity versus system temperature for CO sensing at a response time of 1 h as a function of the CO concentration. (d) Enlarged plot of the data from panel (c) for the ohmic-contacted device [70]. Copyright 2009, American Chemical Society.

NW significantly. However, the Schottky-contacted device shows a fast response and distinctly current change for different concentrations. The devices are immersed in DI water as the signal baseline for measuring the conductance, and in this case, the negatively charged molecules absorbed around the SB area increase the barrier height and decrease the current. In contrast, when introduced positively charged molecules increase the current. The performance of the biosensor is largely controlled by the characteristic of the SBH, which can get different effects for detecting positively and negatively charged molecules.

3.5.2. Piezotronic Effect Enhanced Bio/Chemical-SCZNSs

(1) *Piezotronic Effect Enhanced pH-SCZNSs.* Pan et al. [17] demonstrated the piezotronic effect on the pH-SCZNSs, as shown in Figure 15. They fabricate the device by using the silver paste to get the Schottky-contact, and in order to prevent the two silver electrodes from contacting with

the buffer solutions, the two electrodes are fully covered by a layer of epoxy. The signal of the pH sensor decreases step-by-step with discrete changing in pH from 3 to 12 under no strain condition, and the stable and repeatable performances of the pH sensor are detected in solutions (pH = 5 and pH = 12). The reason for the decrease in different pH value is as follows: at high pH, OH^- correspondingly depletes the electron carriers and decreases the conductance, while at low pH, H^+ increases the electron carriers in the n-type ZnO NW and the conductance. When applying a 0.5 V bias voltage, the signal level of a nonstrain sensor is only 1.2 nA in the buffer solution with pH = 5. However, when a -0.92% compressive strain is applied on the device, the current jumps to 1.75 μA , and equivalently the current increases by about 1500 times in magnitude. Under externally applied strain in different pH value buffer solutions, the signal current increases with applied strain, because the SBH is changed by the strain, and the relative changes of the SBH (ΔSBH) can be calculated according to Yang et al.'s work

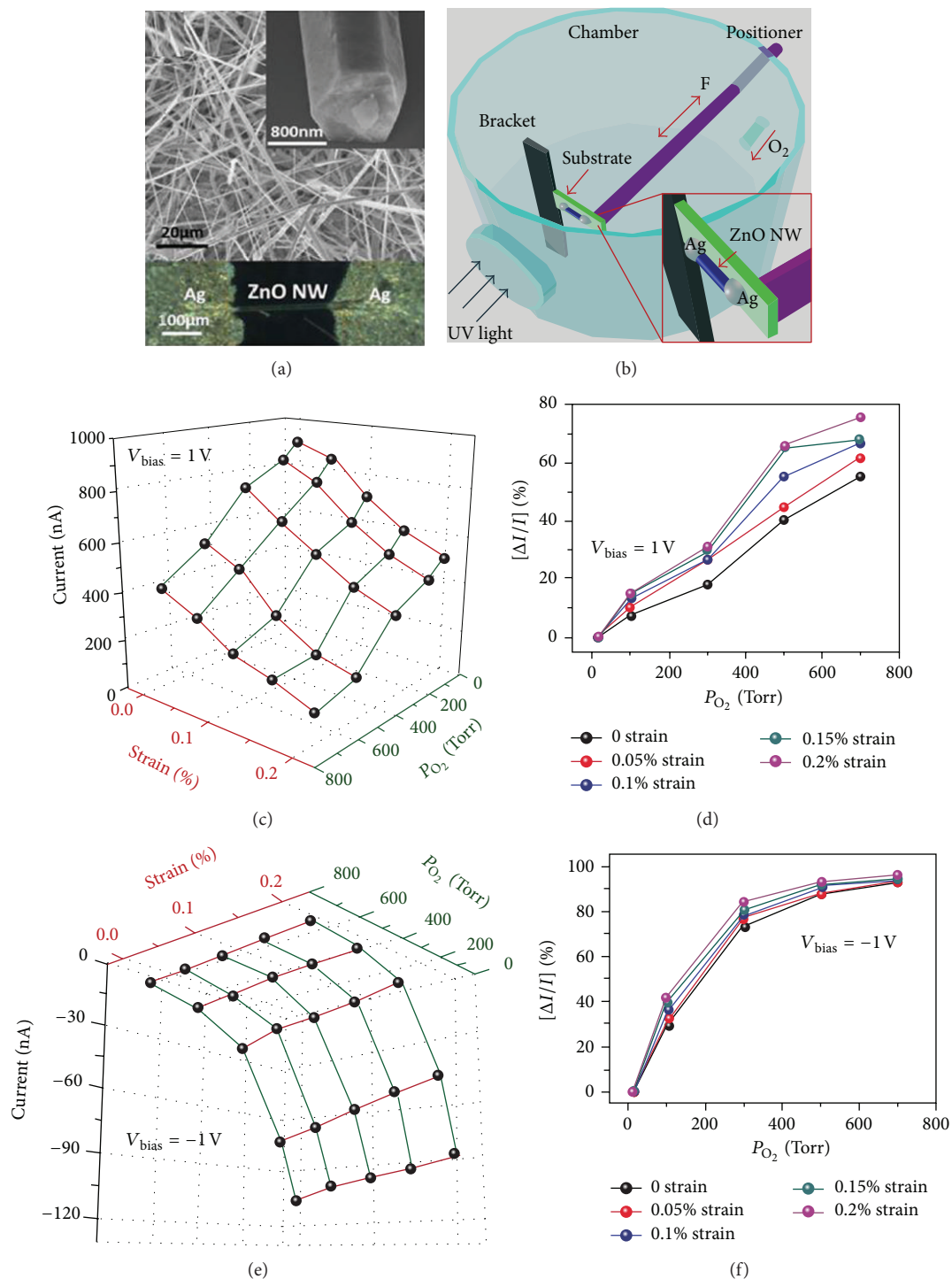


FIGURE 12: Piezotronic effect on the performance of an individual ZnO NW-based room temperature oxygen sensor (a) SEM images of ZnO NWs. The inset is a high-magnification image of an individual wire (top right) and optical microscopy image of a ZnO NW oxygen sensor device (bottom). (b) Schematic of the measurement setups for studying the piezotronic effect in a ZnO NW oxygen sensor (c) 3D graph depicting the current response of the ZnO NW oxygen sensor under different strains and oxygen pressures at a bias voltage equal to 1 V. (d) Magnitude of relative current change with oxygen pressure under different tensile strain from 0% to 0.2% at a bias voltage of 1 V. ((e)-(f) Corresponding results of Figure 12 (c, d) at bias voltage of -1 V [74]. Copyright 2013, John Wiley and Sons.

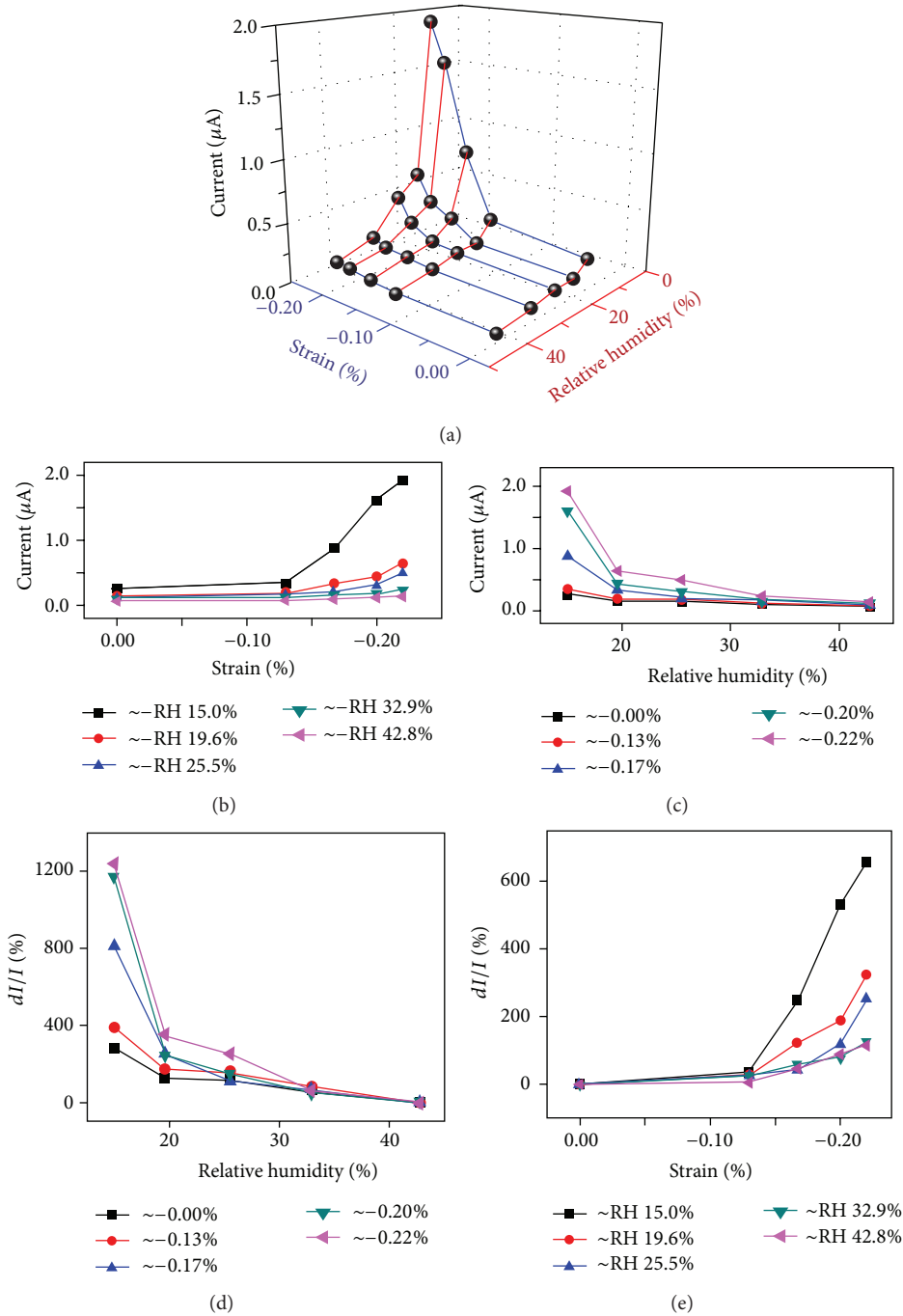


FIGURE 13: (a) 3D graph depicts the current response of the ZnO NW humidity sensor to strain and relative humidity at a bias voltage of 2.8 V. (b) Absolute current response to different compressive strains, with relative humidity ranging from 15.0% to 42.8%. (c) Absolute current response to different relative humidity, with compressive strains ranging from -0.00% to -0.22% . (d) Indicating the relative changes of current with respect to the value at 42.8% RH, under different compressive strains ranging from -0.00% to -0.22% . (e) Indicating the relative changes of current with respect to the value at 0.0% strain, under different RHs ranging from 15.0% to 42.8% [78]. Copyright 2014, Springer.

[80, 81]. The test results demonstrate that the piezotronic effect can enhance the sensitivity of the SCZNSs.

(2) *Piezotronic Effect Enhanced Glucose-SCZNSs*. Yu et al. [18] investigated the piezotronic effect on the performances of

the glucose-SCZNSs. The fabrication method of the glucose sensor is similar to the pH-SCZNSs [17], while in Yu's research, they decorate the glucose oxidases (GO_x) onto the ZnO NW. It is obvious that the current increases with the incremental compressive strains (Figure 16), at a bias voltage

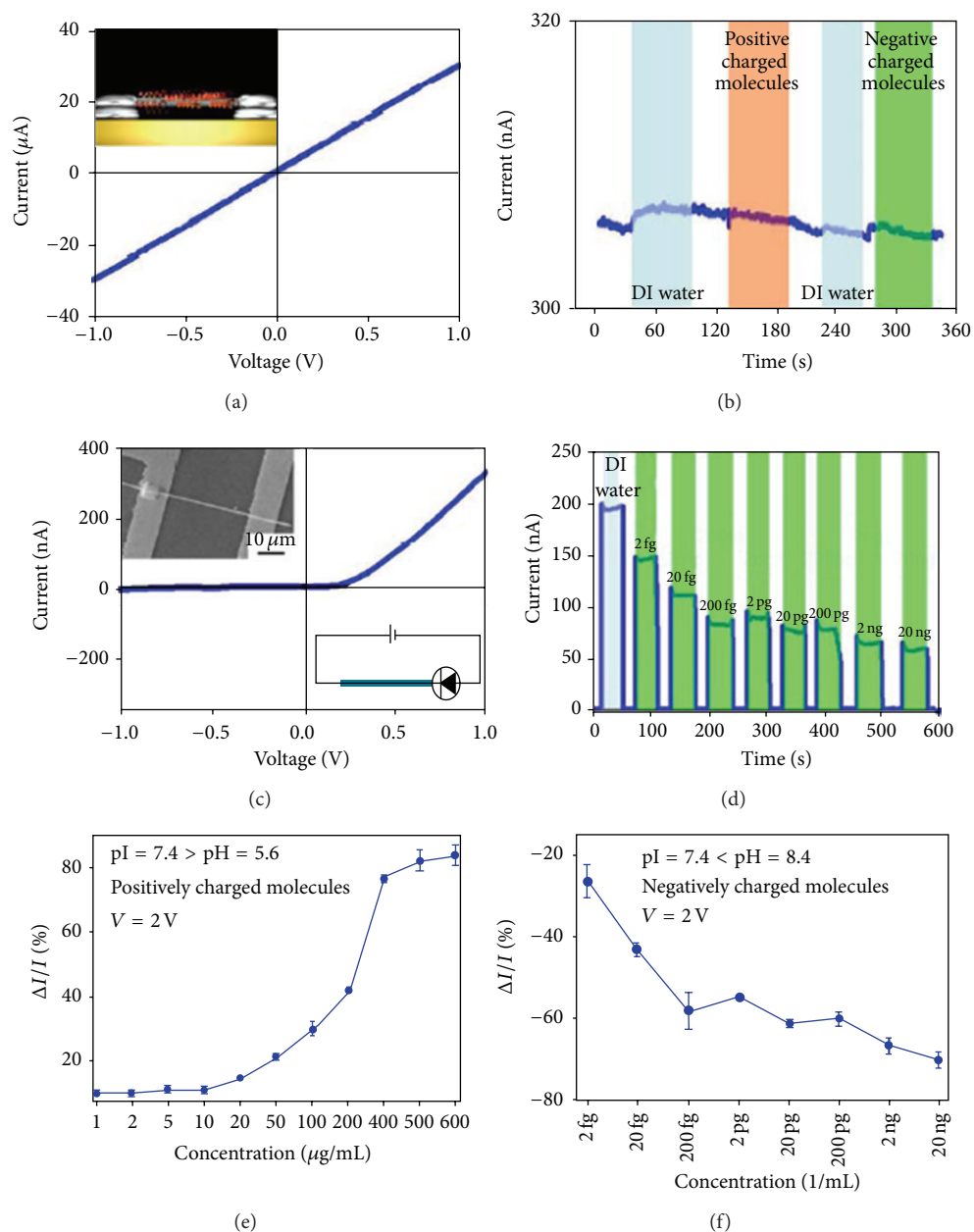


FIGURE 14: The ohmic-contacted biosensor was fabricated using a single-crystal ZnO NW that shows little response to the biomolecules. (a) Pt-Ga was deposited by FIB on both ends of the NW to form ohmic-contact (inset), as proven by its corresponding $I-V$ curve. (b) When either positively charged molecules or negatively charged molecules are introduced, the electrical signal of the device shows little change. (c) SEM image of a Schottky-contacted biosensor is shown in the upper-left inset. The $I-V$ curve shows a typical Schottky characteristic. (d) A fast response and distinct current variations can be seen when the sensor is exposed to a series of concentrations of negatively charged molecules ($pI 7.4 < pH 8.4$). (e) When the molecules are positively charged ($pI 7.4 > pH 5.6$), the conductance of the device increases. (f) The negatively charged molecules result in a decrease in conductance [79]. Copyright 2009, John Wiley and Sons.

of 1.8 V; as a -0.79% compressive strain is applied, the current increases from $0.15 \mu A$ to more than $25 \mu A$, which is about 150 times larger in magnitude. The output signal of a strain-free ZnO NW glucose sensor clearly increases stepwise with gradually adding glucose into the solution, measured at a fixed bias of 2 V.

Furthermore, they studied the response of the glucose sensors to continuously changed glucose concentrations and

compressive strains. It is clear that the current increases stepwise with the glucose concentrations and the relative change in current is around 130% by adding 1.5 g/L glucose without strain. The current difference between two certain glucose concentrations is obviously increased when applying more compressive strain, and this relative change in current has the largest value more than 300% and mostly relative change in current is around 150%. These results indicate that

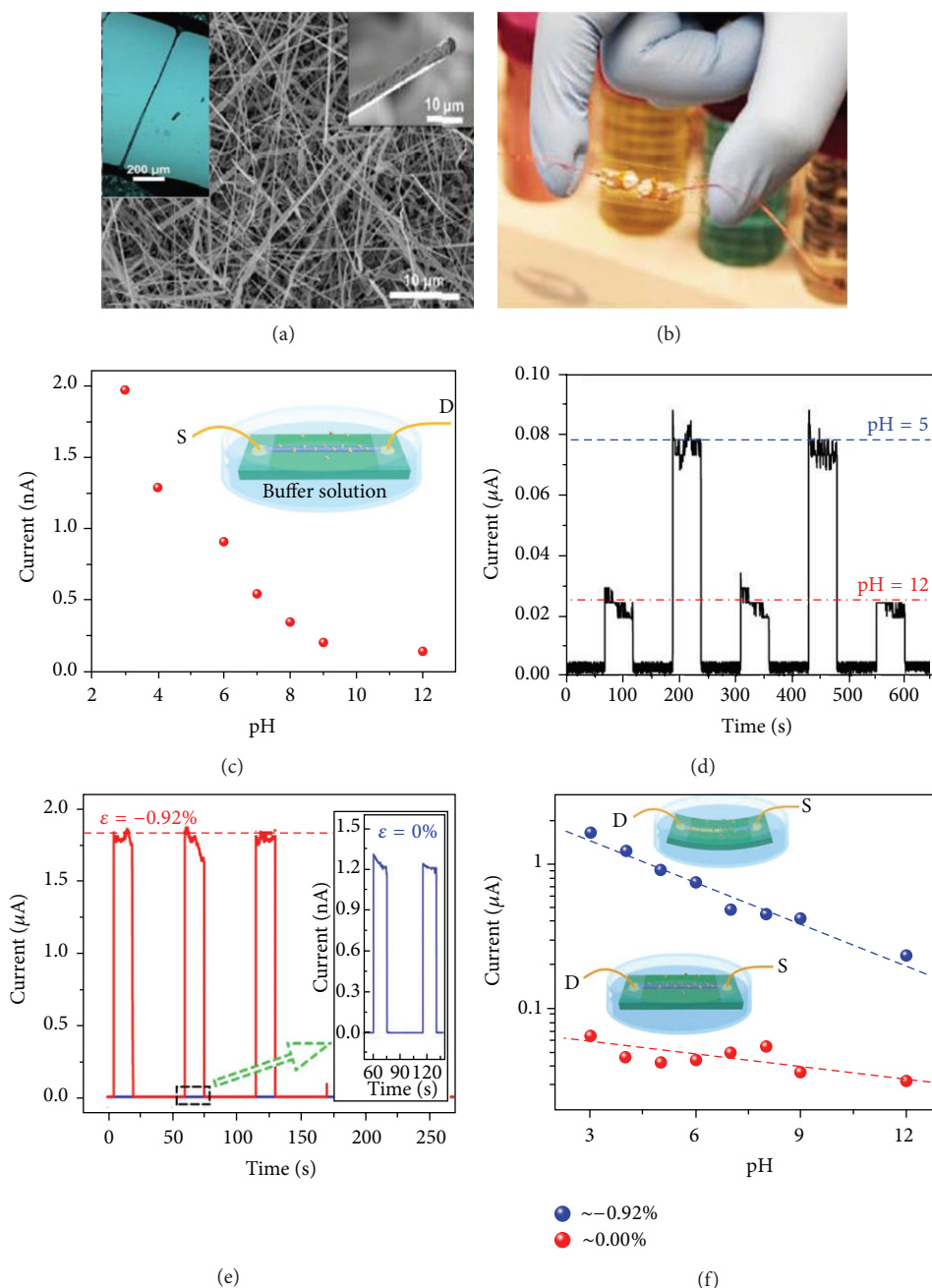


FIGURE 15: (a) SEM image of the morphology of the as-synthesized ZnO NWs. The insert is a high-magnification image of an individual wire and Optical microscopy. (b) Digital image of a ZnO NW pH sensor. (c) The response of the sensor to the pH varying from 3 to 12, no external strain was applied, just like traditional NW based sensors. (d) The repeatability of the ZnO sensor pH sensor at pH 5 and 12. The signal level and the sensitivity of the sensor are increased by the piezotronics effect. (e) The output signal of a sensor in a buffer solution with pH = 5 when the strain is “off” (blue) and “on” (red). The signal is increased about 1500 times when a compressive strain of $\epsilon = -0.92\%$ was applied. (f) The response of the sensor to the pH varying from 3 to 12, when the device is strain off (red) and on (blue) [17]. Copyright 2013, American Chemical Society.

the relative change of output signals in applying strains case is even much larger than that in the adding glucose case. The sensitivity and sensing resolution of the glucose sensor is generally enhanced by the piezotronic effect.

(3) *Piezotronic Effect Enhanced Protein-SCZNSs*. Yu et al. [19] also demonstrated the piezotronic effect on the performances

of the protein-SCZNSs, as shown in Figure 17. The device is fabricated similar to the aforementioned pH-SCZNSs [17], by adding 0.01 mL of gold nanoparticles-anti immunoglobulin G conjugates (Au NP-anti-IgG) colloidal solution on the NW, and then the NW is modified with a blocking buffer (BB), 0.1% fish gelatin, and 1% Bovine Serum Albumin (BSA). BB can efficiently block the nonspecific binding of IgGs

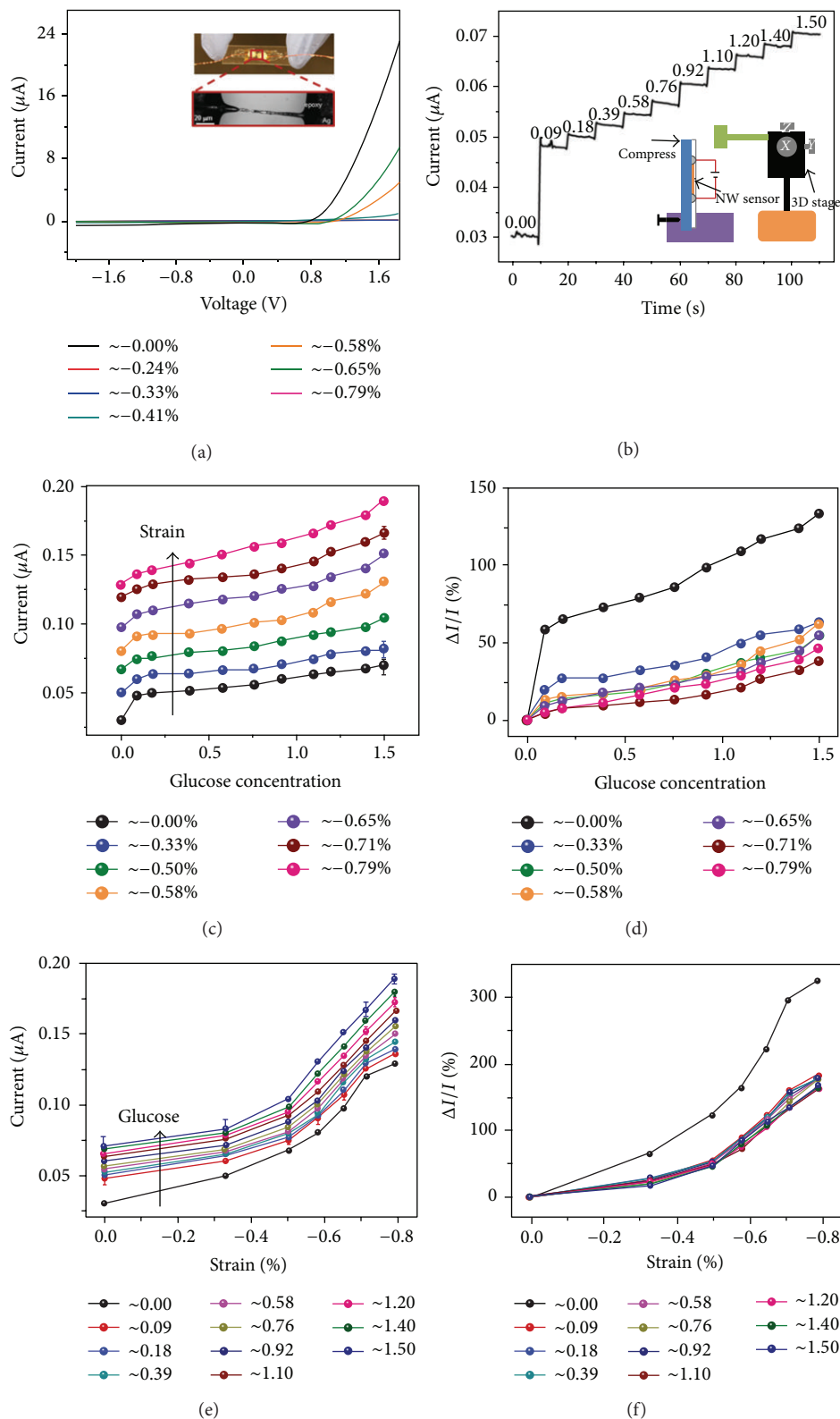


FIGURE 16: (a) I - V characteristics of a ZnO NW glucose sensor under different compressive strains, no glucose added. The inset shows a digital image and an optical microscopy image of the ZnO NW glucose sensor. (b) I - t characteristics of another ZnO NW glucose sensor in different glucose concentrations, no external strains applied. The inset presents a schematic of the experiments setup. (c)-(d) Absolute and relative current response of the ZnO NW glucose sensor in different glucose concentrations, with compressive strain ranging from 0 to -0.79% , respectively. (e)-(f) Absolute and relative current response of the ZnO NW glucose sensor under different compressive strains, with glucose concentration ranging from 0 to 1.50 g/L, respectively [18]. Copyright 2013, John Wiley and Sons.

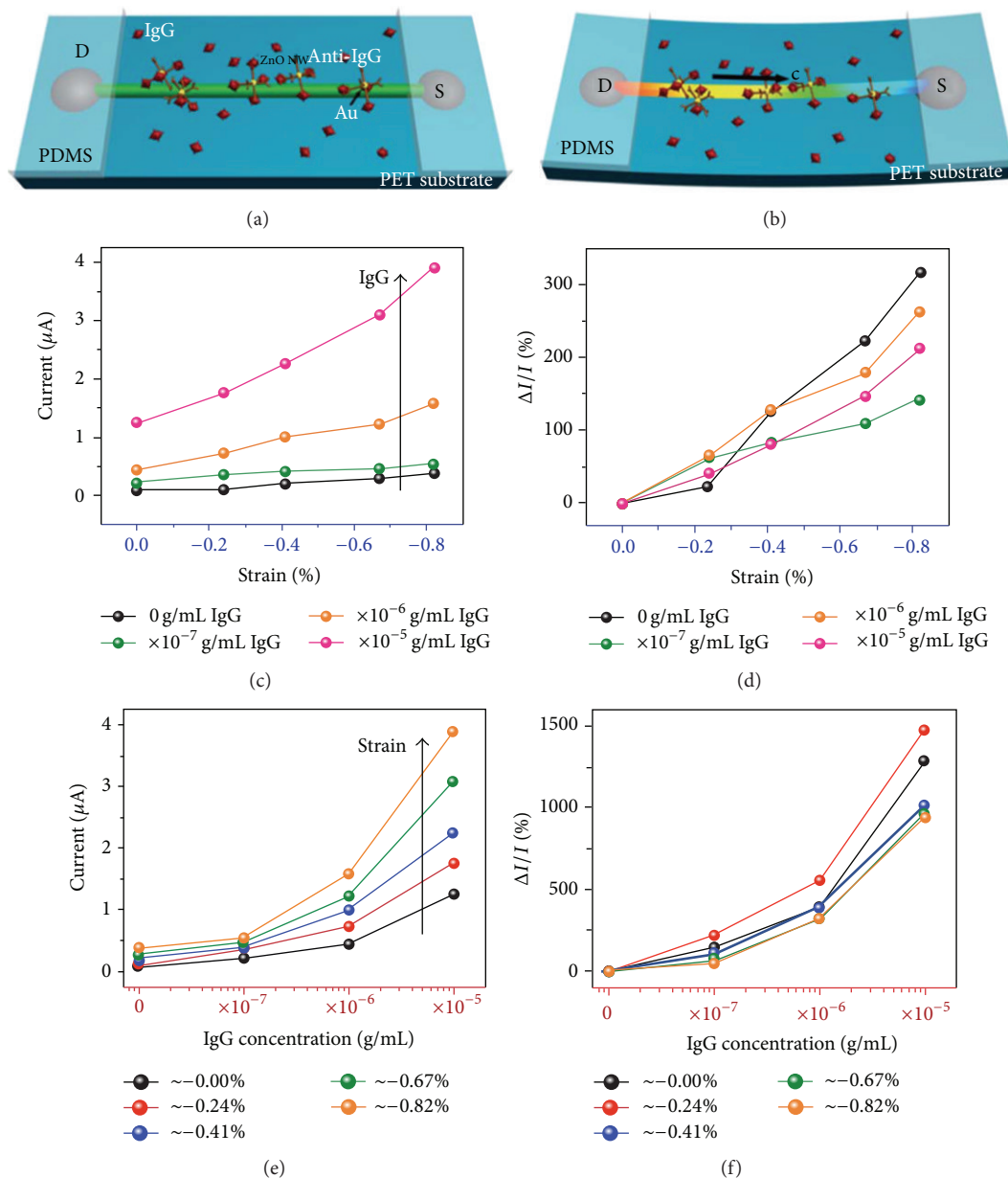


FIGURE 17: (a) Gold nanoparticle anti-IgG surface functionalized ZnO NW protein sensor bonding with target protein IgG. (b) ZnO NW protein sensor under compressive strain. ((c)-(d)) Absolute and relative current response of ZnO NW protein sensor under different compressive strains, with IgG concentration ranging from 0 to 1×10^{-5} g/mL, respectively. ((e)-(f)) Absolute and relative current response of ZnO NW protein sensor at different IgG concentrations, with compressive strain ranging from 0 to -0.82% , respectively [19]. Copyright 2012, Royal Society of Chemistry.

to the devices [82]. Therefore, treating the device with BB can effectively decrease the undesirable response from the nonspecific binding to the device and is essential for the specific function of the sensor.

It is obvious that current increases with increasing the IgG concentrations or compressive strains. The difference between currents related to two adjacent IgG concentrations is enlarged as the strain increases, which is the result from the nonlinear I - V transport properties controlled by the SB at the contacts of the metal-semiconductor-metal (M-S-M) structure. It can also be seen that, at a

fixed IgG concentration, the larger the strain applied, the higher the output current observed. These results obviously show that the piezotronic effect can improve the resolution, the detection limit, and the sensitivity of the protein-SCZNSs.

In general, the SCZNSs exhibit higher sensitivity and faster response than the OCZNSs. For SCZNSs, the adsorption of a few molecules at the junction area could effectively change the local barrier height. The piezotronic effect [83, 84] play a dominant role in optimizing enhance the performance of the SCZNSs.

4. Conclusions and Outlook

In this paper, we introduce ZnO NW sensors based on the ohmic-contacted and Schottky-contacted structure, the working principle, and performance enhancement of the OCZNSs and SCZNSs. For the OCZNSs, the current change is regarded as the result of the “gate voltage” modulating through the external adsorbed molecules. The performance of this kind of devices is usually affected by the bias and gate voltage, the decorated surface, and the size of ZnO NWs. For SCZNSs, the output signals of these devices could be optimized by several orders of magnitudes higher than that of the OCZNSs. By utilizing the piezotronic effect to modulate the SBH, the extremely high sensitivity can be obtained.

The ZnO NW devices should be further optimized in sensitivity to detect force, heat, light, humid, gas, and so forth, and the piezoelectric material system, single NW device, or integrated NW sensor arrays will be further investigated in other research fields. Undoubtedly, the piezotronic-enhanced Schottky-contacted sensors will have potentially important applications in photoelectric detection, environment monitoring, health monitoring, and robotics.

Conflict of Interests

The authors declare that there is no conflict of interests regarding the publication of this paper.

Acknowledgments

The authors acknowledge the support from the “Thousand Talents” program for pioneer researcher and its innovation team, China, President Funding of the Chinese Academy of Sciences, National Natural Science Foundation of China (nos. 51272238, 21321062, 51432005, and 61405040), the Innovation Talent Project of Henan Province (no. 13HASTIT020), Talent Project of Zhengzhou University (ZDGD13001), and Surface Engineering Key Lab of LIPCAST.

References

- [1] A. L. Briseno, T. W. Holcombe, A. I. Boukai et al., “Oligo- and polythiophene/ZnO hybrid nanowire solar cells,” *Nano Letters*, vol. 10, no. 1, pp. 334–340, 2010.
- [2] N. P. Dasgupta and P. Yang, “Semiconductor nanowires for photovoltaic and photoelectrochemical energy conversion,” *Frontiers of Physics*, vol. 9, no. 3, pp. 289–302, 2014.
- [3] Y. Hu, J. Zhou, P. H. Yeh, Z. Li, T. Wei, and Z. L. Wang, “Super-sensitive, fast-response nanowire sensors by using Schottky contacts,” *Advanced Materials*, vol. 22, no. 30, pp. 3327–3332, 2010.
- [4] A. A. Iliadis, R. D. Vispute, T. Venkatesan, and K. Jones, “Ohmic metallization technology for wide band-gap semiconductors,” *Thin Solid Films*, vol. 420–421, pp. 478–486, 2002.
- [5] A. Inumpudi, A. Iliadis, S. Krishnamoorthy, S. Choopun, R. Vispute, and T. Venkatesan, “Pt–Ga Ohmic contacts to n-ZnO using focused ion beams,” *Solid-State Electronics*, vol. 46, no. 10, pp. 1665–1668, 2002.
- [6] K. Ip, Y. W. Heo, K. H. Baik, D. P. Norton, S. J. Pearton, and F. Ren, “Carrier concentration dependence of Ti/Al/Pt/Au contact resistance on n-type ZnO,” *Applied Physics Letters*, vol. 84, no. 4, p. 544, 2004.
- [7] S. T. Jun and G. M. Choi, “CO gas-sensing properties of ZnO/CuO contact ceramics,” *Sensors and Actuators B: Chemical*, vol. 17, no. 3, pp. 175–178, 1994.
- [8] B. M. Kulwicki, “Humidity sensors,” *Journal of the American Ceramic Society*, vol. 74, no. 4, pp. 697–708, 1991.
- [9] Y. Liu, C. R. Gorla, S. Liang et al., “Ultraviolet detectors based on epitaxial ZnO films grown by MOCVD,” *Journal of Electronic Materials*, vol. 29, no. 1, pp. 69–74, 2000.
- [10] S. R. Morrison, “Semiconductor gas sensors,” *Sensors and Actuators*, vol. 2, no. 205, pp. 329–341, 1982.
- [11] M. Ahn, K. Park, J. Heo et al., “Gas sensing properties of defect-controlled ZnO-nanowire gas sensor,” *Applied Physics Letters*, vol. 93, no. 26, 2008.
- [12] A. B. Artyukhin, M. Stadermann, R. W. Friddle, P. Stroeve, O. Bakajin, and A. Noy, “Controlled electrostatic gating of carbon nanotube FET devices,” *Nano Letters*, vol. 6, no. 9, pp. 2080–2085, 2006.
- [13] M. Curreli, C. Li, Y. H. Sun et al., “Selective functionalization of In₂O₃ nanowire mat devices for biosensing applications,” *Journal of the American Chemical Society*, vol. 127, no. 19, pp. 6922–6923, 2005.
- [14] Z. Fan and J. G. Lu, “Gate-refreshable nanowire chemical sensors,” *Applied Physics Letters*, vol. 86, no. 12, Article ID 123510, 2005.
- [15] H. Kind, H. Yan, B. Messer, M. Law, and P. Yang, “Nanowire ultraviolet photodetectors and optical switches,” *Advanced Materials*, vol. 14, no. 2, pp. 158–160, 2002.
- [16] X. Tang, S. Bansaruntip, N. Nakayama, E. Yenilmez, Y. Chang, and Q. Wang, “Carbon nanotube DNA sensor and sensing mechanism,” *Nano Letters*, vol. 6, no. 8, pp. 1632–1636, 2006.
- [17] C. Pan, R. Yu, S. Niu, G. Zhu, and Z. L. Wang, “Piezotronic effect on the sensitivity and signal level of Schottky contacted proactive micro/nanowire nanosensors,” *ACS Nano*, vol. 7, no. 2, pp. 1803–1810, 2013.
- [18] R. Yu, C. Pan, J. Chen, G. Zhu, and Z. L. Wang, “Enhanced performance of a ZnO nanowire-based self-powered glucose sensor by piezotronic effect,” *Advanced Functional Materials*, vol. 23, no. 47, pp. 5868–5874, 2013.
- [19] R. Yu, C. Pan, and Z. L. Wang, “High performance of ZnO nanowire protein sensors enhanced by the piezotronic effect,” *Energy & Environmental Science*, vol. 6, no. 2, p. 494, 2013.
- [20] R. K. Gupta and F. Yakuphanoglu, “Photoconductive Schottky diode based on Al/p-Si/SnS₂/Ag for optical sensor applications,” *Solar Energy*, vol. 86, no. 5, pp. 1539–1545, 2012.
- [21] N. J. Ku, J. H. Huang, C. H. Wang, H. Fang, and C. Liu, “Crystal face-dependent nanopiezotronics of an obliquely aligned InN nanorod array,” *Nano Letters*, vol. 12, no. 2, pp. 562–568, 2012.
- [22] K. Momeni and H. Attariani, “Electromechanical properties of 1D ZnO nanostructures: nanopiezotronics building blocks, surface and size-scale effects,” *Physical Chemistry Chemical Physics*, vol. 16, no. 10, pp. 4522–4527, 2014.
- [23] Z. L. Wang, “The new field of nanopiezotronics,” *Materials Today*, vol. 10, no. 5, pp. 20–28, 2007.
- [24] F. M. Zörgiebel, S. Pregl, L. Römhildt et al., “Schottky barrier-based silicon nanowire pH sensor with live sensitivity control,” *Nano Research*, vol. 7, no. 2, pp. 263–271, 2014.

- [25] Y. Fu, W. L. Zang, P. L. Wang, L. Xing, X. Xue, and Y. Zhang, "Portable room-temperature self-powered/active H₂ sensor driven by human motion through piezoelectric screening effect," *Nano Energy*, vol. 8, pp. 34–43, 2014.
- [26] M. L. Seol, J. M. Choi, J. Y. Kim, J. Ahn, D. Moon, and Y. Choi, "Piezoelectric nanogenerator with a nanoforest structure," *Nano Energy*, vol. 2, no. 6, pp. 1142–1148, 2013.
- [27] X. D. Wang, "Piezoelectric nanogenerators-harvesting ambient mechanical energy at the nanometer scale," *Nano Energy*, vol. 1, no. 285, pp. 13–24, 2012.
- [28] Z. Zhang, Q. L. Liao, Y. H. Yu, X. Wang, and Y. Zhang, "Enhanced photoresponse of ZnO nanorods-based self-powered photodetector by piezotronic interface engineering," *Nano Energy*, vol. 9, no. 284, pp. 237–244, 2014.
- [29] J. He, Y. Zhang, J. Liu, D. Moore, G. Bao, and Z. Wang, "ZnS/Silica nanocable field effect transistors as biological and chemical nanosensors," *The Journal of Physical Chemistry C*, vol. 111, no. 33, pp. 12152–12156, 2007.
- [30] F. Patolsky and C. M. Lieber, "Nanowire nanosensors," *Materials Today*, vol. 8, no. 4, pp. 20–28, 2005.
- [31] Y. Cui and C. M. Lieber, "Functional nanoscale electronic devices assembled using silicon nanowire building blocks," *Science*, vol. 291, no. 5505, pp. 851–853, 2001.
- [32] Z. Fan, D. Wang, P.-C. Chang, W. Tseng, and J. G. Lu, "ZnO nanowire field-effect transistor and oxygen sensing property," *Applied Physics Letters*, vol. 85, no. 24, Article ID 5923, 2004.
- [33] P. Andrei, L. Fields, J. Zheng, Y. Cheng, and P. Xiong, "Modeling and simulation of single nanobelt SnO₂ gas sensors with FET structure," *Sensors and Actuators B: Chemical*, vol. 128, no. 1, pp. 226–234, 2007.
- [34] A. J. Soares and R. J. Perry, "Modeling and simulation of a single tin dioxide nanobelt FET for chemical sensors," *IEEE Sensors Journal*, vol. 10, no. 2, pp. 235–242, 2010.
- [35] R. J. Chen, H. C. Choi, S. Bangsaruntip et al., "An investigation of the mechanisms of electronic sensing of protein adsorption on carbon nanotube devices," *Journal of the American Chemical Society*, vol. 126, no. 5, pp. 1563–1568, 2004.
- [36] E. L. Gui, L. Li, K. Zhang et al., "DNA sensing by field-effect transistors based on networks of carbon nanotubes," *Journal of the American Chemical Society*, vol. 129, no. 46, pp. 14427–14432, 2007.
- [37] I. Heller, A. M. Janssens, J. Männik, E. D. Minot, S. G. Lemay, and C. Dekker, "Identifying the mechanism of biosensing with carbon nanotube transistors," *Nano Letters*, vol. 8, no. 2, pp. 591–595, 2008.
- [38] Y. Cheng, P. Xiong, L. Fields, J. P. Zheng, R. S. Yang, and Z. L. Wang, "Intrinsic characteristics of semiconducting oxide nanobelt field-effect transistors," *Applied Physics Letters*, vol. 89, no. 9, Article ID 093114, 2006.
- [39] C. Soci, A. Zhang, B. Xiang et al., "ZnO nanowire UV photodetectors with high internal gain," *Nano Letters*, vol. 7, no. 4, pp. 1003–1009, 2007.
- [40] W. Kim and K. S. Chu, "ZnO nanowire field-effect transistor as a UV photodetector; optimization for maximum sensitivity," *Physica Status Solidi (A)*, vol. 206, no. 1, pp. 179–182, 2009.
- [41] R. K. Joshi, Q. Hu, F. Am et al., "Au decorated zinc oxide nanowires for CO sensing," *Journal of Physical Chemistry C*, vol. 113, no. 314, pp. 16199–16202, 2009.
- [42] Y.-S. Chiu, C.-T. Lee, L.-R. Lou et al., "Wide linear sensing sensors using ZnO:Ta extended-gate field-effect-transistors," *Sensors and Actuators B: Chemical*, vol. 188, no. 268, pp. 944–948, 2013.
- [43] Y. Cui, "Nanowire nanosensors for highly sensitive and selective detection of biological and chemical species," *Science*, vol. 293, no. 5533, pp. 1289–1292.
- [44] B. Huang, J.-C. Lin, and Y.-K. Yang, "ZnO/Silicon nanowire hybrids extended-gate field-effect transistors as pH sensors," *Journal of the Electrochemical Society*, vol. 160, no. 6, pp. B78–B82, 2013.
- [45] H. H. Li, C. E. Yang, C. C. Kei et al., "Coaxial-structured ZnO/silicon nanowires extended-gate field-effect transistor as pH sensor," *Thin Solid Films*, vol. 529, no. 269, pp. 173–176, 2013.
- [46] X. Liu, P. Lin, X. Q. Yan et al., "Enzyme-coated single ZnO nanowire FET biosensor for detection of uric acid," *Sensors and Actuators B: Chemical*, vol. 176, no. 316, pp. 22–27, 2013.
- [47] A. Menzel, K. Subannajui, F. Güder, D. Moser, O. Paul, and M. Zacharias, "Multifunctional ZnO-nanowire-based sensor," *Advanced Functional Materials*, vol. 21, no. 22, pp. 4342–4348, 2011.
- [48] A. Fulati, S. M. U. Ali, M. Riaz, G. Amin, O. Nur, and M. Willander, "Miniaturized pH sensors based on zinc oxide nanotubes/nanorods," *Sensors*, vol. 9, no. 11, pp. 8911–8923, 2009.
- [49] R. S. Aga, D. Jowhar, A. Ueda et al., "Enhanced photoresponse in ZnO nanowires decorated with CdTe quantum dot," *Applied Physics Letters*, vol. 91, no. 23, Article ID 232108, 2007.
- [50] S.-E. Ahn, H. J. Ji, K. Kim et al., "Origin of the slow photoresponse in an individual sol-gel synthesized ZnO nanowire," *Applied Physics Letters*, vol. 90, no. 15, Article ID 153106, 2007.
- [51] H. Han, J. Kim, H. S. Shin, J. Y. Song, and W. Lee, "Air-bridged Ohmic contact on vertically aligned si nanowire arrays: application to molecule sensors," *Advanced Materials*, vol. 24, no. 17, pp. 2284–2288, 2012.
- [52] J. H. He, C. H. Ho, and C. Y. Chen, "Polymer functionalized ZnO nanobelts as oxygen sensors with a significant response enhancement," *Nanotechnology*, vol. 20, no. 6, Article ID 065503, 2009.
- [53] S. Koizumi, "Ultraviolet emission from a diamond pn junction," *Science*, vol. 292, no. 5523, pp. 1899–1901.
- [54] C. S. Lao, M. Park, Q. Kuang et al., "Giant enhancement in UV response of ZnO nanobelts by polymer surface-functionalization," *Journal of the American Chemical Society*, vol. 129, no. 40, pp. 12096–12097, 2007.
- [55] Y. Li, F. D. Valle, M. Simonnet, I. Yamada, and J. Delaunay, "Competitive surface effects of oxygen and water on UV photoresponse of ZnO nanowires," *Applied Physics Letters*, vol. 94, no. 2, 2009.
- [56] L. Luo, Y. Zhang, S. S. Mao, and L. Lin, "Fabrication and characterization of ZnO nanowires based UV photodiodes," *Sensors and Actuators A: Physical*, vol. 127, no. 2, pp. 201–206, 2006.
- [57] J. Zhou, P. Fei, Y. Gu et al., "Piezoelectric-potential-controlled polarity-reversible schottky diodes and switches of ZnO wires," *Nano Letters*, vol. 8, no. 11, pp. 3973–3977, 2008.
- [58] R. Yan, D. Gargas, and P. Yang, "Nanowire photonics," *Nature Photonics*, vol. 3, no. 10, pp. 569–576, 2009.
- [59] J. Zhou, Y. Gu, Y. Hu et al., "Gigantic enhancement in response and reset time of ZnO UV nanosensor by utilizing Schottky contact and surface functionalization," *Applied Physics Letters*, vol. 94, no. 19, Article ID 191103, 2009.
- [60] Z. L. Wang, "Nanopiezotronics," *Advanced Materials*, vol. 19, no. 125, pp. 889–892, 2007.

- [61] Y. Zhang, Y. Liu, and Z. L. Wang, "Fundamental theory of piezotronics," *Advanced Materials*, vol. 23, no. 27, pp. 3004–3013, 2011.
- [62] Z. L. Wang, "Progress in piezotronics and piezo-phototronics," *Advanced Materials*, vol. 24, no. 34, pp. 4632–4646, 2012.
- [63] M. S. Arnold, P. Avouris, Z. W. Pan, and Z. L. Wang, "Field-effect transistors based on single semiconducting oxide nanobelts," *The Journal of Physical Chemistry B*, vol. 107, no. 3, pp. 659–663, 2003.
- [64] H. R. Byon and H. C. Choi, "Network single-walled carbon nanotube-field effect transistors (SWNT-FETs) with increased Schottky contact area for highly sensitive biosensor applications," *Journal of the American Chemical Society*, vol. 128, no. 7, pp. 2188–2189, 2006.
- [65] S. N. Das, K. Moon, J. P. Kar et al., "ZnO single nanowire-based UV detectors," *Applied Physics Letters*, vol. 97, no. 2, 2010.
- [66] L. Dong, S. Niu, C. Pan, R. Yu, Y. Zhang, and Z. L. Wang, "Piezophototronic effect of CdSe nanowires," *Advanced Materials*, vol. 24, no. 40, pp. 5470–5475, 2012.
- [67] G. Cheng, X. Wu, B. Liu, B. Li, X. Zhang, and Z. Du, "ZnO nanowire Schottky barrier ultraviolet photodetector with high sensitivity and fast recovery speed," *Applied Physics Letters*, vol. 99, no. 20, 2011.
- [68] F. Zhang, Y. Ding, Y. Zhang, X. Zhang, and Z. L. Wang, "Piezophototronic effect enhanced visible and ultraviolet photodetection using a ZnO-CdS core-shell micro/nanowire," *ACS Nano*, vol. 6, no. 10, pp. 9229–9236, 2012.
- [69] S. Lu, J. J. Qi, S. Liu et al., "Piezotronic interface engineering on ZnO/Au-based schottky junction for enhanced photoresponse of a flexible self-powered UV detector," *ACS Applied Materials & Interfaces*, vol. 6, no. 16, pp. 14116–14122, 2014.
- [70] T. Y. Wei, P. H. Yeh, S. Y. Lu, and Z. L. Wang, "Gigantic enhancement in sensitivity using Schottky contacted nanowire nanosensor," *Journal of the American Chemical Society*, vol. 131, no. 48, pp. 17690–17695, 2009.
- [71] R. W. Scott, S. M. Yang, G. Chabanis, N. Coombs, D. E. Williams, and G. A. Ozin, "Tin dioxide opals and inverted opals: near-ideal microstructures for gas sensors," *Advanced Materials*, vol. 13, no. 19, pp. 1468–1472, 2001.
- [72] B. Wang, L. F. Zhu, Y. H. Yang, N. Xu, and G. Yang, "Fabrication of a SnO₂ nanowire gas sensor and sensor performance for hydrogen," *Journal of Physical Chemistry C*, vol. 112, no. 17, pp. 6643–6647, 2008.
- [73] J. Herrán, I. Fernández, R. Tena-Zaera, E. Ochoteco, G. Cabañero, and H. Grande, "Schottky diodes based on electrodeposited ZnO nanorod arrays for humidity sensing at room temperature," *Sensors and Actuators B: Chemical*, vol. 174, no. 319, pp. 274–278, 2012.
- [74] S. Niu, Y. Hu, X. Wen et al., "Enhanced performance of flexible ZnO nanowire based room-temperature oxygen sensors by piezotronic effect," *Advanced Materials*, vol. 25, no. 27, pp. 3701–3706, 2013.
- [75] C. Y. Lu, S. P. Chang, S. J. Chang et al., "ZnO nanowire-based oxygen gas sensor," *IEEE Sensors Journal*, vol. 9, no. 4, pp. 485–489, 2009.
- [76] Z. L. Wang, "Piezopotential gated nanowire devices: piezotronics and piezo-phototronics," *Nano Today*, vol. 5, no. 6, pp. 540–552, 2010.
- [77] L. Wu, F. Song, X. Fang, Z. Guo, and S. Liang, "A practical vacuum sensor based on a ZnO nanowire array," *Nanotechnology*, vol. 21, no. 47, Article ID 475502, 2010.
- [78] G. Hu, R. Zhou, R. Yu, L. Dong, C. Pan, and Z. L. Wang, "Piezotronic effect enhanced Schottky-contact ZnO micro/nanowire humidity sensors," *Nano Research*, vol. 7, no. 7, pp. 1083–1091, 2014.
- [79] P. H. Yeh, Z. Li, and Z. L. Wang, "Schottky-gated probe-free ZnO nanowire biosensor," *Advanced Materials*, vol. 21, no. 48, pp. 4975–4978, 2009.
- [80] Y. Liu, Z. Y. Zhang, Y. F. Hu, C. H. Jin, and L. Peng, "Quantitative fitting of nonlinear current-voltage curves and parameter retrieval of semiconducting nanowire, nanotube and nanoribbon devices," *Journal of Nanoscience and Nanotechnology*, vol. 8, no. 1, pp. 252–258, 2008.
- [81] R. Yang, Y. Qin, L. Dai, and Z. L. Wang, "Power generation with laterally packaged piezoelectric fine wires," *Nature Nanotechnology*, vol. 4, no. 1, pp. 34–39, 2008.
- [82] S. Mao, G. Lu, K. Yu, Z. Bo, and J. Chen, "Specific protein detection using thermally reduced graphene oxide sheet decorated with gold nanoparticle-antibody conjugates," *Advanced Materials*, vol. 22, no. 32, pp. 3521–3526, 2010.
- [83] C. Pan, Z. Li, W. Guo, J. Zhu, and Z. L. Wang, "Fiber-based hybrid nanogenerators for/as self-powered systems in biological liquid," *Angewandte Chemie International Edition*, vol. 50, no. 47, pp. 11192–11196, 2011.
- [84] R. Yu, L. Dong, C. Pan et al., "Piezotronic effect on the transport properties of GaN nanobelts for active flexible electronics," *Advanced Materials*, vol. 24, no. 26, pp. 3532–3537, 2012.

Research Article

Hydrothermal Growth and Hydrogen Selective Sensing of Nickel Oxide Nanowires

Thi Thanh Le Dang, Matteo Tonzzer, and Van Hieu Nguyen

International Training Institute for Materials Science (ITIMS), Hanoi University of Science and Technology (HUST), No. 1, Dai Co Viet Street, Hanoi 100000, Vietnam

Correspondence should be addressed to Thi Thanh Le Dang; thanhle@itims.edu.vn

Received 7 July 2015; Accepted 15 September 2015

Academic Editor: Thierry Baron

Copyright © 2015 Thi Thanh Le Dang et al. This is an open access article distributed under the Creative Commons Attribution License, which permits unrestricted use, distribution, and reproduction in any medium, provided the original work is properly cited.

Low cost synthesis of nanostructured metal oxides for gas sensing application at low temperature is nowadays of crucial importance in many fields. Herein, NiO p-type semiconducting nanowires with polycrystalline structure were prepared by a facile and scalable hydrothermal method. Morphology and crystal structure of the NiO nanowires were investigated by scan electron microscopy, X-ray diffraction, and transmission electron microscopy. The nanostructured material was then tested as hydrogen sensor showing very good performance in terms of sensor response, stability, absence of drifts, and speed of response and recovery. The selectivity of the NiO sensor to hydrogen towards other gases (ethanol, ammonia, and liquefied petroleum gas) was found to be good.

1. Introduction

Metal oxides are very good sensing materials. In the last decade, metal oxide nanostructures have been extensively studied in order to optimize them for several applications, including gas sensing. Semiconducting n-type metal oxides (mainly SnO₂ and ZnO) have been investigated as gas sensing material very deeper than their p-type counterparts. Recently, also p-type metal oxides are being studied, and among them nickel oxide (NiO). Tuning the size and shape of nanostructured materials is a commonly employed strategy to optimize their performance due to their structure-dependent properties [1–3]. Nanowires, one of the quasi-monodimensional (1D) nanostructures, are perfect building blocks for functional nanodevices and represent the smallest dimension for efficient electron and hole transport [4]. As an important p-type semiconductor with wide band gap energy in the range of 3.6–4.0 eV [5], NiO has been considered as a promising material due to its excellent chemical stability and pronounced electrical properties with potential applications in a wide range of fields, including catalysis [6], electrode materials for lithium ion batteries [7], photovoltaic devices [8], fuel cell electrodes, electrochemical supercapacitors [9], electrochromic films [10], magnetic materials [11], and gas sensors [12–14]. To date, various NiO nanostructures have been grown, including nanoparticles [15], nanorods [16], nanotubes [17], and nanosheets [18].

Many growth methods such as aqueous solution [19, 20], electrochemical deposition [21, 22], vapor-based metal etching oxidation method [23], and dehydration method [24] have been used to fabricate NiO nanowires. However, most of the deposition techniques used require strict parameters like high temperature, high vacuum, and complex reactions, leading to expensive processes and preventing a wide use of these materials. Compared to other methods, hydrothermal synthetic method has attracted the broadest attention for its simple operation and low power consumption.

Herein, we report on the growth of nickel oxalate hydrate (NiC₂O₄ · 2H₂O) nanowires by the hydrothermal method and their thermal decomposition during calcination at 500°C, obtaining polycrystalline NiO nanowires. Morphology and structure of the nickel oxide nanowires are characterized, and their gas sensing properties to detect hydrogen gas are investigated.

2. Materials and Methods

2.1. Synthesis of Nickel Oxide Nanowires. The NiO nanowires have been grown via a two-step deposition consisting in a hydrothermal method followed by an annealing at 500°C. All the chemicals used in our experiments were of analytical reagent grade and were directly used without further purification. In a typical procedure, 0.474 g of NiCl₂ · 6H₂O

(Sigma-Aldrich, Germany) was dissolved into a mixture of 32 mL ethylene glycol (EG, Sigma-Aldrich) and 18 mL deionized water in a beaker under continuous magnetic stirring at room temperature. Then 0.1206 g of $\text{Na}_2\text{C}_2\text{O}_4$ was added into the beaker. Half an hour of continuous magnetic stirring was carried out to ensure that Ni^{2+} ions were dispersed homogeneously in the solution. The clear solution was transferred into a Teflon-lined stainless steel autoclave of 100 mL capacity. The autoclave was sealed and heated at 200°C for 24 h. After the heating treatment, the autoclave was let cooling to room temperature naturally. The product was collected by centrifugation, washed three times with deionized water and absolute ethanol, respectively, and then dried naturally in air. As a result, a blue-green product was obtained.

The polycrystalline NiO nanowires were obtained by the calcination of this blue-green precursor, consisting in nickel oxalate hydrate ($\text{NiC}_2\text{O}_4 \cdot 2\text{H}_2\text{O}$) short nanowires, at 500°C .

The as-prepared material and the calcinated nanowires were characterized and analyzed by using X-ray diffraction (XRD), scanning electron microscopy (SEM). The XRD analysis was performed using a Bruker D5005 X-ray diffractometer with $\text{CuK}_{\alpha 1}$ radiation ($\lambda = 1.5406 \text{ \AA}$) at 40 kV and 40 mA. SEM images were obtained using a JEOL7600 scanning electron microscope at an accelerating voltage of 20 kV. Transmission electron microscopy (TEM) and electron diffraction images of the calcinated material were obtained using a JEOL JEM-2100 transmission electron microscope at an accelerating voltage of 200 kV.

2.2. Sensing Devices Fabrication. The fabrication of sensing devices consists of a 2-step procedure. First, 1 mg of as-prepared nickel oxide nanowires was dispersed in ethanol solution under ultrasonic vibration for 3 min. The solution was then dropped onto interdigitated comb Pt/Ti electrodes on thermally oxidized silicon substrate. The interdigitated Pt/Ti contacts were previously deposited onto the SiO_2/Si substrates by sputtering and conventional optical lithography technique. The whole device is $2 \text{ mm} \times 6 \text{ mm}$, while the two electrodes consisted in 18 pairs of fingers, each $800 \mu\text{m}$ long and $20 \mu\text{m}$ wide. The gap between two contiguous fingers is $50 \mu\text{m}$. After the deposition of nickel oxide nanowires, the sensor was heated to 500°C at a rate of $1.0^\circ\text{C min}^{-1}$ in a furnace and then maintained for 2 h in order to increase stability and adhesion between active material and metal electrodes.

2.3. Gas Sensing Measurements. The NiO nanowires sensing properties were measured in dynamic conditions, in which the dilution (dry air) and the tested gas were flowing continuously through the sensing chamber at a total flow rate of 500 sccm. The apparatus was home-built and included a test chamber, a sensor holder which can be heated up to 500°C , and mass flow controllers (connected to high purity calibrated bottles).

The sensors resistance was measured using a Keithley 2400 multimeter connected to a data acquisition system (LabView, National Instruments). The samples, biased with

a voltage of 5 V and operated in air, showed a good ohmic behaviour, with a negligible metal-semiconductor junction resistance. The sensor response S was defined as $S = (R_{\text{gas}} - R_{\text{air}})/R_{\text{air}} \cdot 100$, where R_{gas} and R_{air} are the resistance of the device in the presence of analyte gas (reducing) or without it, respectively. Response and recovery times are defined as the time needed to reach 90% of the response value at its maximum and to get down to 10% of it, respectively.

3. Results and Discussion

3.1. Nanowires Characterization. The hydrothermal growth produces thin nanowires with a diameter of about 60 nm. Figure 1(a) shows a SEM image of the grown material: the nanostructures are thin and straight with a constant diameter and smooth surfaces. Their aspect ratio (ratio between length and diameter) depends on the process temperature, increasing while the temperature augments. Once the material (nickel oxalate hydrate nanowires) is calcinated at 500°C for 2 hours, the nanowires morphology greatly changes, as shown in Figure 1(b).

It is clear that, after the higher temperature annealing, the nanowires material conglomerates in a series of nanoparticles which still resemble the former nanowires. The nanoparticles are roundish with a diameter in the range of 20–50 nm. A confirmation about the composition of the nanowires before and after the calcination is given by the X-ray diffraction spectra shown in Figure 2. In Figure 2(a), relative to the nanowires before calcination, all the numerous diffraction peaks can be assigned to reflections of monoclinic $\text{NiC}_2\text{O}_4 \cdot 2\text{H}_2\text{O}$ (JCPDS 25-0581). Figure 2(b), relative to nanowires after the calcination process, shows instead a well crystallized cubic NiO phase (JCPDS 47-1049). The three intense diffraction peaks at 37.3 , 43.4 , and 62.9° can be indexed to its cubic unit cell, with a lattice parameter of 4.1667 \AA . The absence of peaks for any impurity phase in both spectra of Figure 2 confirms that the nanostructures are pure crystals and that the $\text{NiC}_2\text{O}_4 \cdot 2\text{H}_2\text{O}$ precursor was completely converted to NiO during calcination.

The crystal structure of the NiO nanowires was further characterized by TEM and high-resolution TEM analysis. Figure 3(a) shows a TEM image of a bundle of NiO nanowires with diameters ranging from 40 to 70 nm; the whole bundle has a diameter of 600 nm. The high magnification TEM image reported in Figure 3(b) reveals that the nanowires are assembled from NiO nanoparticles with the diameters of 20–80 nm, with interspaces between the nanoparticles.

The spacing between lattice fringes in Figure 3(b) measures about 0.20 nm, which corresponds to the interplanar distance of (200) lattice planes of cubic NiO. The selected area electron diffraction (SAED) pattern corresponding to the nanogranular NiO nanowires is reported in Figure 3(c), displaying three diffused rings. These rings are assigned to (111), (200), and (220) diffraction lines of cubic NiO phase, respectively. These investigations reveal that the NiO nanowires are made of polycrystalline NiO with cubic structure.

3.2. Gas Sensing Properties. A voltage ranging from -5 V to $+5 \text{ V}$ was applied to the sensors to check the electrical contact

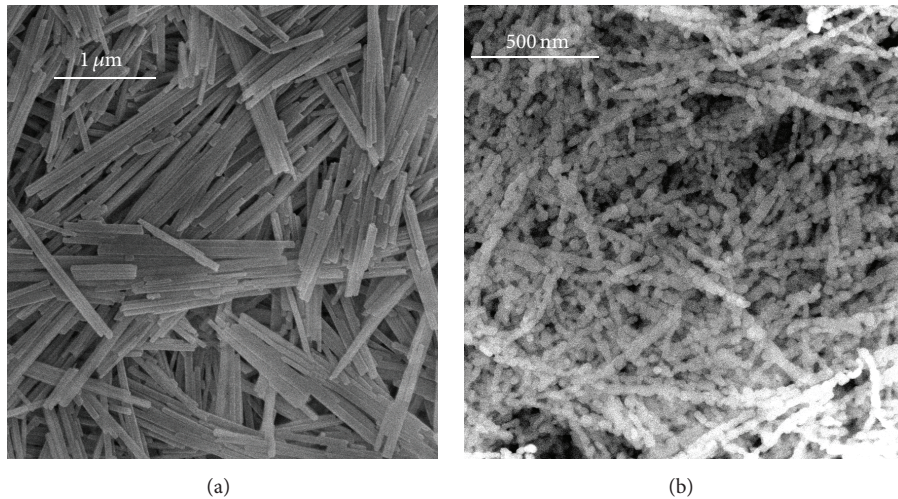


FIGURE 1: SEM images of the nanowires (a) before and (b) after the calcination at 500°C.

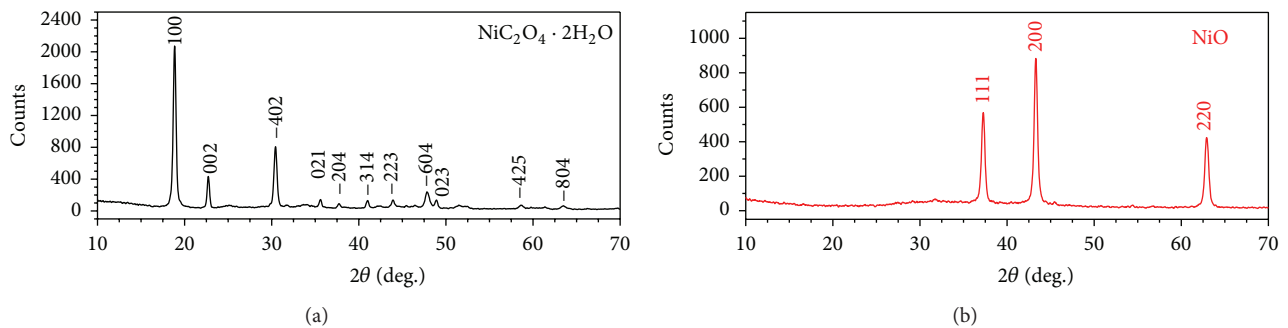


FIGURE 2: XRD spectra of nanowires (a) before and (b) after the calcination at 500°C.

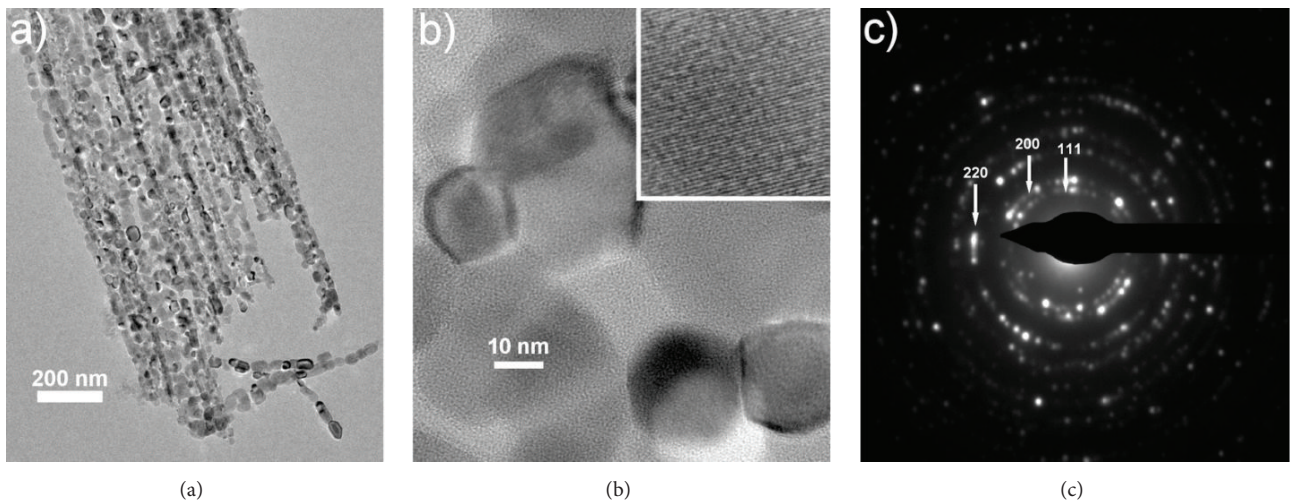


FIGURE 3: (a) TEM, (b) HRTEM, and (c) SAED images of the nanowires once calcinated. The inset in (b) shows a magnification of the lattice fringes of a nanograin.

between the active material and the metal electrodes. A very good ohmic behaviour was observed, which is important for the sensing properties since the sensor response of a conductometric device can be maximized when the metal-semiconductor connection has a negligible junction resistance. The resistance of the sensors ranged from 27 kΩ to

3 MΩ in air while the temperature increases from 200 to 400°C. The sensing performance of the NiO devices was studied at a voltage of 5 V between the electrodes while flowing different gas concentrations into the apparatus.

Figure 4 shows the dynamic resistance of a sensor to different hydrogen concentrations (50, 100, 250, 500, and

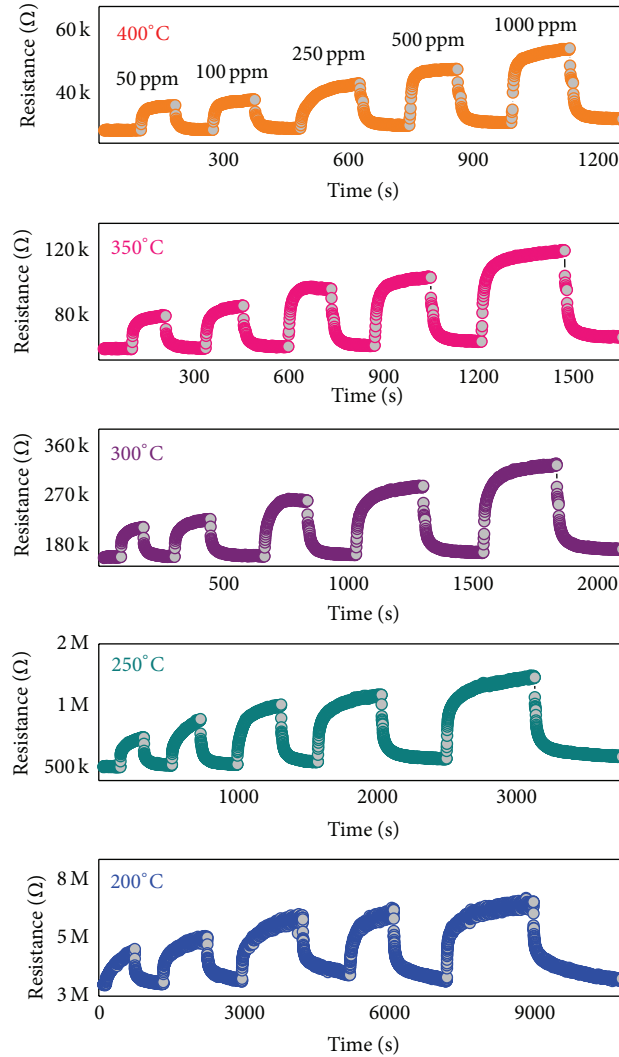


FIGURE 4: Dynamic resistance of a sensor to the injection and evacuation of different hydrogen concentrations at different sensors working temperatures. Please notice that the x -axis presents a different time scale for each plot.

1000 ppm) at different working temperatures (200, 250, 300, 350, and 400°C). All the plots show that the resistance of the NiO nanowires is stable in air and increases when hydrogen gas is injected into the system. When the H_2 flow is interrupted and replaced with air, the sensor resistance decreases to its previous value. This behavior well agrees with that of p-type semiconductor sensors. It is indeed well known that NiO is usually a p-type semiconductor when grown in “normal” conditions. When the NiO nanowires are exposed to air, oxygen molecules will be adsorbed on their surface in the form of O^- and O^{2-} . This high coverage with adsorbed oxygen particles drains electrons from the nanostructure, increasing the number of electrical holes and thus enlarging its conductivity in these base conditions. Once hydrogen is flown on the devices, its molecules interact with the adsorbed oxygen releasing the electrons used in the chemical bonds back to the nanowires bulk. This results in a decrease of holes and a rise in the sensor resistance.

As can be seen in Figure 4, the response magnitude of the sensors improves with increasing hydrogen concentration

at all working temperatures. At all temperature values, the sensor response is sharp and clear, and the recovery is very good with negligible drifts.

The response values calculated from Figure 4 are reported in Figure 5(a) as a function of H_2 concentration. At all temperatures, the sensor response improves with the increasing gas concentration, with a slope (sensitivity) that slowly decreases at high concentrations, indicating the beginning of saturation.

All the curves show a similar trend, with 200 and 250°C plots showing the highest response values. A plot of the response values towards the working temperature is indeed reported in Figure 5(b), showing that the best response is always obtained at 200°C (50 ppm H_2) or 250°C (all other hydrogen concentrations). This is a good property of NiO material compared to other metal oxides, because their sensing properties are usually best at higher temperatures [32, 33]. The lowest sensor response of NiO nanowires based sensors goes from 30.4% to 81.6% at 400°C. The best values go from 56.8% (200°C) to 106.9% (at 250°C). These values

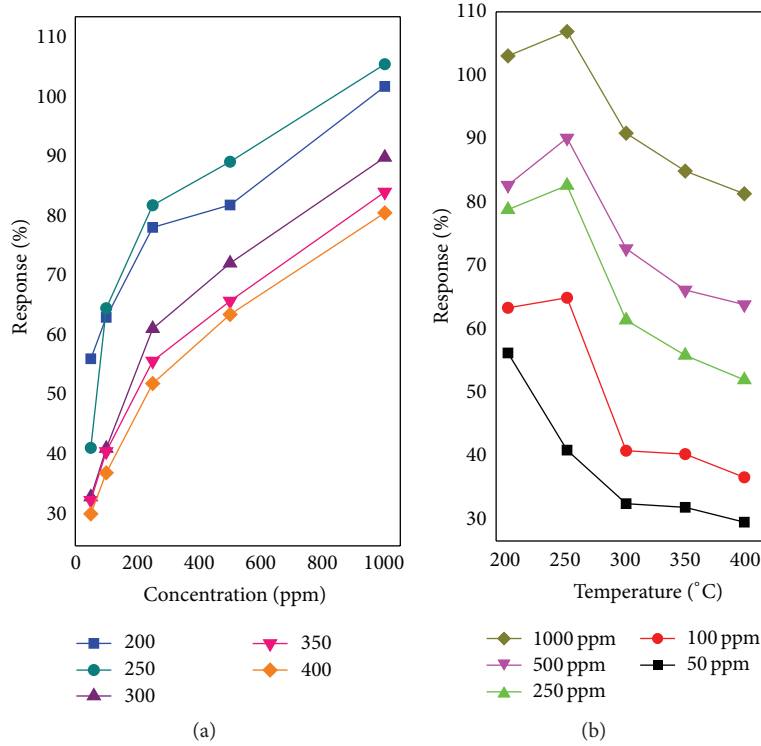


FIGURE 5: Sensor percentage response as a function of (a) hydrogen concentration and (b) working temperature.

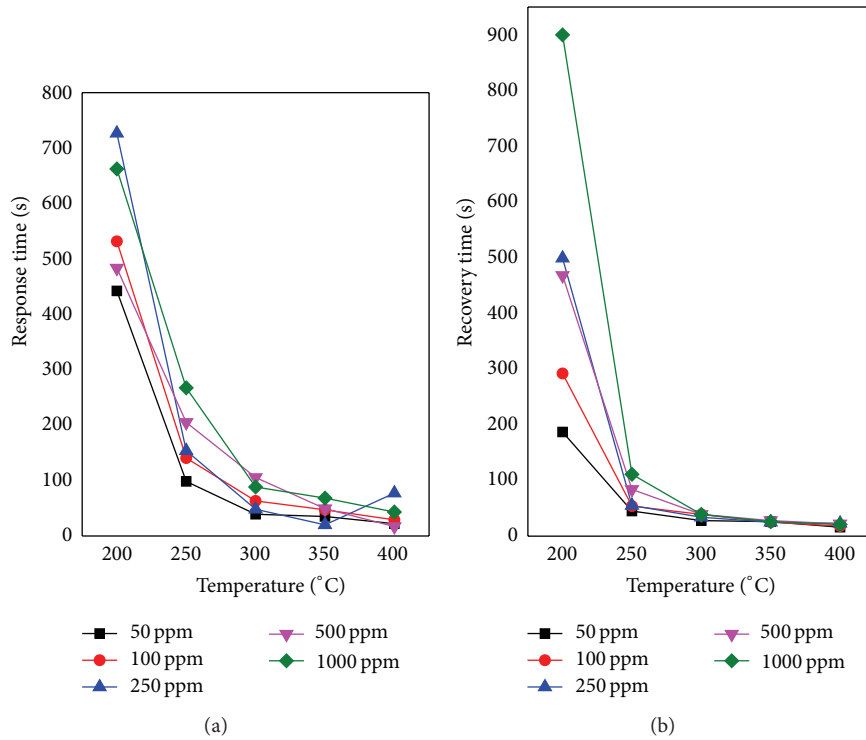


FIGURE 6: (a) Response time and (b) recovery time values as a function of working temperature for different hydrogen concentrations.

are good when compared with literature, as will be shown in Table 1.

The speed of the response and the recovery of the sensors at different gas concentrations and working temperatures, calculated from Figure 4, are presented in Figure 6.

Figure 6(a) shows response times, while Figure 6(b) shows recovery times. It is clear that both response and recovery times decrease while increasing the working temperature. There is no evident dependency on the hydrogen concentration. The response time goes from hundreds of

TABLE 1: Percentage response, response time, and recovery time values of sensors presented in this paper, compared with recent literature.

Note	Work T. [°C]	Concentration [ppm]	Percentage response [%]	Response time [s]	Recovery time [s]	Reference (year)
n-type	Thin film	30000	14	600	540	[25] (2008)
			76	900	600	
	Nanoparticle	1000	10.8			[26] (2012)
			29.6	404		
	Thin film	300	3000	45		[27] (2013)
			6000	42.5	328	
Nanoparticle	3000	150	68	328	1017	[28] (2013)
		175	62.7	200	774	
		200	49.4	243	243	
p-type	Thin film	1000	30			[29] (2015)
			3.65			
	Thin film	1000	9.1			[29] (2015)
			2000	9.5	1980	
	Nanoparticle	1000	22.25	1164	810	[30] (2012)
			32.4	134	406	
	Nanoparticle	1000	103	659	900	[31] (2012)
			107	266	111	
Nanowire	1000	107	266	111	Present work	
		91	88	39		

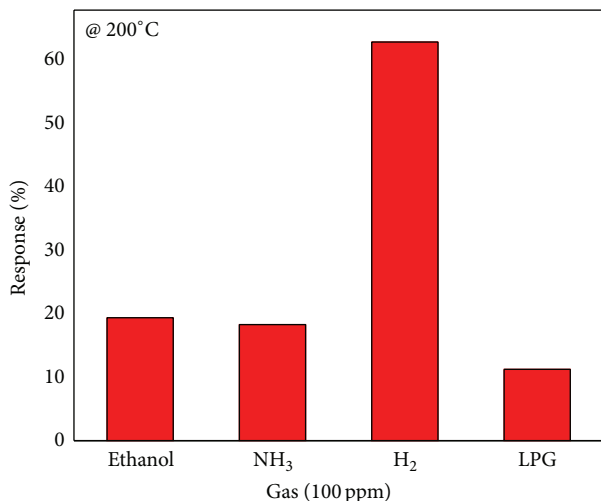


FIGURE 7: Percentage response of a sensor to 100 ppm of ethanol, ammonia, hydrogen, and liquefied petroleum gas at a working temperature of 200°C.

seconds at 200°C to few tens of seconds at 300–400°C. Similarly, the plot in Figure 6(b) shows an even steeper decrease: the recovery times go from some hundreds of seconds at 200°C down to few tens of seconds much more quickly. As can be seen in Table 1, the speed of the sensors presented in this work is good when compared with the present literature.

Selectivity of the NiO polycrystalline nanowires has been studied towards ethanol, ammonia (NH₃), and liquefied petroleum gas (LPG). All these gases behaved as reducing

gases, increasing the devices resistance upon their injection. Figure 7 reports the response value of the NiO nanogranular sensors to 100 ppm of different gases while working at 200°C. It is apparent that hydrogen gives rise to a very high response while compared to ethanol, NH₃, and LPG.

At a low temperature of 200°C, the NiO sensor gives a response of around 65% to H₂, while the response to ethanol and NH₃ is lower than 20% and that to LPG is lower than 10%. This proves that the NiO polycrystalline nanowires can be used as selective hydrogen sensors.

4. Conclusions

We have grown NiO polycrystalline nanowires via a simple and cheap process consisting in hydrothermal growth followed by high temperature calcination. The thin polycrystalline nanowires, composed by NiO nanoparticles, show very good hydrogen sensing properties with response values that exceed 100%, quick response and recovery times (down to tens of seconds at 400°C), and good selectivity to hydrogen against ammonia, ethanol, and liquefied petroleum gas.

Conflict of Interests

The authors declare that there is no conflict of interests regarding the publication of this paper.

Acknowledgments

This research is funded by Vietnam National Foundation for Science and Technology Development (NAFOSTED) under

Grant no. 103.02-2013.23 and by the Italian Ministry of Foreign Affairs and International Cooperation (MAECI) with the Project HyMN. The authors acknowledge to Laboratory of Geology, Geoenvironment and Climate Change at Vietnam National University, Hanoi for HRTEM characterizations.

References

- [1] B.-Y. Wang, D.-S. Lim, and Y.-J. Oh, "CO gas detection of al-doped ZnO nanostructures with various shapes," *Japanese Journal of Applied Physics*, vol. 52, no. 10, Article ID 101103, 2013.
- [2] M. Tonzeller and N. V. Hieu, "Size-dependent response of single-nanowire gas sensors," *Sensors and Actuators B: Chemical*, vol. 163, no. 1, pp. 146–152, 2012.
- [3] M. Tonzeller, T. T. L. Dang, N. Bazzanella, V. H. Nguyen, and S. Iannotta, "Comparative gas-sensing performance of 1D and 2D ZnO nanostructures," *Sensors and Actuators B: Chemical*, vol. 220, pp. 1152–1160, 2015.
- [4] A. Heinzig, T. Mikolajick, J. Trommer, D. Grimm, and W. M. Weber, "Dually active silicon nanowire transistors and circuits with equal electron and hole transport," *Nano Letters*, vol. 13, no. 9, pp. 4176–4181, 2013.
- [5] R. Lo Nigro, S. Battiato, G. Greco, P. Fiorenza, F. Roccaforte, and G. Malandrino, "Metal Organic Chemical Vapor Deposition of nickel oxide thin films for wide band gap device technology," *Thin Solid Films*, vol. 563, pp. 50–55, 2014.
- [6] M. A. Bhosale and B. M. Bhanage, "Rapid synthesis of nickel oxide nanorods and its applications in catalysis," *Advanced Powder Technology*, vol. 26, pp. 422–427, 2015.
- [7] B. Varghese, M. V. Reddy, Z. Y. Yanwu et al., "Fabrication of NiO nanowall electrodes for high performance lithium ion battery," *Chemistry of Materials*, vol. 20, no. 10, pp. 3360–3367, 2008.
- [8] K.-C. Wang, J.-Y. Jeng, P.-S. Shen et al., "p-type mesoscopic nickel oxide/organometallic perovskite heterojunction solar cells," *Scientific Reports*, vol. 4, article 4756, 2014.
- [9] M. Zhou, Y. Deng, K. Liang, X. Liu, B. Wei, and W. Hu, "One-step route synthesis of active carbon@La₂NiO₄/NiO hybrid coatings as supercapacitor electrode materials: significant improvements in electrochemical performance," *Journal of Electroanalytical Chemistry*, vol. 742, pp. 1–7, 2015.
- [10] J. Denayer, G. Bister, P. Simonis et al., "Surfactant-assisted ultrasonic spray pyrolysis of nickel oxide and lithium-doped nickel oxide thin films, toward electrochromic applications," *Applied Surface Science*, vol. 321, pp. 61–69, 2014.
- [11] S. D. Tiwari and K. P. Rajeev, "Magnetic properties of NiO nanoparticles," *Thin Solid Films*, vol. 505, no. 1–2, pp. 113–117, 2006.
- [12] J. A. Dirksen, K. Duval, and T. A. Ring, "NiO thin-film formaldehyde gas sensor," *Sensors and Actuators B: Chemical*, vol. 80, no. 2, pp. 106–115, 2001.
- [13] C.-Y. Lee, C.-M. Chiang, Y.-H. Wang, and R.-H. Ma, "A self-heating gas sensor with integrated NiO thin-film for formaldehyde detection," *Sensors and Actuators B: Chemical*, vol. 122, no. 2, pp. 503–510, 2007.
- [14] C. Luyo, R. Ionescu, L. F. Reyes et al., "Gas sensing response of NiO nanoparticle films made by reactive gas deposition," *Sensors and Actuators B: Chemical*, vol. 138, no. 1, pp. 14–20, 2009.
- [15] E. R. Beach, K. Shqau, S. E. Brown, S. J. Rozeveld, and P. A. Morris, "Solvothermal synthesis of crystalline nickel oxide nanoparticles," *Materials Chemistry and Physics*, vol. 115, no. 1, pp. 371–377, 2009.
- [16] N. Srivastava and P. C. Srivastava, "Synthesis and characterization of (single- and poly-) crystalline NiO nanorods by a simple chemical route," *Physica E: Low-Dimensional Systems and Nanostructures*, vol. 42, no. 9, pp. 2225–2230, 2010.
- [17] S. A. Needham, G. X. Wang, and H. K. Liu, "Synthesis of NiO nanotubes for use as negative electrodes in lithium ion batteries," *Journal of Power Sources*, vol. 159, no. 1, pp. 254–257, 2006.
- [18] Z.-H. Liang, Y.-J. Zhu, and X.-L. Hu, "β-nickel hydroxide nanosheets and their thermal decomposition to nickel oxide nanosheets," *Journal of Physical Chemistry B*, vol. 108, no. 11, pp. 3488–3491, 2004.
- [19] Y. Zhan, C. Zheng, Y. Liu, and G. Wang, "Synthesis of NiO nanowires by an oxidation route," *Materials Letters*, vol. 57, no. 21, pp. 3265–3268, 2003.
- [20] L. Wu, Y. Wu, H. Wei, Y. Shi, and C. Hu, "Synthesis and characteristics of NiO nanowire by a solution method," *Materials Letters*, vol. 58, no. 21, pp. 2700–2703, 2004.
- [21] Y. Lin, T. Xie, B. Cheng, B. Geng, and L. Zhang, "Ordered nickel oxide nanowire arrays and their optical absorption properties," *Chemical Physics Letters*, vol. 380, no. 5–6, pp. 521–525, 2003.
- [22] K. Nielsch, F. Müller, A.-P. Li, and U. Gösele, "Uniform nickel deposition into ordered alumina pores by pulsed electrodeposition," *Advanced Materials*, vol. 12, no. 8, pp. 582–586, 2000.
- [23] Z. P. Wei, M. Arredondo, H. Y. Peng et al., "A template and catalyst-free metal-etching-oxidation method to synthesize aligned oxide nanowire arrays: NiO as an example," *ACS Nano*, vol. 4, no. 8, pp. 4785–4791, 2010.
- [24] H. Pang, Q. Lu, Y. Zhang, Y. Li, and F. Gao, "Selective synthesis of nickel oxide nanowires and length effect on their electrochemical properties," *Nanoscale*, vol. 2, no. 6, pp. 920–922, 2010.
- [25] M. Stamatakis, D. Tsamakidis, N. Brilis, I. Fasaki, A. Giannoudakis, and M. Kompitsas, "Hydrogen gas sensors based on PLD grown NiO thin film structures," *Physica Status Solidi (A) Applications and Materials Science*, vol. 205, no. 8, pp. 2064–2068, 2008.
- [26] Y. Du, W. Wang, X. Li et al., "Preparation of NiO nanoparticles in microemulsion and its gas sensing performance," *Materials Letters*, vol. 68, pp. 168–170, 2012.
- [27] I. Garduño-Wilches and J. C. Alonso, "Hydrogen sensors fabricated with sprayed NiO, NiO:Li and NiO:Li,Pt thin films," *International Journal of Hydrogen Energy*, vol. 38, no. 10, pp. 4213–4219, 2013.
- [28] A. M. Soleimanpour, Y. Hou, and A. H. Jayatissa, "Evolution of hydrogen gas sensing properties of sol-gel derived nickel oxide thin film," *Sensors and Actuators, B: Chemical*, vol. 182, pp. 125–133, 2013.
- [29] I. Sta, M. Jlassi, M. Kandyla et al., "Hydrogen sensing by sol-gel grown NiO and NiO:Li thin films," *Journal of Alloys and Compounds*, vol. 626, pp. 87–92, 2015.
- [30] A. M. Soleimanpour and A. H. Jayatissa, "Preparation of nanocrystalline nickel oxide thin films by sol-gel process for hydrogen sensor applications," *Materials Science and Engineering C*, vol. 32, no. 8, pp. 2230–2234, 2012.
- [31] A. M. Soleimanpour, S. V. Khare, and A. H. Jayatissa, "Enhancement of hydrogen gas sensing of nanocrystalline nickel oxide by pulsed-laser irradiation," *ACS Applied Materials and Interfaces*, vol. 4, no. 9, pp. 4651–4657, 2012.

- [32] C. Wang, L. Yin, L. Zhang, D. Xiang, and R. Gao, "Metal oxide gas sensors: sensitivity and influencing factors," *Sensors*, vol. 10, no. 3, pp. 2088–2106, 2010.
- [33] M. Tonezzer and S. Iannotta, "H₂ sensing properties of two-dimensional zinc oxide nanostructures," *Talanta*, vol. 122, pp. 201–208, 2014.

Research Article

Research on the Preparation and Mechanism of the Organic Montmorillonite and Its Application in Drilling Fluid

Xiaolong Wang,^{1,2} Baolin Liu,^{1,2} and Peizhi Yu¹

¹School of Engineering and Technology, China University of Geosciences, Beijing 100083, China

²Key Laboratory on Deep Geo-Drilling Technology of the Ministry of Land and Resources, China University of Geosciences, Beijing 100083, China

Correspondence should be addressed to Baolin Liu; lbaolin@cugb.edu.cn

Received 6 April 2015; Accepted 7 May 2015

Academic Editor: Matteo Tonezzer

Copyright © 2015 Xiaolong Wang et al. This is an open access article distributed under the Creative Commons Attribution License, which permits unrestricted use, distribution, and reproduction in any medium, provided the original work is properly cited.

The study focused on the relation of structure, property, and application of composite prepared by organic cation intercalated montmorillonite (Mt). Herein a new kind of green and steady ionic liquid, 1-hexadecyl-3-methylimidazolium chloride monohydrate (C₁₂mimCl), was chosen as the intercalated agent. This study used molecular dynamics (MD) modeling to examine the interlayer microstructures of montmorillonite intercalated with C₁₂mimCl. The C₁₂mimCl intercalation was relatively fast with a large rate constant. The process was affected by the initial concentration of the solution; the basal spacing increased to 2.08 nm after intercalation. The coordination of electrostatic interaction and hydrogen bonding expelled water molecules out of the clay gallery and bound the layer together, which led to the dehydration of clay. The intercalation of C₁₂mimCl into Mt interlayer space affected rheology of the system and improved various properties. This organic clay composite was environmentally friendly and could be used in drilling fluid system. These models provided insights into the prediction of synthesized organic cationic-clay microstructure and guidelines for relevant engineering applications.

1. Introduction

Montmorillonites (Mts) are clay minerals with regular layer structure composed of octahedral sheet between two tetrahedral sheets. Intercalating organic and inorganic species into layered host materials has drawn researchers' increasing interests. It is an effective way to construct ordered inorganic-organic and inorganic-inorganic assemblies with unique microstructures and properties [1, 2]. The montmorillonite's group of clay minerals provides attractive features, including large surface area, swelling behavior, adsorption, and ion exchange [3, 4]. The intercalated single layer nanosized Mt particles (0.6–1 nm in width) are ideal dispersing additives for the synthesis of organic-inorganic hybrid nanocomposites to enhance mechanical, thermal, and chemical stabilities. Montmorillonites have been extensively used as the host materials and in other possible ways because of their attractive properties and ability to accommodate various kinds of organic and inorganic guest species [5].

Numerous reports about studies and applications on organics modified Mt have been published, while few work has been reported on the application of geological drilling fluids [6, 7]. Water-based drilling fluid system is composed of clay, water, and treatment agent. Mt is a significant mineral material to adjust rheology and fluid loss of drilling fluid. As a drilling fluid material, organic Mt has excellent rheology and viscosity [8]. The drilling slurry, mainly composed of Mt, is used for protecting wall, clearing away cuttings, and cooling drill.

In oil-well drilling, bentonite is added in drilling fluids for viscosity control, to aid the transfer of cuttings from the bottom of the well to the surface, and for filtration control to prevent filtration of drilling fluids into the pores of productive formations [9]. Compared to water-based drilling fluid, oil-based drilling fluid has many inherent advantages, including excellent clay inhibition, wellbore stability, lubricity, antiaccretion property, temperature stability, tolerance to contamination, and corrosion protection [6]. The high clay

solids content in drilling fluid has several adverse effects: (1) greatly reduces the rate of penetration [7]; (2) increased chances of differential sticking; and (3) is the major cause of excessive torque and drag [10]. Thus, low bentonite content is desired to control the total amount of solids. At low concentration, bentonite clay is unable to provide satisfactory rheological properties required for optimum performance in oil-well drilling. Hence, polymers are added to achieve the desired result. In addition, if dispersion and rheological property of organic Mt are poor, highly flocculating and its presence in the mud can adversely affect rheology and filtration control [8].

Most commonly, Na-montmorillonite is used as the base clay and its sodium cations can be exchanged with quaternary ammonium cations [11, 12]. QAC-coated montmorillonite exhibits higher zeta potential [13], enhanced strength, lower compressibility, and stronger retention of organic compounds [14, 15] in the environment, yielding a variety of potential applications in the waste containment, landfill liners, and slurry walls [16–19]. Because of low saturated vapor pressure of quaternary ammonium surfactants and potential toxicity to environment, the application of surfactants is restricted.

Ionic liquids are composed solely of ions. Since they are nonvolatile, nonflammable, highly conductive, and chemically and thermally stable, they can be used in catalysis, electrochemistry extraction and other technological applications [20]. This new technology, so-called supported ionic liquid phase (SILP) catalysis, combines the advantages of ionic liquids with those of a heterogeneous material supported on the solid phase, resulting in materials of low toxicity, which are environmentally benign and have a wide range of applications [21–24]. Ionic liquid modified clays have recently been paid attention to due to their unique properties, such as negligible vapor pressure, no flammability, and electrical conductivity. Ionic liquids are all favorable for fabricating the inorganic clay-organic intercalation compounds with a high thermal stability or compositing materials with an improved flame retardant property.

In the present work, C_{12} mimCl is used as intercalant agent for montmorillonite. X-ray diffraction (XRD) technique is used to study properties of the modified montmorillonite. The cation exchange capacity of modified montmorillonite is also measured and the obtained result proves that the intercalation is successful. Based on these experimental results, molecular dynamics simulation on intercalation process of using C_{12} mimCl as intercalant agent for montmorillonite is conducted.

2. Materials and Methods

2.1. Materials. The montmorillonite (Mt) used was obtained from the Clay Mineral Repositories in Purdue University (West Lafayette, IN) without further purification. It had a chemical formula of $(Ca_{0.12} Na_{0.32} K_{0.05})[Al_{3.01} Fe(III)_{0.41} Mg_{0.54}][Si_{7.98} Al_{0.02}]O_{20}(OH)_4$, a cation exchange capacity (CEC) of 85 ± 3 mmol_c/100 g [25], a layer charge of 0.32 eq/mol per $(Si, Al)_4O_{10}$ [26], an external surface area

(ESA) of 23 m²/g [27], and a mean particle size of 3.2 μm with a d_{25} to d_{75} in the range of 3~10 μm.

The 1-dodecyl-3-methylimidazolium Chloride monohydrate (CAS#: 114569-84-5, C_{12} mimCl), was obtained from Shanghai Darui Fine Chemical Co. Ltd. (Shanghai, China). They had pKa values of 7.08 ± 0.1 , calculated on ACD online services website, due to protonation of both nitrogen atoms. When the solutions' pH value was less than 5.2, C_{12} mimCl exists as C_{12} mimH⁺; when pH value was between 5.2 and 9.2, its existence would change to monovalent cation and neutral molecule, and when pH value was above 9.2, it would be of nonion form.

2.2. Methods. The initial C_{12} mimCl concentrations varied from 10 to 5000 mg/L for the adsorption isotherm study. The mass of Mt used was 0.2 g while the volume of solution used was 25 mL for all studies except the kinetic study. The solid and solution were combined in each 50 mL centrifuge tube and shaken for 2 h at 150 rpm. All experiments, except kinetic experiment, were performed at room temperature. After the mixtures were centrifuged at 10000 rpm for 20 min, the supernatants were filtered through 0.22 μm syringe filters before being analyzed for equilibrium C_{12} mimCl concentrations.

The equilibrium C_{12} mimCl concentrations were analyzed with a UV-Vis spectrophotometer (Model T6 New Century 1650, made by General Instrument, Inc. LLT, Beijing China) at the wavelength of 210 nm, corresponding to its maximal absorbance. Calibrations were made using standards of 10, 20, 30, 40, 50, and 60 mg/L with a regression coefficient of 0.9998. The amount of C_{12} mimCl adsorbed was calculated from the difference between the initial and final concentrations.

Powder XRD analyses were performed on a Rigaku D/max-III A diffractometer (Tokyo, Japan) with a Ni-filtered $CuK\alpha$ radiation at 30 kV and 20 mA. Orientated samples were scanned from 3° to 10° at 2°/min with a scanning step of 0.01°. The changes in the XRD peak positions reflected the hydrated size of the metal cations in the interlayer space of Mt.

FTIR spectra of samples were collected on a Nicolet-560 spectrometer (Thermal Nicolet Co., USA) from 400 to 4000 cm⁻¹ with a nominal resolution of 4 cm⁻¹. For each spectrum 16 runs were collected and averaged. The Mt specimens were prepared by adding approximately 1% of the sample powder to dry KBr powder.

The water contact angle (CA) and sliding angle (SA) were measured at ambient temperature with a SL200B apparatus from ZhongChen Digital Equipment Co. Ltd., Shanghai. The CAs reported here were the mean values measured with ca. 5 μL water droplets at five different positions on each sample. The samples used were shaped into a circle piece using a tablet machine under 15 Mpa at room temperature.

Thixotropic loop area of the composite material was tested by Rotational Rheometer (RotoVisco1), Thermo Fisher Scientific Company, and viscosity was tested by Digital Viscometer (SNB-3), Shanghai Jingtai Electronic Instrument Co., Ltd. Thixotropy meant gels or fluids get thin or less viscous when stirred or under some mechanical action and back to thick or static condition after being placed for a certain time. At a certain shear speed, the shear stress acting

on a thixotropic system lowered as time was getting longer. The experiment used reading value of Viscometer after 10 s of start as the viscosity of composite material, shearing and recovering both taking for 3 min. It was solution of C_{12} -Mt, Xylene as solvent, and the concentration was 3%. Thixotropic ring method was used for recording viscosity of paint successively during speed of viscometer which increased (shearing) then decreased (recovering), drawn into a reciprocating curve. Flow curve of composite material was determined by HAAKE RotoVisco1 rheometer, with shear rate range of upstream $0\text{ s}^{-1}\sim 200\text{ s}^{-1}$, downstream $200\text{ s}^{-1}\sim 0\text{ s}^{-1}$, up and down each 3 min, thermostat 25°C . Automatically fit the measured data by the computer, drew the shear stress and shear rate curve, integral calculated the area of thixotropic loop between ascending and descending curve.

2.3. Computation Details. Molecular simulation was performed under the module "CASTEP" of Materials Studio 6.0 software to investigate the sorption sites of Na^+ on Mt. The primitive unit cell of Mt was optimized with the generalized gradient approximation (GGA) for the exchange-correlation potential (PW91) which was appropriate for the relatively weak interactions present in the models studied. The resulting primitive unit cell was characterized by the parameters $a = 15.540\text{ \AA}$, $b = 17.940\text{ \AA}$, $c = 12.56\text{ \AA}$, and $\alpha = \gamma = 90^\circ$, $\beta = 99^\circ$. Based on the primitive unit cell, a series of $(3 \times 2 \times 1)$ super cells were built.

In order to investigate the intercalated mechanism of $C_{12}\text{mim}^+$ in pure Mt layer, simulated annealing algorithm was used to perform canonical Monte Carlo (MC) simulation with $C_{12}\text{mim}^+$ simulated as adsorbate on the layer of pure Mt. The number of cycles was 3 and the steps of one cycle was 10^6 a representative part of the interface devoid of any arbitrary boundary effects. Based on the structure of the preferential adsorption model of $C_{12}\text{mim}^+$ in the layer of Mt predicted by MC calculation, GGA-PW91 was used to optimize the structure again and to predict the interaction energy between $C_{12}\text{mim}^+$ and Mt layer to a greater accuracy. All of the GGA-PW91 calculations were performed using a double numerical plus polarization function (DNP) as basis set and DFT-D correction. So all calculations, the heavy atoms of Mt were frozen, whereas the hydrogen of Mt, cationic molecules was fully relaxed.

3. Results and Discussion

3.1. Amount of $C_{12}\text{mimCl}$ Intercalated into the Mt. The reaction time (Figure 1(a)) and initial concentration (Figure 1(b)) of solution were two important factors affecting Mt's intercalation by $C_{12}\text{mimCl}$. It was a rapid process of organic cations intercalated into Mts; half of maximum amount of intercalation could be reached in 5 min, while full maximum amount of intercalation would be achieved in 20 min. It was similar to organic cations adsorbed or intercalated clay minerals. Organic cations intercalating Mt were mainly of cations exchange in accordance with the second-order kinetic equation.

The kinetic study aimed to investigate the time needed to reach equilibrium for intercalation with $C_{12}\text{mimCl}$ so that

future studies could be unified into a fixed time by which equilibrium would be established. Intercalation of $C_{12}\text{mimCl}$ into Mt was instantaneous (Figure 1(a)). The experiment data were fitted to several kinetic models and the pseudo-second-order kinetic was confirmed by fitting t/q_t (where q_t was amount of $C_{12}\text{mimCl}$ removed, t denotes time) into a straight line [28]. The coefficient of determination r^2 was 0.999 for both Mts. For Mt intercalated with $C_{12}\text{mimCl}$, an initial rate of 132 mmol/g h , a rate constant of 254 g/mmol h , and q_e , the amount of $C_{12}\text{mimCl}$ adsorbed at equilibrium, of 0.21 mmol/g were obtained. The instantaneous Mt intercalation with $C_{12}\text{mimCl}$ suggested a great affinity of $C_{12}\text{mimCl}$ for Mt surfaces. Thus, for the intercalation with cationic drugs, such as $C_{12}\text{mimCl}$ from water, swelling clays-like Mts offered a great advantage due to their larger initial rate, rate constants, and higher capacity.

Initial concentration of solution had a profound influence on the amount of intercalation (Figure 1(b)). The intercalation amount of $C_{12}\text{mimCl}$ to Mt increased as the concentration of solution increased. When the concentration of $C_{12}\text{mimCl}$ was $10\sim 2000\text{ mg/L}$, the rate of intercalation increased sharply. When concentration was above 2000 mg/L , it increased slowly. After intercalation reached the balance point at 5000 mg/L concentration, the intercalation amount of $C_{12}\text{mimCl}$ to Mt did not change. At last, maximum amount of intercalation was 0.75 mmol/g . As the basal spacing increased because of intercalation, it followed that hydrophobic and repel force among alkyl chains of organic cations cause organic cations to intercalate into layers of Mt. The quantity of the organic cations entered into Mt's layer was larger than that was swapped out. Klebow and Meleshyn discussed this problem in one of their papers [29], and the extra charge could be offset by the absorption of the negative ion from the solution on the surface of montmorillonite [30, 31].

3.2. Performance of $C_{12}\text{mimCl}$ Intercalated into the Mt. With the ion exchange of the sodium ion for the $C_{12}\text{mim}^+$, expansion of the Na-Mt layers occurred. This expansion was readily measured by XRD. Modified by the $C_{12}\text{mimCl}$, the basal spacing of the Mt was expanded; the basal and basal spacing were observed for the different clays (Figure 2). The trend for the basal spacing d_{001} was the same as that in the basal spacing. The differences between the organo-Mt were due to the different incorporation and arrangement of the surfactants.

$C_{12}\text{mimCl}$ exchanged Na^+ ion in Na-Mt interlayer, leading to obvious increase in d_{001} value of Mt. The raw Mt and Mt equilibrated with 1000 mg/L of $C_{12}\text{mimCl}$ were further analyzed from 3° to 10° . The information of $C_{12}\text{mimCl}$ intercalating towards Mt could be obtained more directly by examining the change of basal spaces from XRD results (Figure 2(a)). Mt's basal space was $14.34\sim 14.59\text{ \AA}$ under the intercalating time ranging from 5 min to 18 h, with no obvious difference. This result demonstrated that the intercalation balance under this concentration could be reached in 5 min, which was consistent with the experiment data.

The basal space for $C_{12}\text{mimCl}$ intercalated Mt would change according to the change in amount of $C_{12}\text{mimCl}$ and

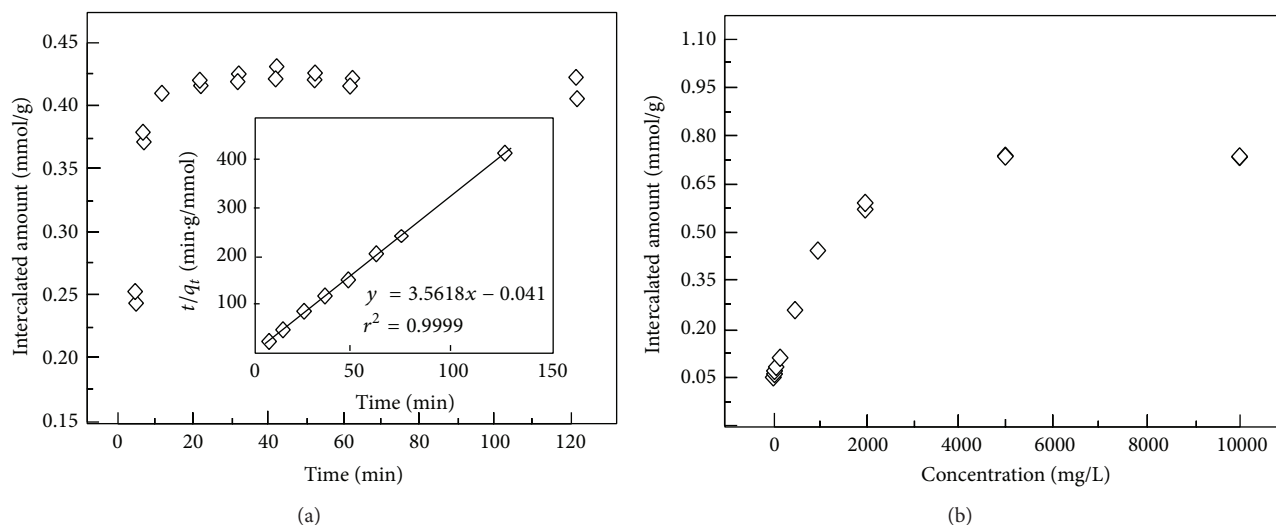


FIGURE 1: Kinetics of $C_{12}mimCl$ intercalated into Mt (a). The solid line is pseudo-second-order fit to the observed data. Inserts are plot of t/q_t against t for Mt. Effect of $C_{12}mimCl$ concentration on intercalated quantities (b).

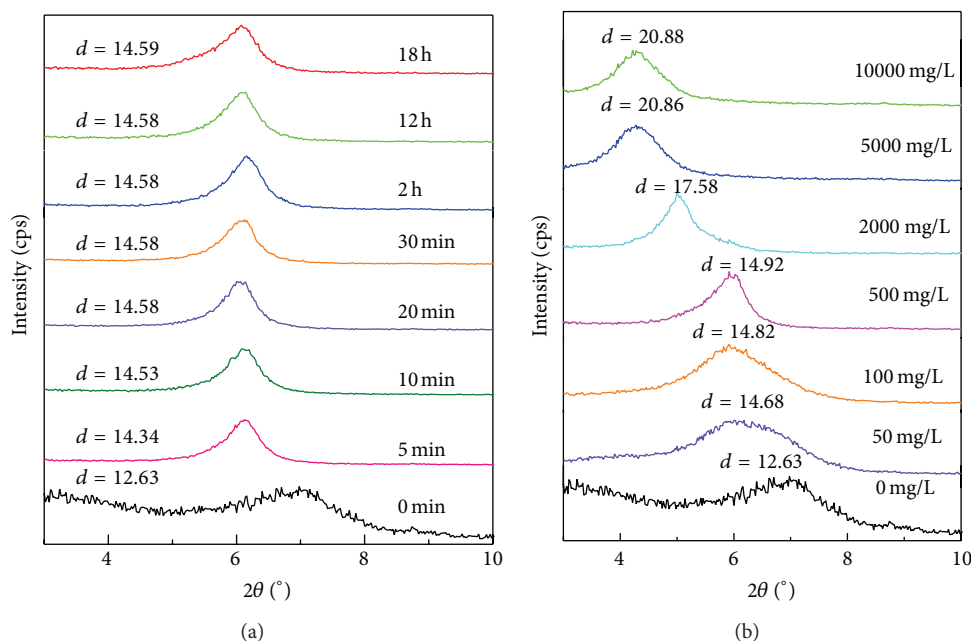


FIGURE 2: X-ray diffraction patterns of Mt before and after equilibrated at different contact time (a) and initial concentrations (mg/L) (b) of $C_{12}mimCl$ ($d/\text{\AA}$).

the way they arranged themselves in the interlayer. The XRD results (Figure 2(b)) showed that the d_{001} value remained at 14.92 \AA as the initial concentration changes from 10 mg/L to 500 mg/L, which was larger than unmodified Mt by 2 \AA . As the initial concentration increased, the amount of $C_{12}mimCl$ intercalated into Mt increased and its configuration in the interlayer changed as well. At concentration of 5000 mg/L, basal spacing of Mt expanded to 20.88 \AA . The basal spacing reached the maximal value and would not change as the concentration increases.

Vibrational spectroscopy had been extensively used to probe the local environments of cationic surfactants in the basal space of Mt [32–35]. FTIR studies had revealed detailed correlation of the spectra with structural features. The position, splitting, and intensities of methylene stretching modes in the FTIR spectra had been acknowledged as useful indices in the study of conformation of alkyl chain assemblies [36–39].

FTIR spectra of before and after $C_{12}mimCl$ intercalated Mt displayed formation and breakage of chemical bond were

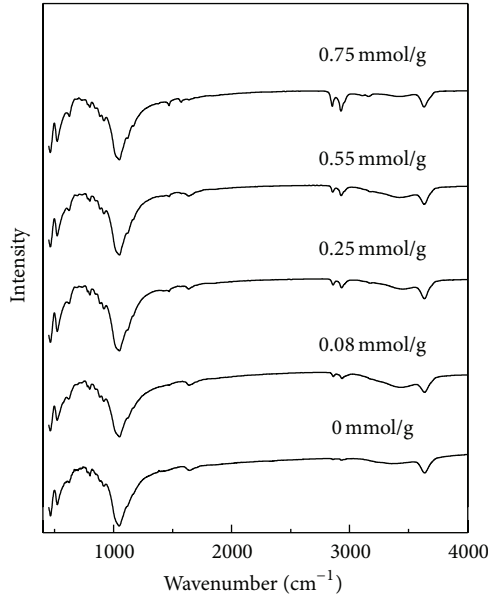


FIGURE 3: FTIR analyses of Mt intercalated with $C_{12}\text{mimCl}$.

clear in Figure 3. Only one variation in $2850\sim 3000\text{ cm}^{-1}$ was detected when scanning in $450\sim 4000\text{ cm}^{-1}$. The FTIR absorption bands at $3000\text{ to }2850\text{ cm}^{-1}$ were attributed to the symmetric CH_2 stretching ($\nu_s(\text{CH}_2)$) and antisymmetric ($\nu_{as}(\text{CH}_2)$) modes. It had been well established that the frequencies of the CH_2 stretching bands of hydrocarbon chains were extremely sensitive to the gauche/trans conformer ratio of the hydrocarbon chains [32, 39]. Only when the chains were highly ordered (all-trans), the narrow absorption bands appeared around $2850\sim 2885\text{ cm}^{-1}$ and $2921\sim 2965\text{ cm}^{-1}$ in the infrared spectrum. $1450\sim 1480\text{ cm}^{-1}$ and $1550\sim 1600\text{ cm}^{-1}$ were C=C stretching vibration of absorption valley. We explain that $C_{12}\text{mim}^+$ has been intercalated into the Mt layers. If conformational disorder was included in the chains, their frequencies might shift upward or downward, depending upon the average content of gauche conformers [34].

The contact angle of a material could probe whether it was hydrophobic or hydrophilic: When the contact angle $\leq 90^\circ$, it was hydrophilic. And when contact angle $\geq 90^\circ$, it was hydrophobic. For Mt, the contact angle increased as the amount of intercalation increased. The contact angle of Mt is 48° before being intercalated. As the concentrations of the solution were 50, 100, 500, and 10000 mg/L, the contact angle was 54° , 59° , 63° , and 72° , respectively (Figure 4).

To clay used in drilling fluid, good thixotropy and rheology were necessary. Thixotropy of Mt and organic modified Mt were compared to study application performance of Mt. Table 1 showed parameters of structure and property of $C_{12}\text{minCl}$ modified Mt. It could be found that after being modified by $C_{12}\text{minCl}$, d_{001} value of Mt increased from 1.26 nm to 2.08 nm and colloidal rate increased from 5 to 46. The increase in thixotropy was performed as increasing thixotropic ring area and thixotropic index. Because $C_{12}\text{minCl}$ entered interlayer region of Mt, Mts with expanded interlayers were easier to swell than unintercalated

TABLE 1: Performance parameters of Mt and organic Mt.

Concentration of $C_{12}\text{minCl}$ (mg/L)	Viscosity curve	Contact angle pattern ($^\circ$)	Viscosity (mPa·s)	d_{001} (\AA)
0 mg/L	—	48	—	12.63
50 mg/L	25	54	22.8	14.68
100 mg/L	36	59	29.0	14.82
500 mg/L	44	63	36.3	14.92
2000 mg/L	51	67	43.4	17.58
5000 mg/L	58	71	49.3	20.86
10000 mg/L	58	72	49.8	20.88

Mt raw material. At stirring condition of drilling fluid, a “house of cards” structure had been formed by layers and it provided better thixotropy. Increasing contact angle indicated increased organic degree of Mt (lipophilicity-hydrophobicity). Mt material was more compatible to drilling fluid at a higher organic degree, whose thixotropy was easier to be utilized. As intercalation amount of $C_{12}\text{minCl}$ to Mt increased, basal spacing, thixotropic index, and thixotropic ring area of Mt increased and it had a better thixotropy. Figure 5 was thixotropic curve of organic Mt as concentration of $C_{12}\text{minCl}$ increased. As intercalation amount of $C_{12}\text{minCl}$ increased, the curve became smoother and enclosed area was bigger than unmodified Mt. In addition, viscosity of organic Mt was another important parameter to express performance of drilling fluid system. Viscosity of organic Mt increased as organic degree increased, but in application it should be kept about $40\sim 60\text{ MPa}\cdot\text{s}$, for excessive viscosity had an impact on mobility. Therefore, viscosity, rheology, contact angle, and thixotropic ring area should be considered for the application of Mt in drilling fluid. In conclusion, various performances of Mt had been improved after $C_{12}\text{minCl}$ modification and it could be used as an environmentally friendly and effective composition of drilling fluid [23, 24, 40].

3.3. Molecular Dynamics. The research simulated the interlayer $C_{12}\text{minCl}$ ion’s interaction with Mt layers, amount of intercalation and its arrangement. After working out size of unit cell and basal spacing from the amount of intercalation, it could be calculated that numbers of intercalated $C_{12}\text{minCl}$ is 4 (Figure 6). Their arrangements were as follows: The $C_{12}\text{min}^+$ molecules arrange in bilayers parallel to Mt layers. The obtained results were in good agreement with the experiment. When $C_{12}\text{minCl}$ was located in interlayer, N^+ of pentagonal ring was close to oxygen of silicon-oxygen tetrahedron in Mt layer and the alkyl chain of another $C_{12}\text{minCl}$ and forms a cross-pattern. As electrostatic field of N^+ acted on alkyl chain of $C_{12}\text{minCl}$, the amount of intercalation exceeds CEC value of Mt. The amount of $C_{12}\text{minCl}$ intercalating into Mt reaches 1.2 times of CEC value of Mt.

The energies before and after $C_{12}\text{minCl}$ intercalating Mt were different due to the vector sum of the interaction force, which existed among organic cations themselves, organic cations, and layers and determines the final energy. In addition, the bond length and angle of organic cation to oxygen hexagonal ring of silicon-oxygen tetrahedron in Mt layer

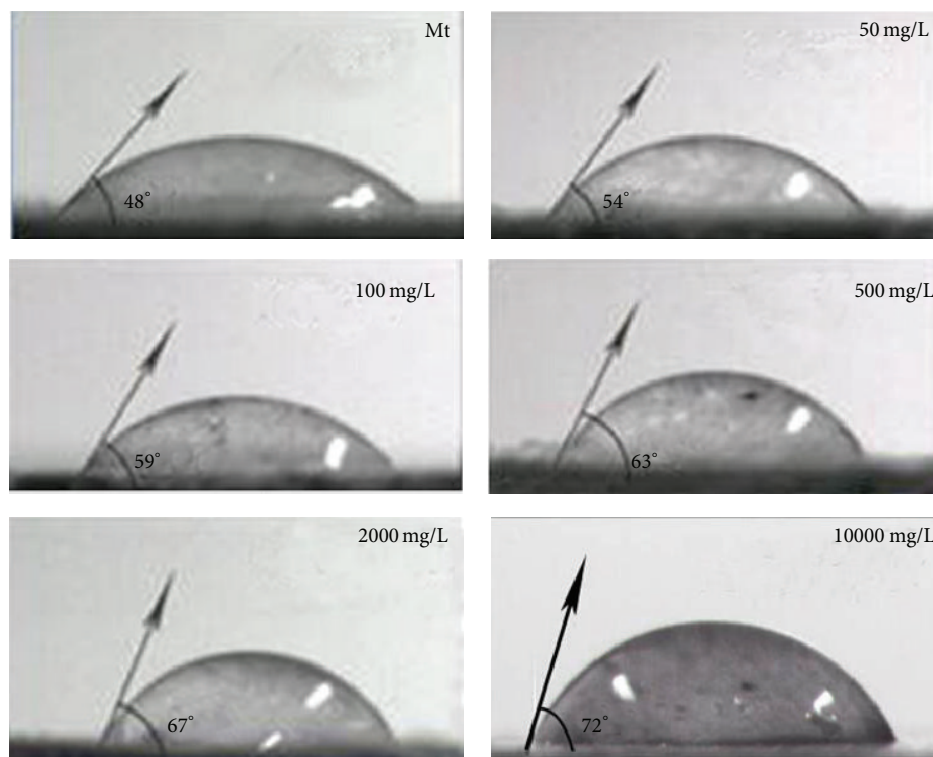


FIGURE 4: Contact angle pattern of Na-Mt and the organic Mt samples.

affected the arrangement of $C_{12}mim^+$ ions in Mt interlayer. In the simulation process, two $C_{12}mimCl$ were put into interlayer without H_2O , in consideration of the interaction between organic cations and layers.

The headgroup of the $C_{12}mimCl$, which carried the positive charge of the organic cation, was attracted to the clay surface via electrostatic forces ($C_{12}mimCl$ head and mineral interface were shown in Figure 7). Figure 7 of the clay surface oxygen versus $C_{12}mim^+$ nitrogen indicates that the minimum distance of $C_{12}mim^+$ nitrogen to the surface oxygen was 3.121 Å. The minimum distances of H ($-CH_3$) in $C_{12}mim^+$ to O in silica-tetrahedron were 2.071 Å, which were smaller than 2.5 Å. It should be addressed that the interaction force of H and O in $C_{12}mim^+$ was bigger than that of N^+ and O. The N^+ atom of $C_{12}mimCl$ molecule played the most dominant role in the stabilization and the localization of the molecule in the basal space. Take the intercalating mode of $N-CH_3$ group form hydrogen bonds with nearby two upright $-N-O$ groups of the tetrahedron Si sheet with the O-N-O angles of 45.18° (Figure 7). In contrast to previous observations for the $R-N^+-CH_2$ group, no hydrogen bond was formed between the N^+ methyl group (CH_3) and the clay surface oxygen, which also indicated that the $C_{12}mim^+$ headgroup could have lateral rearrangement across cavities [41]. However, comparing the $N-CH_3$ head group with carbon tails, the simulation results indicated that the $C_{12}mim^+$ head could be considered as an immobile phase near the clay surface, when compared with the nonpolar carbon tails, which was in agreement with what had been reported by Heinz et al. [42].

In Section 3.1, it had been established in the contact angle discussion that Mt became hydrophobic after being intercalated with $C_{12}mim^+$ and there were no free water molecules in the interlayer after drying process at low temperature. However, the intercalation of Mt with organic cations occurred in solution, which meant that water molecules could enter the interlayer of Mt and interacted with $C_{12}mim^+$ (Figure 8). Interaction between $C_{12}mim^+$ and water deserved further discussion. In order to prove the theory above, a simulation was conducted. To simplify the model, one $C_{12}mim^+$ with 10 water molecules around were arranged in the interlayer of Mt to simulate the state in solution and to discuss the interaction between $C_{12}mim^+$ and water molecules. The closest distance between N^+ in $C_{12}mim^+$ and the oxygen in silicon-oxygen tetrahedron was 4.614 Å, so $C_{12}mim^+$ could not form chemical bond with oxygen in silicon-oxygen tetrahedron. The interaction between $C_{12}mim^+$ and water molecules was also weak because the closest distance between N^+ in $C_{12}mim^+$ and the oxygen in water molecules was 4.058 Å. The distance between alkyl chains in $C_{12}mim^+$ and oxygen in water was more than 5 Å, indicating totally hydrophobic. Therefore, in organic environment, intercalation with organic cations could change the interlayer of Mt from hydrophobic to hydrophilic.

4. Conclusions

$C_{12}mimCl$ had been successfully intercalated into the interlayer of Mt. Molecular dynamic simulation was used to study the effect of initial concentration and time on the

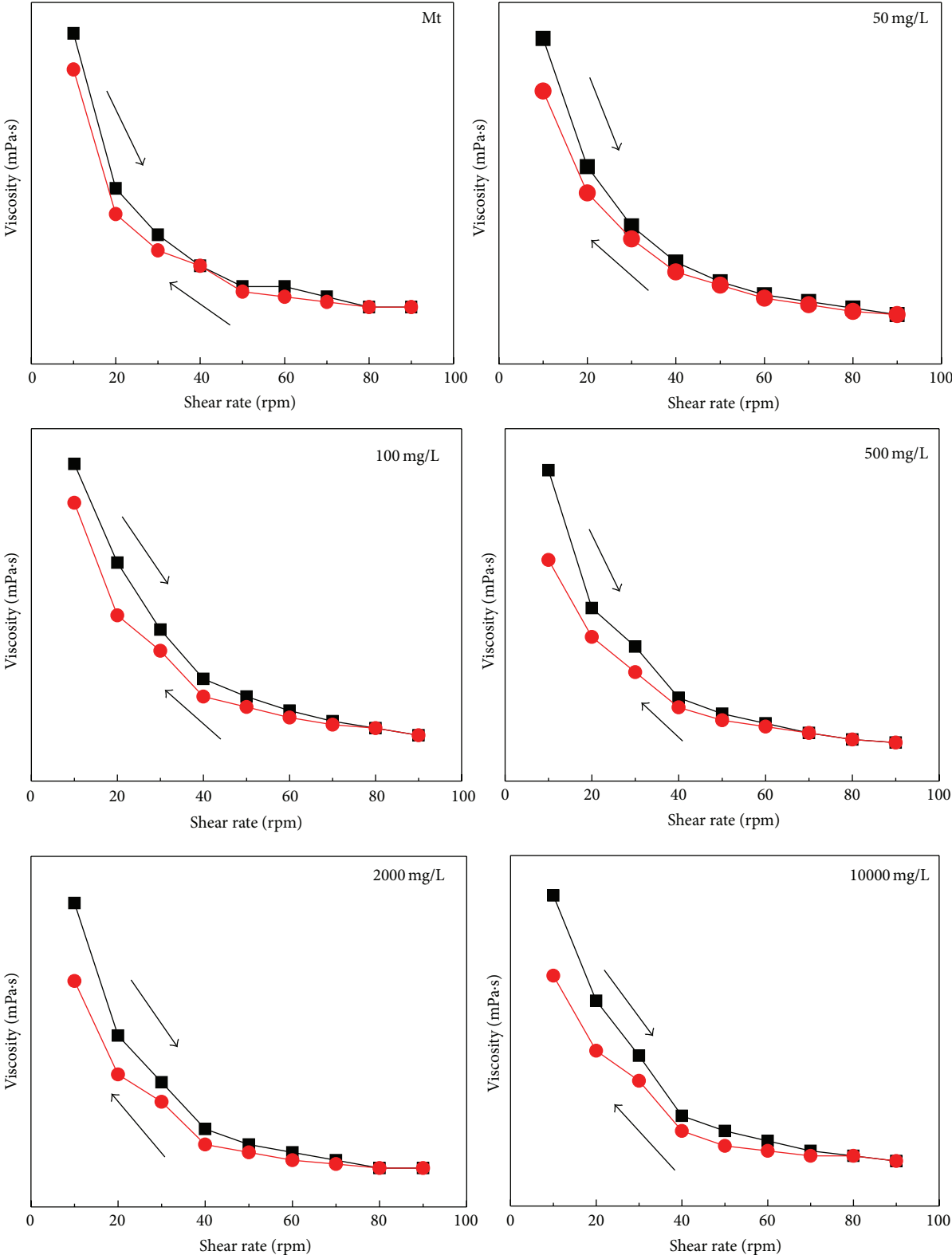


FIGURE 5: Viscosity curve of Mt and organic Mt.

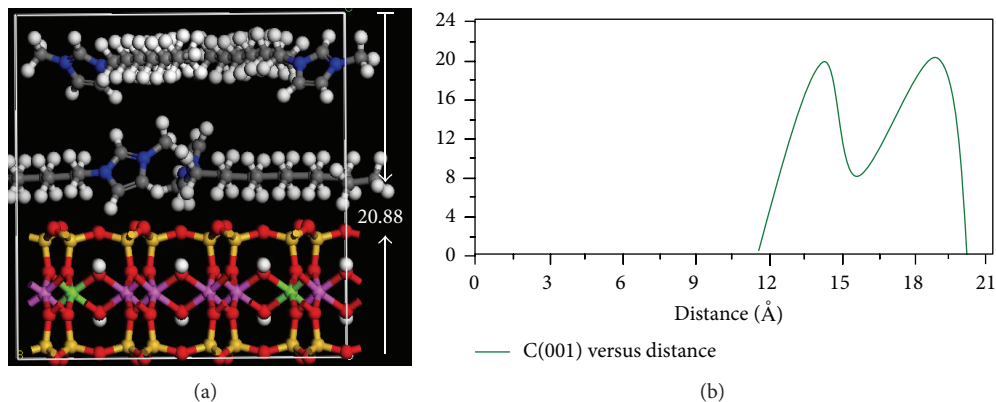


FIGURE 6: Molecular dynamic simulation of intercalation of $C_{12}mimCl$ into Mt (a). $C_{12}mimCl$ molecules (b) from the origin. For all species, C = gray, N = blue, H = white, O = red, Si = yellow, Al = purple, and Mg = green.

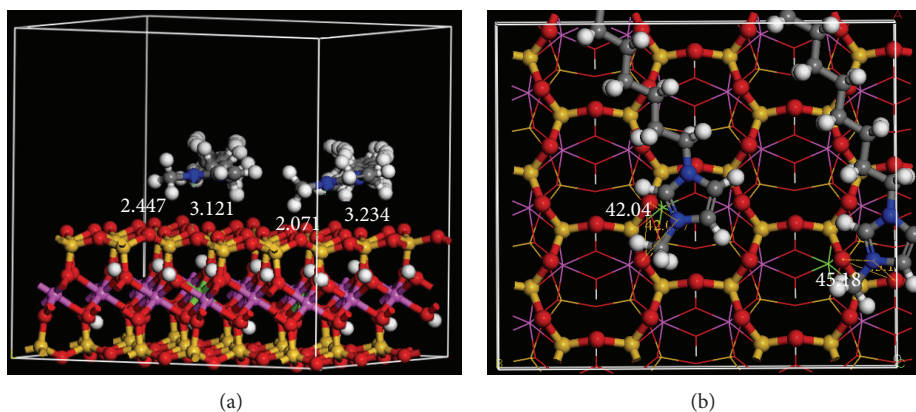


FIGURE 7: Molecular dynamic simulation of the distance (a) and angle (b) of $C_{12}mim^+$ and $[SiO_4]$.

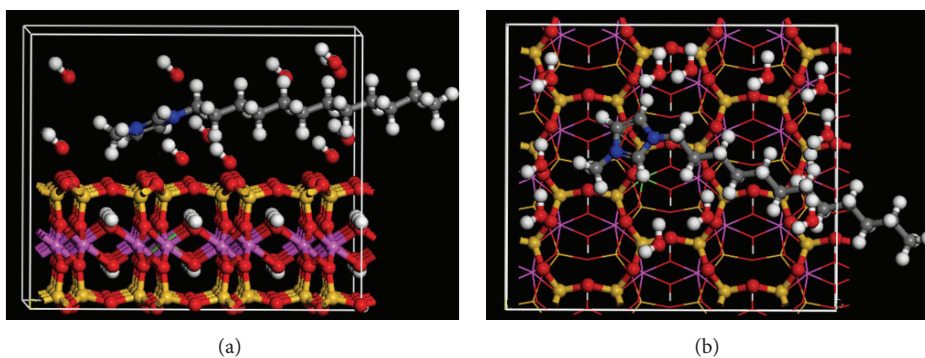


FIGURE 8: Molecular dynamic simulation of the distance of $C_{12}mim^+$ with $[SiO_4]$.

intercalation process. The intercalation processes were rapid and could reach the equilibrium in 5 min. Overall results confirmed that for different amount of organic loading, the interlayer organic carbon would have a different configuration, including lateral monolayers, lateral bilayers, and paraffin structure. They were in agreement with previous observations. The mechanisms of $C_{12}mimCl$ intercalation to Mt interlayer were electrostatic attraction and intermolecular force. The amount of intercalation affected application

parameters of composite material, such as viscosity, contact angle, and thixotropic loop area. This composite material was a kind of environmentally friendly organic clay composite and could be used in drilling fluid system.

Conflict of Interests

The authors declare that there is no conflict of interests regarding the publication of this paper.

Acknowledgments

This work is supported by National High-tech R&D Program (863 Program) (no. 2014AA06A614). Meanwhile, great thanks also go to former researchers for their excellent works, which give great help for our academic study.

References

- [1] M. Ogawa, *Photoprocesses in Clay-Organic Complexes*, Marcel Dekker, New York, NY, USA, 2004.
- [2] G. Lagaly, M. Ogawa, and I. Dékány, *Clay Mineral Organic Intercalation*, Elsevier, Amsterdam, The Netherlands, 2006.
- [3] N. Khaorapong, A. Ontam, J. Khemprasit, and M. Ogawa, "Formation of MnS- and NiS-montmorillonites by solid-solid reactions," *Applied Clay Science*, vol. 43, no. 2, pp. 238–242, 2009.
- [4] N. Khaorapong and M. Ogawa, "Solid-state intercalation of 8-hydroxyquinoline into Li(I)-, Zn(II)- and Mn(II)-montmorillonites," *Applied Clay Science*, vol. 35, no. 1-2, pp. 31–38, 2007.
- [5] N. Khaorapong, A. Ontam, and M. Ogawa, "Formation of ZnS and CdS in the interlayer spaces of montmorillonite," *Applied Clay Science*, vol. 50, no. 1, pp. 19–24, 2010.
- [6] W. Dye, K. d'Augereau, N. Hansen et al., "New water-based mud balances high-performance drilling and environmental compliance," in *Proceedings of the SPE/IADC Drilling Conference*, SPE/IADC Paper 92367, pp. 23–25, Amsterdam, The Netherlands, 2006.
- [7] C. Gatlin, *Petroleum Engineering: Drilling and Well Completions*, Prentice-Hall, Englewood Cliffs, NJ, USA, 1960.
- [8] B. G. Chesser, "Design considerations for an inhibitive, stable water-based mudsystem," in *Proceedings of the IADC/SPE Drilling Conference*, SPE Paper 14757, pp. 10–12, Dallas, Tex, USA, 1987.
- [9] V. C. Kelessidis, R. Maglione, C. Tsamantaki, and Y. Aspridakis, "Optimal determination of rheological parameters for Herschel-Bulkley drilling fluids and impact on pressure drop, velocity profiles and penetration rates during drilling," *Journal of Petroleum Science and Engineering*, vol. 53, no. 3-4, pp. 203–224, 2006.
- [10] S. Z. Jilani, H. Menouar, A. A. Al-Majed, and M. A. Khan, "Effect of overbalance pressure on formation damage," *Journal of Petroleum Science and Engineering*, vol. 36, no. 1-2, pp. 97–109, 2002.
- [11] N. M. Soule and S. E. Burns, "Effects of organic cation structure on behavior of organobentonites," *Journal of Geotechnical and Geoenvironmental Engineering*, vol. 127, no. 4, pp. 363–370, 2001.
- [12] S. E. Burns, S. L. Bartelt-Hunt, J. A. Smith, and A. Z. Redding, "Coupled mechanical and chemical behavior of bentonite engineered with a controlled organic phase," *Journal of Geotechnical and Geoenvironmental Engineering*, vol. 132, no. 11, pp. 1404–1412, 2006.
- [13] B. Bate and S. E. Burns, "Effect of total organic carbon content and structure on the electrokinetic behavior of organoclay suspensions," *Journal of Colloid and Interface Science*, vol. 343, no. 1, pp. 58–64, 2010.
- [14] A. Z. Redding, S. E. Burns, R. T. Upson, and E. F. Anderson, "Organoclay sorption of benzene as a function of total organic carbon content," *Journal of Colloid and Interface Science*, vol. 250, no. 1, pp. 261–264, 2002.
- [15] I. M.-C. Lo, "Organoclay with soil-bentonite admixture as waste containment barriers," *Journal of Environmental Engineering*, vol. 127, no. 8, pp. 756–759, 2001.
- [16] J. A. Smith and P. R. Jaffer, "Adsorptive selectivity of organic-cation-modified bentonite for nonionic organic contaminants," *Water, Air, and Soil Pollution*, vol. 72, no. 1–4, pp. 205–211, 1994.
- [17] J.-W. Park and P. R. Jaffé, "Partitioning of three nonionic organic compounds between adsorbed surfactants, micelles, and water," *Environmental Science & Technology*, vol. 27, no. 12, pp. 2559–2565, 1993.
- [18] G. Y. Sheng and S. A. Boyd, "Relation of water and neutral organic compounds in the interlayers of mixed Ca/trimethylphenylammonium-smectites," *Clays and Clay Minerals*, vol. 46, no. 1, pp. 10–17, 1998.
- [19] R. J. Lorenzetti, S. L. Bartelt-Hunt, S. E. Burns, and J. A. Smith, "Hydraulic conductivities and effective diffusion coefficients of geosynthetic clay liners with organobentonite amendments," *Geotextiles and Geomembranes*, vol. 23, no. 5, pp. 385–400, 2005.
- [20] J. Dupont, "On the solid, liquid and solution structural organization of imidazolium ionic liquids," *Journal of the Brazilian Chemical Society*, vol. 15, no. 3, pp. 341–350, 2004.
- [21] J. Dupont, G. S. Fonseca, A. P. Umpierre, P. F. P. Fichtner, and S. R. Teixeira, "Transition-metal nanoparticles in imidazolium ionic liquids: recyclable catalysts for biphasic hydrogenation reactions," *Journal of the American Chemical Society*, vol. 124, no. 16, pp. 4228–4229, 2002.
- [22] C. P. Mehnert, "Supported ionic liquid catalysis," *Chemistry—A European Journal*, vol. 11, no. 1, pp. 50–56, 2005.
- [23] A. Riisager, R. Fehrmann, M. Haumann, and P. Wasserscheid, "Supported ionic liquids: versatile reaction and separation media," *Topics in Catalysis*, vol. 40, no. 1–4, pp. 91–102, 2006.
- [24] P. Lozano, E. García-Verdugo, R. Piamtongkam et al., "Bioreactors based on monolith-supported ionic liquid phase for enzyme catalysis in supercritical carbon dioxide," *Advanced Synthesis and Catalysis*, vol. 349, no. 7, pp. 1077–1084, 2007.
- [25] S. J. Chipera and D. L. Bish, "Baseline studies of the clay minerals society source clays: powder X-ray diffraction analyses," *Clays and Clay Minerals*, vol. 49, no. 5, pp. 398–409, 2001.
- [26] D. Borden and R. F. Giese, "Baseline studies of the clay minerals society source clays: cation exchange capacity measurements by the ammonia-electrode method," *Clays and Clay Minerals*, vol. 49, no. 5, pp. 444–445, 2001.
- [27] A. R. Mermut and G. Lagaly, "Baseline studies of the clay minerals society source clays: layer-charge determination and characteristics of those minerals containing 2:1 layers," *Clays and Clay Minerals*, vol. 49, no. 5, pp. 393–397, 2001.
- [28] S. Azizian, "A novel and simple method for finding the heterogeneity of adsorbents on the basis of adsorption kinetic data," *Journal of Colloid and Interface Science*, vol. 302, no. 1, pp. 76–81, 2006.
- [29] B. Klebow and A. Meleshyn, "Monte Carlo study of the adsorption and aggregation of alkyltrimethylammonium chloride on the montmorillonite-water interface," *Langmuir*, vol. 28, no. 37, pp. 13274–13283, 2012.
- [30] S. Dultz, B. Riebe, and C. Bunnenberg, "Temperature effects on iodine adsorption on organo-clay minerals. II. Structural effects," *Applied Clay Science*, vol. 28, no. 1–4, pp. 17–30, 2005.
- [31] J. Bors, S. Dultz, and B. Riebe, "Retention of radionuclides by organophilic bentonite," *Engineering Geology*, vol. 54, no. 1-2, pp. 195–206, 1999.

- [32] R. L. Frost, Q. Zhou, H. He, and Y. Xi, "An infrared study of adsorption of para-nitrophenol on mono-, di- and tri-alkyl surfactant intercalated organoclays," *Spectrochimica Acta—Part A: Molecular and Biomolecular Spectroscopy*, vol. 69, no. 1, pp. 239–244, 2008.
- [33] N. V. Venkataraman and S. Vasudevan, "Conformation of methylene chains in an intercalated surfactant bilayer," *The Journal of Physical Chemistry B*, vol. 105, no. 9, pp. 1805–1812, 2001.
- [34] B. Ha and K. Char, "Conformational behavior of dodecyl-diamine inside the confined space of montmorillonites," *Langmuir*, vol. 21, no. 18, pp. 8471–8477, 2005.
- [35] R. A. Vaia, R. K. Teukolsky, and E. P. Giannelis, "Interlayer structure and molecular environment of alkylammonium layered silicates," *Chemistry of Materials*, vol. 6, no. 7, pp. 1017–1022, 1994.
- [36] Y. Li and H. Ishida, "Concentration-dependent conformation of alkyl tail in the nanoconfined space: hexadecylamine in the silicate galleries," *Langmuir*, vol. 19, no. 6, pp. 2479–2484, 2003.
- [37] Y. Xi, Z. Ding, H. He, and R. L. Frost, "Infrared spectroscopy of organoclays synthesized with the surfactant octadecyltrimethylammonium bromide," *Spectrochimica Acta—Part A: Molecular and Biomolecular Spectroscopy*, vol. 61, no. 3, pp. 515–525, 2005.
- [38] H. Hongping, F. L. Ray, and Z. Jianxi, "Infrared study of HDTMA⁺ intercalated montmorillonite," *Spectrochimica Acta Part A: Molecular and Biomolecular Spectroscopy*, vol. 60, no. 12, pp. 2853–2859, 2004.
- [39] K. Suga and J. F. Risling, "Structural characterization of surfactant and clay-surfactant films of micrometer thickness by FT-IR spectroscopy," *Langmuir*, vol. 9, no. 12, pp. 3649–3655, 1993.
- [40] L. Wu, C. Yang, L. Mei, F. Qin, L. Liao, and G. Lv, "Microstructure of different chain length ionic liquids intercalated into montmorillonite: a molecular dynamics study," *Applied Clay Science*, vol. 99, pp. 266–274, 2014.
- [41] H. Heinz, W. Paul, U. W. Suter, and K. Binder, "Analysis of the phase transitions in alkyl-mica by density and pressure profiles," *Journal of Chemical Physics*, vol. 120, no. 8, pp. 3847–3854, 2004.
- [42] H. Heinz, H. J. Castelijns, and U. W. Suter, "Structure and phase transitions of alkyl chains on mica," *Journal of the American Chemical Society*, vol. 125, no. 31, pp. 9500–9510, 2003.

Research Article

In-Channel-Grown Polypyrrole Nanowire for the Detection of DNA Hybridization in an Electrochemical Microfluidic Biosensor

Thi Luyen Tran,¹ Thi Xuan Chu,¹ Phuc Quan Do,² Duc Thanh Pham,¹
Van Vu Quan Trieu,¹ Dang Chinh Huynh,¹ and Anh Tuan Mai¹

¹Hanoi University of Science and Technology, No. 1, Dai Co Viet Road, Hanoi 100000, Vietnam

²University of Science, Vietnam National University (Hanoi), 334 Nguyen Trai Road, Hanoi 100000, Vietnam

Correspondence should be addressed to Thi Xuan Chu; xuan@itims.edu.vn and Anh Tuan Mai; tuan.maianh@hust.edu.vn

Received 17 June 2015; Revised 10 August 2015; Accepted 31 August 2015

Academic Editor: Matteo Tonezzer

Copyright © 2015 Thi Luyen Tran et al. This is an open access article distributed under the Creative Commons Attribution License, which permits unrestricted use, distribution, and reproduction in any medium, provided the original work is properly cited.

A triple electrode setup with a Pt pseudo-reference electrode integrated in a polydimethylsiloxane- (PDMS-) based microchamber was designed and fabricated. The integrated electrodes were deposited onto SiO₂/Si substrate by sputtering. The PDMS microchamber was patterned using an SU-8 mold and sealed with electrodes in oxygen plasma. Polypyrrole nanowires (PPy NWs) were electrochemically grown in situ at an accurate position of the working electrode in the sealed microchamber instead of in an open system. The DNA probe sequences were simply introduced into the channel to form bonds with the nanowires. A detection limit of 20 pM was achieved using a lock-in amplifier. The electrochemical characteristics produced by the hybridization of DNA strands in the microchamber showed a good signal/noise ratio and high sensitivity. Measurement of the DNA sensor in narrow space also required much less volume of the analytical sample compared with that in an open measuring cell. Results showed that this simple system can potentially fabricate nanostructures and detect bio/chemical molecules in a sealed system.

1. Introduction

In the 1990s, microfluidics emerged as a powerful technology and is now widely used in many fields, such as chemistry, biology, and biomedicine [1]. The combination of microfluidic technique and biosensors has attracted increasing attention [2–4] because of its many advantages, including small sample consumption, fast analysis, high sensitivity, and portability. The development of microfluidics integrated with biosensors is also considered a stepping stone for future lab-on-chip device. Instead of carrying out individual steps, all steps are combined in a small handy kit consisting of a number of components, such as pumps, chamber, mixing chamber, and controllable valves [5, 6]. Almost all manipulations have occurred within the system, including preparation of reagents, reaction, detection, data acquisition, and treatment [7, 8]. The combined microfluidic technique and biosensor not only develop the analytical ability and results but also broaden the perspective of possible application.

In this study, electrochemical sensors were used because of high precision and integration ability [2, 9–12]. The sensor consists of working, counter, and reference electrodes. Given that these electrodes are integrated in the microchamber, the replacement of the conventional reference electrode by a pseudo-reference electrode (PRE) facilitates the miniaturization of the analytical system. The microfluidic biosensor integrated PRE has been used in many studies for the determination of medicament [13], cell morphological changes [12], heavy metals [14], and glucose [2] in aqueous solution. However, little research has been dedicated to the synthesis of nanostructures inside the integrated three-electrode chip.

Nowadays, one-dimensional nanoscale structures, such as rod, tube, and wire, become indispensable for microfluidic devices because of their unique properties at micro- and nanoscales [11, 15]. The fabrication of nanostructures at accurate position inside the packed devices is also very important for bioelement immobilization and detection. The conducting polymers, such as PPy, polyaniline, and polythiophene,

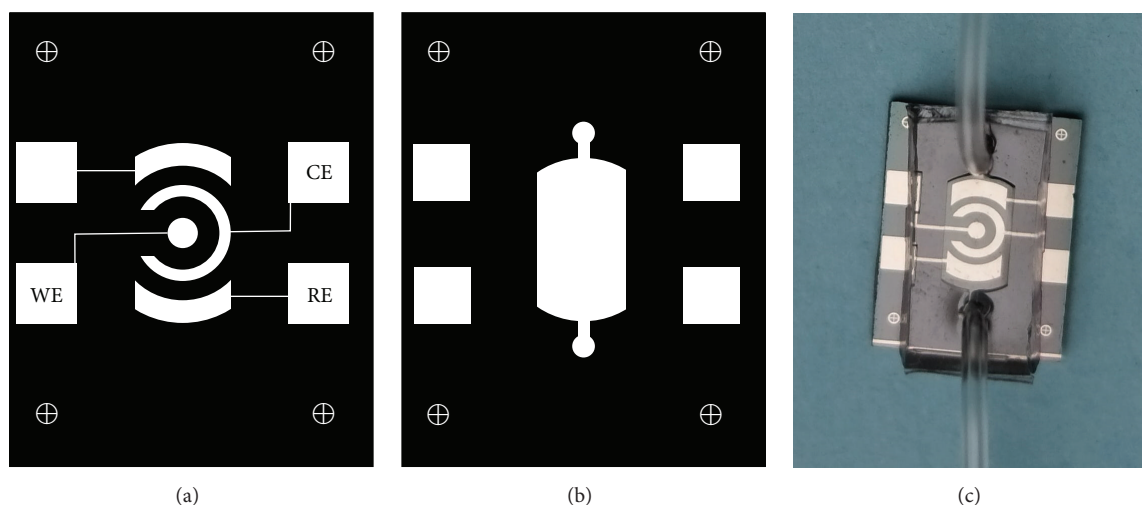


FIGURE 1: (a) The mask for Pt electrode fabrication (Mask 1) and (b) for SU-8 mold (Mask 2); (c) the integrated three-electrode sensor using Pt pseudo-reference electrode in the microchamber. The size of the chip: 12×15 mm.

play an important role in immobilizing bioelements to enhance the sensitivity and stability of the electrochemical biosensors [16, 17]; PPy is one of the most popular polymers because of its good electrical conductivity, ease of preparation, and chemical stability [18, 19]. Recent works [20, 21] reported the synthesis of PPy NWs in an open system. PPy NWs facilitate the immobilization of biorecognition on the sensor's surface and increase the sensitivity of the sensor compared with the PPy bulk film [22].

The present work aims to study the growth of PPy NWs in microchamber. We hypothesize that the nanostructure of polypyrrole, microchamber, and triple-electrode integration may improve the biosensor's characteristics.

2. Materials and Methods

2.1. Chemicals. SU-8 3050 and PDMS Sylgard 184 were obtained from Microchem and Dow Corning, respectively. Meanwhile, pyrrole (99.9%) and phosphate buffer solution (PBS) were purchased from Merck. The supporting chemicals $\text{LiClO}_4 \cdot 3\text{H}_2\text{O}$, gelatin, KCl, $\text{K}_2\text{Cr}_2\text{O}_7$ (99%), H_2SO_4 (98%), N_2 (99.9%), $\text{K}_3\text{Fe}(\text{CN})_6$, and $\text{K}_4\text{Fe}(\text{CN})_6$ are of analytical grade. ssDNA were obtained from Sigma Aldrich.

The ssDNA probe and the complementary and noncomplementary target are as follows:

Probe: thiol- C_6 -5'-AGACCTCCAGTCTCCATGGTACGTC-3'.

Complementary target: 5'-GACGTACCATGGAGACTGGAGGTCT-3'.

Noncomplementary target: 5'-ACGCTGAGTACGGTGCAAGAGTCA-3'.

2.2. Integrated Three-Electrode Setup Using

Pt PRE Associated with the Microchamber

Fabrication of the Three-Electrode Setup. The integrated Pt electrode consists of a round working electrode with 0.8 mm^2

area, a 5 mm^2 counter electrode, and a reference electrode (Figure 1(a)). These electrodes were deposited on SiO_2/Si substrate by cathode sputtering technique. The fabrication process was previously discussed in detail [20].

Fabrication of the Microchamber. The SU-8 mold was prepared by using a conventional photolithography technique (Figure 1(b)). After cleaning with $\text{K}_2\text{Cr}_2\text{O}_7$, the silicon wafer was deposited with $250 \mu\text{m}$ thick SU-8 3050 using simple spin coating at 500 rpm for 60 s [25]. By applying Mask 2, the wafer was exposed to the UV light (250 W , 12 mW/cm^2) for 30 s. The development was followed by the immersion of wafer in a sonicated 1-ethoxy-2-propyl acetate solution for 7 min to remove the unexposed parts. Finally, the wafer was rinsed with deionized water and blown dry with nitrogen. The SU-8 on the wafer was defined as the mold for the next step. The microchamber was first formed by locating the mold in a plastic Petri dish. Subsequently, the PDMS prepolymer and curing agent solution (10 : 1 in volume) were poured into the dish. The mixture was degassed in a vacuum desiccator and solidified at 70°C in 2 h.

Bonding of Microchamber and Electrodes. The electrodes were bonded with the PDMS microchamber in oxygen plasma (10 Pa and 20 W for 20 s, Figure 1(c)). Sealing was stabilized by further heat treatment in 15 min at 70°C and cooled down to room temperature.

2.3. Electrochemical Synthesis of PPy NWs inside the

Microchamber. The PPy NWs were synthesized using the PGSTAT30 AutoLab electrochemical workstation (Eco Chemie, Netherlands) inside the sealed system fabricated above. Before the experiment, the electrode system was cleaned in a saturated solution of $\text{K}_2\text{Cr}_2\text{O}_7/\text{H}_2\text{SO}_4$ and electrochemically activated in $0.5 \text{ M H}_2\text{SO}_4$ solution by sweeping the voltage from -0.5 V to 1 V until the cyclic voltammetry characteristics were stable. Electrolyte solution, which is composed of 0.1 M pyrrole monomer, 0.08%

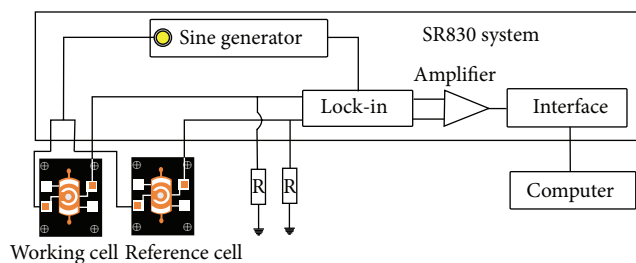


FIGURE 2: The differential measurement setup using SR830 DSP lock-in amplifier.

gelatin in weight, 0.1 M LiClO₄, and PBS buffer (pH = 7.4), was pumped into the microchamber. To purge the dissolved oxygen in the electrolyte, N₂ gas was blown into the chamber for 15 min. Polymerization was conducted at room temperature for 1200 seconds. The applying polarized voltage was set at 0.5 V.

The surface morphology of the working electrode was investigated using Hitachi S4800 Scanning Electron Microscope (SEM). Meanwhile, the structure of the obtained PPy NWs was investigated using Thermo Nicolet 6700 Fourier Transform Infrared (FTIR) spectroscopy. Cyclic voltammograms (CV) measurements were performed in 0.03 M K₃Fe(CN)₆/K₄Fe(CN)₆ and 0.1 M KCl solution at 25 mV/s scan rate to investigate the electrochemical behavior of the integrated three-electrode system inside the microchamber. Electrochemical impedance spectroscopy (EIS) measurements of PPy NWs/Pt electrodes were performed within the frequency range of 5·10⁴–0.05 Hz at an applied DC potential and amplitude of 50 and ±5 mV, respectively, in an electrolyte solution containing 0.03 M K₃Fe(CN)₆/K₄Fe(CN)₆ and 0.1 M KCl in the microchamber.

2.4. Probe DNA Immobilization on the PPy NWs/Pt Electrodes. DNA probe sequences were immobilized on the PPy NWs/Pt electrode using the adsorption method. A volume of 4 μL of 10 μM probe DNA solution was pumped into the electrode-integrated microchamber for 2 h. The system was cleaned by deionized water to remove the unspecific probe DNA molecules, which did not bind or have weak linkage with PPy NWs. The DNA electrodes were dried and prepared for further measurements.

2.5. DNA Hybridization Detection Using Lock-In Amplifier. The measurement of DNA hybridization was performed at room temperature by using SR830 DSP lock-in amplifier from the Stanford Research (Figure 2). The lock-in amplifiers are used to detect and measure very small AC signals, down to a few nanovolts. The SR830 generates its own sine wave, named reference signal, which has a frequency and amplitude of 10 kHz and 100 mV, respectively. This reference signal was then set on two identical electrodes of two different systems for excitation and amplification. The surface of one electrode was immobilized with the probe DNA/PPy nanowires (as working electrode), and the surface of the remaining electrode was modified using PPy nanowires only (as reference electrode). When about 4 μL of the solution

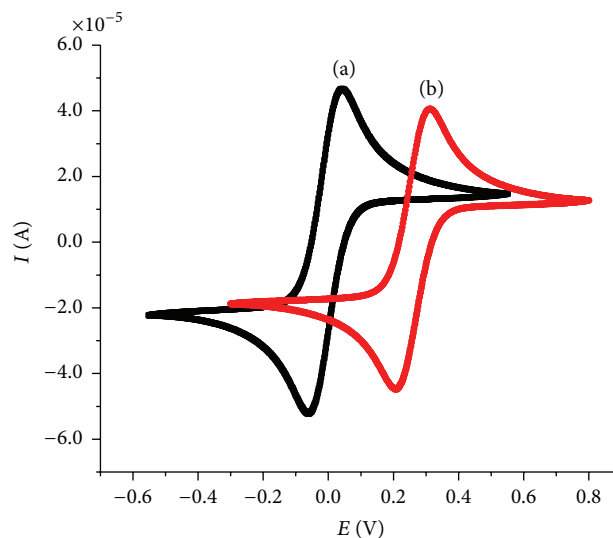


FIGURE 3: Cyclic voltammograms measured in 0.03 M K₃Fe(CN)₆/K₄Fe(CN)₆ and 0.1 M KCl solution at 25 mV/s scan rate of (a) integrated three-electrode system inside the microchamber using Pt electrode as pseudo-reference electrode and (b) three-electrode system using Ag/AgCl (in saturated KCl) reference electrode in the open cell.

containing the complementary target DNA was pumped into the microchamber, DNA hybridization occurred on the working electrode (with the immobilized probe DNA), and thus the change in the charges of the conducting membrane and thereby the output signal compared with that in reference electrode (without the immobilized probe DNA) as the final output signal.

3. Results and Discussion

3.1. Electrochemical Behavior of the Integrated Three-Electrode System in the Microchamber. Figure 3 shows the CV of the three-electrode system inside the microchamber using Pt electrode as pseudo-reference electrode (Figure 3(a)) and in the open cell using Ag/AgCl (in saturated KCl) conventional reference electrode (Figure 3(b)), measured in 0.03 M K₃Fe(CN)₆/K₄Fe(CN)₆ and 0.1 M KCl solution at 25 mV/s scan rate. The performance of the integrated system using the Pt pseudo-reference electrode (located inside the microchamber) was as good as that obtained in the open cell. In both cases, two peaks (0.05 V/−0.05 V and 0.31 V/0.21 V) corresponded to the oxidation of Fe²⁺ and reduction of Fe³⁺ on the CV curves, respectively. The difference between the anodic and cathodic peak potentials, ΔE, was almost unchanged after 10 CV cycles. In the microchamber, an increase in the electron transfer of the redox couple (ferro/ferricyanide) caused the total measured current to increase to about 10% compared with the open system. The electrochemical characteristics are well stable because of the narrow, packed microchamber. The use of such microchamber can reduce the analytical volume and is expected to increase accuracy, enhance the rate of signal/noise, and contribute

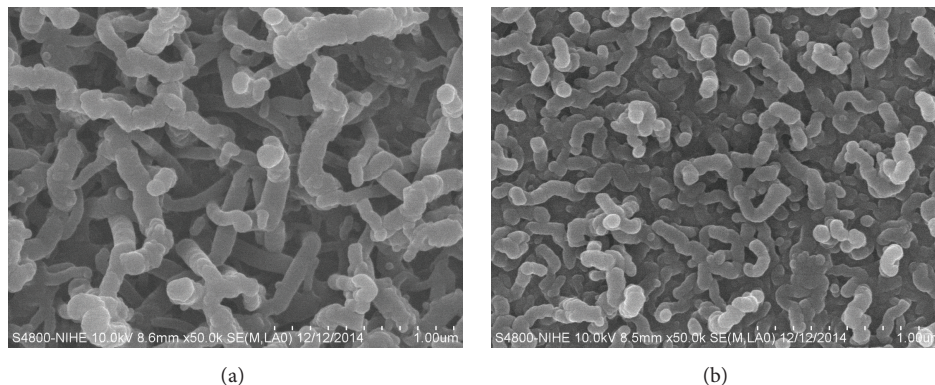


FIGURE 4: FE-SEM images of PPy nanowires synthesized in 0.1 M Py, 0.1 M LiClO₄, PBS, and gelatin 0.08% wt in the microchamber by using (a) potentiostatic mode (0.5 V, 1200 s) and (b) cyclic voltammetry mode (0–0.6 V, 6 scans, 25 mV/s scan rate).

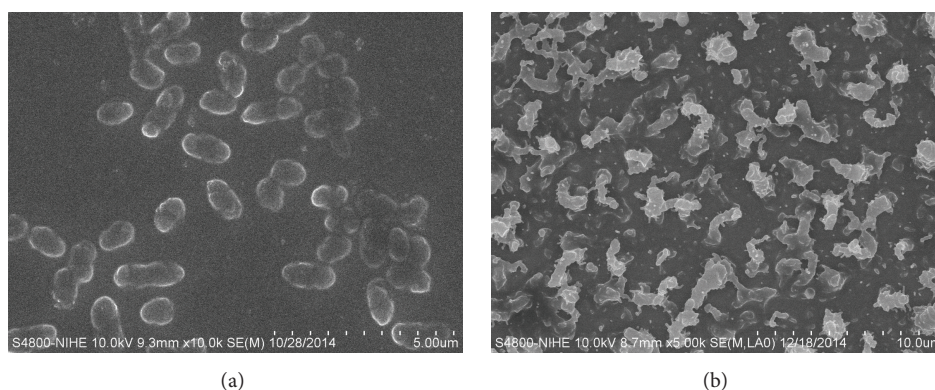


FIGURE 5: FE-SEM images of products synthesized in 0.1 M LiClO₄, PBS, and gelatin 0.08% wt and (a) without Py; (b) 0.1 M Py in the microchamber by using potentiostatic mode (0.5 V, 150 s).

to improvement of the sensitivity of electrochemical sensors. These advantages make this microchamber suitable for biosensor application.

The voltage corresponding to the peak of Fe²⁺ oxidation was reduced by 0.26 V compared with the use of Ag/AgCl (in saturated KCl) as reference electrode (Figure 3). The replacement of a conventional reference electrode (normally confined in a saturated KCl solution) by a pseudo-electrode caused the shift on the potential. Fortunately, this shift in potential did not influence the final result as the data were acquired and processed in differential mode. Thus, the applied polarized voltage was set at 0.50 V for the synthesis of PPy NWs in the microchamber, instead of 0.75 V in the case of an open cell in previous works [20, 21].

3.2. Electrochemical Synthesis of PPy NWs in the Microchamber

FE-SEM Images of PPy NWs. Figure 4 shows the SEM images of PPy synthesized using potentiostatic mode (Figure 4(a)) and cyclic voltammetry mode (Figure 4(b)). When using the two electrochemical techniques, PPy NWs with 80–110 nm diameter and few micrometers long were formed on the surface of the working electrode. The size of the synthesized PPy NWs is uniform, and the nanowires are

evenly distributed throughout the surface of the working electrode. Generally, the electrochemical polymerization in narrow space (4 μL in this work) without agitation caused the difficulty of growing PPy NWs. However, the isolated sealed cell could reduce the interference and influence of the surrounding environment significantly. PPy NWs were grown with high uniformity and distributed porosity that is favorable for the immobilization process of DNA through the linkages between the amino groups of PPy NWs and phosphate groups of DNA strands.

Gelatin and the Growth of PPy NWs in the Microchamber. The synthesized PPy with cauliflower structure was previously reported [20, 21]. Gelatin, as a soft mold, helped in the growth of PPy in nanowire form. To understand the role of gelatin in the polymerization process, electrochemical synthesis was performed in potentiostatic mode (0.5 V, 150 s), with 0.08 wt% gelatin but without Py monomers (Figure 5(a)) and with 0.1 M Py monomers (Figure 5(b)). In Figure 5(a), the capsule-shaped blocks of gelatin were formed with a diameter of about 1 μm. Meanwhile, in Figure 5(b), PPy NWs (D~100 nm) began to grow around the gelatin blocks. This behavior could be observed because polymerization was established in 150 s, which is the propagation phase of a polymerization reaction. The long chain structure of gelatin

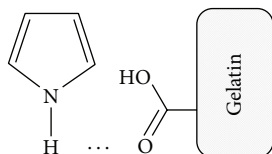


FIGURE 6: Hydrogen bond between pyrrole monomer and gelatin.

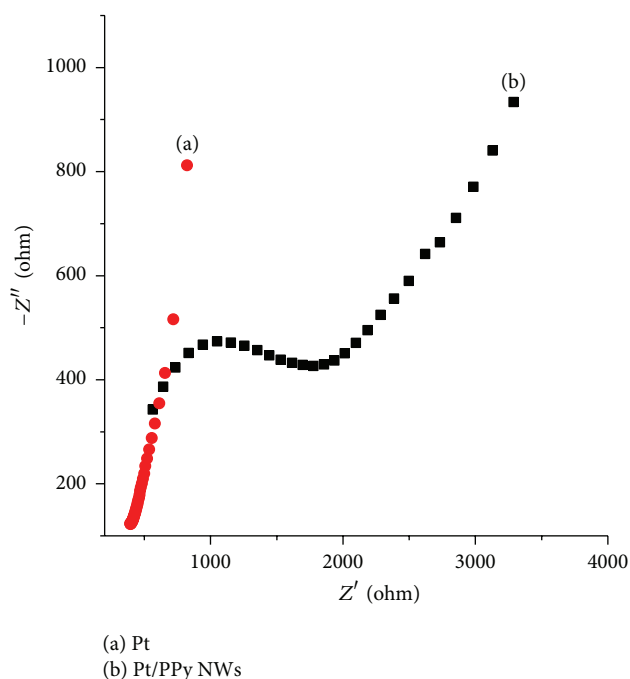


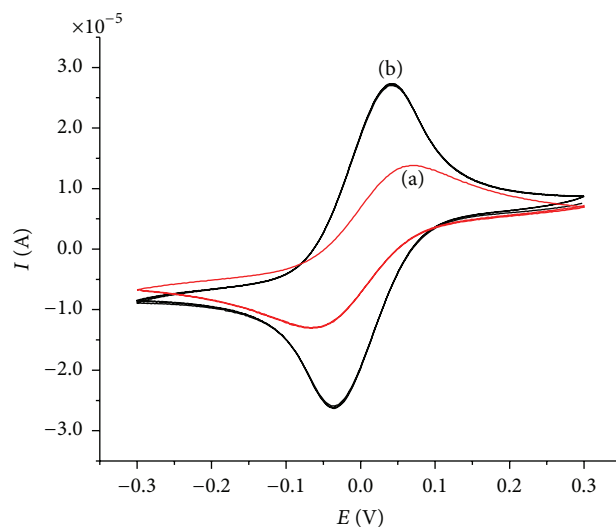
FIGURE 7: Electrochemical impedance spectra of (a) Pt and (b) Pt/PPy NWs electrodes.

contains various amino acids (functioned with $-\text{NH}_2$ and $-\text{COOH}$ groups). The $-\text{COOH}$ group can bind with $-\text{NH}$ group of pyrrole monomer, by means of hydrogen bond (Figure 6). Consequently, pyrrole monomers are adsorbed onto the surfaces of the gelatin chains, and polymerization continued to form PPy nanowires. Gelatin is supposed to act as the “soft template” to guide the PPy nanowire formation [26].

Electrochemical Impedance Spectra of Pt and Pt/PPy NW Electrodes. Figure 7 shows electrochemical impedance spectra in the Nyquist form of Pt and Pt/PPy NW electrodes; EIS was performed in the frequency range of $5 \cdot 10^4 - 0.05$ Hz at an applied DC potential and amplitude of 50 and ± 5 mV, respectively, in the electrolyte solution containing 0.03 M $\text{K}_3\text{Fe}(\text{CN})_6/\text{K}_4\text{Fe}(\text{CN})_6$ and 0.1 M KCl. Generally, the impedance is represented by

$$Z_{(\omega)} = Z_{\text{re}} - jZ_{\text{im}}, \quad (1)$$

where Z_{re} and Z_{im} are the real and imaginary parts of the impedance, respectively. Unlike the electrochemical impedance of Pt electrode, the electrochemical impedance spectrum of Pt/PPy NW electrode consists of two parts:



(a) WE: Pt
(b) WE: Pt/PPy NWs

FIGURE 8: Cyclic voltammograms measured in 0.03 M $\text{K}_3\text{Fe}(\text{CN})_6/\text{K}_4\text{Fe}(\text{CN})_6$ and 0.1 M KCl solution at 25 mV/s scan rate of the integrated three-electrode system inside the microchamber (a) before and (b) after electrochemical synthesis of PPy NWs on the working electrode.

a semicircle that characterizes charge transfer process and a linear region that characterizes diffusion process. This result further confirms that PPy NWs were formed on the electrode surface.

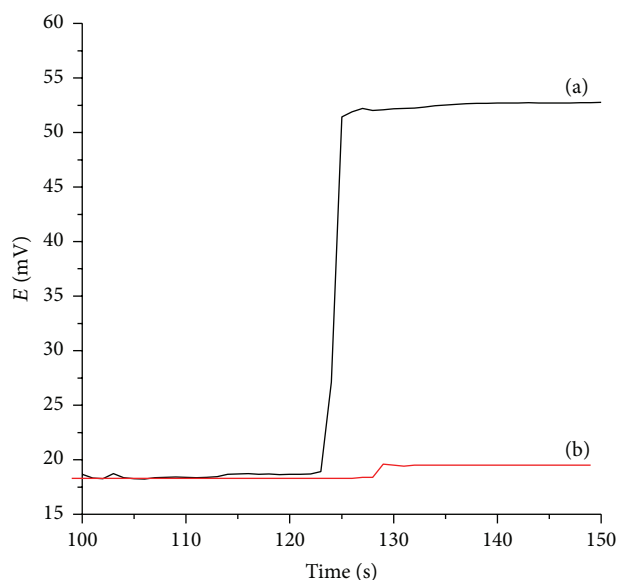
Cyclic Voltammograms of Pt and Pt/PPy NW Electrodes. Figure 8 shows the CV measured in 0.03 M $\text{K}_3\text{Fe}(\text{CN})_6/\text{K}_4\text{Fe}(\text{CN})_6$ and 0.1 M KCl solution at 25 mV/s scan rate of the integrated three-electrode system inside the microchamber before and after the electrochemical synthesis of PPy NWs. The potentials corresponding to the oxidation of Fe^{2+} and reduction of Fe^{3+} do not change. This result demonstrates that PPy NWs material formed on the working electrode has stable electrochemical behavior. Moreover, in the case of Pt/PPy NW working electrode (Figure 8(b)), the peak current is higher than that of Pt working electrode (Figure 8(a)). This observation is explained by the increase in specific surface area, thereby leading to the accumulation of the electroactive species on the surface, as well as the current density.

3.3. Determination of DNA Hybridization. When about $4 \mu\text{L}$ of sample containing 2 nM complementary target DNA was pumped into the microchamber, the DNA hybridization occurred rapidly; the response time was only few seconds and represented by the change in output signal (Figure 9(a)). We repeated the injection of a volume containing 2 nM noncomplementary target DNA; the output signal almost remained unchanged and was stable after one minute (Figure 9(b)).

The different concentrations of the target were tested with the microfluidics-based biosensor. The output signals increase linearly with the DNA target concentration and

TABLE 1: Comparison of the DNA sensor with some other works.

Technique of detection	Surface modification	Measurement system	Limit of detection	Reference
EIS	PPy NWs	Open system	10 pM	[20]
Lock-in amplifier	MWCNTs	Open system	1 nM	[23]
Lock-in amplifier	PPy NWs	Open system	100 pM	[21]
Electrochemical method	PPy film-AuNPs	Open system	150 pM	[24]
Lock-in amplifier	PPy NWs	Sealed system	20 pM	Current work



(a) 2 nM complementary DNA
(b) 2 nM noncomplementary DNA

FIGURE 9: The signals of DNA hybridization, $C_{\text{DNA probe}} = 10 \mu\text{M}$, $T = 298 \text{ K}$: (a) 2 nM complementary target DNA and (b) 2 nM noncomplementary target DNA.

reach the saturated value at $2 \cdot 10^{-7} \text{ M}$. The empirical data showed a detection limit of 20 pM (Figure 10). Table 1 shows that the obtained results in this work are much better than in our previous work [21] that used a similar detection method in an open system. The obtained results in this study are interesting because the fabrication processes for both electrodes and microchamber are simple (they do not require many photomasks or high-end etching machines); meanwhile, the limit of detection is comparable with other works. The injection volume is also much smaller than that required for the measurement in an open system. Performing measurements in the sealed microchamber could reduce possible noise and improve the response time.

4. Conclusion

We developed a platform consisting of an integrated three-electrode configuration fabricated with sputtering method and a PDMS-based microchamber. The PPy NWs were in situ synthesized in the sealed system at desired position using electrochemical method. The growth mechanism of

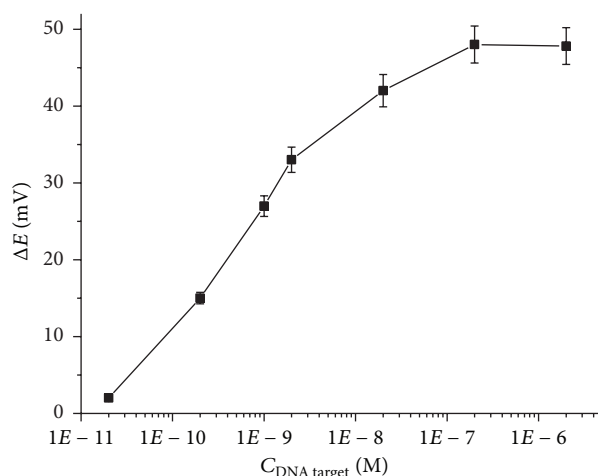


FIGURE 10: The signals of DNA hybridization corresponding to complementary DNA with different concentrations.

PPy NWs in the presence of gelatin was investigated and proposed. DNA probe sequences were effectively immobilized on the surface of the DNA sensor through linkages with polypyrrole nanowires. DNA sensor can respond until the 20 pM addition of the target DNA into the microchamber at 25°C , which is greater than that reported previously in an open system under similar conditions. Moreover, the volume of the analytical sample was reduced when using the DNA sensor integrated with the microchamber compared with that in the open measuring cell. These results show that this simple and low-cost microfluidic platform has potential application for lab-on-chip electroanalytical device, in which the working electrode can be modified with conducting polymer in the microchamber.

Conflict of Interests

The authors declare that there is no conflict of interests regarding the publication of this paper.

Acknowledgment

This research is supported by the Vietnam National Foundation for Science and Technology Development (NAFOSTED) under Grant no. 103.02-2012.78.

References

- [1] P. Tabeling, *Introduction to Microfluidics*, Oxford University Press, Oxford, UK, 2010.
- [2] Y. Wang, Q. He, Y. Dong, and H. Chen, "In-channel modification of biosensor electrodes integrated on a polycarbonate microfluidic chip for micro flow-injection amperometric determination of glucose," *Sensors and Actuators, B: Chemical*, vol. 145, no. 1, pp. 553–560, 2010.
- [3] H. Baccar, M. B. Mejri, R. Prehn et al., "Interdigitated micro-electrode arrays integrated in microfluidic cell for biosensor applications," *Journal of Nanomedicine & Nanotechnology*, vol. 5, no. 6, article 243, 2014.
- [4] J. Wu, R. Wang, H. Yu et al., "Inkjet-printed microelectrodes on PDMS as biosensors for functionalized microfluidic systems," *Lab on a Chip*, vol. 15, no. 3, pp. 690–695, 2015.
- [5] S. Choi, M. Goryll, L. Y. M. Sin, P. K. Wong, and J. Chae, "Microfluidic-based biosensors toward point-of-care detection of nucleic acids and proteins," *Microfluidics and Nanofluidics*, vol. 10, no. 2, pp. 231–247, 2010.
- [6] S. Prakash, M. Pinti, and B. Bhushan, "Theory, fabrication and applications of microfluidic and nanofluidic biosensors," *Philosophical Transactions of the Royal Society A: Mathematical, Physical and Engineering Sciences*, vol. 370, no. 1967, pp. 2269–2303, 2012.
- [7] Y.-J. Yoon, K. H. H. Li, Y. Z. Low, J. Yoon, and S. H. Ng, "Microfluidics biosensor chip with integrated screen-printed electrodes for amperometric detection of nerve agent," *Sensors and Actuators, B: Chemical*, vol. 198, pp. 233–238, 2014.
- [8] P. Neuzil, S. Giselbrecht, K. Länge, T. J. Huang, and A. Manz, "Revisiting lab-on-a-chip technology for drug discovery," *Nature Reviews Drug Discovery*, vol. 11, no. 8, pp. 620–632, 2012.
- [9] Z. Nie, C. A. Nijhuis, J. Gong et al., "Electrochemical sensing in paper-based microfluidic devices," *Lab on a Chip*, vol. 10, no. 4, pp. 477–483, 2010.
- [10] N. M. M. Pires, T. Dong, U. Hanke, and N. Hoivik, "Recent developments in optical detection technologies in lab-on-a-chip devices for biosensing applications," *Sensors*, vol. 14, no. 8, pp. 15458–15479, 2014.
- [11] K. N. Han, C. A. Li, M.-P. N. Bui et al., "On-chip electrochemical detection of bio/chemical molecule by nanostructures fabricated in a microfluidic channel," *Sensors and Actuators, B: Chemical*, vol. 177, pp. 472–477, 2013.
- [12] S. K. Srivastava, R. Ramaneti, M. Roelse et al., "A generic microfluidic biosensor of G protein-coupled receptor activation—impedance measurements of reversible morphological changes of reverse transfected HEK293 cells on microelectrodes," *RSC Advances*, vol. 5, no. 65, pp. 52563–52570, 2015.
- [13] H. E. A. Ferreira, D. Daniel, M. Bertotti, and E. M. Richter, "A novel disposable electrochemical microcell: construction and characterization," *Journal of the Brazilian Chemical Society*, vol. 19, no. 8, pp. 1538–1545, 2008.
- [14] R. A. B. da Silva, E. G. N. de Almeida, A. C. Rabelo, A. T. C. da Silva, L. F. Ferreira, and E. M. Richter, "Three electrode electrochemical microfluidic cell: construction and characterization," *Journal of the Brazilian Chemical Society*, vol. 20, no. 7, pp. 1235–1241, 2009.
- [15] J. Puigmarti-Luis, M. Rubio-Martínez, U. Hartfelder, I. Imaz, D. Maspocho, and P. S. Dittrich, "Coordination polymer nanofibers generated by microfluidic synthesis," *Journal of the American Chemical Society*, vol. 133, no. 12, pp. 4216–4219, 2011.
- [16] M. Y. Elahi, S. Z. Bathaie, S. H. Kazemi, and M. F. Mousavi, "DNA immobilization on a polypyrrole nanofiber modified electrode and its interaction with salicylic acid/aspirin," *Analytical Biochemistry*, vol. 411, no. 2, pp. 176–184, 2011.
- [17] M. Gerard, A. Chaubey, and B. D. Malhotra, "Application of conducting polymers to biosensors," *Biosensors and Bioelectronics*, vol. 17, no. 5, pp. 345–359, 2002.
- [18] W. Wernet, "Thermoplastic and elastic conducting polypyrrole films," *Synthetic Metals*, vol. 41, no. 3, pp. 843–848, 1991.
- [19] J. Kochana, K. Hnida, G. Sulka, P. Knihnicki, J. Kozak, and A. Gilowska, "Application of polypyrrole nanowires for the development of a tyrosinase biosensor," *Chemical Papers*, vol. 69, no. 8, pp. 1130–1135, 2015.
- [20] T. L. Tran, T. X. Chu, D. C. Huynh, D. T. Pham, T. H. T. Luu, and A. T. Mai, "Effective immobilization of DNA for development of polypyrrole nanowires based biosensor," *Applied Surface Science*, vol. 314, pp. 260–265, 2014.
- [21] A. T. Mai, T. P. Duc, X. C. Thi, M. H. Nguyen, and H. H. Nguyen, "Highly sensitive DNA sensor based on polypyrrole nanowire," *Applied Surface Science*, vol. 309, pp. 285–289, 2014.
- [22] J. Jang, "Conducting polymer nanomaterials and their applications," in *Emissive Materials Nanomaterials*, vol. 199 of *Advances in Polymer Science*, pp. 189–260, Springer, Berlin, Germany, 2006.
- [23] N. T. Thuy, P. D. Tam, M. A. Tuan et al., "Detection of pathogenic microorganisms using biosensor based on multi-walled carbon nanotubes dispersed in DNA solution," *Current Applied Physics*, vol. 12, no. 6, pp. 1553–1560, 2012.
- [24] E. Spain, T. E. Keyes, and R. J. Forster, "Polypyrrole-gold nanoparticle composites for highly sensitive DNA detection," *Electrochimica Acta*, vol. 109, pp. 102–109, 2013.
- [25] L. T. H. Thuong, T. T. Luyen, D. P. Quan et al., "Design and fabrication of microfluidic biosensor composed of a PDMS microchannel and three electrode platform for electrochemical measurement," in *Proceedings of the 2nd International Conference on Advanced Materials and Nanotechnology (ICAMN '14)*, pp. 254–260, Hanoi, Vietnam, October–November 2014.
- [26] D. Ge, J. Mu, S. Huang et al., "Electrochemical synthesis of polypyrrole nanowires in the presence of gelatin," *Synthetic Metals*, vol. 161, no. 1–2, pp. 166–172, 2011.